SURFACE HEATING IN METALS IRRADIATED BY FAST I.R LASER PULSES

by

CHARLES ADYEERI BYABAGAMBI

Thesis submitted for the degree of Ph.D under General Regulations.

Department of Mechanical Engineering,

University Of Glasgow

January 1987

SYNOPSIS

For the laser output to be optimized to the requirements of the workpiece the behaviour of the irradiated material must be known with reasonable accuracy. This requires modelling of the interaction processes for the materials concerned. The validity of the Fourier conduction theory within the context of high powered laser irradiation has been raised by several workers who have proved it to be invalid both in terms of its resolution of sharp energy gradients and inability to cope with non-equilibrium energy transport between electrons and lattice phonons. An alternative theory of energy transport based on the Electron Kinetic theory is therefore presented and the results compared with those obtained using the Fourier conduction theory. It is found that the results obtained using the Electron theory are in better agreement with available experimental results.

The new model is then extended to include evaporation effects.

Previous computer simulations of high mean power, high pulse repetition frequency (p.r.f) lasers have predicted the characteristics of the first output pulse only. This pulse, however, is not representative of the subsequent pulses as the simulation is initiated using conditions based on thermodynamic equilibrium. Using a modified kinetic model which incorporates plasma temperature variation, optical cavity characteristics and transverse gas flow, the simulation was extended to include the

second output power pulse. A substantial difference was found between the first and second pulse profiles. This extended model, is essential as it identifies further the control variables which can be used to optimize beam characteristics for material processing applications. It also gives closer agreement with experimental measurements made under continuously running conditions.

ACKNOWLEDGEMENT

I wish to express my sincere thanks and gratitude to my supervisors, Prof. Brian F. Scott and Dr. Chris R. Chatwin, for their encouragement, advice and patience throughout this project.

I am also very grateful to the University of Glasgow and the Overseas Research Scheme for their financial help.

Thanks are again due to Prof. B. F. Scott for making the departmental facilities available.

CONTENTS PAGE NUMBER

CHAPTER 1

INTRODUCTION

1.1 The case for a Pulsed CO_2 Laser

Due to their ability to deliver very high power intensities to localized regions, lasers are now considered practical and economical tools for several industrial material processing applications such as welding, drilling, cutting, heat treatment and surface engineering. Power intensities in the range 10^{10}-10^{13} W/m^2 are required to generate non-conduction limited processes, the actual power intensities being dependent upon workpiece properties and process requirements. These large power intensities are easily produced using commonly available commercial solid state laser systems.

Solid state devices operating in pulsed mode are used for drilling, spot welding and cutting of metals. These devices utilise elements of Neodymium in either glass (Nd^{3+}:Glass) or Yttrium Aluminium Garnet (Nd^{3+}:Yag) hosts. They are restricted to operate at low mean powers of the order of 300 watts and to low repetition frequencies resulting in melt-freeze processing which is used for continuous operations but produces cuts that are more correctly thought of as a series of drilled holes of sufficient proximity to give the appearance of a continuous process. Instantaneous powers are in excess of 100kW. These systems will only cope with material thicknesses of a few millimeters.

CO_2 gas lasers, capable of both continuous and pulsed

operations are used for many heavy duty material processing applications. Continuous wave (cw) systems operate at high mean powers of up to 20 kW, but have a restricted peak power capability and depend upon gas jet enhancement for successful operation. Existing commercial pulsed gas systems are able to deliver power intensities that compete well with solid state systems but at pulse repetition frequencies too low for true continuous processing.

Power intensity and the intensity profile in the workpiece are key parameters affecting performance when machining engineering materials. Control and tuning of these parameters strongly influence laser design and material processing characteristics. They are therefore examined herein.

Solid state systems:

The normal operating wavelength of the solid state laser is 1.06 microns. At this wavelength the power absorption of most materials and metals in particular, is sufficiently high for the material to be readily driven into the highly absorbing state in which non-conduction limited processes occur. This results in easy machining and the effective use of available energy.

The overall laser efficiency is however very low, of the order of 2 %, so that the thermal loading of the laser rod is substantial. This factor limits solid state laser perfomance and applications. Also the pulse repetition rate is low, typically 100Hz, so that the workpiece cools substantially during the inter-pulse period.

Currently the maximum mean power available is 600 watts with

a promise of 1 kW in the near future. Although, new designs using slabs or discs offer higher powers in the future, there are severe problems of divergence and hence beam quality. This restricts their usefulness for materials processing.

Gas systems:

Unlike solid state devices, CO_2 lasers useful for machining processes can be operated both in the continuous and pulsed mode.

(i) Continuous mode

When working in the continuous mode, the instantaneous power and mean power are identical. At mean powers much greater than 5 kW thermal distortion of the optical chain often results in focused irradiances that are lower than a laser with lower mean power. High mean power devices also pose a substantial waste heat removal problem, for example, a typical 200 kW cw system has about 180 kW of degraded electrical energy which must be removed through the heat exchangers.

(ii) The pulsed CO_2 Laser

Nitrogen-Carbon dioxide mixtures can be pulsed to give high output pulse intensities and a relatively low average output power which minimizes thermal distortion of the optical system. Pulsed excitation allows power intensities and intensity profiles to be carefully matched to the machining requirements of any material. This fine tuning is exerted by variation of

the gas mixture total pressure, constituent partial pressure, injection of radiation and electrical pumping pulse. Quasi-continuous heating of the material workpiece can be sustained if the pulse repetition frequency is sufficiently high. Fig.(1.1) as reported by Bakewell [1] shows the response of Aluminium to pulsed CO_2 laser heating vis-a-vis surface temperature, absorbed flux and incident flux. Extrapolation shows that once the surface temperature has been raised it remains in the enhanced absorption region for some 100 microseconds, which means that if the pulse is repeated every 100 microseconds (i.e a pulse repetition frequency (prf) of 10KHz) successive pulses encounter the high surface temperature caused by the previous pulse. Thus, a pulse repetition frequency of 10KHz ensures that the metal surface remains in the enhanced absorption region between pulses, giving the virtual continuous heating alluded to previously.

If the instantaneous power is too high a plasma is produced at the metal surface which is highly absorbent and causes severe attenuation of the incident beam. These high instantaneous powers are normally produced by pulsed CO_2 lasers due to the large intital gain-switched spike. Several methods for control of this initial spike have been developed [2,3], though of course this spike is important in producing the initial rise of the surface temperature which drives the material into the enhanced absorption region.

1.2 The design of the Pulsed CO_2 Laser machining system

The high PRF CO_2 laser was designed with a transverse discharge system, thus giving a large discharge volume with a relatively short discharge length. This design also has the advantage that with a gas recirculator, high gas velocities can be produced in the discharge region, ensuring rapid replacement of the working gas and allowing the system to be run at the high frequencies required. Volumetric preionisation is used to produce a homogeneous glow discharge within the cavity with pulse durations of up to 10 microseconds.

A three-dimensional model of the CO_2 laser system is shown in fig.(1.2). The gas is circulated around the system by two Root's blowers, each capable of delivering 7,500 m^3/hr of gas. The gas is cooled by four heat exchangers, placed at the inlet and exit of each blower. Auxiliary cooling is also provided for the electrodes and blower gearbox oil.

The power supply comprises, fig.(1.3), a high voltage transformer, three phase bridge rectifier and a pulser. A Line Type pulser was chosen because of the ability to match this to the gas discharge, giving very high power transfer efficiencies.

1.3 Salient features of the interaction mechanism

Examination of laser induced heating interaction (laser-workpiece interaction) plays an important role in the development and understanding of the machining processes.

Firstly, consideration of the case where the peak temperature of the surface absorbing the laser radiation is below the melting point and the absorber is a metal (i.e a conductor):

The light is absorbed in a very thin layer at the surface, typically of the order of 10^{-8}m thick, by interaction with the conduction electrons. A model for this case was first developed by Ready [4]. He assumed that the energy gained by the electrons in such an interaction was rapidly dissipated as phonons by collisions with the lattice, implying that the irradiance may be regarded as converted instantaneously into heat at the surface of the metal. He also interpreted the energy absorbed as a surface phenomenon. This led him to utilise the Fourier conduction theory for modelling the interaction process. Harrington [5], Anisimov et al [6], Riley [7] and Compaan et al [8] have suggested that for such high absorption rates, it can not be assumed that the electrons have completely interacted with the phonons. In such circumstances, the electrons and phonons will not be in thermal equilibrium and consequently will have different temperatures. Hence new models based on the Kinetic theory approach were proposed by Harrington [5] though he obtained no tenable solution from the resulting transport equations.

Secondly, once heating induces melting, i.e the surface reaches its melting temperature:

> Once the material surface has become molten, the interface between the molten and solid material propagates into the workpeice. Conservation of energy at at the moving boundary leads to the determination of the rate of melting. Modelling of this process is useful for welding applications [9].
>
> Vaporization of the metal surface takes place when the surface temperature reaches the boiling point. Modelling of this event is useful for predicting process performance for cutting and drilling operations and extensive studies exist; a model for hole formation was developed by Ready [10]. The possibilty of homogeneous nucleation occuring below the surface was considered by Afanasev [11] and Hodgett [12]. Radial liquid ejection from the solid was examined by Chun and Rose [13] but more comprehensive work was carried out by Bakewell [1] who solved the Navier-Stokes equation with a moving boundary. Mazumder et al [14] describes a three dimensional heat transfer model for cw laser material processing with a moving heat source. Hugenschmidt et al [15] and Anisimov et al [16] have used high repetition frequency, high mean power lasers to study pulsed laser target interactions.
>
> The drilling application was studied, using factorial design of his experiments by Lee [17]. Also, the power

intensity distribution in the focussed beam and consequent interaction mechanisms were examined in more detail by Shayler [18] who introduced new models thereby providing new physical insight into the phenomenon, particularly in the understanding of plasma transients.

1.4 Control of the machining process.

The laser machining performance is controlled by the laser beam output characteristics, workpiece material properties and machining environment. The important features of each of these items are detailed below:

The laser beam output characteristics:

(i) The temporal variation of the pulse power intensity is important in determining the material removal mechanism. A high power pulse is more favourable because the heat affected zone is smaller and the thickness of the residual liquid layer is minimized. An initial spike approximately twice the height of the pulse plateau is beneficial as it ignites the plasma and thereby increases the amount of laser energy coupled into the workpiece.

(ii) The spatial power intensity profile: For material processing applications, it is desirable to obtain operation in the fundamental transverse mode, TEM_{00}. This transverse mode has a spatial distribution of

intensity I, which varies in accordance with the relationship

$$I(r) = I_{max} \exp(-2r^2/r_0^2) \qquad (1.1)$$

where I_{max} is the intensity of beam at the centre and r_0 is the Gaussian radius, i.e, the radius at which the intensity is reduced from its central value by a factor of e^2.

(iii) Focussing: In drilling, the focal position, that is the position of maximum irradiance relative to the workpiece surface is highly significant in controlling the hole quality which is characterised by such parameters as resolidification, taper inlet cone and barrelling [19].

Workpiece material properties:

(i) Thermal properties - the laser energy transported in the material is dependent on the thermal conductivity as well as the specific heat per unit volume. These properties are considerably different for different materials and are also functions of temperature.

(ii) Optical properties - Metals exhibit large reflectivities which results in poor coupling of energy into the workpiece. Reflectivity is a function of several variables notably the radiation frequency and surface finish. The CO_2 laser operates in the infrared where the surface reflectivity for cold metals is very high. Hence most of the incident energy is reflected. The problems

are compounded at this long wavelength as the focussed spot area is proportional to the square of wavelength, hence the irradiance is inversely proportional to the square of the wavelength resulting in reduced energy per unit area. High power beams are therefore essential. Hugenschmidt et al [15] have studied the dependence of the reflectivity of alumunium upon wavelength and temperature. They concluded that the reflectivity can be described by equations developed by Kubelka [20], for wavelegths above six microns. These are made use of in chapter 2.

Machining environment:

The CO_2 laser system offers incident intensities, at the workpiece surface, of sufficient magnitude that non-conduction limited processes dominate the machining mechanisms, but at intensities not much greater than the machining threshold level, deleterous plasma effects can ensue. Yousif [21], Arata et al [9] and Dufresne et al [22] examined plasma control means and discovered techniques to increase the proportion of incident energy coupled into the workpiece. Two possibilities were considered:

Firstly, that atmospheres of electrophilic gases like SF_6 and O_2 might reduce the number density of electrons in the plasma.

Secondly, that operation at reduced pressures might

influence the dynamics of plasma propagation.

They concluded that an optimum pressure exists which depends on the physical properties of the target material, and that the use of electrophilic gases can increase drilling performance (judged on the basis of material removal) by an order of magnitude compared with machining in ambient air.

The importance of gas flow parameters in laser processing of materials has been proved [23]. The use of axial and transverse nozzles (subsonic and supersonic) have been examined with the latter giving better performance [24].

1.5 Scope of the present work

This work is part of a continuing programme in the design and development of a high power pulsed CO_2 laser for material processing applications. A two pronged thrust has been attempted:

(i) Chapter two deals with the interaction of the focussed beam and the workpiece.

To control laser-machining performance and make the interaction mechanism amenable to understanding during the first few microseconds of the laser pulse, the transient heating phenomenon is modelled using the Electron Kinetic theory. Computer programmes are developed for the numerical solution of the equations and comparisons with the classical Fourier conduction theory made. Experimental verification of this new

theory is also sought by comparing the theoretical results with experimental results obtained by Yilbas [25].

The model is extended, in chapter three, to take account of evaporation and comparision made to see whether the Electron Kinetic thoery and the classical Fourier theory converge once evaporation becomes significant.

In the analysis, a broad spectrum of different metals are used because of their industrial usefulness and diversity of properties which covers the whole range of metal properties allowing one to predict for other metals. The metals dealt with are Aluminium, Copper, Iron, Nickel, Titanium and Tantalum.

(ii) Chapter four develops and exercises a model that simulates the CO_2 laser system, paying particular attention to performance characterisation for optimisation of a design giving maximum control and hence tunability of the laser machining characteristics obtainable from the above model.

1.6 References

1 B.A.Bakewell Performance of pulsed laser systems in relation to machining mechanisms.
Ph.D Thesis, University of Birmingham, 1973

2 M.Autric, D. Dufresene, J.P.Caressa, P.Vigliano, F. Carrer and V.Chhim
Aerosol clearing using a high power CO_2 laser pulse, in Gas flow and Chemical lasers, 1984.
Ed. A.S.Kaye and A.C.Walker
Published by Adam Higler Ltd, 1985

3 C.R.Chatwin and B.F.Scott
High PRF Nitrogen-Carbon dioxide lasers for continuous manufacturing processes in metals,
1st Int. Conf. on Lasers in manufacturing,
Brighton, U.K Nov. 1983

4 J.F.Ready Effects due to absorption of laser radiation
J. Appl. Phys. 36 p.462 (1965)

5 R.E. Harrington
Thermal conduction near a metal surface exposed to black body radiation.
J. Appl. Phys. 39 p.8 (1968)

6 S.I.Anisimov, B.L.Kapeliovich and T.L.Perel'man
Electron emission from metal surfaces exposed to ultrashort laser pulses.
Sov.Phys. JETP, Vol.39, No.2, August 1974

7 K. Riley The thermodynamics of laser induced interaction processes in solids
Ph.D Thesis, University of Birmingham, 1974

8 A.Compaan, A. Aydinli, M.C.Lee and H.W.Lo
Raman and optical properties of the pulsed laser anealing of Si, in Laser and Electron-beam Interactions with solids.
Ed., B.R.Appleton and G.K. Celler
Published by Elsevier, 1982

9. Y.Arata, N.Abe and T.Oda
Fundamental phenomena in laser welding, in Gas Flow and Chemical lasers,1984. Ed.,A.S.Kaye And A.C.Walker, Adam Hilger ltd, 1985

10 J.F. Ready Industrial applications of lasers
Published by Academic Press, 1978

11 B.F.Scott and D.L.Hodgett
Pulsed solid-state lasers for engineering fabrication processes, Proc. Instn. Mech. Engrs, vol.183 pt.3D p.75, 1968

12 D.L. Hodgett, Pulsed laser working of engineering materials
Ph.D Thesis, University of Birmingham, (1970)

13 M.K.Chun and K.Rose
Interaction of high intensity laser beams with metals
J. Appl. Phys. Vol.41, No.2, p.614, 1970

14 J. Mazumder and W.M.Steen

Heat transfer model for cw laser material processing J.Appl.Phys. vol.51 no.2, 1980

15 M. Hugenschmidt and R. Joecktel

Continuous wave and pulsed laser target interactions, In Gas flow and Chemical lasers, 1984. Ed. A.S.Kaye and A.C.Walker

Published by Adam Higler Ltd, 1985

16 V.N.Anisimov et al

Metal processing by high-repetition-rate pulsed excimer and carbon dioxide lasers

Appl. Optics vol. 23 No. 1 Jan. 1984

17 T. H. Lee Parameters affecting hole geometry in pulsed laser drilling of sheet metals

M.Sc Thesis, University of Birmingham, 1973

18 P.J.Shayler Laser drilling phenomenon inclunding beam/vaporized material interactions

Ph.D Thesis, University of Birmingham, 1975

19 N.Rykalin, A.Uglov and A.Kokora

Laser machining and welding

Pergamon Press, 1978

20 H.C.Hamaker Radiation and heat conduction in light scattering materials

Philips Res. Rep. 2, p.55-67, 1947

21 E. G. Yousif, Effects of electrophilic gases at sub-atmospheric pressures on laser induced plasmas in machining of metals
Ph.D Thesis, University of Birmingham, (1980)

22 D.Dufresne, F.Puech, P. Giovanneschi, M.Autric and J.P.Cavessa
Experimental study on interaction of high power CO_2 laser pulse with a solid target in a rarefied atmosphere
In Gas flow and Chemical lasers, 1984.
Ed. A.S.Kaye and A.C.Walker
Published by Adam Higler Ltd, 1985

23 J.N. Kamalu and W.M. Steen
The importance of gas flow parameters in laser cutting
In Proc. of Symposium on lasers in metallurgy, pp 263-8, Oct. 1981.
Eds., K. Mukherjee and J. Mazumder

24 D.W. Macdonald
Final Year Undergraduate project,
Mechanical Engineering Department,
University of Glasgow, 1983

25B.S.Yilbas Heat transfer mechanisms initiating the laser drilling of metals
Ph.D Thesis, University of Birmingham 1982.

Fig. 1·1. RESPONSE OF ALUMINIUM TO PULSED CO_2 LASER HEATING

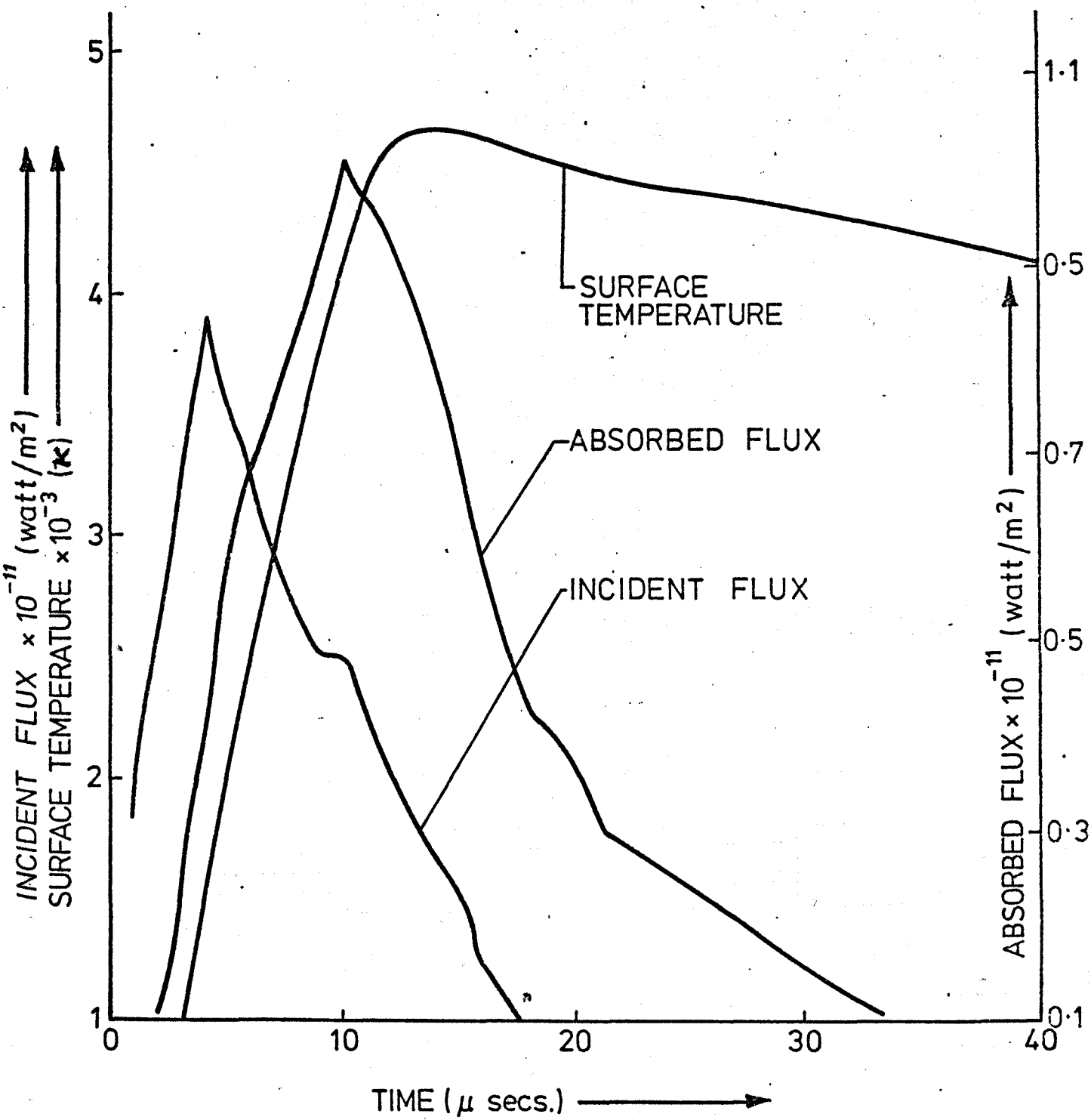

3D MODEL OF THE PULSED CARBON DIOXIDE LASER

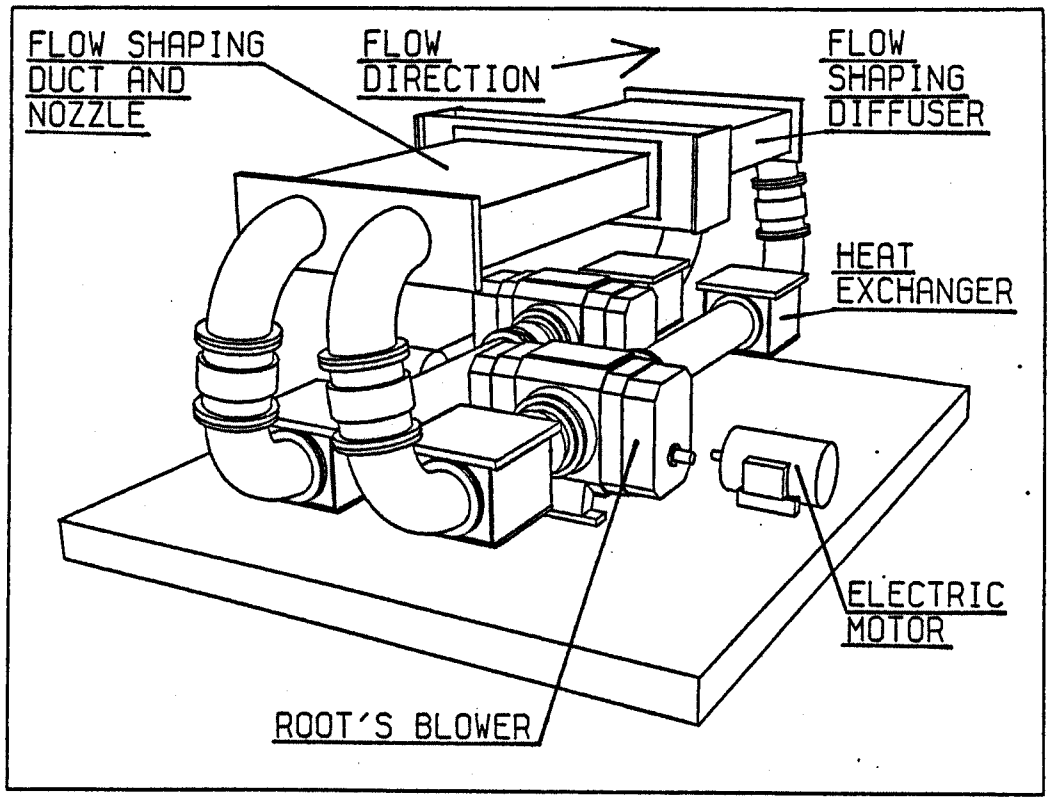

FIG. (1.2)

SCHEMATIC OF THE LASER POWER SUPPLY

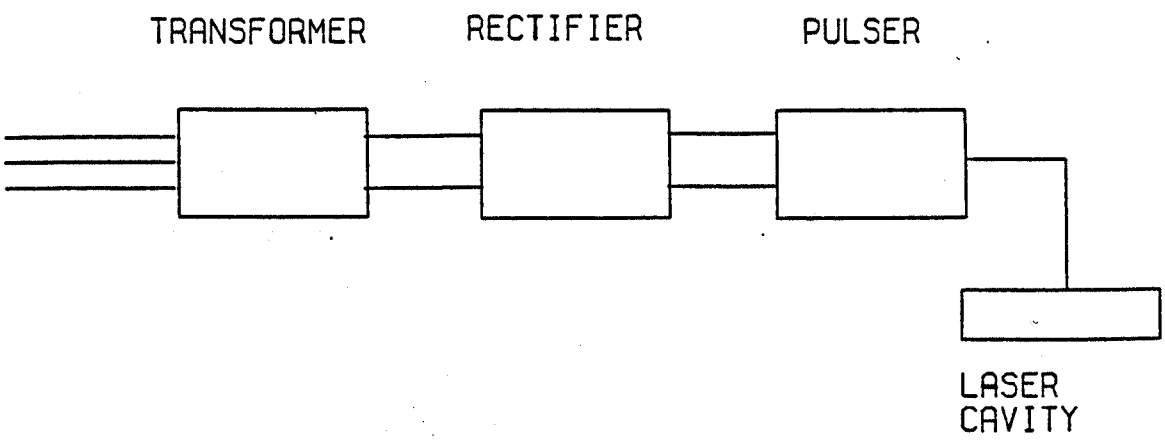

FIG. (1.3)

Chapter 2

A new model of heat transfer in metals irradiated by high intensity laser pulses

Nomenclature

C_p	Specific heat (J/kg.K)
dV	Volume element (m^3)
E(x,t)	Electron energy (J)
$E_p(x,t)$	Lattice (phonon) energy (J)
f	Fraction of excess energy transferred to the phonons by electrons
$I_o(t)$	Power intensity incident on the surface (W/m^2)
I(x,t)	Power intensity at position x (W/m^2)
k	Boltzmann constant = 1.380×10^{-23} J/K
K	Thermal conductivity (W/m^2K)
N'	Number density of participating electrons (m^{-3})
N	Number density of valency electrons (m^{-3})
n(x,t)	Phonon (atoms) number density (m^{-3})
p,r,s	Distances (m)
R(t)	Reflectivity at the metal surface
t	time (sec)
T_e	Kinetic Electron temperature (K)
T	Lattice (phonon) temperature (K)
T_f	Fermi electron temperature (K)
v	Fermi electron velocity (m/s)

z	Electron collision frequency (sec^{-1})
δ	Absorption coefficient (m^{-1})
ε	Distance (m)
ω	Angle subtended by element
λ	Electron mean free path for collisions with phonons (m)

2.1 Introduction

When high intensity optical radiation is incident on a metallic surface, the transmitted flux is fully absorbed by the electrons above the Fermi surface. Phonons are too slow to respond significantly to the incident radiation [1]. These electrons are thermally excited and their kinetic energy increases. They then suffer collisions with lattice phonons giving up part of their kinetic energy. The phonons, in turn undergo Umklapp processes in a time scale sufficiently rapid for the relaxation to equilibrium to be consi dered instantaneous between phonons in any given region. The opposite process also takes place where 'cold' electrons collide and obtain energy from hot phonons.

For high intensity radiation delivered in a pulse with a fast rise time, the rate of energy transfer from electrons to phonons is too slow to maintain equilibrium and the effective electron temperature departs from that of the phonons. So the electron and phonon temperatures will be different, the magnitude of the difference being dependent on the incident power and on the rate of energy transfer between electrons and phonons.

Since the mean free path for electron-electron collisions is several orders of magnitude greater than that of electron-phonon collisions [2], the former interaction can be excluded.

A SIMPLE DESCRIPTION OF THE PHYSICAL MODEL

The model for metal target irradiating by a laser beam is based on the following:

(i) The laser beam is treated as a radiation field that decays exponentially with distance travelled into the target.

(ii) The target is treated as a phonon field with electrons moving randomly in this field.

(iii) The laser energy is absorbed by the conduction electrons travelling through the laser radiation field. Some of this energy is then transferred to the phonons by electron-phonon collisions.

All other energy transport mechanisms, for example, photon-phonon interactions, are considered negligible.

In summary, the energy transport mechanism is :

Photon (radiation field) $\longrightarrow$ electron $\longrightarrow$ phonons

This allows the electrons and phonons to move out of equilibrium if energy transport rates demand.

2.2 Kinetic theory of energy transport

2.2.1 Background

Theoretical results [3] produced using the classical Fourier method to describe conduction within metals irradiated with fast rise time, high intensity pulses do not agree with experimental results [4]. It is important to determine the temperature profile in metals accurately, since the temperature distribution within the workpiece greatly affects the phase transitions and, hence, the machining characteristics. Therefore, new models must be sought in order to reduce this discrepancy.

In his development of the Electron Kinetic theory, Harrington [5,6] described the electron movement as one-dimensional, and assumed equilibrium between electrons and phonons. He also assumed unnecessarily that the temperature distribution would follow an exponential law. The results presented herein prove these and other assumptions to be unjustifiable during the initial phase of the beam-workpiece interaction. Some errors were corrected by Yilbas [7] and Riley [8]. However, they assumed that the electrons and phonons are in equilibrium and at the same time suggested that only a fraction of the excess electron energy is transfered to the phonons, which is inconsistent. Bakewell et al [9] moved away from this equilibrium assumption. However, their analysis failed to take into account the three-dimensional movement of electrons and also assumed that the energy storage capacity of the electrons is negligible compared to that of the lattice. S.I.Anisimov et al

[10] assumed a two temperature system in the metal but used macroscopic means to relate the energy transfer process between electrons and phonons.

2.2.2 Electron kinematics

The model utilised in this description of the electron transport phenomena is one where electrons transport energy from all regions of the metal and deliver a fraction of the energy to the lattice by collisions with phonons [11]. This is shown diagramatically in fig.(2.1) where only the top half of the cone is drawn. The problem then is to determine the number of electrons which leave an element $d\varepsilon$ after colliding there, and then suffer their next collision in a volume element dV a distance s away in time dt in a conical element subtending an angle $d\omega$ with the x axis. The solid angle subtended at dV by the area at (r,s) is

$$2\pi r(sd\omega)/s^2 \qquad (2.1)$$

Written as a fraction of the total solid angle, equation (2.1) becomes

$$2\pi r(sd\omega)/4\pi s^2 = rd\omega/2s \qquad (2.2)$$

and therefore the number of electrons originating in $d\varepsilon$ which have their first collision in dV is

$$\frac{N'zrd\omega}{2s}\exp(-s/\lambda)\frac{d\varepsilon dV}{\lambda\cos\omega} \qquad (2.3)$$

where λ is the electron-phonon mean free path, N' is the number of participating electrons, those at the Fermi surface, and z is the collision frequency in dV which is given by

$$z = v/\lambda \qquad (2.4)$$

where v is the Fermi electron velocity. Therefore the number of electrons colliding in dV which come directly from dε , that is, follow path B-C (see fig.(2.1)) is

$$\frac{N'v}{\lambda}\frac{d\omega}{2}\sin\omega\exp(-(x-\varepsilon)/\lambda\cos\omega)\frac{d\varepsilon dV}{\lambda\cos\omega} \qquad (2.5)$$

A similar expression is required for electrons coming from the right of dV, that is, for $\varepsilon > x$. Also some electrons in dε travel via the 'wall' at x=0 into the volume element dV, that is, follow path B-A-C. These must also be taken into account. Though some of these electrons escape to the surroundings, a steady state charge is assumed where the number of electrons escaping at any given temperature are equal to those returning from the space charge in the vicinity of the interaction at the same temperature. Hence a mirror image method (see fig. (2.2)) is employed to avoid this difficulty of electrons reflected from the surface. The problem then reduces to that of determining the energy transported into dV from all electrons in dε at ε, then intergrating over all ε and ω to allow for contributions from all samples i.e $-\infty < \varepsilon < \infty$ and $0 < \omega < \pi/2$.

Therefore the number of electrons arriving in dV which come from dε is

$$\frac{N'v}{\lambda}\frac{d\omega}{2}\sin\omega\exp(-|x-\varepsilon|/\lambda\cos\omega)\frac{d\varepsilon dV}{\lambda\cos\omega} \qquad (2.6)$$

2.2.3 Energy carried by electrons

The energy carried into the elemental volume dV in time dt by electrons depends upon the specific time at which the electron free path was generated. This depends on the relationship between the mean free path (λ) and the time interval dt. Hence, electrons can be divided into two groups:

(i) Those travelling a distance s which is less than v dt. For this case, electrons generated within the time interval dt will arrive in the elemental volume during the same time interval.

(ii) Those travelling a distance s which is equal to or greater than v dt - These electrons must be generated in the previous time intervals if they are to arrive in dV during the current dt.

It is essential to incorporate this fact in the model. Considering the transfer process at time t, the earliest time of generation at which an electron with a given mean free path can enter dV during dt is

$$t-|s|/v \qquad (2.7)$$

giving the energy of the electron as

$$E = E(\varepsilon,t) - \frac{|s|}{v}\frac{\partial E(\varepsilon,t)}{\partial t} \qquad (2.8)$$

The latest corresponding time is

$$(t + dt) - |s|/v \qquad (2.9)$$

giving the energy of the electron as

$$E = E(\varepsilon,t) + \{dt - \frac{|s|}{v}\}\frac{\partial E(\varepsilon,t)}{\partial t} \qquad (2.10)$$

Therefore the average energy E stored in the electron at ε is

$$E = E(\varepsilon,t) + \frac{1}{2}\{dt - \frac{2|s|}{v}\}\frac{\partial E(\varepsilon,t)}{\partial t} \qquad (2.11)$$

If a check is performed by putting $|s|/v=dt$ in equation (2.11), this should give the average temperature of the previous time interval. That is to say only electrons generated in the previous time interval arrive giving, the average energy of the previous time interval.

A similar result is required for the photon absorption process which depends on the time of flight of the electrons and the temporal rate of change of the photon flux. These photons which come from the laser beam are assumed to be absorbed by electrons. Quantum mechanics shows that photons may be absorbed both by free and bound electrons. This process can only occur with the transfer of discrete quanta of energy. However to simplify the model, these quantum effects will be ignored and the free electrons assumed to acquire the laser energy by merely passing through the electromagnetic field of the incident beam. This field can be described by Lambert's law which is expressed as

$$I(x,t) = I_0(1-R(t))\exp(-\delta x) \qquad (2.12)$$

where $I(x,t)$ is the beam intensity at time t after propagating a distance x in the material, $I_0(t)$ is the intensity at the surface, $R(t)$ is the reflection coefficient and δ is the absorption coefficient.

Considering a small element dp situated between ε and x (see fig.(2.3)), the power absorbed per unit area by electrons at time

t is

$$I_o(t)(1-R(t))\delta\exp(-\delta p)dp \qquad (2.13)$$

This must be equal to the increase in the energy of the electrons in the element. Hence,

$$\Delta E.dp = I_o(t)(1-R(t))\delta\exp(-\delta p)dp\Delta t \qquad (2.14)$$

where Δt is the average time an electron stays in the element dp giving the energy absorbed per electron as

$$\frac{I_o(t)(1-R(t))\delta\exp(-\delta p)dp\Delta t}{N'} \qquad (2.15)$$

The time interval Δt is given by (see fig. 2.3)

$$\Delta t = dp/v\cos\omega \qquad (2.16)$$

hence the energy absorbed per electron is

$$\frac{I_o(t)(1-R(t))\delta\exp(-\delta p)dp}{N'v\cos\omega} \qquad (2.17)$$

Since $I_0(t)$ and R(t) are continuous functions of time, the values of $I_o(t)$ and R(t) are continuously changing as electrons move from ε to x and hence it is very difficult to determine the energy absorbed by electrons. But, since the electron velocity is very high, it can be safely assumed that $I_o(t)$ and R(t) are constants in the time required for the electrons to move from ε to x. Hence substituting equation (2.16) into (2.15) and intergrating, the energy absorbed per electron in moving from ε to x becomes

$$\frac{(1-R)I_o\delta}{N'v\cos\omega}\left|\int_{\varepsilon}^{x}\exp(-\delta p)dp\right| \qquad (2.18)$$

2.2.4 Energy transport equations

From equations (2.11) and (2.18), the average energy of an electron entering dV at x from ε after dt is

$$E(\varepsilon,t) + \frac{1}{2}\{dt - \frac{2|s|}{v}\}\frac{\partial E(\varepsilon,t)}{\partial t}$$

$$+ \frac{(1-R)I_o\delta}{N'v\cos\omega}\left|\int_{\varepsilon}^{x} \exp(-\delta p)dp\right| \qquad (2.19)$$

If $E_p(x,t)$ is the average energy of phonons in dV at x, the energy given up by electrons to the phonons on collision is

$$f\{E(x,t+dt)-E_p(x,t)\} \qquad (2.20)$$

where f is the fraction of the energy difference between an electron and a phonon given up by an electron on collision with a phonon. This parameter is further discussed in Appendix 2A.

The total energy transferred to the lattice from all electrons colliding in dV at x over the time interval dt is

$$dV\int_{-\infty}^{\infty}\int_{0}^{\pi/2} \frac{N'v}{2\lambda} \exp(-|x-\varepsilon|/\lambda\cos\omega)\ \frac{\sin\omega}{\cos\omega}\frac{f}{\lambda}\Big[E(\varepsilon,t)$$

$$+\frac{1}{2}\{dt - \frac{2|s|}{v}\}\frac{\partial E(\varepsilon,t)}{\partial t}$$

$$+ \frac{(1-R)I_o\delta}{N'v\cos\omega}\left|\int_{\varepsilon}^{x} \exp(-\delta p)dp\right| - E_p(x,t)\Big]\,d\omega\,d\varepsilon \qquad (2.21)$$

Given that the number density of atoms is n(x,t), the energy increase of the lattice is

$$\frac{\partial nE_p(x,t)}{\partial t}dV = dV\int_{-\infty}^{\infty}\int_{0}^{\pi/2} \frac{N'v}{2\lambda} \exp(-|x-\varepsilon|/\lambda\cos\omega)\frac{\sin\omega}{\cos\omega}\frac{f}{\lambda}$$

$$\Big[E(\varepsilon,t) + \frac{1}{2}\{dt - \frac{2|s|}{v}\}\frac{\partial E(\varepsilon,t)}{\partial t}$$

$$+ \frac{(1-R)I_o\delta}{N'v\cos\omega}\left|\int_{\varepsilon}^{x} \exp(-\delta p)dp\right| - E_p(x,t)\Big]\,d\omega\,d\varepsilon$$

(2.22)

Now the average energy change of electrons at x equals the energy left in the electrons after collision less the energy carried away by electrons leaving the elemental volume dV during dt. Hence

$$\frac{\partial N'E\ (x,t)}{\partial t}dV = dV\int_{-\infty}^{\infty}\int_{0}^{\pi/2} \frac{N'v}{2\lambda}\exp(-|x-\varepsilon|/\lambda\cos\omega)\frac{\sin\omega}{\cos\omega}\frac{1}{\lambda}$$

$$\left[E(\varepsilon,t) + \frac{1}{2}\{dt - \frac{2|s|}{v}\}\frac{\partial E(\varepsilon,t)}{\partial t}\right.$$

$$\left. + \frac{(1-R)I_o\delta}{N'v\cos\omega}\left|\int_{\varepsilon}^{x}\exp(-\delta p)dp\right|\right] d\omega d\varepsilon$$

$$- dV\frac{\partial nE_p(x,t)}{\partial t} - dV\frac{N'v}{\lambda}E(x,t) \qquad (2.23)$$

which on further simplification and use of equation (2.22) becomes

$$\frac{\partial N'E\ (x,t)}{\partial t} = (1-f)\int_{-\infty}^{\infty}\int_{0}^{\pi/2} \frac{N'v}{2\lambda^2}\exp(-|x-\varepsilon|/\lambda\cos\omega)\frac{\sin\omega}{\cos\omega}$$

$$\left[E(\varepsilon,t) + \frac{1}{2}\{dt - \frac{2|s|}{v}\}\frac{\partial E(\varepsilon,t)}{\partial t}\right.$$

$$\left. + \frac{(1-R)I_o\delta}{N'v\cos\omega}\left|\int_{\varepsilon}^{x}\exp(-\delta p)dp\right|\right] d\omega d\varepsilon$$

$$- f\int_{-\infty}^{\infty}\int_{0}^{\pi/2} \frac{N'v}{2\lambda^2}\exp(-|x-\varepsilon|/\lambda\cos\omega)\frac{\sin\omega}{\cos\omega}E_p(x,t)d\omega\, d\varepsilon,$$

$$- \frac{N'v}{\lambda}\ E\ (x,t) \qquad (2.24)$$

Furthermore, the continuity equation for electrons must be satisfied, namely

$$\frac{\partial N'(x,t)}{\partial t} = \int_{-\infty}^{\infty}\int_{0}^{\pi/2} \frac{N'v}{2\lambda^2} \exp(-|x-\varepsilon|/\lambda\cos\omega)\frac{\sin\omega}{\cos\omega}\, d\omega d\varepsilon$$

$$- \frac{N'v}{\lambda} \qquad (2.25)$$

2.2.5 Thermal properties

In order to solve the electron and lattice energy equations, the number of participating electrons is required. Since it has been assumed that the electron gas is in a state of equilibrium, the number of participating electrons can be obtained by use of the ordinary Fermi distribution function [2]. This is given as

$$N' = N\pi^2 T_e/2T_F \qquad (2.26)$$

where T_F is the Fermi temperatue, T_e is the electron temperature and N is the number density of valency electrons. Implicit in the above equation is the assumption that $T_e < T_F$. Also, from statistical considerations, it can be shown that the thermal conductivity of the material is [12]

$$K = N'v\lambda k/3 \qquad (2.27)$$

and the heat capacity is

$$\rho C_p = 3nk \qquad (2.28)$$

where k is the Boltzmann constant, ρ is the material density and C_p is the specific heat.

2.2.6 Electron and Lattice temperatures

While the energy absorbed by the phonons goes to increase both their kinetic and translational energies, it is the difference in the kinetic energies of the electrons and phonons

that determines the energy transfer rate. Hence after substituting equations (2.27) and (2.28), equations (2.23) and (2.24) become

$$\frac{\partial}{\partial t}\left[\rho C_p T\right] = f\int_{-\infty}^{\infty}\frac{9K}{4\lambda^3}\int_0^{\pi/2} \exp(-|x-\varepsilon|/\lambda\cos\omega)\frac{\sin\omega}{\cos\omega}$$

$$\left[T_e(\varepsilon,t) + \frac{1}{2}\{dt - \frac{2|s|}{v}\}\frac{\partial T_e(\varepsilon,t)}{\partial t} - T(x,t)\right] d\omega d\varepsilon$$

$$+f\frac{(1-R)I_o\delta}{2\lambda^2}\int_{-\infty}^{\infty}\int_0^{\pi/2} \exp(-|x-\varepsilon|/\lambda\cos\omega)\frac{\sin\omega}{\cos^2\omega}$$

$$\left|\int_\varepsilon^x \exp(-\delta p)dp\right| \; d\omega d\varepsilon \qquad (2.29)$$

and

$$\frac{\partial}{\partial t}\left[\frac{9KT_e}{2\lambda v}\right] = (1-f)\int_{-\infty}^{\infty}\frac{9K}{4\lambda^3}\int_0^{\pi/2} \exp(-|x-\varepsilon|/\lambda\cos\omega)\frac{\sin\omega}{\cos\omega}$$

$$\left[T_e(\varepsilon,t) + \frac{1}{2}\{dt - \frac{2|s|}{v}\}\frac{\partial T_e(\varepsilon,t)}{\partial t}\right] d\omega d\varepsilon$$

$$+ f\int_{-\infty}^{\infty}\frac{9K}{4\lambda^3}\int_0^{\pi/2} \exp(-|x-\varepsilon|/\lambda\cos\omega)\frac{\sin\omega}{\cos\omega}T(x,t)d\omega d\varepsilon$$

$$+f\frac{(1-R)I_o\delta}{2\lambda^2}\int_{-\infty}^{\infty}\int_0^{\pi/2} \exp(-|x-\varepsilon|/\lambda\cos\omega)\frac{\sin\omega}{\cos^2\omega}$$

$$\left|\int_\varepsilon^x \exp(-\delta p)dp\right| \; d\omega d\varepsilon$$

$$-\frac{9K}{2\lambda^2}T_e(x,t) \qquad (2.30)$$

respectively where $T_e(x,t)$ is the electron temperature and $T(x,t)$ is the phonon temperature.

The continuity equation becomes

$$\frac{\partial K}{\partial t} = \int_{-\infty}^{\infty}\int_{0}^{\pi/2} \frac{Kv}{2\lambda^2} \exp(-|x-\varepsilon|/\lambda\cos\omega)\frac{\sin\omega}{\cos\omega}\, d\omega d\varepsilon - \frac{Kv}{\lambda} \qquad (2.31)$$

An attempt at reducing the double integrals to a single one by substitution did not produce useful results save for the energy term which is shown in Appendix 2B to be

$$\int_{-\infty}^{\infty}\int_{0}^{\pi/2} \exp(-|x-\varepsilon|/\lambda\cos\omega)\ \frac{\sin\omega}{\cos^2\omega}\left|\int_{\varepsilon}^{x}\exp(-\delta p)dp\right| d\omega d\varepsilon$$

$$= \frac{\lambda}{\delta}\left\{\exp(-\delta x)\ln\left|\frac{1+\lambda\delta}{1-\lambda\delta}\right| - 2\lambda^2\delta^2\int_{1}^{\infty}\frac{\exp(-xu/\lambda)du}{u(u^2-\lambda^2\delta^2)}\right\} \qquad (2.32)$$

The integral part of equation (2.32) has a singularity at $u = \lambda\delta$ when $\lambda\delta > 1$, therefore the proof of the existence of the intergral is required. This is done in Appedix 2C.

Incorporating equation (2.32) in equations (2.29) and (2.30) and simplifying further,

$$\frac{\partial}{\partial t}\left[\rho C_p T\right] = Af\int_{-\infty}^{\infty} K \int_{0}^{1}\left[T_e(\varepsilon,t) + \frac{1}{2}\{dt - \frac{2|s|}{vu}\}\frac{\partial T_e(\varepsilon,t)}{\partial t}\right.$$

$$\left. - T(x,t)\right] \exp(-|x-\varepsilon|/\lambda u)\ \frac{du}{u}\, d\varepsilon + BfI_o g(x) \qquad (2.33)$$

$$\frac{\partial}{\partial t}\left[KT_e\right] = C(1-f)\int_{-\infty}^{\infty} K \int_{0}^{1}\left[T_e(\varepsilon,t) + \frac{1}{2}\{dt - \frac{2|s|}{vu}\}\frac{\partial T_e(\varepsilon,t)}{\partial t}\right]$$

$$\exp(-|x-\varepsilon|/\lambda u)\ \frac{du}{u}\, d\varepsilon - \sigma KT_e$$

$$+ CfT\int_{-\infty}^{\infty} K \int_{0}^{1}\exp(-|x-\varepsilon|/\lambda u)\ \frac{du}{u}\, d\varepsilon + D(1-f)I_o g(x) \qquad (2.34)$$

and

$$\frac{\partial K}{\partial t} = C\int_{-\infty}^{\infty} K \int_0^1 \exp(-|x-\varepsilon|/\lambda u)\,\frac{du}{u}\,d\varepsilon - \sigma K \qquad (2.35)$$

where $T_e = T_e(x,t)$, $T = T(x,t)$, $K = K(x,t)$, $A = 9/4\lambda^3$, $B = (1-R(t))/2\lambda$, $C = v/2\lambda^2$, $D = (1-R(t))v/9$, $\sigma = \lambda C$ and

$$g(x) = \frac{\lambda}{2}\left\{\exp(-\delta x)\ln\left|\frac{1+\lambda\delta}{1-\lambda\delta}\right| - 2\lambda^2\delta^2\int_1^{\infty}\frac{\exp(-xu/\lambda)\,du}{u(u^2-\lambda^2\delta^2)}\right\} \qquad (2.36)$$

The above equations give a system of nonlinear partial integro-differential equations which do not readily render themselves to analytical methods, therefore numerical procedures were employed.

2.3 Solution of energy equations

2.3.1 Simplifications made

In solving the transport equations, simplifications are needed to reduce the equations to manageable proportions:

In determining the electron energy transport term,

$$E(\varepsilon,t) + \frac{1}{2}\{dt - \frac{2|s|}{vu}\}\frac{\partial E(\varepsilon,t)}{\partial t} \qquad (2.37)$$

the ratio $|s|/v$ is very small for the region of interest, since the value of s which is of interest extends to only a few microns and the electron velocity v is of the order of 10^6 m/s. Also, the time step dt is small, the second term in equation (2.37) can be neglected compared to the first, giving the electron energy as $E(\varepsilon,t)$ and a corresponding temperature of $T_e(\varepsilon,t)$.

2.3.2 Method of solution

The equations to be solved are (2.34) to (2.36) with initial conditions

$$T_e(0,x) = T(0,x) = T_o \qquad (2.38)$$

where T_o is the initial temperature of both electrons and phonons. Also,

$$T_e(t,\infty) = T(t,\infty) = T_o \qquad (2.39).$$

Writing

$$h(x-\varepsilon) = \int_0^1 \exp(-|x-\varepsilon|/\lambda u)\,\frac{du}{u} \qquad (2.40)$$

leads to

$$\frac{\partial}{\partial t}\left[\rho C_p T\right] = Af\int_{-\infty}^{\infty} K\,T_e(\varepsilon,t)h(x-\varepsilon)d\varepsilon - AfT\int_{-\infty}^{\infty} K\,T_e(\varepsilon,t)h(x-\varepsilon)d\varepsilon + BfI_o g(x) \qquad (2.41)$$

$$\frac{\partial}{\partial t}\left[KT_e\right] = C(1-f)\int_{-\infty}^{\infty} KT_e(\varepsilon,t)h(x-\varepsilon)d\varepsilon - \sigma KT_e + CfT\int_{-\infty}^{\infty} Kh(x-\varepsilon)d\varepsilon + D(1-f)I_o g(x) \qquad (2.42)$$

and

$$\frac{\partial K}{\partial t} = C\int_{-\infty}^{\infty} Kh(x-\varepsilon)d\varepsilon - \sigma K \qquad (2.43)$$

To solve the above equations, the line method was used (Baker[13] and Mikhlin [14]). This approach is similar to that used in the numerical solution of partial differential equations (see Gladwell et al [15]). A quadrature rule of the form

$$\int_{-\infty}^{\infty} T(\varepsilon)d\varepsilon \simeq \sum_{j=1}^{n} w_j T_e(\varepsilon_j) \qquad (\varepsilon_j \quad [-\infty,\infty]) \qquad (2.44)$$

was used to replace the integrals in equations (2.41) to (2.43) where $T_{ej}(j=1,n)$ are the abscissas and $w_j(j=1,n)$ are the weights accompanying these points [16]. A system of ordinary differential equations for the functions

$$f_i(t) = T_e(t,x_i) \qquad (2.46)$$

where (for $|x| < \infty$, t $[0,\infty]$)

were then obtained. The equations then become

$$\frac{d}{dt}\left[\rho C_p T\right] = Af \sum_{j=1}^{n} \omega_j h(x-\varepsilon_j)KT(t,\varepsilon_j) - AfT \sum_{j=1}^{n} \omega_j h(x-\varepsilon_j)K(t,\varepsilon_j)$$

$$+ BfI_o g(x) \qquad (2.46)$$

$$\frac{d}{dt}\left[KT_e\right] = C(1-f) \sum_{j=1}^{n} \omega_j h(x-\varepsilon_j)KT_e(t,\varepsilon_j) - \sigma KT_e(t,x)$$

$$+ CfT \sum_{j=1}^{n} \omega_j h(x-\varepsilon_j)K(t,\varepsilon_j) + D(1-f)I_o g(x) \qquad (2.47)$$

$$\frac{dK}{dt} = C \sum_{j=1}^{n} \omega_j h(x-\varepsilon_j)K(t,\varepsilon_j) - \sigma K \qquad (2.48)$$

and

$$\left.\begin{aligned} T_e(0,x) &= T(0,x) = T_0 \\ T_e(t,\infty) &= T(t,\infty) = T_0 \end{aligned}\right\} \qquad (2.49)$$

The value of x is given by

$$x = \varepsilon_i (i = 1,2,3,\ldots \quad m) \quad m < n \qquad (2.50)$$

This gives a system of 3m differential equations which can be solved numerically for the values of $f_i(t) = T_e(t,x_i)$ and therefore $T(t,x_i)$. To define the values of $f_i(t) = T_e(t,x_i)$ for all $|x| < \infty$, conventional interpolation is used. The system of 3m ordinary differential equations can be reduced to 2m by

incorporating equation (2.48) in equation (2.47) since,

$$d(KT_e)/dt = T_e dK/dt + K dT_e/dt \qquad (2.51)$$

The computational procedure outlined above is incomplete, there being another stage to consider. This is the finding of a quadrature rule for the integrals. Before this is done, the problems involved in evaluating the integrals are examined and methods suggested that can be used to overcome each problem:

(i) Singularity

The integral has two forms of singularities. Firstly, the limits of the integral equation are both infinite and secondly the kernel has a logarithmic singularity at $x = \varepsilon$.

Examining the infinite singularity first, it has been shown by Baker [17] that the theory for the solvability of the general equation of an integral equation with infinite ranges is not complete. However, for the numerical treatment of a general equation of that form, a natural technique involves replacing the infinite limits of integration by finite limits. The resulting solution should be well behaved and its approximate solution can be easily achieved. For any integral of the form

$$\int_a^\infty T(\varepsilon)d\varepsilon \qquad (2.52)$$

a value c is sought such that

$$\int_c^\infty T(\varepsilon)d\varepsilon = \int_0^\infty e^{-\varepsilon}\,(e^{+\varepsilon}\,T(\varepsilon+c))d\varepsilon \qquad (2.53)$$

is negligible. Then

$$\int_a^{\infty} T(\varepsilon)d\varepsilon \simeq \int_a^{c} T(\varepsilon)d\varepsilon \qquad (2.54)$$

Some practical problems are however encountered if it becomes necessary to make the interval of integration large because then a large number of pivotal points will be required if standard equal-interval finite approximations are used. Therefore, in such cases, more economical methods which have the effect of increasing the integration interval as ε increases should be utilised. This suggests quadrature of the Gauss-type, but these are impractical due to the second form of singularity as explained later and due to the nature of the double integral (kernel is not degenerate). A practical method was suggested by Mayers [18]. This divides the range of integration [a,c] into p blocks each of length H and a different polynomial of degree q is used in the various blocks. For example, the integral

$$\int_a^{c} T(\varepsilon)d\varepsilon \qquad \text{becomes}$$

$$\sum_{r=1}^{p} \int_{a+(r-1)H}^{a+rH} T(\varepsilon)d\varepsilon \qquad (2.55)$$

and in each block, a quadrature formula

$$\int_{a+(r-1)H}^{a+rH} T(\varepsilon)d\varepsilon = w_i^r \, T_{e,i}^r(\varepsilon) \qquad (2.56)$$

is used obtaining a set of equations to determine p(q+1) pivotal values. The advantages of this approach are easily seen; compared with the method of standard

equal-interval finite approximation, the number of equations to be solved is reduced. A better result is also obtained, particularly when the solution itself behaves somewhat irregularly, for in this case, an approximation by a set of polynomials is more successful than by that of a single polynomial of high degree [18]. Moreover, it is not difficult to arrange for blocks to be of unequal length and to take more values in the neighbourhood of the irregularities which is the region near the boundary in this particular case.

In the second case, that is the logarithmic singularity, the integral exists only as a Cauchy principal value. In such circumstances, the integral operators involved are not necessarily compact and therefore the existence of a unique solution may be difficult to prove. Also in practical terms, there may be problems in approximating the integrals over Cauchy principal values. Writing the integral in the form

$$\int_{-\infty}^{\infty} K \int_{0}^{1} \exp(-|x-\varepsilon|/\lambda u)\frac{du}{u}\, d\varepsilon \qquad (2.57)$$

and letting

$$h(s) = \int_{|s|/\lambda}^{\infty} \exp(-y)\,\frac{dy}{y} \qquad (2.58)$$

then h(s) has a logarithmic singularity at 0 (i.e $h(s)/\log s \longrightarrow$ constant as $s \longrightarrow 0$).

On writing

$$y = \exp(-|x-\varepsilon|/\lambda) \text{ in} \qquad (2.57)$$

the following formula

$$\int_{-\infty}^{\infty} KT_e h(x-\varepsilon)d\varepsilon \qquad (2.59)$$

is obtained.

Clearly there must be some form of restriction on the singularity since the integral above must exist for all values of x. Methods of treatment of singular multidimensional integrals have been given by Mikhlin [19]. Mayers [20] gives those for the one dimension case. Because of the singularity, any simple quadrature formula will fail. Hence methods must be sought to remove this singularity. The technique applied by Mayers transforms this severe singularity into a mild one. Equation (2.59) is then written in the form

$$\int_{-\infty}^{\infty} h(x-\varepsilon)\left[KT_e(\varepsilon,t) - KT_e(t,x)\right]d\varepsilon$$

$$+ \int_{-\infty}^{\infty} h(x-\varepsilon)\, KT_e(x,t)d\varepsilon$$

$$= \int_{-\infty}^{\infty} h(x-\varepsilon)\left[KT_e(\varepsilon,t) - KT_e(t,x)\right]d\varepsilon$$

$$+ KT_e(x,t)H(x) \qquad (2.60)$$

where $H(x) = \int_{-\infty}^{\infty} h(x-\varepsilon)d\varepsilon$ is assumed to be a known function. In this form, the integrand has only a mild singularity. Although $h(x-x)$ is infinite, the other factor $\left[KT_e(t,\varepsilon) - KT_e(t,x)\right]$ vanishes when $\varepsilon = x$, and the product must also vanish or the singularity would be

so severe that the integral would not exist at all.

(ii) Multidimensionality of integral

The integral in question is two-dimensional which further complicates matters because of the need to keep a reasonable accuracy with minimum computing time [21]. Methods attempting to reduce the double integrals to a single integral did not work. Since the kernel is not degenerate, the methods of separation of variables were not useful. Hence the product rule method was utilised. This uses a one dimensional method applied to each dimension. Then

$$\int_{-\infty}^{\infty} KT_e(t,\varepsilon) \int_0^1 \exp(-|x-\varepsilon|/\lambda u)\frac{du}{u}\, d\varepsilon \qquad (2.61)$$

can be approximated by

$$\sum_{i=1}^{n} w_i KT_e(t,\varepsilon_i) \int_0^1 \exp(-|x-\varepsilon|/\lambda u)\frac{du}{u}$$

$$= \sum_{i=1}^{n} w_i KT_e(t,\varepsilon_i) \sum_{j=1}^{n} p_j \exp(-|x-\varepsilon_i|/\lambda u_j)\frac{1}{u_j} \qquad (2.62)$$

where (w_i, ε_i) and (p_j, u_j) are the weights and abscissae of the rules used in the respective dimensions.

Equation (2.62) can however be simplified by splitting the range of integration. Let $s = |x-\varepsilon|/\lambda u$, then (2.62) becomes

$$\int_{-\infty}^{\infty} KT_e(t,\varepsilon) \int_{|x-\varepsilon|/\lambda}^{\infty} \frac{ds}{s}\, d\varepsilon \qquad (2.63)$$

Splitting the range of integration and removing the modulus sign gives

$$\int_{-\infty}^{x} KT_e(t,\varepsilon) \int_{(x-\varepsilon)/\lambda}^{\infty} \frac{ds}{s}\, d\varepsilon + \int_{x}^{\infty} KT_e(t,\varepsilon) \int_{-(x-\varepsilon)/\lambda}^{\infty} \frac{ds}{s}\, d\varepsilon$$

$$= \int_{-\infty}^{0} KT_e(t,\varepsilon) \int_{(x-\varepsilon)/\lambda}^{\infty} \frac{ds}{s}\, d\varepsilon + \int_{0}^{x} KT_e(t,\varepsilon) \int_{(x-\varepsilon)/\lambda}^{\infty} \frac{ds}{s}\, d\varepsilon$$

$$+ \int_{x}^{\infty} KT_e(t,\varepsilon) \int_{-(x-\varepsilon)/\lambda}^{\infty} \frac{ds}{s}\, d\varepsilon \qquad (2.64)$$

which on further simplification becomes

$$\int_{0}^{\infty} KT_e(t,\varepsilon) \int_{(x+\varepsilon)/\lambda}^{\infty} \frac{ds}{s}\, d\varepsilon + \int_{0}^{x} KT_e(t,\varepsilon) \int_{(x-\varepsilon)/\lambda}^{\infty} \frac{ds}{s}\, d\varepsilon$$

$$+ \int_{x}^{\infty} KT_e(t,\varepsilon) \int_{-(x-\varepsilon)/\lambda}^{\infty} \frac{ds}{s}\, d\varepsilon \qquad (2.65)$$

The inner integral exists provided $|x-\varepsilon|>0$. At $|x-\varepsilon|=0$, there occurs the singularity which can be made mild by changing equation (2.65) to

$$\int_{0}^{\infty} \left[KT_e(\varepsilon,t) - KT_e(t,x)\right] E_1((x+\varepsilon)/\lambda)\, d\varepsilon$$

$$+ \int_{0}^{x} \left[KT_e(\varepsilon,t) - KT_e(t,x)\right] E_1((x-\varepsilon)/\lambda)\, d\varepsilon$$

$$+ \int_{x}^{\infty} \left[KT_e(\varepsilon,t) - KT_e(t,x)\right] E_1(-(x-\varepsilon)/\lambda)\, d\varepsilon$$

$$+ KT_e(x,t) \int_{-\infty}^{\infty} E_1(|x-\varepsilon|/\lambda)\, d\varepsilon \qquad (2.66)$$

where $E_1(p)$ is the special function defined as in [22],

namely

$$E_1(p) = \int_p^{\infty} e^{-u}\, du/u \quad , \quad p > 0 \qquad (2.67).$$

To calculate an approximate value $E_1(p)$, the Chebyshev polynomials are used:

For $0 < p < 4$, the approximation is

$$E_1(p) = y(z) - \ln(p) = \sum_r a'_r T_r(z) - \ln(p) \qquad (2.68)$$

where $z = (p/2) - 1$.

For $p > 4$,

$$E_1(p) = \frac{e^{-p}}{p} y(p) = \frac{e^{-p}}{p} \sum a'_r T_r(z) \qquad (2.69)$$

$$z = -1.0 + 14.5/(p+3.25)$$

where $|z| <$ in both cases.

A routine to calculate $E_1(p)$ using the above approximation is given in the NAG library and is therefore used.

2.3.3 Quadrature formula used

A quadrature formula has still to be found for the outer intergral. The use of the Gauss-type quadrature is not practicable in this case because of the position of the singularity and therefore the pivotal points will vary with x. The use of Simpson's rule requires an even number of strips which cannot be guaranteed for all values of x. This therefore leaves the trapezium rule as the only alternative, if generally applied numerical integration methods are to be used. But as already stated in the last section, this involves using a lot of pivotal points which makes this method uneconomical. Hence the region of integration is approximated by polynomials or cubic splines [21]. This allows equation (2.66) to be written in the form

$$\sum_{r=1}^{n} \int_{(r-1)H}^{rH} \left[KT_e(\varepsilon,t) - KT_e(t,x)\right] E_1((x+\varepsilon)/\lambda)\,d\varepsilon$$

$$+ \sum_{r=m}^{n} \int_{(r-1)H}^{rH} \left[KT_e(\varepsilon,t) - KT_e(t,x)\right] E_1((x-\varepsilon)/\lambda)\,d\varepsilon$$

$$+ \sum_{r=m}^{n} \int_{(r-1)H}^{rH} \left[KT_e(\varepsilon,t) - KT_e(t,x)\right] E_1(-(x-\varepsilon)/\lambda)\,d\varepsilon \qquad (2.70)$$

where

$$\int_{(r-1)H}^{rH} \left[KT_e(\varepsilon,t) - KT_e(t,x)\right] E_1((x+\varepsilon)/\lambda)\,d\varepsilon$$

is approximated either by a polynomial or spline function by determining the coefficients of the polynomial or spline function to make them exact. This method allows for smoothing and interpolation. At the end ranges the introduction of external points is avoided by not smoothing.

After some preliminary runs, it was found that polynomials of degree less than three did not give reasonable results. A fitting of cubic polynomials or cubic spline functions gave the same results for the same tolerance but the use of the latter required more computing time. Hence cubic polynomials were chosen. The algorithm used is that given by Gill and Miller [24] and is included in the NAG library as routine D01GAF.

2.3.4 Ordinary differential equations

Since the quadrature formula has been decided upon, the temperature equations (2.46) to (2.49) can be written as

$$\frac{d}{dt}\left[\rho C_p T\right] = Af \sum_{j=-n}^{n} \omega_j h(x-\varepsilon_j) \left[KT(t,\varepsilon_j) - KT_e(t,x)\right]$$

$$- Af \sum_{j=1}^{n} \omega_j h(x-\varepsilon_j) \left[K(t,\varepsilon_j) - K_e(t,x)\right]$$
$$+ Af.H(x)\ KT_e(t,x)) - Af.H(x).T.K(t,x)$$
$$+ BfI_o g(x) \qquad (2.71)$$

$$\frac{d(KT_e)}{dt} = C(1-f) \sum_{j=1}^{n} \omega_j h(x-\varepsilon_j)\left[KT_e(t,\varepsilon_j) - KT_e(t,x)\right]$$
$$+ C(1-f).H(x)\ KT_e(t,x)) - \sigma KT_e(t,x)$$
$$+ CfT \sum_{j=1}^{n} \omega_j h(x-\varepsilon_j)\left[K(t,\varepsilon_j) - K(t,x)\right]$$
$$+ CfTKH(x) + D(1-f)I_o g(x) \qquad (2.72)$$

$$\frac{dK}{dt} = C \sum_{j=1}^{n} \omega_j h(x-\varepsilon_j)\left[K(t,\varepsilon_j) - K(t,x)\right]$$
$$+ CH(x).K(t,x) - \sigma K(t,x) \qquad (2.73)$$

and

$$\left.\begin{aligned} T_e(0,x) &= T(0,x) = To \\ T_e(t,\infty) &= T(t,\infty) = To \end{aligned}\right\} \qquad (2.74)$$

where

$$H(x) = \int_{-\infty}^{\infty} \int_{0}^{1} \exp(-|x-\varepsilon|/\lambda u)\, \frac{du}{u} d\varepsilon = 2\lambda \qquad (2.75)$$

is found by changing the order of intergration.

Combining (2.73) and (2.74) and making ρ and C_p independent of temperature, the following set of equations are obtained, namely,

$$\rho C_p \frac{dT}{dt} = Af \sum_{j=1}^{n} \omega_j h(x-\varepsilon_j)\left[KT(t,\varepsilon_j) - KT_e(t,x)\right]$$
$$- Af \sum_{j=1}^{n} \omega_j h(x-\varepsilon_j)\left[K(t,\varepsilon_j) - K_e(t,x)\right]$$
$$+ Af.2\lambda\left[KT_e(t,x) - KT(t,x)\right] + BfI_o g(x) \qquad (2.76)$$

$$\frac{d(KT_e)}{dt} = C(1-f) \sum_{j=1}^{n} \omega_j h(x-\varepsilon_j)\left[KT_e(t,\varepsilon_j) - KT_e(t,x)\right]$$
$$+ C(1-f).H(x)\ KT_e(t,x)) - \sigma KT_e(t,x)$$
$$+ CfT \sum_{j=1}^{n} \omega_j h(x-\varepsilon_j)\left[K(t,\varepsilon_j) - K(t,x)\right]$$
$$+ CfTK.H(x) + D(1-f)I_o g(x) \qquad (2.77)$$

The initial conditions are given as before by

$$T_e(0,x) = T(0,x) = To$$
$$T_e(t,\infty) = T(t,\infty) = To \qquad (2.78)$$

This gives a set of 2n coupled differential equations which are stiff [25]. The solution of these equations therefore requires a special method which is due to Gear [26]. The number of pivotal points, that is, the value of n, is determined by doing an energy balance on the energy in the electrons and phonons after each time interval. The total energy should be equal to the energy passing the metal surface from the laser. The final value decided upon was thirty two.

2.4 Numerical results and Discussion

2.4.1 Input power

The temporal variation of the incident laser beam was taken from a typical CO_2 laser pulse [27], illustrated by graph (2.1).

2.4.2 Metals used

In obtaining the results, the following metals were used: Aluminium , Copper, Iron, Tantalum and Nickel. These materials have been selected because they provide a comprehensive coverage of the various combinations of optical and thermal properties exhibited by metals.

2.4.3 Electron and Lattice temperature distribution

Simulations of the laser pulse-material interaction with the five metals are illustrated by graphs (2.2) to (2.6), which show the spatial electron and lattice temperature distributions. They are shown at time intervals of 50 nanoseconds.

For aluminium, graph (2.2), virtually all the laser energy is deposited within a distance of about 2.4 μm (140 meanfree-paths), while for copper the distance is around 6 μm (see graph (2.3)) and for the rest of the metals, this distance is of the order of a micron (see graphs (2.4) to (2.6)). This is consistent with the fact that copper and aluminium are good conductors of thermal energy. It implies that for the same input power, the surface temperature of copper and aluminium will rise more slowly as energy is transported away from the metal surface at a greater rate. This is shown by graphs (2.7) to (2.11). The high reflectivities of copper and aluminium [8] also contribute to the slow rate at which the surface temperature increases as less energy is absorbed.

Graphs (2.7) to (2.11), which also show the variation of surface electron and lattice temperatures below the boiling point, indicate that these temperature profiles follow closely the input power profile, at least up to the peak input power. They also show a substantial difference between the electron and phonon temperatures at the surface of approximately 2000K when the surface temperature approaches the boiling point. This difference is more marked for copper (4000K), this is due to the small number of electrons involved in the energy transfer process

(valency of copper is one).

2.4.4 Comparison between Electron Kinetic theory and Fourier conduction theory

Using the same input power and time interval a comparison has been made, for the metals considered, between the Electron Kinetic theory and the classical Fourier theory (Appendix 2D). This is depicted in graphs (2.12) to (2.16). It can be seen that the Electron Kinetic theory gives, at the same instant of time, a lattice temperature that is greater in magnitude at the surface and a profile which penetrates far less than that predicted by the Fourier model. These results are in good agreement with the experimental results of Yilbas [7].

The differences between the Electron Kinetic and Fourier theories are:

(i) In the Fourier theory, the electrons and phonons are assumed to be in equilibrium. But as can be seen from using the electron theory, this is not true especially for high input power intensities with a rapid rise time.

(ii) The Fourier theory assumes that between two succesive isothermal planes, at temperatures T_1 and T_2 and a distance Δx apart, the temperature gradient $(T_2-T_1)/\Delta x$ is constant, i.e higher order terms are ignored. Since the absorption coefficient (δ) and the irradiance (I_o) are very large, the higher order terms in such a solution are significant.

(iii) In the Fourier theory, the laser energy is assumed to be absorbed instantaneously by the material at any given distance whilst in the Electron Kinetic theory, the energy is absorbed by the electrons passing through the electomagnetic field.

(iv) Harrington [5] and later Riley [8] have shown that in the numerical solution of the Fourier conduction, the minimum distance Δx, such that the energy transported is characterised by the temperature of a particular isothermal plane, is 10λ, where λ is the electron-phonon mean free path. It therefore follows that the Fourier result

$$Q = -K\frac{dT}{dx} \qquad (2.79)$$

is not valid for situations where significant higher order temperature gradients occur within distances of the order of 10λ. Since the optical absorption depths, $1/\delta$, for most metals are of the order of λ, it follows that the Fourier equation of heat conduction for laser heated metals is not valid; the requirement for taking adequate account of the absorption process

$$\Delta x \ll 2/\delta \qquad (2.80)$$

conflicts with the requirement

$$\Delta x > 10\lambda. \qquad (2.81)$$

For aluminium, at 3.5 microseconds, the areas under both curves using the Electron Kinetic and Fourier theories (see graph (2.12)) are roughly the same, hence the energy held by the electrons is small. However for copper, (graph (2.13)), there is a significant area difference, about 80 %. This is because a

substantial fraction of the input energy is taken up by the electrons, hence their high temperature, see graph (2.3).

For Tantalum and Nickel (transition metals), the difference between the lattice temperatures using the two theories is markedly greater than that of other metals, see graphs (2.15) and (2.16). In the Electron Kinetic theory, this may be due to the underestimation of the significance of electron-electron collisions in the s and d shells [28] which results in an electron-phonon mean freepath that is smaller than it should be. This artificially small mean freepath leads to an increased phonon-electron collision rate which results in most of the laser energy being deposited near the metal surface. It is very difficult, at present, to evaluate this effect quantitatively.

It should be noted that in all the graphs using the Fourier theory the gradient is zero at the surface, this phenomenon is not visible because of the small distance over which the temperature is constant.

2.5 Conclusion

A new model based on the Electron Kinetic theory, for the transport of energy within a metal solid has been developed and shown to give much more accurate simulations of target behaviour. In order to illustrate the strengths of the Electron Kinetic theory, a comparision with the classical Fourier theory, has been produced. For the conditions addressed herein, the classical treatment overestimates the ability of metals to transport energy.

Because the Electron Kinetic theory properly incorporates the effects of high order temperature gradients and non-equilibrium energy transport, it predicts far higher temperature gradients and a smaller heat affected zone in agreement with available experimental results.

2.6 REFERENCES

1. J.M.Ziman, Electrons and Phonons
   Clarendon Press, Oxford 1960

2. C.Kittel, Introduction to solid state Physics
   John Wiley and Sons, Inc. 1971

3. N.Rykalin, A. Uglov and A.Kokora
   Laser machining and welding
   Mir Publishers 1978

4. J.F.Ready, Industrial Applications of Lasers
   Academic press, 1978

5. R.E.Harrington
   Application of the theory of heat conduction to the absorption of blackbody radiation
   J.Appl.Phys. vol.38, no.8, p. 3266 1967

6. R.E.Harrington
   Thermal conduction near a metal surface exposed to black body radiation
   J.Appl. Phys. vol.39 p.3669 1968

7. B.S.Yilbas, Heat transfer mechanisms initiating the laser drilling of metals
   Ph.D Thesis, University of Birmingham 1982

8. K.Riley, The thermodynamics of laser induced interaction processes in solids
Ph.D Thesis, University of Birmingham 1974

9. B.Bakewell and B.F. Scott
Electron Kinetic theory
Unpublished work,
University of Birmingham 1976

10. S.I.Anisimov, B.L.Kapeliovich and T.L.Perel'man
Electron emission from metal surfaces exposed to ultrashort laser pulses
Sov. Phys. JETP vol.39 No.2 p. 375 1974

11. J.F.Lee, F.W.Sears and D.L.Turcotte
Statistical Thermodynamics
Addison-Wesley 1963

12. M.A.Omar, Elementary solid state physics
Addison-Wesley Publishing Company 1975

13. C.T.H Baker
chapter 14 in Numerical solution Of Integral Equations
edited by L.M.Delves and J.Walsh.
Clarendon Press, Oxford 1974

14. S.G.Mikhlin and K.L.Smolitsky
Approximate methods for solutions of differential and integral equations.
New York American Elsevier 1967

15. I.Gladwell and R.Wait (eds)
A survey of Numerical Methods for partial differential equations
Clarendon Press, Oxford 1979.

16. P.J.Davis and P.Rabinowitz
Methods of Numerical Integration
Academic Press 1975

17. C.T.H.Baker
The numerical treatment of Integral Equations
Clarendon Press, Oxford 1977

18. D.F.Mayers, p.145-197 in Numerical Solution Of ordinary and partial differential equations.
edited by L.Fox, Pergamon Press 1962

19. S.G.Mikhlin
Multidimensional singular intervals and integral equations
Pergamon Press, 1965

20. D.F.Mayers, chapter 10 in Numerical solution of Integral equations
edited by L.M.Delves and J.Walsh
Clarendon Press, Oxford 1974

21. A.H.Stroud, Approximate calculation of multiple integrals
Prentice-Hall Inc. 1971

22. A.M.Abramowitz and I.A.Stegun

Handbook of Mathematical Functions

Dover Publications 1968

23. D.Jacobs (ed)

The state Of the Art in Numerical Analysis.

Academic Press 1977

24. P.E.Gill and G.F.Miller

An algorithm for the intergration of unequally spaced data

Comp. Journal 15 p. 80-83, 1972

25. G.Hall and M.Watts (eds)

Modern Numerical methods for Ordinary Differential Equations

Clarendon Press, Oxford 1976

26.C.W.Gear, Numerical initial value problems in Ordinary Differential Equations

Prentice-Hill Inc., New Jersey 1971

27. C.A.Byabagambi, C.R.Chatwin and B.F.Scott

Prediction of output power from high pulse repetition frequency CO_2 laser for use in manufacturing processes.

Third Int. Conf. on Optical and Optoelectronic Applied Science and Engineering, April 1986

28. J.S.Dugdale

Electrical properties of Metals and Alloys

Edward-Arnold 1977

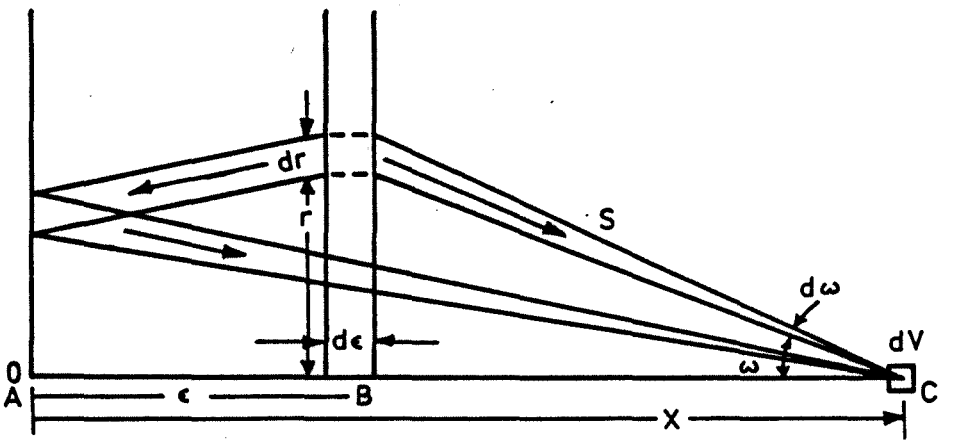

SCHEMATIC TO SHOW THE ELECTRON MOVEMENT INSIDE METALS. (x=0, REPRESENTS THE FREE SURFACE

FIG. (2·1)

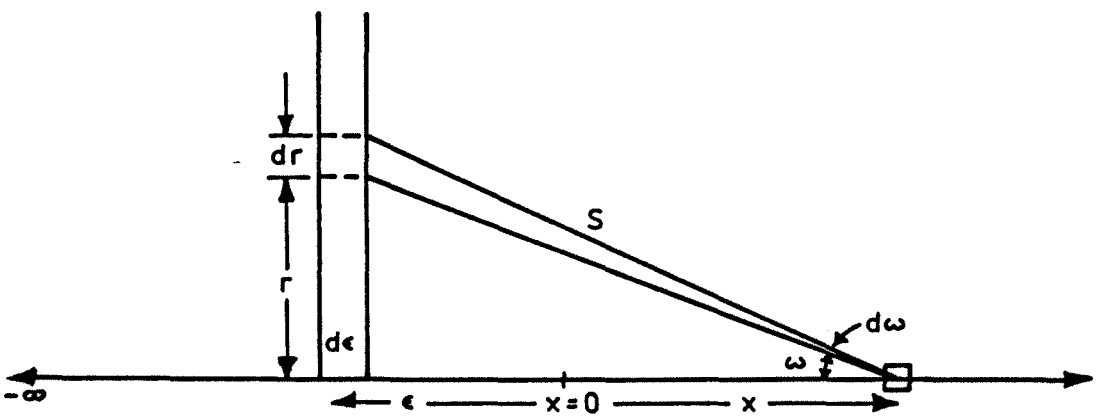

SCHEMATIC TO SHOW THE ELECTRON MOVEMENT INSIDE METALS AFTER CONSIDERING MIRROR IMAGE METHOD

FIG. (2·2)

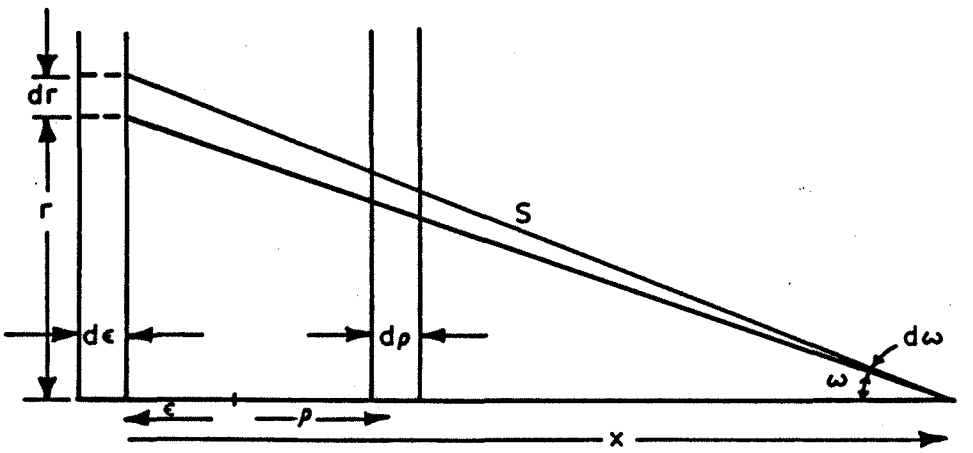

SCHEMATIC TO SHOW THE PHOTON ABSORPTION PROCESS FROM ϵ TO x

FIG. (2·3)

LASER OUTPUT POWER VERSUS TIME

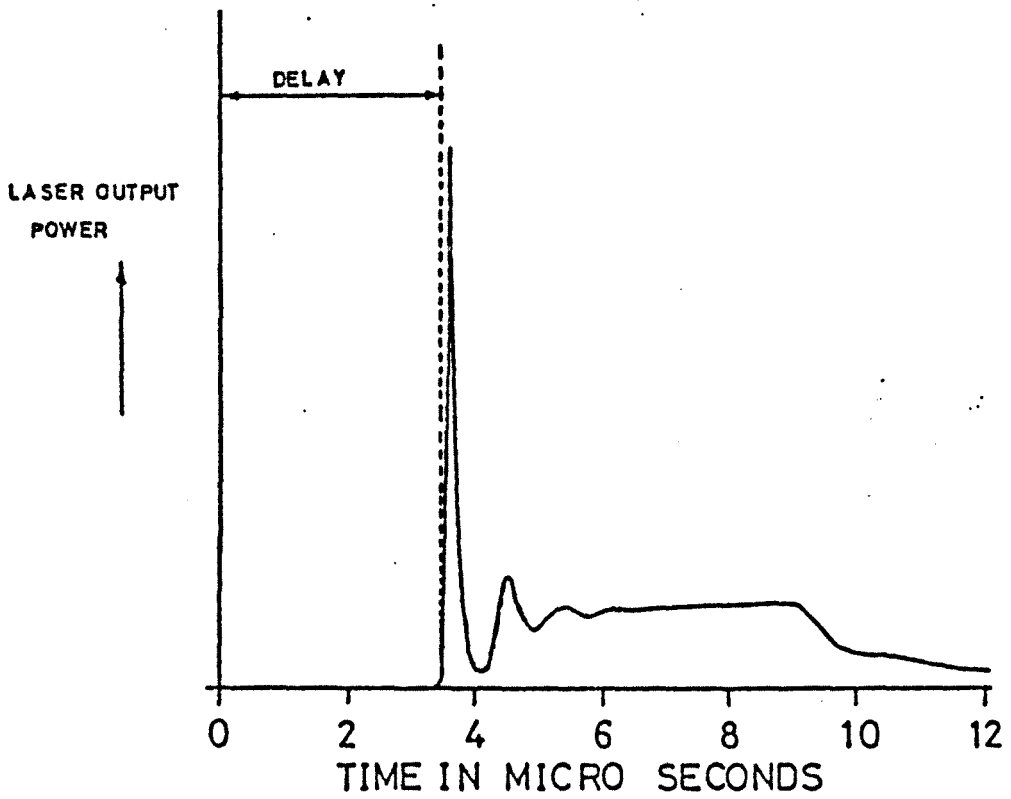

GRAPH (2.1)

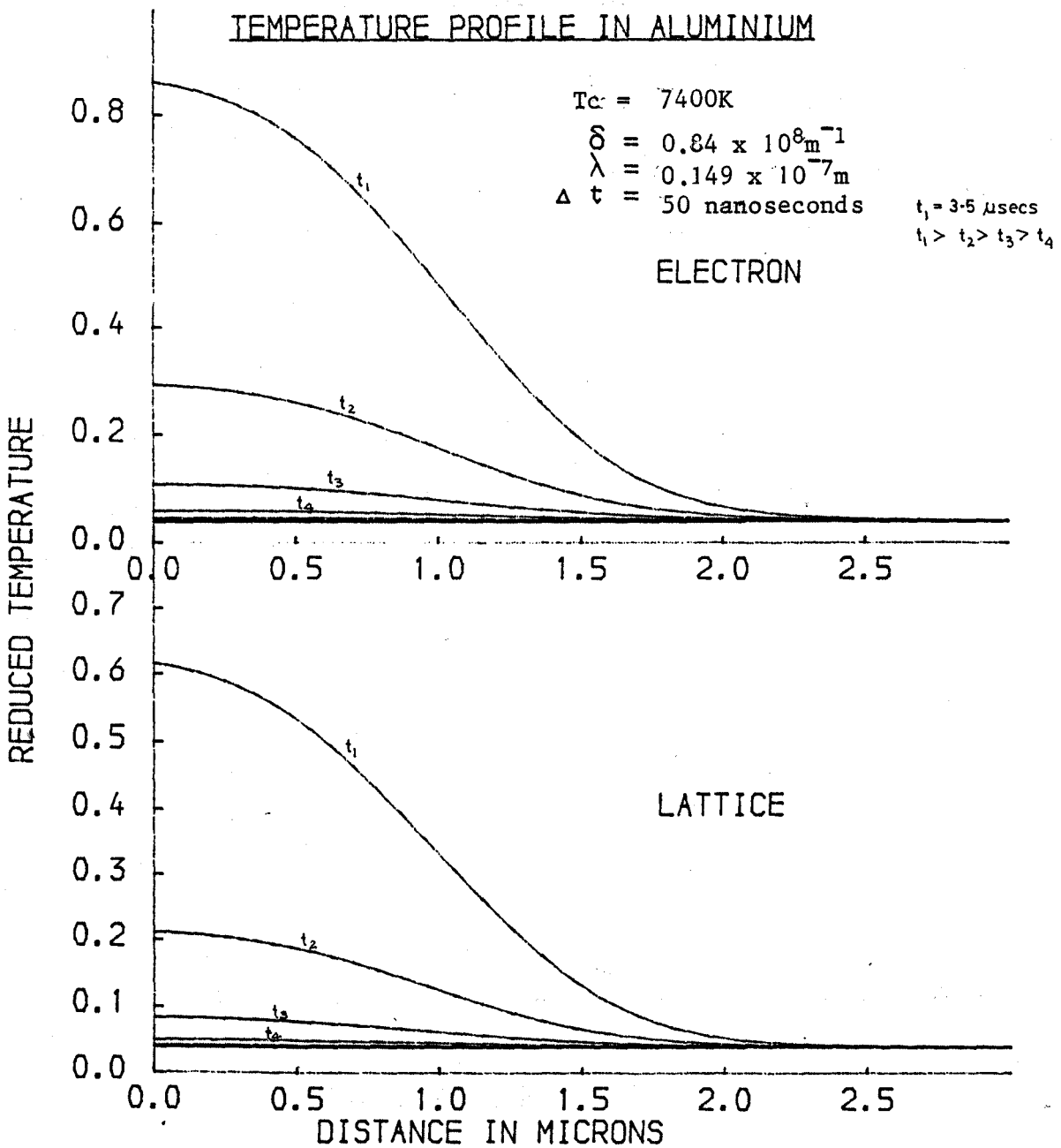
TEMPERATURE PROFILE IN ALUMINIUM
Tc = 7400K
δ = 0.84 x 10^8 m^-1
λ = 0.149 x 10^-7 m
Δ t = 50 nanoseconds
t1 = 3·5 μsecs
t1 > t2 > t3 > t4
ELECTRON
LATTICE
REDUCED TEMPERATURE
DISTANCE IN MICRONS
0.0
0.2
0.4
0.6
0.8
0.1
0.3
0.5
0.7
0.5
1.0
1.5
2.0
2.5

GRAPH (2.2)

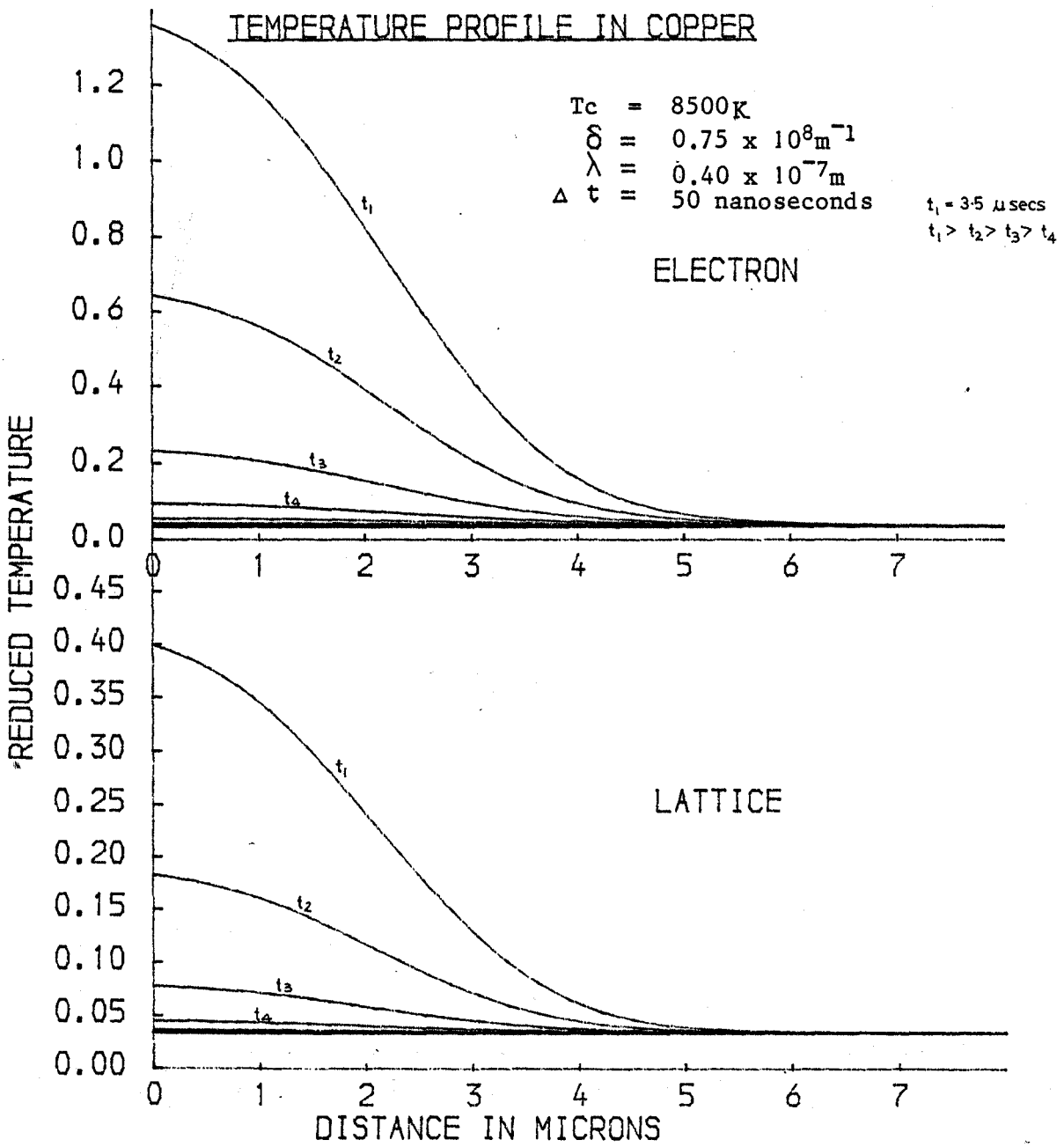
TEMPERATURE PROFILE IN COPPER
Tc = 8500K
δ = 0.75 x 10^8 m^-1
λ = 0.40 x 10^-7 m
Δ t = 50 nanoseconds
t1 = 3·5 μsecs
t1 > t2 > t3 > t4
ELECTRON
LATTICE
REDUCED TEMPERATURE
DISTANCE IN MICRONS
1.2
1.0
0.8
0.6
0.4
0.2
0.0
0.45
0.40
0.35
0.30
0.25
0.20
0.15
0.10
0.05
0.00
0
1
2
3
4
5
6
7

GRAPH (2.3)

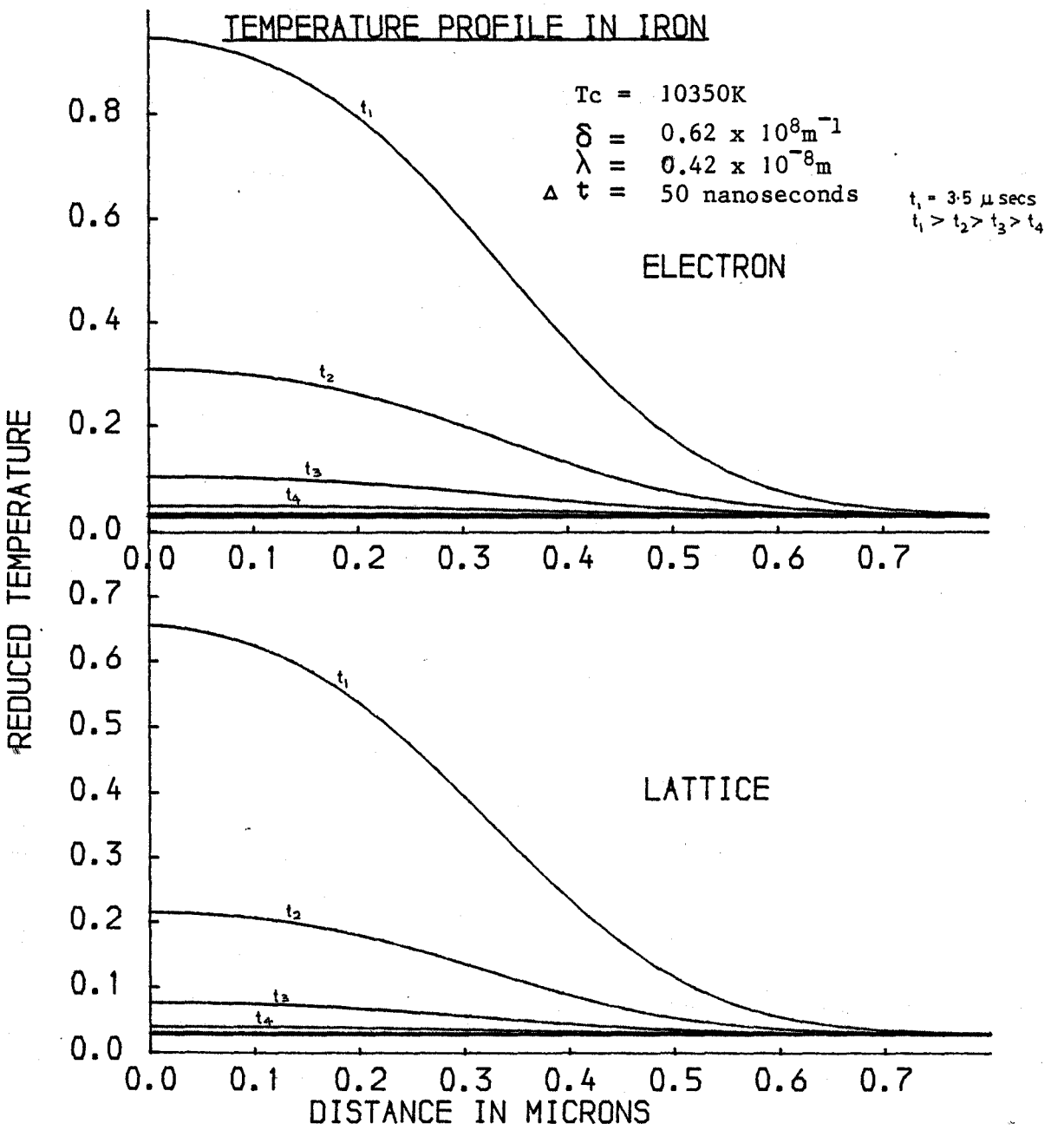
TEMPERATURE PROFILE IN IRON
Tc = 10350K
δ = 0.62 x 10^8 m^-1
λ = 0.42 x 10^-8 m
Δ t = 50 nanoseconds
t1 = 3·5 μ secs
t1 > t2 > t3 > t4
ELECTRON
LATTICE
REDUCED TEMPERATURE
DISTANCE IN MICRONS
0.0
0.1
0.2
0.3
0.4
0.5
0.6
0.7
0.8

GRAPH (2.4)

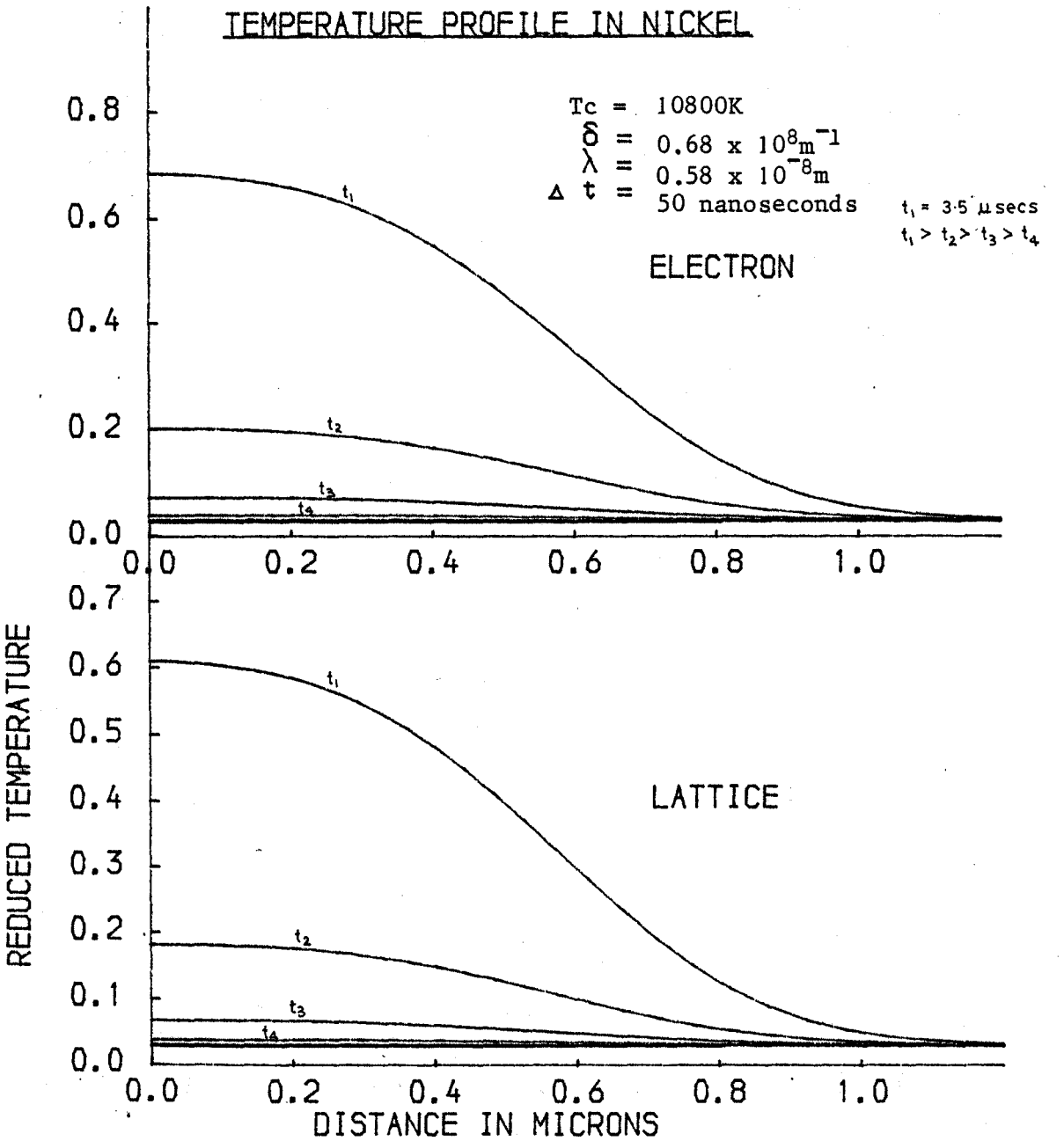
TEMPERATURE PROFILE IN NICKEL
Tc = 10800K
δ = 0.68 x 10^8 m^-1
λ = 0.58 x 10^-8 m
Δ t = 50 nanoseconds
t1 = 3·5 μsecs
t1 > t2 > t3 > t4
ELECTRON
LATTICE
REDUCED TEMPERATURE
DISTANCE IN MICRONS
0.0
0.2
0.4
0.6
0.8
1.0

GRAPH (2.5)

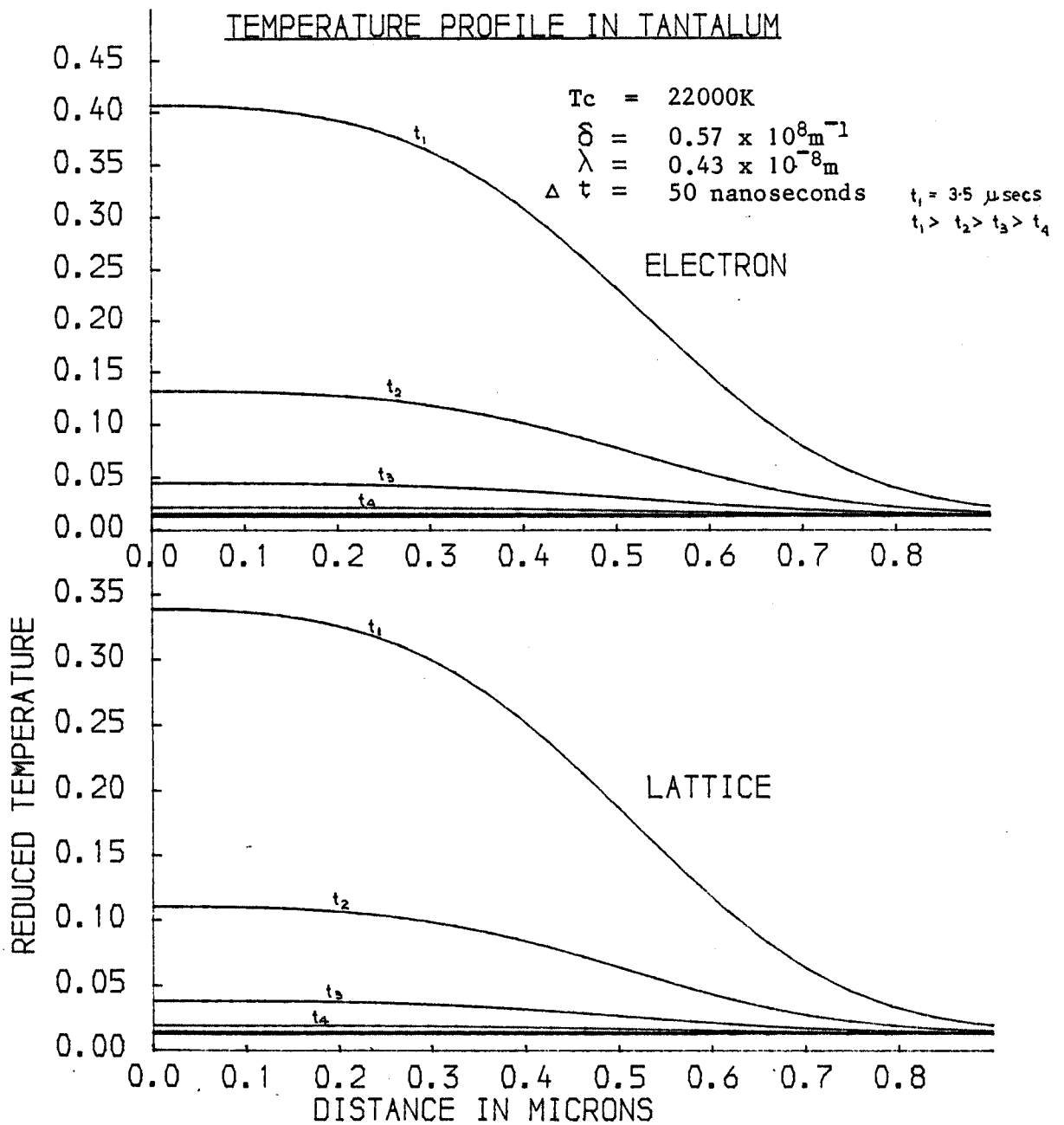
TEMPERATURE PROFILE IN TANTALUM
Tc = 22000K
δ = 0.57 x 10^8 m^-1
λ = 0.43 x 10^-8 m
Δ t = 50 nanoseconds
t1 = 3·5 μsecs
t1 > t2 > t3 > t4
ELECTRON
LATTICE
REDUCED TEMPERATURE
DISTANCE IN MICRONS
0.00
0.05
0.10
0.15
0.20
0.25
0.30
0.35
0.40
0.45
0.0
0.1
0.2
0.3
0.4
0.5
0.6
0.7
0.8

GRAPH (2.6)

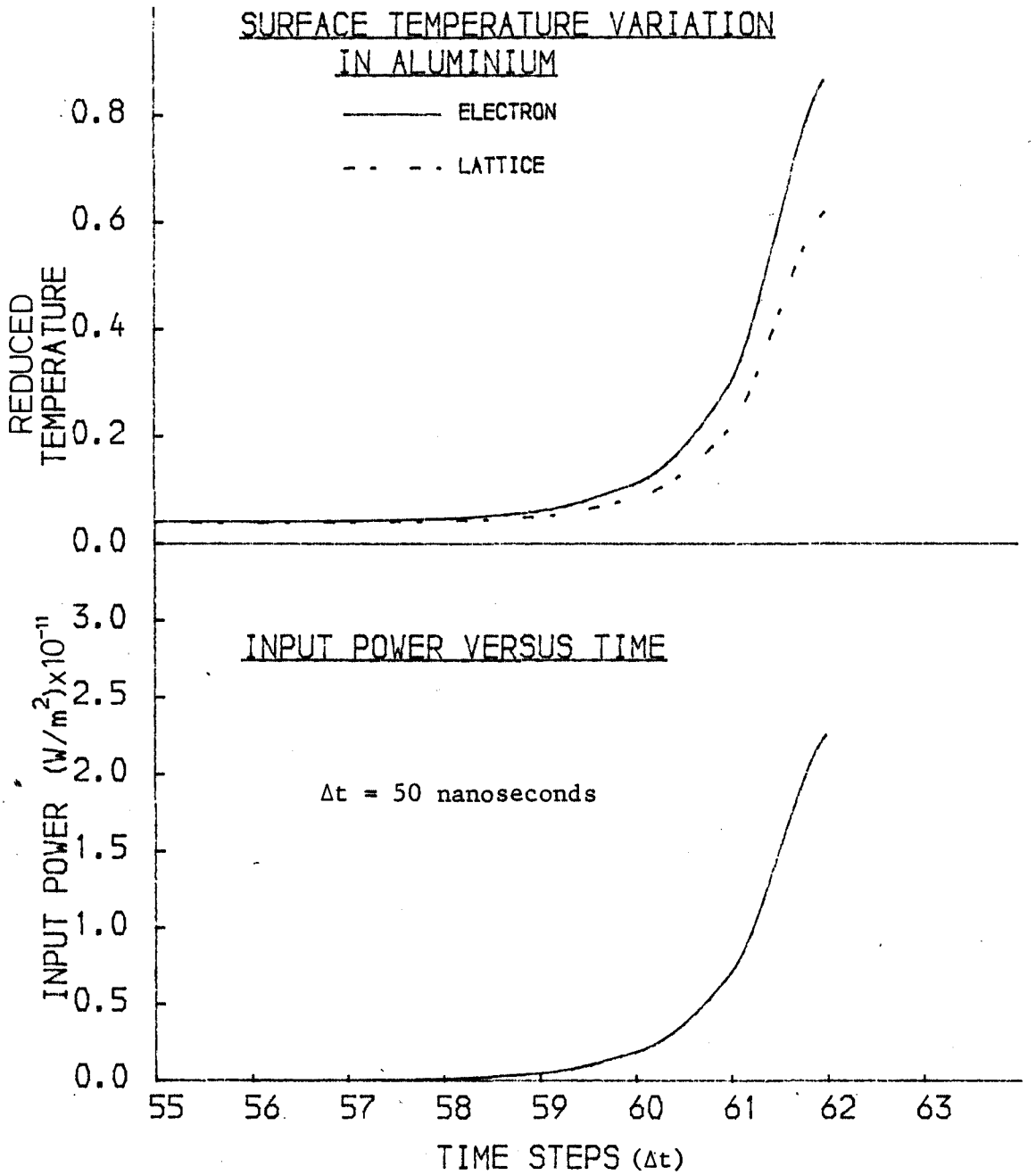
SURFACE TEMPERATURE VARIATION
IN ALUMINIUM
ELECTRON
LATTICE
REDUCED TEMPERATURE
0.8
0.6
0.4
0.2
0.0
INPUT POWER VERSUS TIME
Δt = 50 nanoseconds
INPUT POWER (W/m²)x10⁻¹¹
3.0
2.5
2.0
1.5
1.0
0.5
0.0
55
56
57
58
59
60
61
62
63
TIME STEPS (Δt)

GRAPH (2.7)

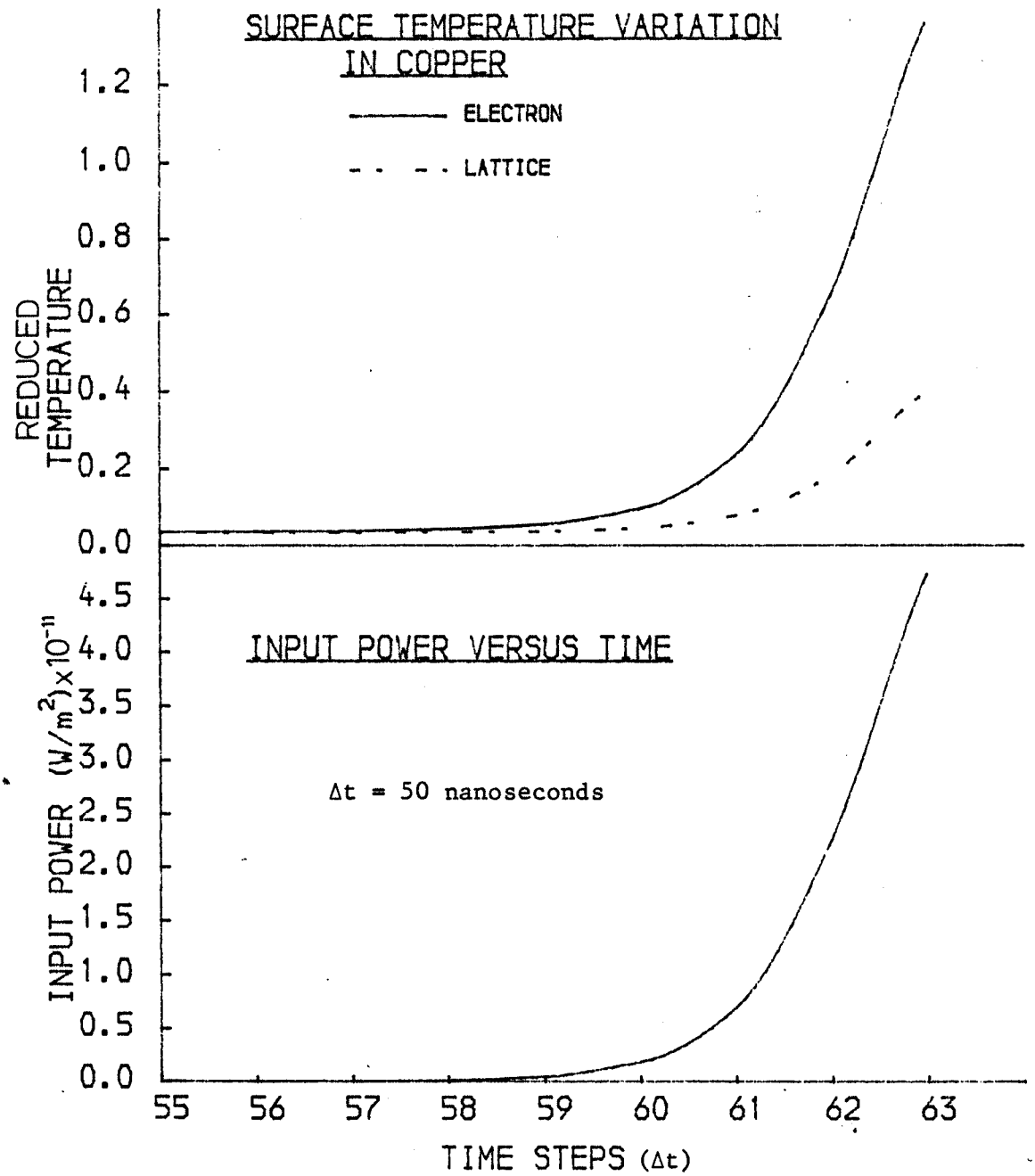
SURFACE TEMPERATURE VARIATION IN COPPER
ELECTRON
LATTICE
REDUCED TEMPERATURE
1.2
1.0
0.8
0.6
0.4
0.2
0.0
INPUT POWER VERSUS TIME
Δt = 50 nanoseconds
INPUT POWER (W/m²)x10⁻¹¹
4.5
4.0
3.5
3.0
2.5
2.0
1.5
1.0
0.5
0.0
55
56
57
58
59
60
61
62
63
TIME STEPS (Δt)

GRAPH (2.8)

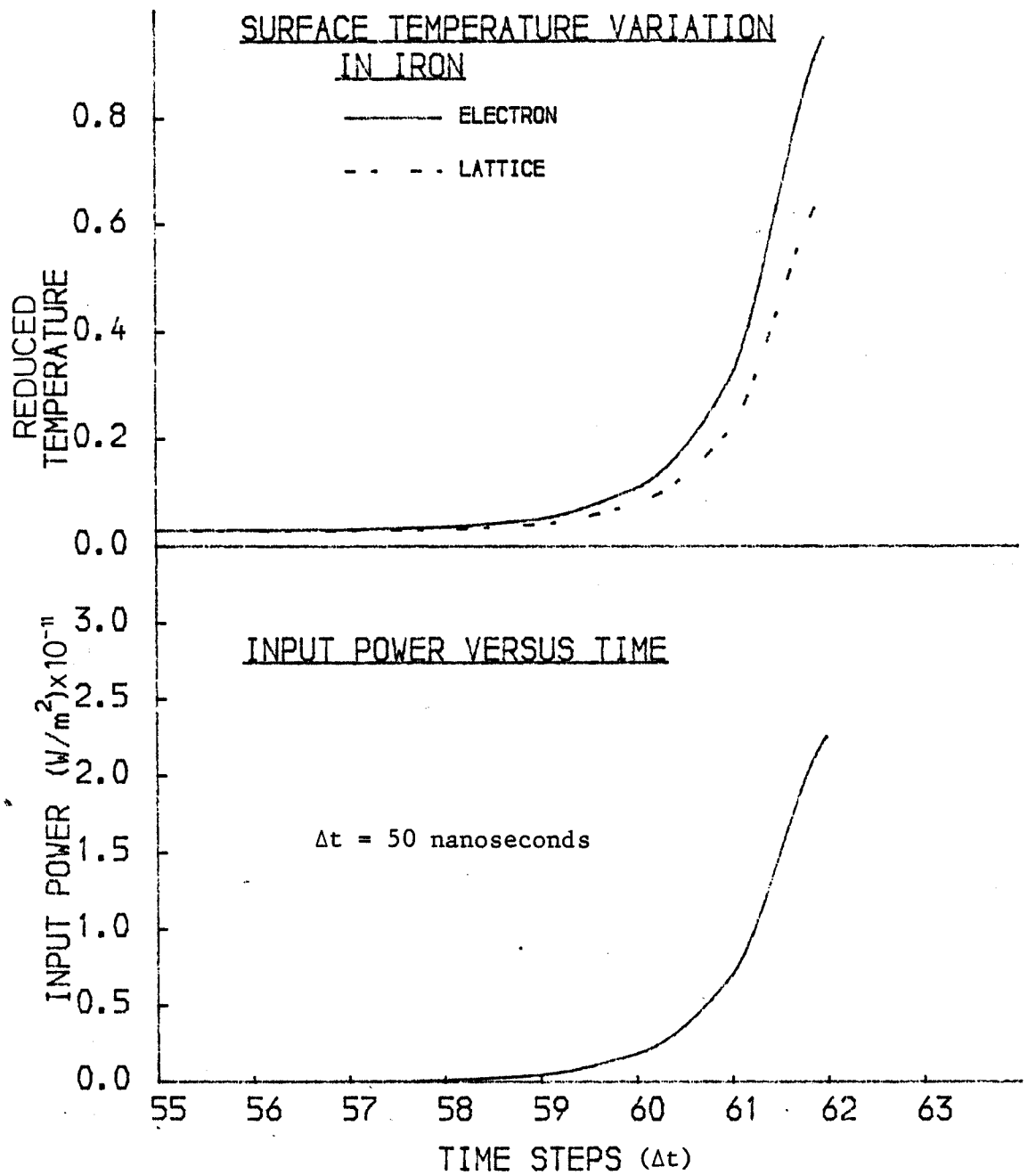
SURFACE TEMPERATURE VARIATION IN IRON
ELECTRON
LATTICE
REDUCED TEMPERATURE
0.8
0.6
0.4
0.2
0.0
INPUT POWER VERSUS TIME
INPUT POWER (W/m²)x10⁻¹¹
3.0
2.5
2.0
1.5
1.0
0.5
0.0
Δt = 50 nanoseconds
55
56
57
58
59
60
61
62
63
TIME STEPS (Δt)

GRAPH (2.9)

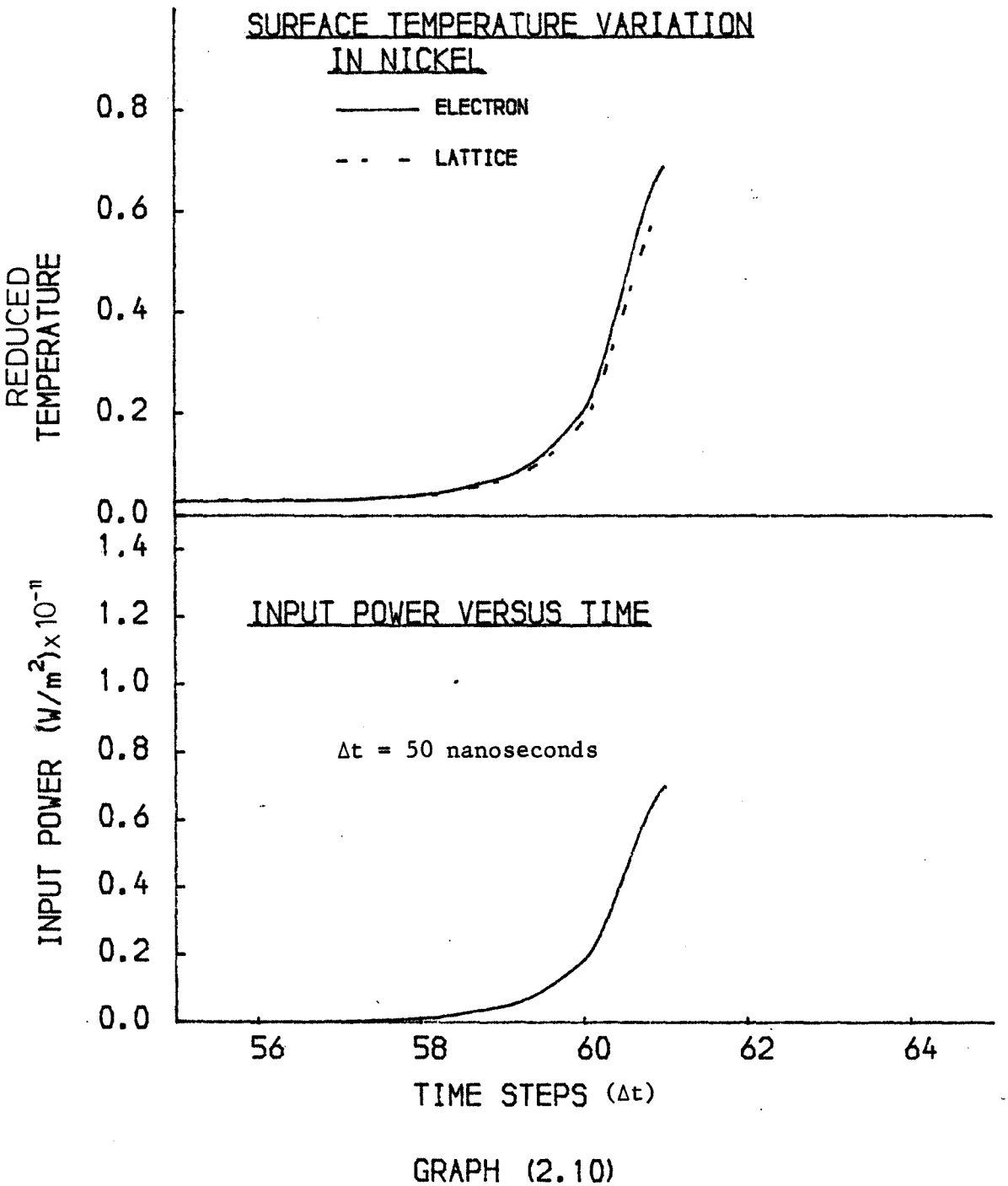
SURFACE TEMPERATURE VARIATION
IN NICKEL
ELECTRON
LATTICE
REDUCED TEMPERATURE
0.8
0.6
0.4
0.2
0.0
INPUT POWER VERSUS TIME
Δt = 50 nanoseconds
INPUT POWER (W/m²)x10⁻¹¹
1.4
1.2
1.0
0.8
0.6
0.4
0.2
0.0
56
58
60
62
64
TIME STEPS (Δt)

GRAPH (2.10)

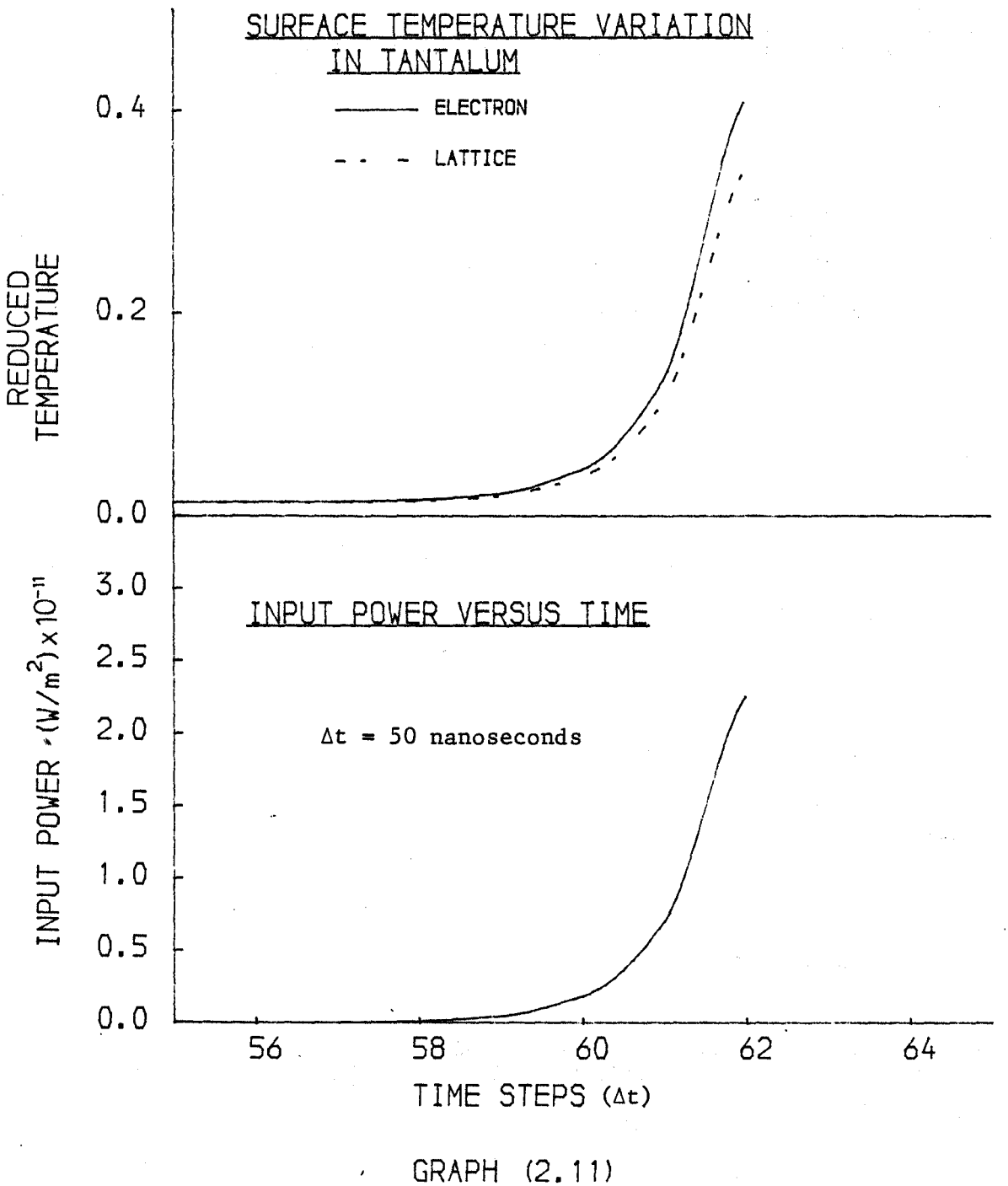
SURFACE TEMPERATURE VARIATION
IN TANTALUM
ELECTRON
LATTICE
REDUCED TEMPERATURE
0.4
0.2
0.0
INPUT POWER VERSUS TIME
Δt = 50 nanoseconds
INPUT POWER (W/m²) x 10⁻¹¹
3.0
2.5
2.0
1.5
1.0
0.5
0.0
56
58
60
62
64
TIME STEPS (Δt)

GRAPH (2.11)

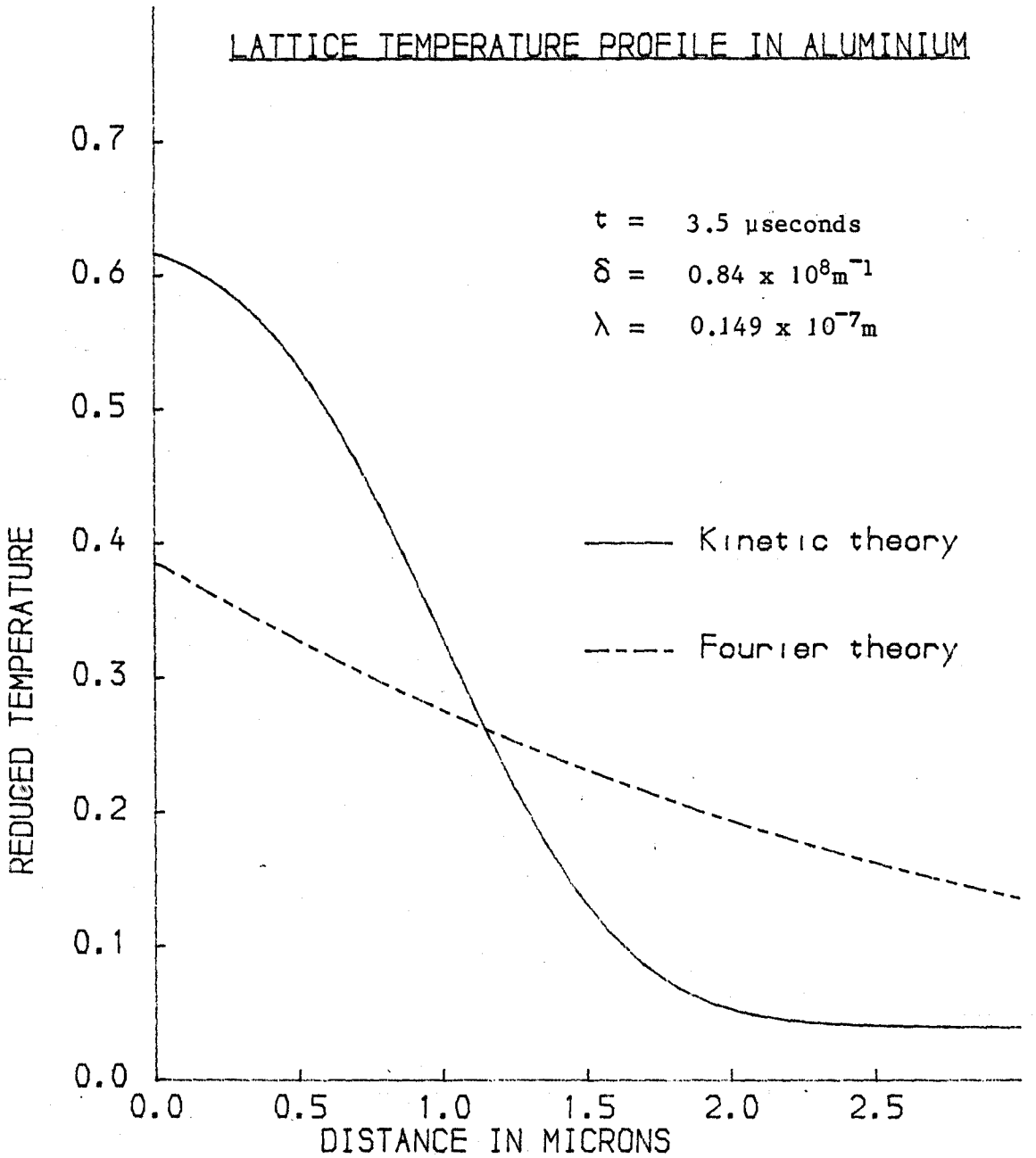
LATTICE TEMPERATURE PROFILE IN ALUMINIUM
t = 3.5 μseconds
δ = 0.84 x 10^8 m^-1
λ = 0.149 x 10^-7 m
Kinetic theory
Fourier theory
REDUCED TEMPERATURE
0.0
0.1
0.2
0.3
0.4
0.5
0.6
0.7
0.0
0.5
1.0
1.5
2.0
2.5
DISTANCE IN MICRONS

GRAPH (2.12)

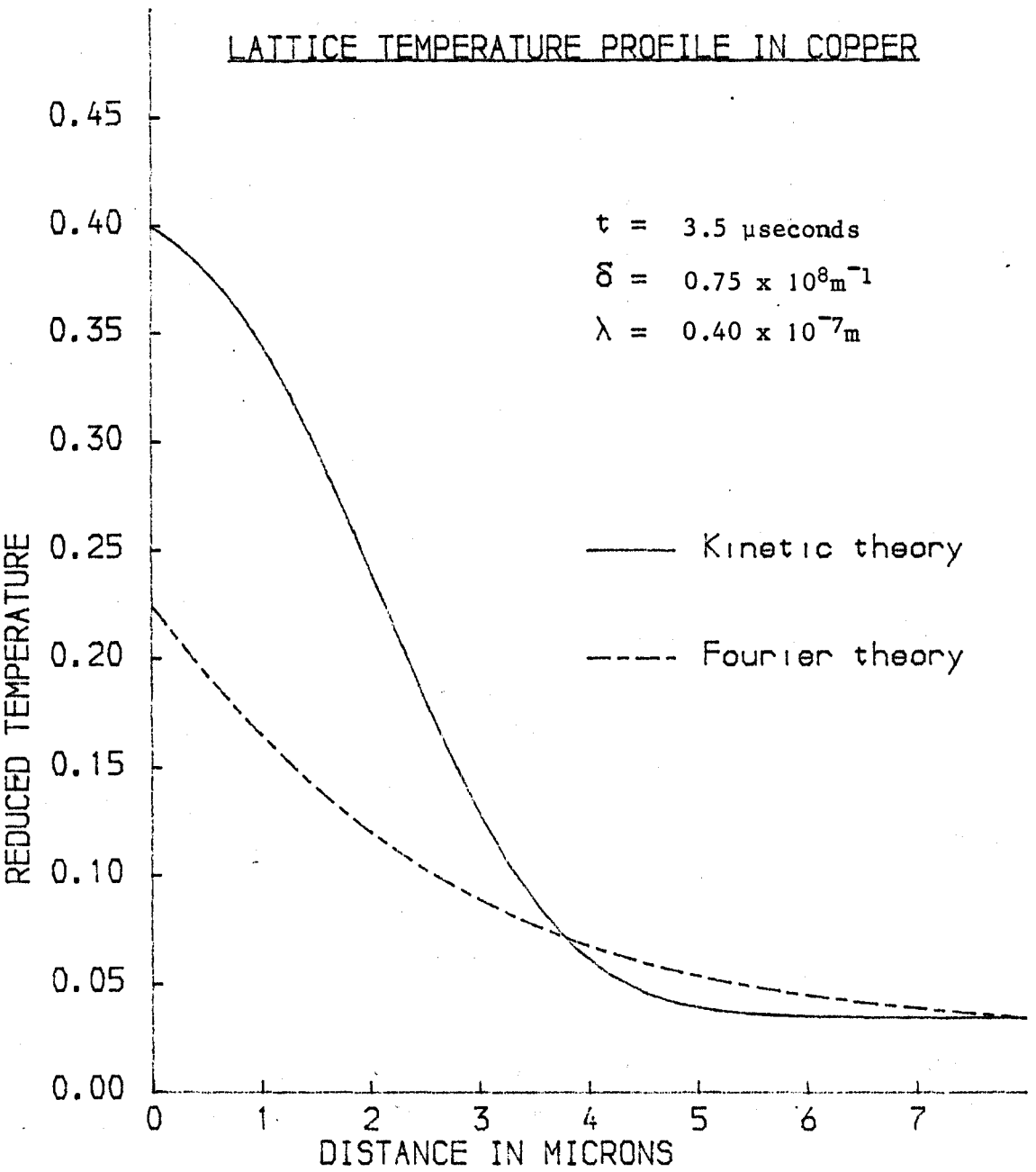
LATTICE TEMPERATURE PROFILE IN COPPER
0.45
0.40
0.35
0.30
0.25
0.20
0.15
0.10
0.05
0.00
REDUCED TEMPERATURE
t = 3.5 μseconds
δ = 0.75 x 10^8 m^-1
λ = 0.40 x 10^-7 m
Kinetic theory
Fourier theory
0
1
2
3
4
5
6
7
DISTANCE IN MICRONS

GRAPH (2.13)

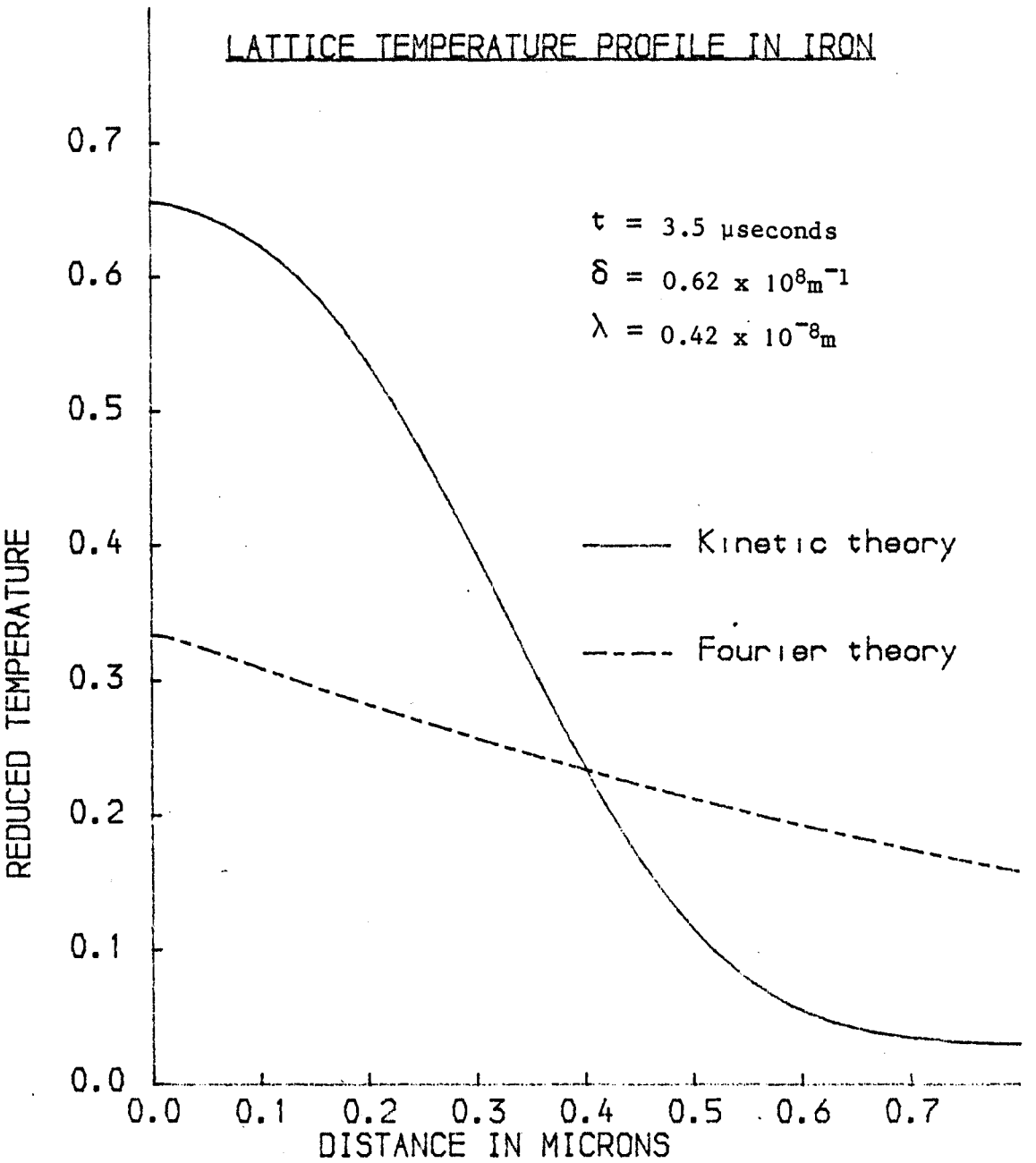
LATTICE TEMPERATURE PROFILE IN IRON
t = 3.5 μseconds
δ = 0.62 x 10^8 m^-1
λ = 0.42 x 10^-8 m
Kinetic theory
Fourier theory
REDUCED TEMPERATURE
0.0
0.1
0.2
0.3
0.4
0.5
0.6
0.7
DISTANCE IN MICRONS

GRAPH (2.14)

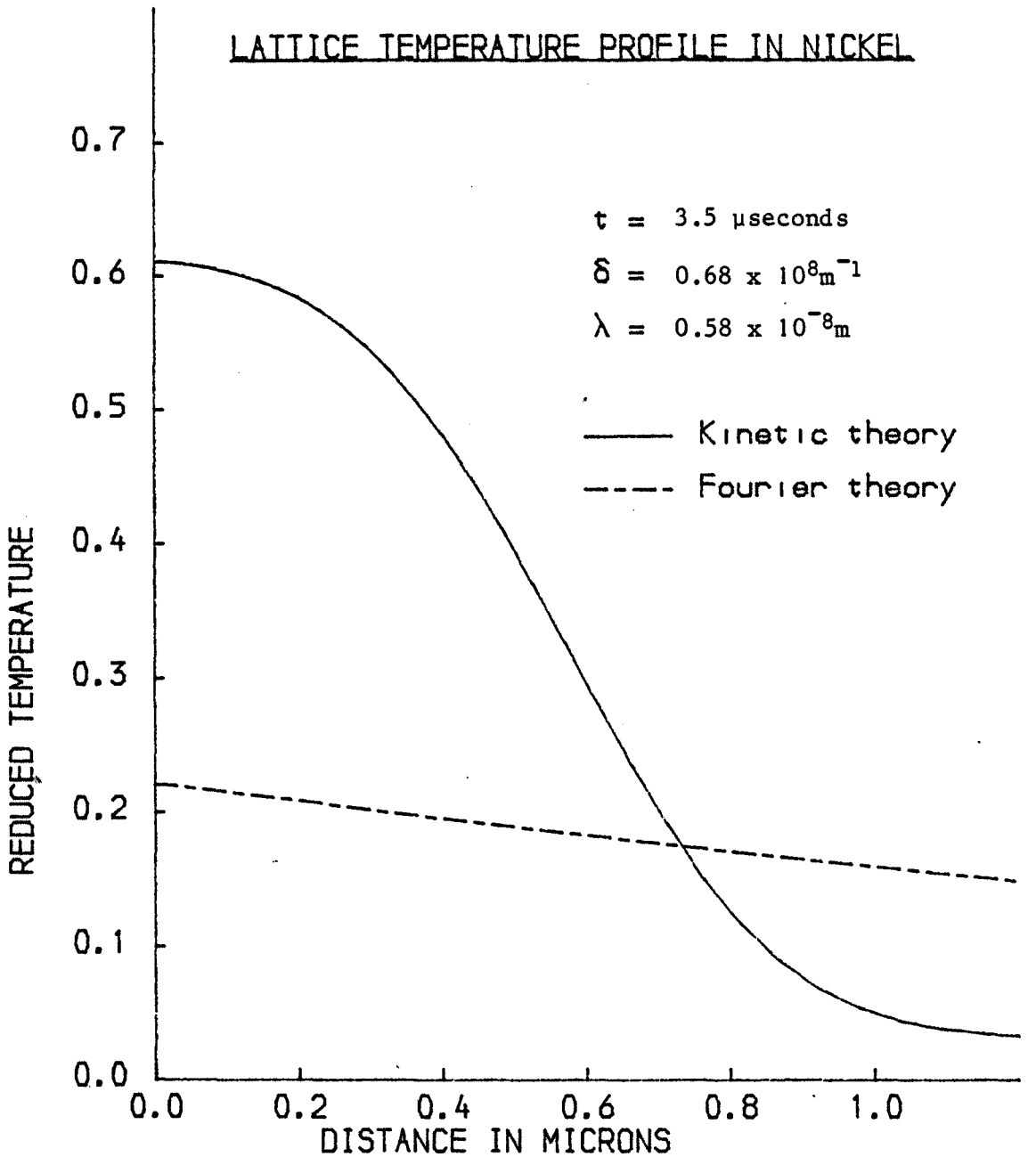
LATTICE TEMPERATURE PROFILE IN NICKEL
t = 3.5 μseconds
δ = 0.68 x 10^8 m^-1
λ = 0.58 x 10^-8 m
Kinetic theory
Fourier theory
REDUCED TEMPERATURE
0.0
0.1
0.2
0.3
0.4
0.5
0.6
0.7
0.0
0.2
0.4
0.6
0.8
1.0
DISTANCE IN MICRONS

GRAPH (2.15)

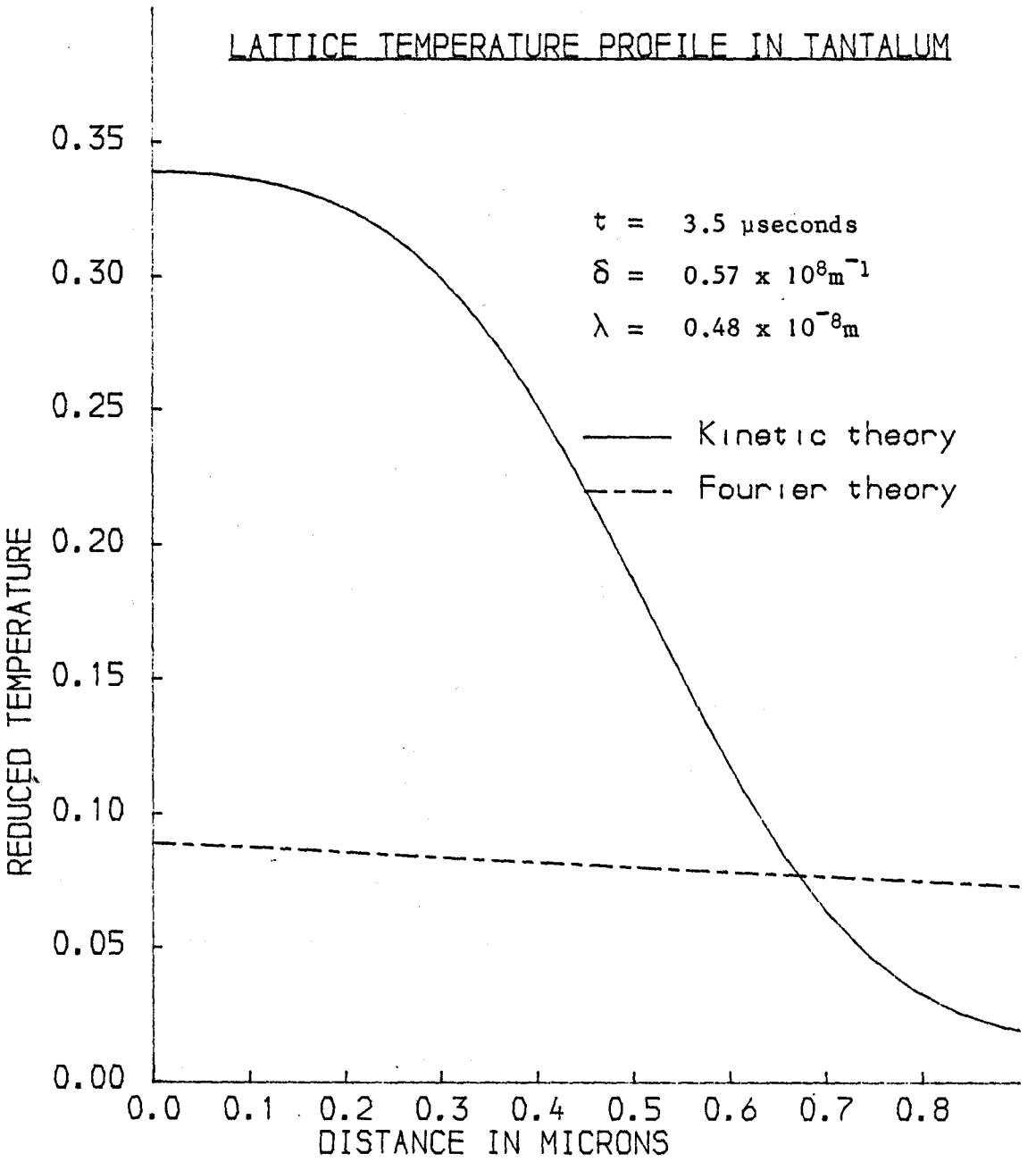
LATTICE TEMPERATURE PROFILE IN TANTALUM
0.35
0.30
0.25
0.20
0.15
0.10
0.05
0.00
REDUCED TEMPERATURE
t = 3.5 μseconds
δ = 0.57 x 10^8 m^-1
λ = 0.48 x 10^-8 m
Kinetic theory
Fourier theory
0.0 0.1 0.2 0.3 0.4 0.5 0.6 0.7 0.8
DISTANCE IN MICRONS

GRAPH (2.16)

CHAPTER THREE

Extension of the heat transfer theories to include evaporation

Nomenclature

C_p	Specific heat capacity (J/kg.K)
dV	Volume element (m^3)
E(x,t)	Electron energy (J)
$E_p(x,t)$	Lattice (phonon) energy (J)
f	Fraction of excess energy transferred to the phonons
G	Evaporation rate (atoms/sec)
$I_o(t)$	Surface power intensity (W/m^2)
I(x,t)	Power intensity at position x (W/m^2)
k	Boltzmann constant = 1.380×10^{-23} J/K
K	Thermal conductivity (W/m K)
L	Specific latent heat of evaporation (J/kg)
m	Mass of atom (kg)
N'	Number density of participating electrons (m^{-3})
N	Number density of valency electrons (m^{-3})
n(x,t)	Phonon (atoms) number density (m^{-3})
p,r,s	Distances (m)
R(t)	Surface metal reflectivity
t	time (sec)
T_e	Electron temperature (K)
T	Lattice (phonon) temperature (K)
T_f	Fermi electron temperature (K)
T_s	Surface lattice temperature (K)

U_o	Latent heat of evaporation per atom (J)
V_s	Velocity of evaporating surface (m/s)
v	Fermi electron velocity (m/s)
x, X(t)	Distance (m)
z	Electron collision frequency (sec^{-1})
δ	Absorption coefficient (m^{-1})
ε	Distance (m)
ω	Angle subtended by element
λ	Electron-phonon mean free path (m)
ρ	Density of metal (kg/m^3)

3.1 Introduction

It has been shown in chapter 2 that the Electron Kinetic theory predicts, in agreement with experimental data, higher surface temperatures, for a given power intensity profile, than the classical Fourier treatment. This accuracy is however obtained at an extra cost because the integral equations involved in the Electron Kinetic theory require more computing time.

In this chapter, both theories are extended to include the effects of evaporation. Since in the process of metal evaporation, a lot of energy is carried away in the removed material, the temperature profiles in the two theories may become comparable. If this does happen, then a switch can be made from the electron theory to the Fourier conduction theory the moment the two profiles become coincident. This strategy will maximise computational efficiency.

3.2 Evaporation

3.2.1 Evaporation rate

Beyond the evaporation temperature, allowance must be made for the loss of material by evaporation. Von Allmen [1] derived the evaporation rate using the theory of Landau et al [2] while Prokhorov et al [3] derived an expression based on the Clapeyron-Clausius equation. Both expressions are based on continuum thermodynamics.

The model used here to account for evaporation is that due

to Frenkel [4]. It is based on the application of statistical thermodynamics and leads to the rate of evaporation being given as

$$G = n\sqrt{\left(\frac{kT}{2\pi m}\right)} \exp(-U_o/kT_s) \qquad (3.1)$$

where n is the number of atoms per unit volume at the surface, m is the mass of the atom, k is the Boltzmann constant and U_o is the energy required to completely remove one atom from the material i.e the latent heat of vaporization per atom. Therefore the velocity of the evaporating surface is given by

$$G = V_s = n\sqrt{\left(\frac{kT}{2\pi m}\right)} \exp(-U_o/kT_s) \qquad (3.2)$$

The effect of molecules coming from the interior is neglected since the energy required is twice that needed for those at the surface.

3.2.2 Effects of the solid-liquid phase change

Melting is accompanied by a relatively small change in physical properties compared with the effects which occur on evaporation. This means that the character of the thermal motion is not fundamentally different from that in solids, that is, small molecular vibrations about fixed lattice sites.

As the temperature is increased, these vibrations are augmented by larger, irreversible movements which shift the equilibrium site to a new position a distance of the order of the intermolecular spacing. Finally, at high enough temperatures, the whole lattice structure is destroyed and the material is completely composed of free molecules (vapour). This model of a

material, is thus able to explain all these effects and is particurlarly suited as a starting point for the analysis of the laser heating process where very high temperature gradients exist.

3.3 Heat transfer theory

3.3.1 Electron Kinetic theory

The method of analysis is similar to that in the previous chapter except for two important features:

(i) At the surface, there is a mathematical singularity due to the vaporization of the material

(ii) The boundary is receeding and therefore the mirror image method cannot be applied directly.

Due to these important features, the mathematics of the problem is simplified by changing the coordinate system such that the material moves with velocity V_s towards the origin, where V_s is the receeding velocity of the material surface. This has the effect of keeping the origin stationary as shown in fig.(3.1).

The problem is then to determine the energy transported into dV at x from all electrons in dε at ε, then integrate for ε to allow for contributions from the whole of the material, bearing in mind that the bulk material is moving through the coordinate system with velocity V_s.

In developing the transport equations using the Electron Kinetic theory, which incorporates evaporation, the moving surface has two effects on the equations developed in chapter 2:

(i) Effect on electron transport: the material is moving with velocity V_s and therefore all mass transport processes involve relative velocities. In the case of the electron transport this relative velocity is

$$(v \pm V_s) = v(1 \pm V_s/v) \qquad (3.3)$$

depending on wether the electrons come from the right or left of the elemental volume (see fig. (3.1)). Now the thermal electron velocities are of the order of 10^6m/s whilst the evaporating surface velocity is not expected to exceed 10m/s. Therefore

$$V_s/v \quad << 1 \qquad (3.4)$$

and the effect on the electron transport by the moving material can be safely neglected. This allows the results of Chapter 2, for electron transport, to be made use of without any modification.

(ii) Effect on the lattice energy in the elemental volume: Initially the lattice energy at x is $E_p(x,t)$. This is influenced by the electron transport and the convective heat transfer due to the moving material. This allters the equations describing the lattice and electron energy distributions, which are modified to:

$$\frac{\partial nE_p(x,t)}{\partial t} - V\frac{\partial}{\partial x}(nE_p(x,t))$$

$$= \int_{-\infty}^{\infty}\int_0^{\pi/2} \frac{N'v}{2\lambda}\exp(-|x-\varepsilon|/\lambda\cos\omega)\frac{\sin\omega}{\cos\omega}\frac{f}{\lambda}$$

$$\left[E(\varepsilon,t) + \frac{1}{2}\{dt - \frac{2|s|}{v}\}\frac{\partial E(\varepsilon,t)}{\partial t}\right.$$

$$\left. + \frac{(1-R)I_o\delta}{N'v\cos\omega}\left|\int_\varepsilon^x \exp(-\delta p)dp\right| - E_p(x,t)\right] d\omega d\varepsilon$$

(3.5)

with the evaporation term $\rho L(T_s)V_s$ added at x=0. Therefore the energy left in the electrons is given by

$$\frac{\partial}{\partial t}\left[N'E(x,t)\right]$$

$$= dV \int_{-\infty}^{\infty}\int_{0}^{\pi/2} \frac{N'v}{2\lambda} \exp(-|x-\varepsilon|/\lambda\cos\omega)\ \frac{\sin\omega}{\cos\omega}\frac{1}{\lambda}$$

$$\left[E(\varepsilon,t) + \frac{1}{2}\left\{dt - \frac{2|s|}{v}\right\}\frac{\partial E(\varepsilon,t)}{\partial t}\right.$$

$$\left. + \frac{(1-R)I_o\delta}{N'v\cos\omega}\left|\int_{\varepsilon}^{x} \exp(-\delta p)dp\right|\right] d\omega d\varepsilon$$

$$- \frac{N'v}{\lambda} E(x,t) - \frac{\partial nE_\rho(x,t)}{\partial t}$$

$$+ V\frac{\partial}{\partial x}(nE_\rho(x,t)) \qquad (3.6)$$

3.3.2 Fourier conduction theory

In order to determine the temperature profile within the material, the Fourier heat conduction equation with a spatially distributed heat source moving with the material surface (i.e vapour-liquid interface) is used. Referring to fig.(3.2) for nomenclature,

$$\frac{\partial}{\partial t}\left[\rho C_\rho T\right] = \frac{\partial}{\partial x}\left[K\frac{\partial T}{\partial x}\right] + \delta I_0 \exp(-\delta(x-X(t)) \qquad x > X(t) \qquad (3.7)$$

An energy balance at the surface requires that the energy given to the vaporized material equals the energy conducted from the solid. Hence,

$$\rho L(T)\frac{dX(t)}{dt} = K\frac{\partial T}{\partial x}\Big|_{x=X(t)} \qquad (3.8)$$

where $L(T_s)$, the specific latent heat of vaporisation is given by Riley [5] as $L(T_s) = L_0\left[1 - (T_s/T_c)^2\right]$. L_0 is the normal specific

latent heat of vaporisation and T_c is the critical temperature of the metal.

In order to solve equations (3.7) and (3.8) for temperature and velocity, the following boundary conditions are required:

From equation (3.2)

$$\frac{dX(t)}{dt} = Vs = \sqrt{\left(\frac{kTs}{2\pi m}\right)} \exp\ (-Uo/kTs) \qquad (3.9)$$

Hence the boundary conditions (3.9) become

$$\rho L(Ts)Vs = K\frac{dT}{dx}\Big|_{x=X(t)} \qquad (3.10)$$

This allows the surface temperature to vary from the boiling point as opposed to fixing it at a constant value [6]. The other boundary condition is

$$T(\infty,t) = T_0 \qquad (3.11)$$

An initial condition is required for the heat conduction equation at time t=0. It is assumed that the material to be heated is at room temperature T_0. Hence

$$T(o,x) = T_0 \qquad (3.12)$$

3.4 Solution of the transport equations

3.4.1 Electron Kinetic theory

From equation (3.5) and (3.6) and using the simplifications made in chapter 2, the following equations are obtained, namely,

$$\frac{d}{dt}\left[\rho C_p T\right] = Af\int_{-\infty}^{\infty} KT(t,\varepsilon)\ h(x-\varepsilon)\ d\varepsilon - AfT\int_{-\infty}^{\infty} KT(t,\varepsilon)\ h(x-\varepsilon)\ d\varepsilon$$

$$+ BfI_o g(x) + V_s \frac{\partial}{\partial x}\left[\rho\ C_p T\right] \qquad (3.13)$$

$$\frac{d}{dt}\left[KT_e\right] = C(1-f)\int_{-\infty}^{\infty} KT_e(t,\varepsilon)\, h(x-\varepsilon)\, d\varepsilon + CfT\int_{-\infty}^{\infty} KT_e(t,\varepsilon\, h(x-\varepsilon)\, d\varepsilon$$

$$- \sigma KT_e + D(1-f)I_0 g(x) \qquad (3.14)$$

A boundary condition is needed for equation (3.13) due to vaporisation, that is at x=0, the term ρLV_s must be incorporated.

The above equation is in a diffusion-convective form and special methods of solution may be required depending on the relative magnitudes of the convective and diffusive terms. This magnitude is determined by the Peclet number i.e the non-dimensional quantity

$$P = \rho C_p V_s x/K \qquad (3.15)$$

where x is the length of the domain of interest. For very large P, the convective term dominates making the use of the central difference scheme unstable [7] whilst for moderate values of P, the finite difference scheme can be applied. Spalding [8] proposed a method of solution called the hybrid scheme where for $P < 2$, the usual methods of solution for partial differential equations are used. For $P > 2$, the diffusive term is assumed to be zero and the equation becomes a first order hyperbolic equation.

Hence to solve the above equation with accompanying initial and boundary conditions, the line method [9] is initially used. This method allows the integro-differential equation to be approximated by a system of ordinary differential equations, obtained by replacing the space derivatives by finite differences and integrals. The resulting system of stiff ordinary

Gear's method [10]. Also a value of the Peclet number is computed to make sure it falls within the range $-2 < P < 2$. This is especially important when evaporation becomes significant. If the Peclet number becomes numerically greater than 2, then a switch to the Hybrid scheme must be made.

3.4.2 Fourier conduction theory

To simplify the derived equations (3.7) to (3.9) which describe the heat transfer process, taking into account evaporation, a change of the coordinate system (see fig. (3.2))

$$s = x - X(t) \qquad (3.16)$$

is introduced. The equations to be solved then become

$$\frac{\partial}{\partial t}\left[\rho C_p T\right] - V_s \frac{\partial}{\partial s}\left[\rho C_p T\right] = \frac{\partial}{\partial s}\left[K\frac{\partial T}{\partial s}\right] + \delta I_0 \exp(-\delta s) \qquad s > 0 \qquad (3.17)$$

and

$$\rho L(Ts) Vs = K\frac{\partial T}{\partial s}\Big|_{s=0} \qquad (3.18)$$

with boundary and initial conditions

$$\left.\begin{aligned} T(\infty, t) &= T_0 \\ T(0, s) &= T_0 \end{aligned}\right\} \qquad (3.19)$$

To solve the above set of equations, the line method [10] is again used and its description for integral equations is given in section 2.3.2. The Peclet number must again be computed to make sure it does not exceed two and an energy balance performed to check the accuracy of the solution (see Appendix 3A).

3.5 Results and Discussion

3.5.1 Input Power

Since this is a continuation of the analysis done in chapter 2, the input power profile used is the same as that mentioned in section 2.4.1, namely, a temporal profile shown in graph (2.1).

3.5.2 Metals used

Only two metals were investigated because of the large computing time required for the solution of the equations. The metals used here are Aluminium and Copper.

3.5.3 Electron and Lattice temperatures using the Kinetic theory

Graphs (3.1) and (3.2) show the temporal Electron and lattice temperature variation, at different time intervals for Aluminium and Copper respectively.

After the surface temperature exceeds the normal boiling point, evaporation becomes significant. This leads to a large negative gradient at the surface because of the high energy evaporating material being removed. However, graphs (3.1) and (3.2) do not show this phenomenon due to the lack of resolution of the x-axis. Hence the first five mean free paths are expanded and graphs (3.3) and (3.4) drawn to show this large lattice temperature negative gradient. The electron temperature gradient at the surface is hardly affected by evaporation because evaporation is a lattice phonemenon and thus has little effect upon the electrons.

Graphs (3.5) and (3.6), which show the variation of surface electron and lattice temperatures and the input temporal distribution, indicate that the electron temperature profile closely follows that of the input power, with a small time lag. This is expected as thermalisation of the electrons is rapid. The lattice surface temperature stays reasonably constant due to the clamping caused by evaporation. Because of this clamping, the difference between electron and lattice temperatues becomes quite large for the input powers considered. This implies that the electrons and lattice do not return to equilibrium with the onset of vaporisation.

As the inner surface temperatures are higher, a superheated liquid phase must be formed leading to a series of explosions and an increase in the rate of material removal. This is consistent with the experimental observations of Shayler [11].

3.5.4 Lattice temperature profile using the Fourier conduction theory

Results using the Fourier conduction theory are presented in graphs (3.7) and (3.8) for aluminium and copper respectively. These graphs show the temporal variation at time intervals of 50 nanoseconds and go beyond the evaporation temperature up to a time of 3.3 μseconds after the start of the laser output pulse. They show a small negative gradient at the surface and have a high penetration depth especially when evaporation becomes steady. Graphs (3.9) and (3.10) show the variation of the surface temperature with time. These graphs are compared with

the input power profile which is drawn on the same graphs. They show that after evaporation begins, the surface temperature dependence on the input power is reduced. This is because a large percentange of the laser energy goes into the evaporation process.

3.5.5 Comparison between the Kinetic and Fourier theories.

A comparision has been made between the Fourier theory and the Electron Kinetic theory. As shown in chapter 2, the Electron Kinetic theory gives higher temperature gradients and therefore higher surface temperatures for the same input intensities. This leads to a faster vaporization rate.

From graphs (3.3) and (3.4), the Kinetic theory shows a high negative gradient at the surface once evaporation becomes important leading to the possibilty of explosion. This is not evident in the Fourier conduction theory. Also, the graphs show that the two theories do not converge even when evaporation becomes significant ruling out the idea of a switch from one theory to another (this also means that the Fourier theory continues to be invalid). This also implies that the energy transport term (conduction) is still important during evaporation and cannot be neglected as is done in a lot of publications on the subject [1]. The results also indicate the independence of the lattice surface temperature (derived from the Electron Kinetic theory) from the input power (if this is high enough to cause vaporization) and the dependence of the same on the input power when the Fourier theory is used.

3.6 Conclusion

A comparision between the Electron Kinetic theory and the Fourier conduction theory has been extended to include evaporation. It has been shown that the two theories give different temporal temperature profiles at the surface, with the Electron Kinetic theory giving a larger negative gradient at the surface leading to the possiblity of superheated liquid forming inside the material resulting in explosions, this is in agreement with the observed experimental behaviour of metal targets. Also the predicted velocity of 1m/s for the mass removal rate agrees quite well with the experimental results of Bakewell [12].

The surface temperature gradients obtained using the Fourier analysis are almost zero therefore removing the possibility of significant nucleation and explosion. This is in agreement with the theoretical results of von Allmen [1] who therefore discounted the idea of explosion, though experiments with cine cameras indeed show explosions occuring.

Also, the Kinetic theory results show that energy transport by electrons, remains significant even after evaporation becomes important, hence the need to keep the transport term even after evaporation becomes significant. This also means that the two theories never converge within the time scale considered (the Fourier theory continues to be invalid).

REFERENCES

1 M von Allmen Laser drilling velocity in metals
J.Appl. Phys., vol. 47, no.12, 1976 p. 5460-63

2 L.D. Landau and E.M. Lifshitz
Statistical Physics Pergamon Press, New York, 1959

3 A.M.Prokhorov, V.A.Batanov, F.V.Bunkin and V.B.Fedorov
Metal evaporation under powerful optical radiation
J.Quant. Elect., vol.QE-9, no.5. p.503, 1973

4 J.Frenkel Kinetic theory of liquids
Clarendon Press, Oxford, 1946

5K.Riley The thermodynamics of laser induced interaction processes in metals
Ph.D Thesis, University of Birmingham, 1974

6 J.F. Ready Industrial applications of Lasers
Academic Press, 1978

7 S.V.Pantaker Numerical Heat Transfer and Fluid flow
Hemisphere Publishing coorporation, 1980

8 D.B.Spalding A novel finite-difference formulation for differential expressions involving both first and second derivatives
Int. J. Num. methods Eng., Vol. 4, p.551, 1972

9 I.Gladwell and R.Wait (eds)
A survey of Numerical methods for partial differential equations Clarendon Press, Oxford 1979

10 C.W.Gear Numerical initial value problem in Ordinary Differential Equations
Prentice-Hill Inc., New Jersey 1971

11 P.J.Shaylor Laser drilling phenomenon including beam/vaporized material interaction
Ph.D Thesis, University of Birmingham, 1975

12 B.A.Bakewell Performance of a pulsed laser system in relation to machining mechanisms
Ph.D Thesis, University of Birmingham, 1973

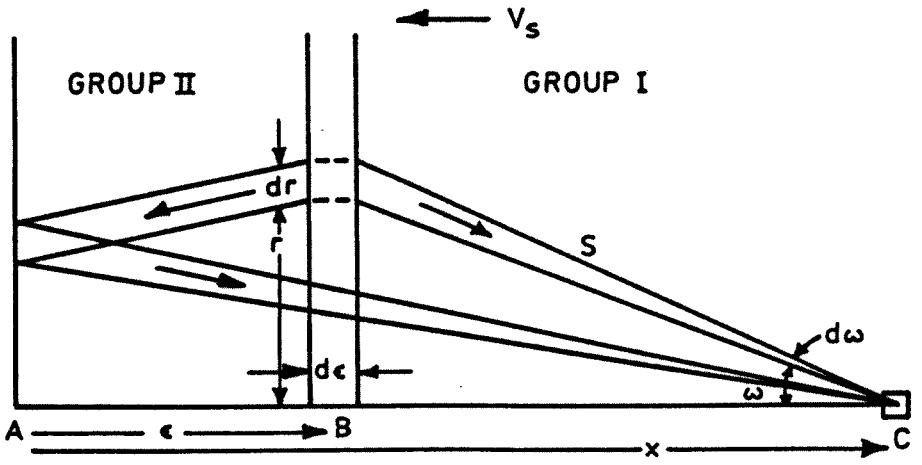

SCHEMATIC TO SHOW THE ELECTRON MOVEMENT INSIDE METALS. (x = 0, REPRESENTS THE FREE SURFACE AND THE MATERIAL IS MOVING WITH VELOCITY s

FIG. (3·1)

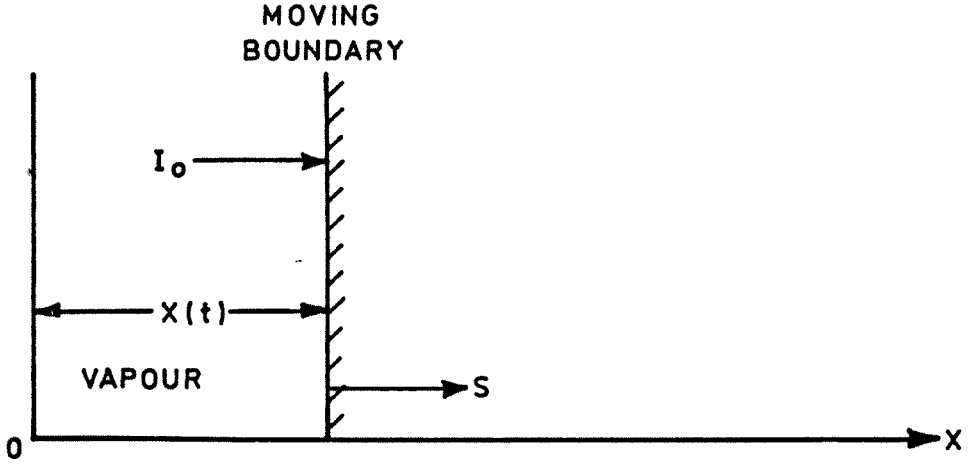

SCHEMATIC OF A ONE DIMENSIONAL MOVING BOUNDARY PROBLEM

FIG. (3·2)

Temperature Profile in Aluminium using the Kinetic Theory.

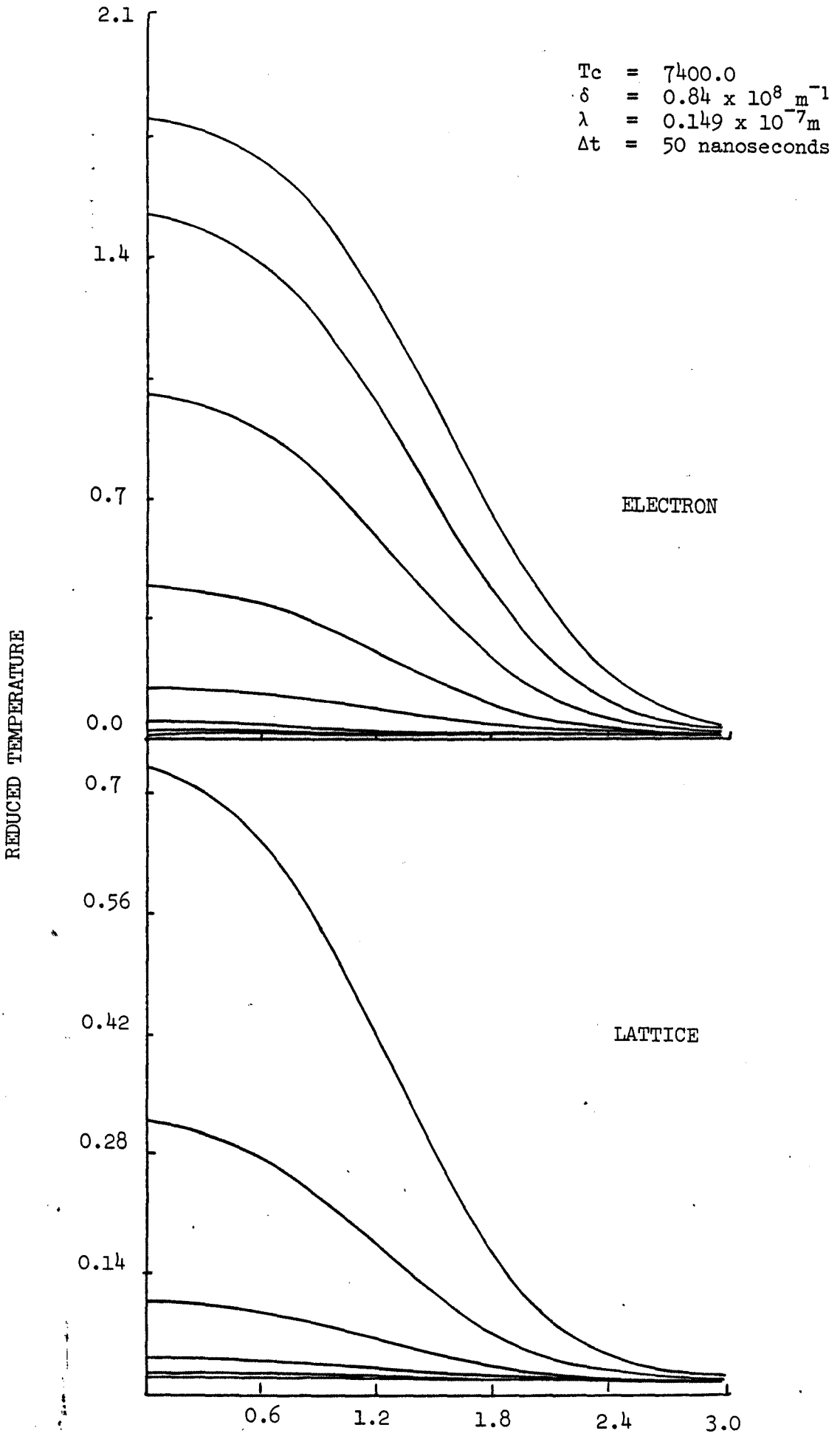

Graph (3.1)

Temperature Profile in Copper using the Kinetic Theory.

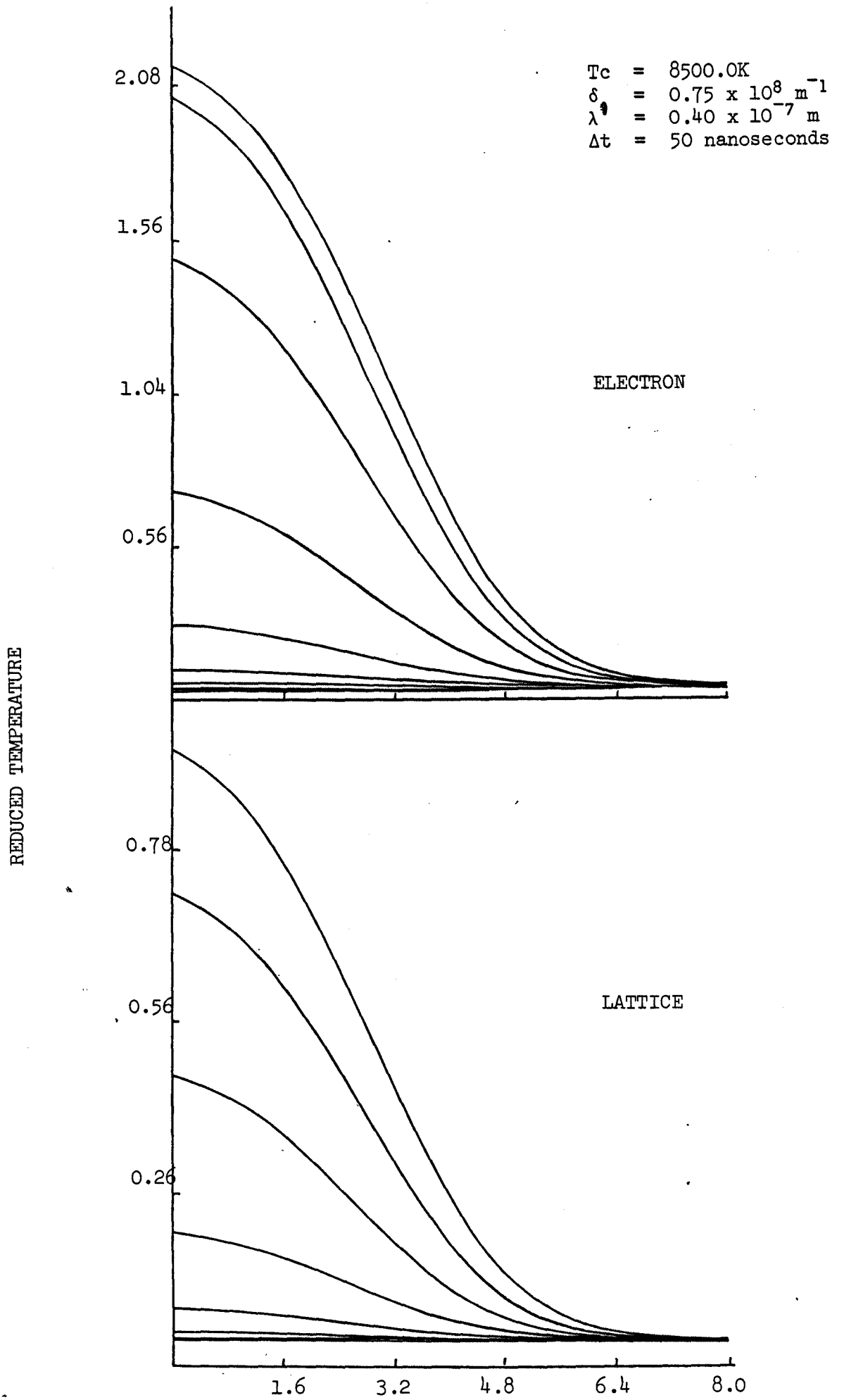

Graph (3.2)

Lattice Temperature Profile in Aluminium.

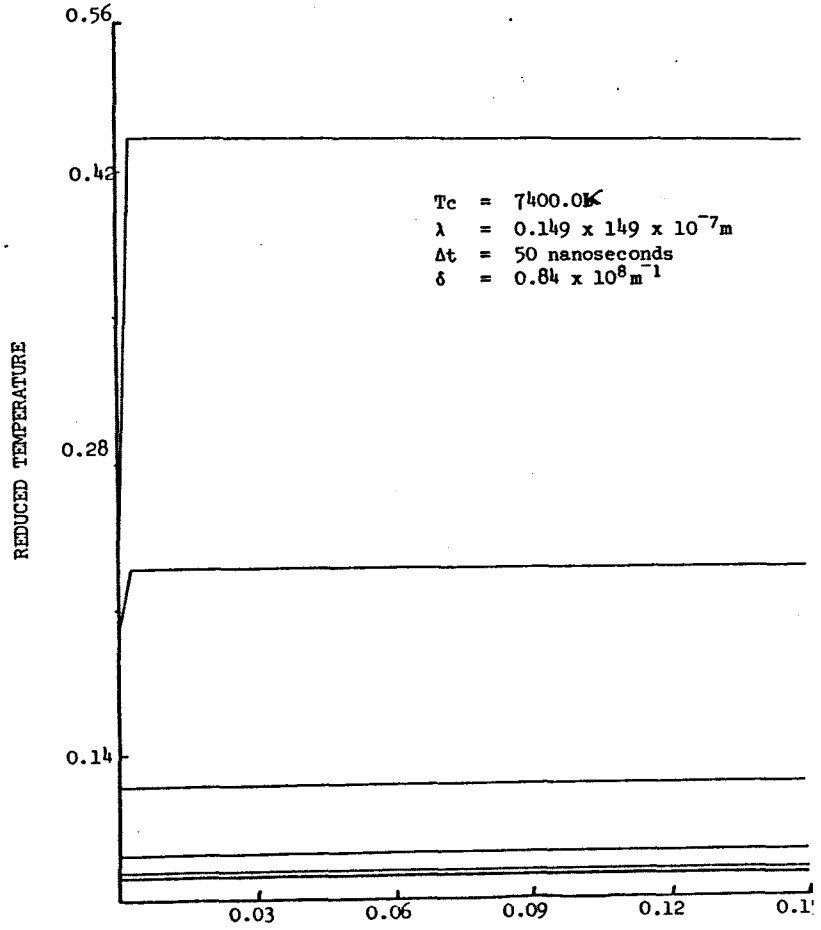

Graph (3.3)

Lattice Temperature Profile in Copper.

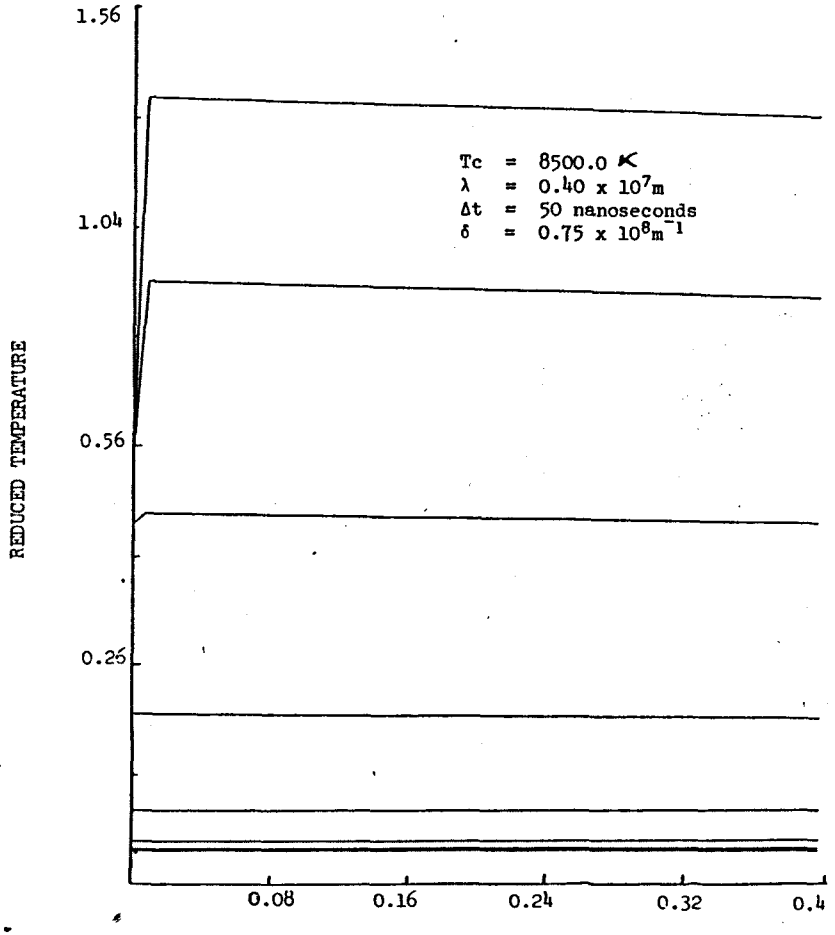

Graph (3.4)

Surface Temperature Variation in Aluminium using the Kinetic Theory.

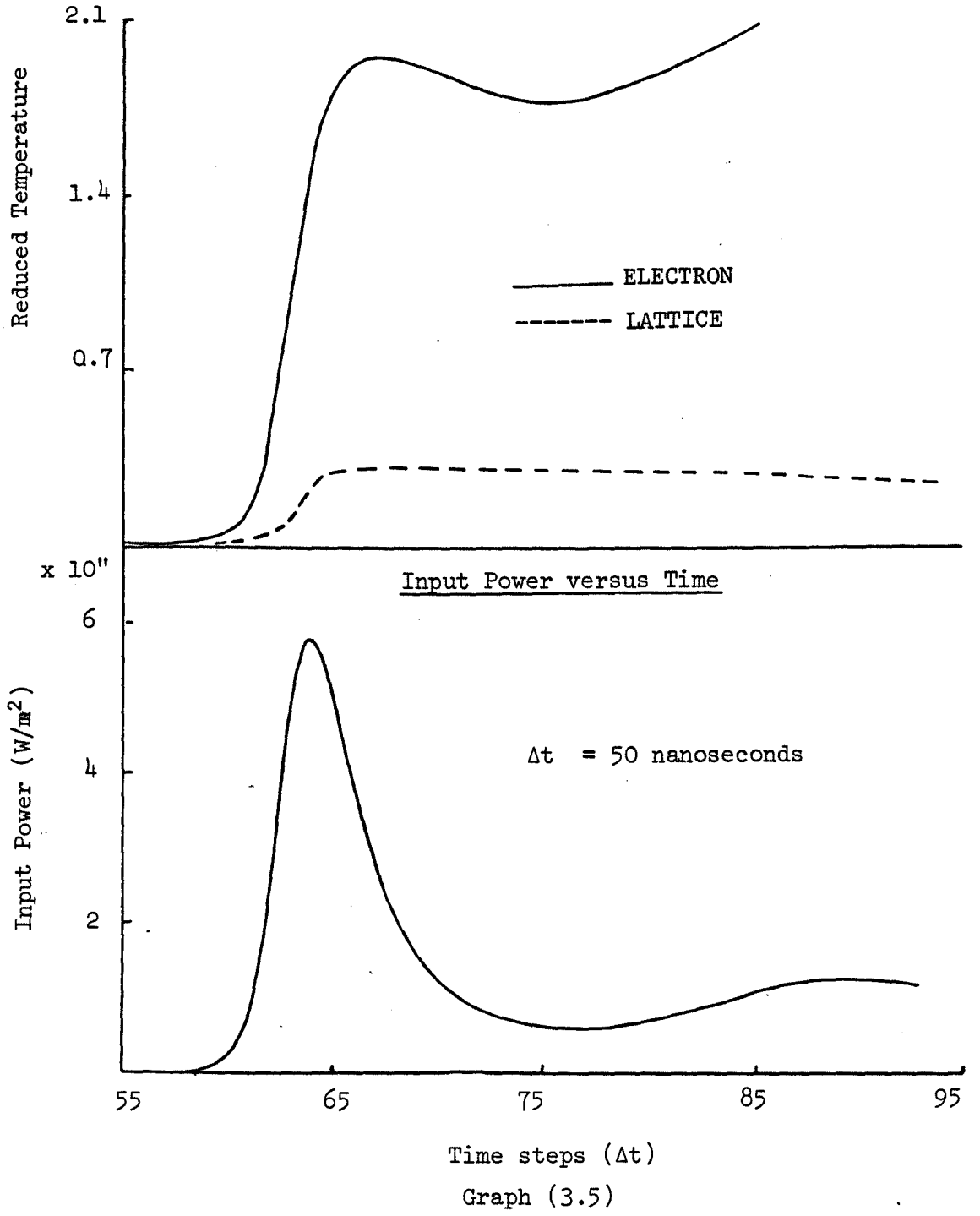

Graph (3.5)

Surface Temperature Variation in Copper using Kinetic Theory.

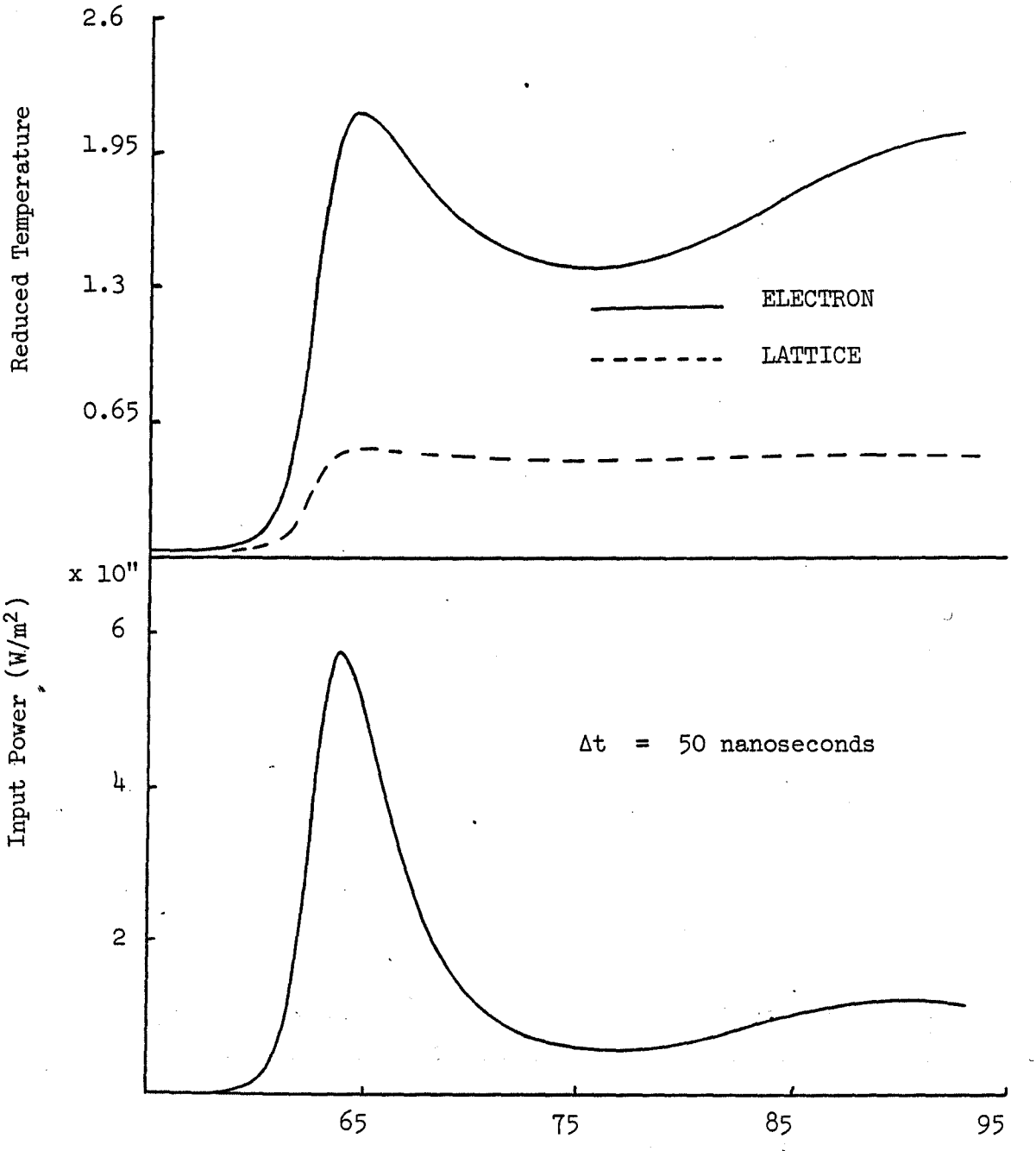

Graph(3.6)

Lattice Temperature Profile in Aluminium using the Fourier Theory.

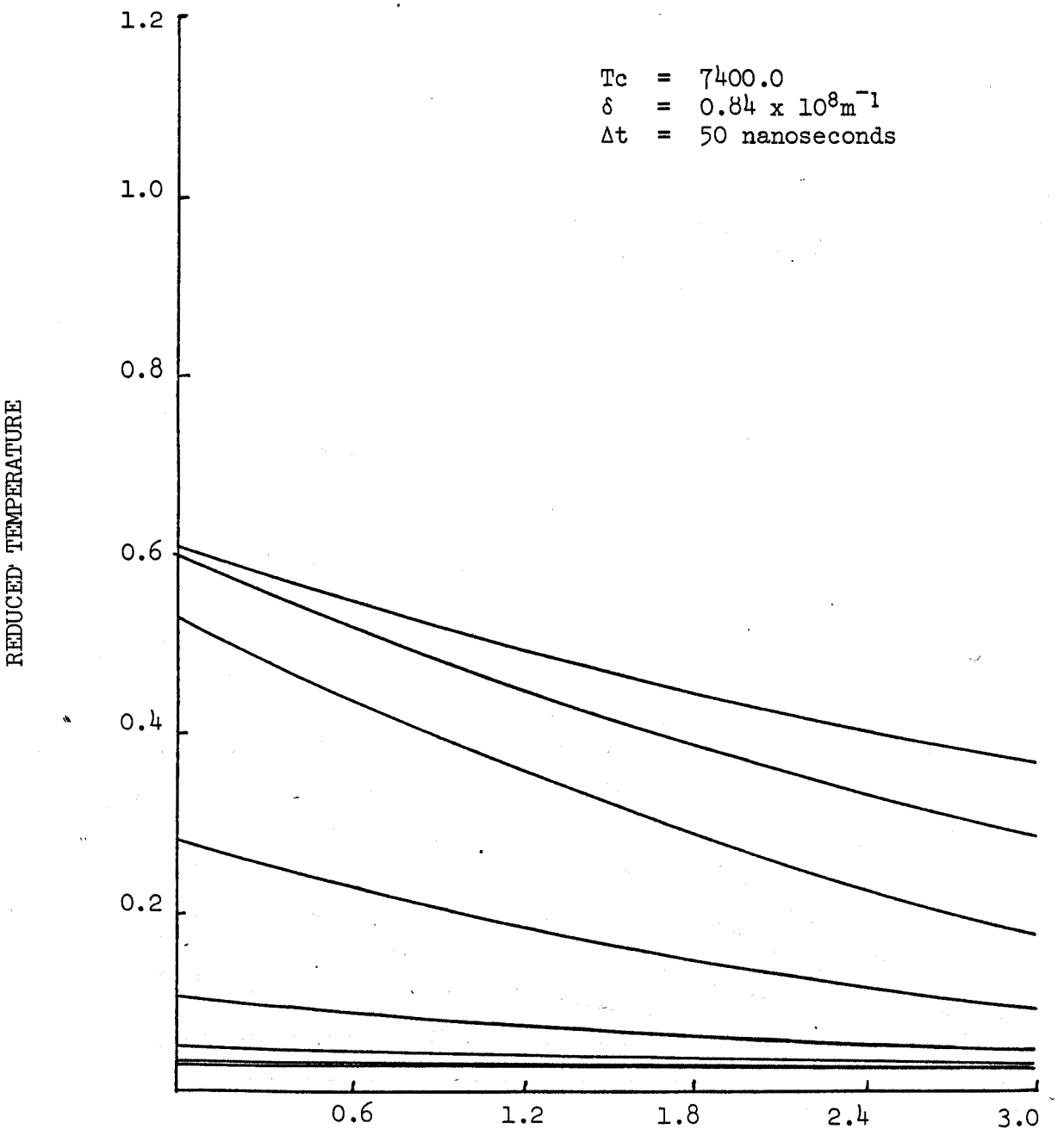

Graph (3.7)

Temperature Profile in Copper
using the Fourier Theory

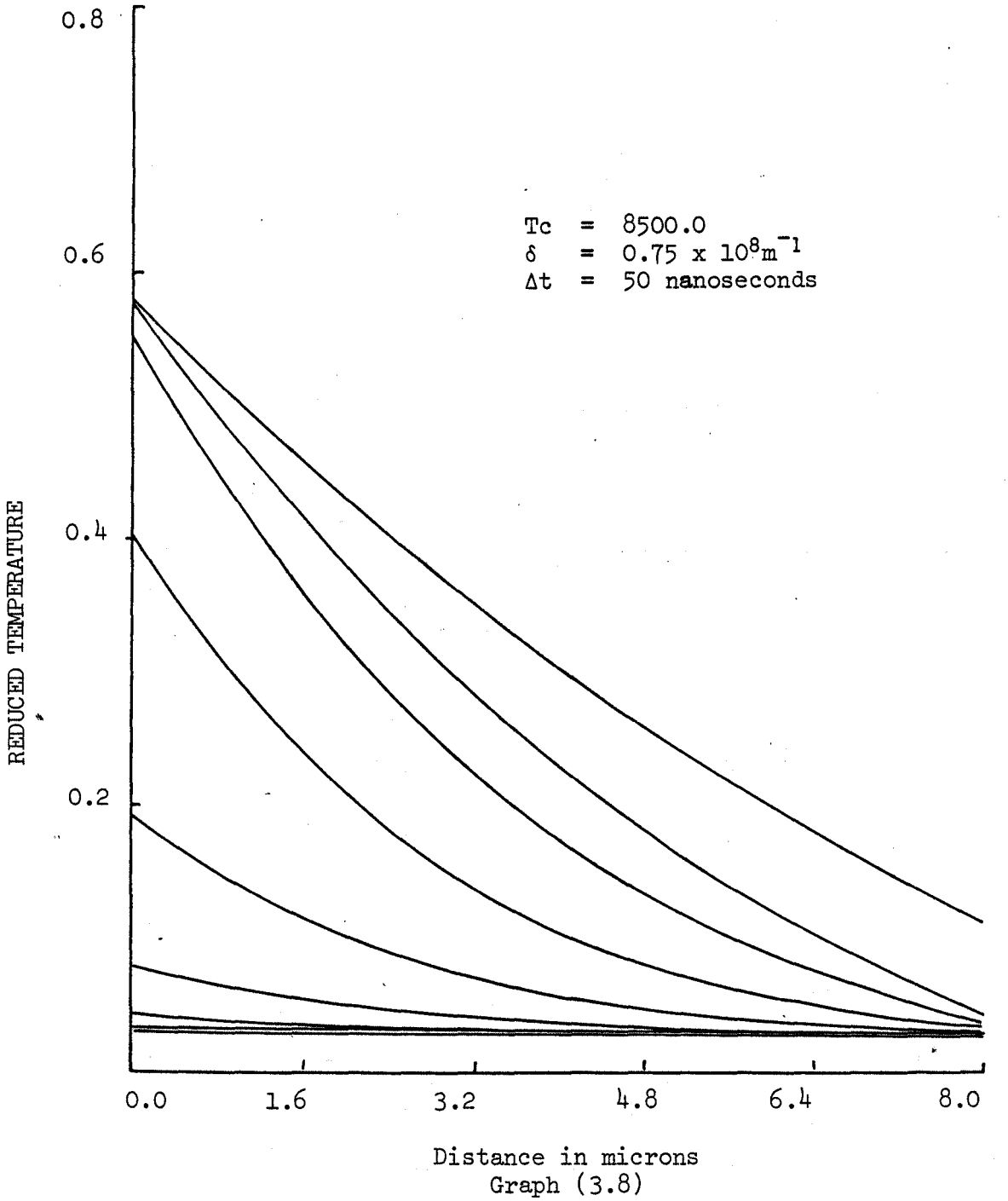

Graph (3.8)

Surface Temperature Variation in Aluminium using the Fourier Theory.

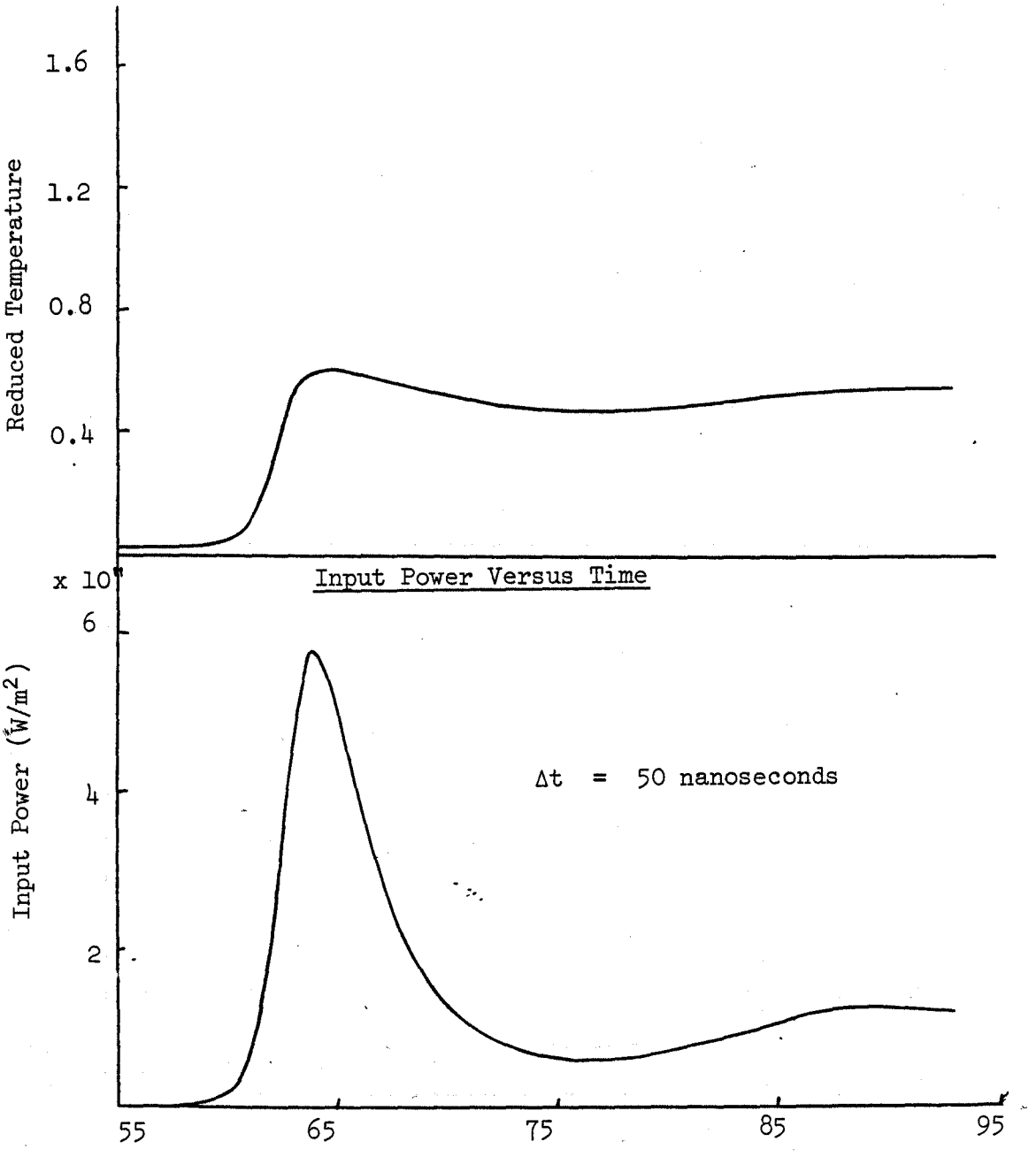

Graph (3.9)

Surface Temperature Variation in Copper using the Fourier Theory.

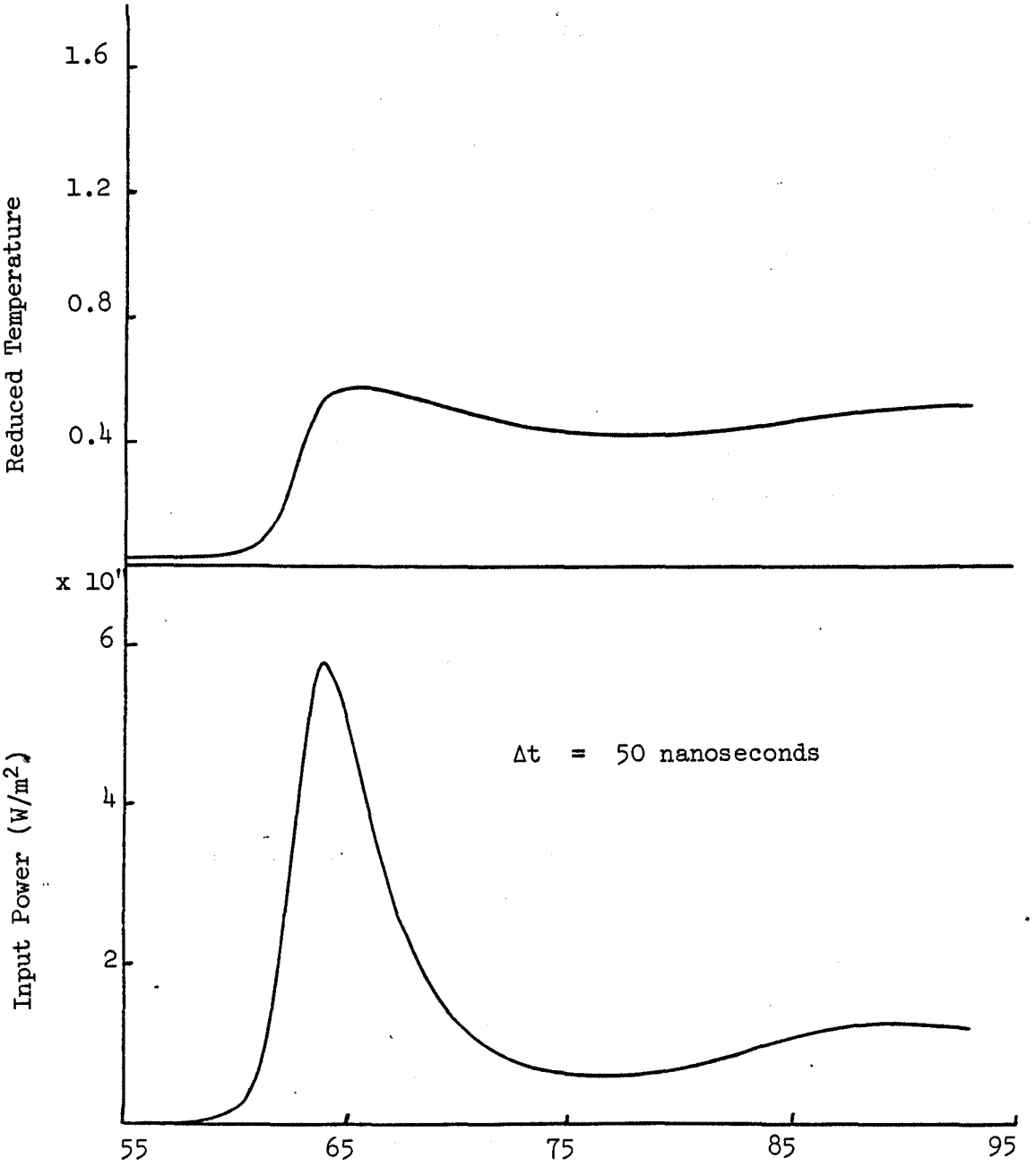

Graph (3.10)

CHAPTER FOUR

OPTIMISATION OF THE OUTPUT POWER FROM A HIGH PRF CO_2 LASER SYSTEM FOR USE IN MANUFACTURING PROCESSES

NOMENCLATURE

A	Effective area of the smallest cavity mirror for reflection (cm^2)
c	Speed of light = 2.997927 X 10^{10} cm/sec
C_p	Specific heat at constant pressure (J/kg.K)
C_v	Specific heat at constant volume (J/kg.K)
E	Energy (J)
g	Gain (cm^{-1})
g_1, g_2	Degeneracies of energy levels (1) and (2)
G	Fraction of photons spontaneously radiated into a small angular aperture
H	Laser cavity height (cm)
h	Enthalpy (J/kg)
IP	Electrical input power (Watts/cm^2)
I_p	Photon density (photons/cm^3)
k	Boltzmann constant = 1.38026 X 10^{-23} (J/K)
K	Thermal conductivity (W/m K)
k_e	Equilibrium constant between level 02^20 and 01^10.
K_{51}	Transfer rate constant between levels 5 and 1 (sec^{-1}
K_{15}	Transfer rate constant between levels 1 and 5 (sec^{-1})
K_{132}	Transfer rate constant between levels 1 and 32 (sec^{-1})
K_{2131}	Transfer rate constant between levels 21 and 31 (sec^{-1})

K_{2231}	Transfer rate constant between levels 22 and 31 (sec^{-1})
K_{320}	Transfer rate constant between levels 32 and 0 (sec^{-1})
K_{sp}	Spontaneous emission rate (sec^{-1})
L	Laser cavity length
m	Mass of gas mixture (kg)
$\dot{m}$	Mixture gas mass flow rate (kg/sec)
n	Population density of excited states ($molecules/cm^3$)
p	Gas pressure (Torr) or (N/m^2)
Q	Power density (W/m^3)
R_F	Front mirror reflectivity
T	Gas temperature (K)
T_o	Photon decay time (sec)
V_x	Velocity of gas in x-direction (m/s)
z	Height of gas above datum (m)
α	Rate of direct excitation of CO_2 (sec^{-1})
η	Rate of direct de-excitation of CO_2 (sec^{-1})
γ	Rate of direct excitation of N_2 (sec^{-1})
β	Rate of direct de-excitation of N_2 (sec^{-1})
η_{ov}	Laser efficiency based on 120 μseconds of laser output
η_{us}	Laser efficiency based on the pulse duration
λ	Wavelength of the output power (cm)
ρ	Density of gas (kg/m^3)
σ	Absorption cross-section (cm^2)
ω	Solid angle subtended by the laser cavity mirrors

4.1 Introduction

The purpose of developing a pulsed CO_2 laser is to produce a machine tool that overcomes the limitations of continuous wave systems. To this end it has been proven necessary to build a system which will be operable at high pulse repetition frequencies (prf), giving an output suitable for drilling and welding. A pulse repetition rate variable up to 10KHz has been found sufficient to span the range of process requirements. A power supply with these capabilities was designed and built by Spall [1].

This chapter focusses its attention on the parameters, other than the pumping pulse, that allow the laser pulse ouput profile to be matched to workpiece requirements: namely the optical resonator design, gas composition and gas flow rate. Gas flow rate is of importance for waste heat removal, in stopping the generation of shock and expansion waves [2] which are caused by the sudden energy input in the laser cavity and for preventing output degradation due to dissociation. The waste heat originates from the low coupling efficiency of electrical energy into the active medium, from excited molecules in the lower laser level relaxing back to equilibrium conditions and to a lesser extent the other relaxation processes shown in fig (4.1)

4.2 Physical basis for the theoretical model

A model, which assumes constant photon flux throughout the cavity length and bases the calculation of stimulated emission on an average unit volume, has been developed for the pulsed, transverse

electric discharge CO_2 laser. The four vibrational energy groups shown in fig. (4.1) include all the significantly populated energy levels. Internal relaxation rates within these groups are considered to be infinitely fast compared with the rates between groups, so that the molecular population distribution within the energy levels of a particular group can be calculated using the Boltzmann relationship for thermodynamic equilibrium. The model is a modification of that given by Chatwin et al [3], the major improvements being:

(i) Due to the low laser efficiency of less than 20 %, much energy is dumped into the gas mixture. This therefore increases the temperature, populates the lower laser level and results in a lower output power. This process can be roughly described by the steady state energy equation:

$$\rho C_p V_x \frac{dT}{dx} + \sum_{i=1}^{3} \frac{\partial}{\partial x}\left|K \frac{\partial T}{\partial x}\right| = Q \qquad (4.1)$$

Here T is the gas temperature, ρ is the density, C_p is the specific heat, K is the thermal conductivity and Q is the heat source. The first term is the rise in temperature along the flow direction which has velocity V_x. The second term is due to the heat conduction by the gas to the walls. The third term is the volumetric heat source. If $V_x=0$, all the heat loss has to be dissipated by conduction. For high pressure (density) devices, which require high input powers for optimum performance, the heat source term increases

proportionately with pressure. If on the other hand, the convective term dominates, then the pressure dependence of Q cancels out. It is therefore desirable to control the temperature by forced convection rather than by conduction. This can be effected by making the gas flow rate through the laser cavity fast compared with the diffusion time of a particle from the centre of the medium to the walls. This condition is given by Avizonis [4] as being satisfied if

$$\left|\frac{\rho C_p}{K}\right|\left|\frac{H}{2}\right|^2 \gg L/V_x \qquad (4.2)$$

where H is the height of the medium at right angles to flow direction and L is the length of the lasing medium along the flow. Hence in modelling the laser cavity an extra equation is needed to take into account the temperature increase and the convective cooling needed to keep the temperature low. For gases, the thermal diffusivity ($K/\rho C_p$) is of the order of 10^{-5} and for the proposed laser system, the following reasonable values:

V_x =200 m/s, L=300 cm, H=4cm

easily satisfy the condition given above.

(ii) In describing the model the temperature dependence of both the Boltzmann equilibrium populations and rate constants must be incorporated.

(iii) The results of the first pulse are based on initial and boundary conditions which assume thermodynamic equilibrium. Whilst this is true for the first pulse, it is inaccurate for subsequent pulses where non-

equilibrium conditions prevail. Also since molecular relaxation rates are of the same order of magnitude as the p.r.f., the perfomance predictions of the second pulse reflect much more realistically the likely characteristics of the subsequent pulses, these being of prime importance as they will be used for materials processing. Hence, results are produced to optimise the parameters of the second pulse as these are more representative of subsequent pulses.

(iv) In Chatwin et al [3]'s model the 02^20 and 01^10 levels (see fig.(4.1)) are assumed to be in equilibrium i.e the Boltzmann equilibrium law applies. But the partition between the two levels is not taken into account so that all the molecules are assumed to go into the 02^20 level. In this model, a constant k_e is introduced to ensure that the Boltzmann law always applies between the two levels.This value of k_e is given by

$$k_e = n_{31}/(n_{31}+n_{32}) = n_{31}/n_3 \qquad (4.3)$$

where n stands for the populations per cm^3 in the respective levels.

(v) In providing an initial signal, Chatwin et al [3] used an arbitrary small external injection signal. It will be shown that the laser action can be initiated by spontaneous emission in the cavity, hence there is no need for external injection.

4.3 The energy rate equations

4.3.1 Stimulated emission

Considering a laser oscillator with two mirrors one placed at each end of the active medium with one of them partially transmitting, laser action will be initiated by spontaneous emission that happens to produce radiation whose direction is normal to the end mirrors and falls within the resonant mode of the laser cavity. The rate of change of photon population density (I_p) within this laser cavity can be written as

$$dI_p/dt = -I_p/T_o + I_p cg + n_1 K_{sp} G \qquad (4.4)$$

where T_o is the photon decay time. This parameter relates principally to the reflectivity of the end coupling mirror and cavity length. It is given by

$$T_o = 2L/c \ \ln(1/R_F) \qquad (4.5)$$

where the back mirror is fully reflecting and R_F is the front mirror reflectivity.

For the first pulse, the stimulated emission process is initiated by the spontaneous emission term ($n_1 K_{sp} G$) where the rate constant K_{sp} is the inverse radiative lifetime of the lasing transition. The quantity G denotes the fraction of photons being spontaneously radiated into a small angular aperture defined by the resonator. This small fraction of radiation is $\omega/4\pi$ where ω is the solid angle subtended by the mirrors. From Gilbert et al [5], and assuming monochromatic radiation,

$$G = \omega/4\pi = \lambda^2/A \qquad (4.6)$$

where A is the reflectivity area of the smallest cavity mirror and λ is the wavelength of the output radiation. Andrews

et al [6] have reported the insensitivity of the rate equations to the precise value of G, though of course, this term is required in the initiation of the laser radiation. Excepting the modifications due to the spontaneous emission term, equation (4.4) is the conventional method employed in the literature to evaluate the effects of laser action.

These equations apply only to a small volume model of the laser and are thus valid provided 1/To and the round trip gain coefficient 2g are both smaller than unity. These are reasonable assumptions to make provided the laser is short enough so that variation of photon density and gain with position inside the medium can be neglected.

4.3.2 The rate equations

Referring to fig.(4.1) for nomenclature and introducing the stimulated emission term into the rate equations for the upper and lower laser levels, the following set of six simultaneous differential equations are obtained:

$$\begin{aligned} dn_1/dt = {} & \alpha n_0 - \eta n_1 + K_{51} n_5 - K_{15} n_1 \\ & - K_{132}(n_1 - (n_1/n_{32})_e \, n_{32}) \\ & - K_{sp} n_1 - I_p c g \end{aligned} \qquad (4.7)$$

$$\begin{aligned} dn_2/dt = {} & K_{sp} n_1 + I_p c g - K_{2131}\{n_{21} - (n_{21}/n_{31})_e \, n_{31}\} \\ & - K_{2231}\{n_{22} - (n_{22}/n_{31})_e \, n_{32}\} \end{aligned} \qquad (4.8)$$

$$\begin{aligned} dn_3/dt = {} & \{2K_{2131}/(1+k_e)\}\{n_{21} - (n_{21}/n_{31})_e \, n_{31}\} \\ & + K_{132}\{n_1 - (n_{22}/n_{32})_e \, n_{32}\} \\ & + \{2K_{2231}/(1+k_e)\}\{n_{22} - (n_{22}/n_{31})_e \, n_{31}\} \end{aligned}$$

$$-K_{320}\{n_{32}-(n_{32}/n_0)_e n_0\} \qquad (4.9)$$

$$dn_5/dt = \gamma n_4 - \beta n_5 - K_{51} n_5 + K_{15} n_1 \qquad (4.10)$$

$$dI_p/dt = -I_p/T_o + I_p cg + K_{sp} n_1 G \qquad (4.11)$$

$$dT_e/dt = \{2/mc_v\}dQ/dt - 2\frac{\dot{m} c_p}{m c_v}(T_e - T_i) \qquad (4.12)$$

These equations are discussed later.

4.3.3 Assumptions of the model

Inherent in the model are the following assumptions:

(i) The fraction of CO_2 or N_2 in vibrational states higher than those shown in fig.(4.1) can be assumed to be incorporated in the upper N_2 and CO_2 levels. This assumption is justified since the relaxation of higher levels to $N_2(v=1)$ and $CO_2(00^01)$ levels is rapid [7] compared with the $CO_2(00^01)$and $N_2(v=1)$ lifetimes so that the higher levels can be included in the upper nitrogen and carbon dioxide levels.

(ii) Thermodynamic equilibrium exists within the vibrational energy groupings of fig. (4.1) allowing the use of the Boltzmann equation for the evaluation of both vibrational and rotational energy level molecular populations.

(iii) The electrical excitation and de-excitation of the lower laser levels have been omitted because, although the populations are relatively high, the excitation

cross-sections are very small as shown by Cheo [8]. This is further justified by the extremely rapid depopulation ensured by the helium.

(iv) The cavity dimensions and flow velocities (Reynolds number) are such that boundary layer development and diffusion processes can be neglected. And because of the high velocity transverse flow, dissociation is neglected.

4.4 Parameters used in the model

4.4.1 Direct excitation and de-excitation rates

The direct excitation of CO_2 and N_2 ground state molecules proceeds via inelastic collisions with moving electrons. This process can be quantified by using effective rates α and γ which are given by,

$$\alpha = F_{CO_2} \times IP/E_{00^0_1} \times n_0 \quad (sec^{-1}) \qquad (4.13)$$

$$\gamma = F_{N_2} \times IP/E_{v=1} \times n_4 \quad (sec^{-1}) \qquad (4.14)$$

where F_{CO_2} = fraction of input power (IP) coupled into the excitation of the $CO_2(00^01)$ level

F_{N_2} = fraction of input power(IP) coupled into the excitation of the N_2 (v=1)

The values of F_{CO_2} and F_{N_2} are obtained from Khahra's [9] solution of the Boltzmann transport equation, tabulated in Table (4.1).

Also, the reverse of the above process takes place where molecules lose energy to the electrons who in turn gain an equivalent amount of kinetic energy. These rates are given by:

$$\eta = \alpha \exp(E_n/E) \qquad (4.15)$$

$$\beta = \gamma \exp(E_n/E) \qquad (4.16)$$

where E_n is the energy of level n and E is the mean discharge electron energy obtained by solving the Boltzmann transport equation.

4.4.2 Resonant energy transfer

Resonant energy transfer between the CO_2 and N_2 (v=1) energy levels proceeds via excited molecules colliding with ground state molecules. This process is a major contributor to the excitation of the upper laser level where excited N_2 molecules collide and excite ground state CO_2 molecules. It also improves the laser efficiency as direct coupling of electrical energy into N_2 is more efficient than into CO_2 i.e $F_{N_2} > F_{CO_2}$. In describing this rate of energy transfer, the following values of K_{15} and K_{51} were used,

$$K_{15} = 9.657 \times 10^6 \exp(-10.7/T^{-1/2}) \times P_{N_2}/T \qquad (4.17)$$

and

$$K_{51} = 9.657 \times 10^6 \exp(-10.7/T^{-1/2}) \times P_{CO_2}/T \qquad (4.18)$$

The temperature dependence of these rates was obtained from Taylor et al [10] where for a temperature of less than 1000K, the rate constant K_r is proportional to the exponential of the temperature T. Hence an equation of the form

$$K_r = a \exp(-bT^{-1/2}) \qquad (4.19)$$

is assumed and the constants a and b determined by a least

squares fit to the data. The factor $9.657 \times 10^{18}/T$ was used to convert equations (4.17) and (4.18) into units of $torr^{-1}$ sec^{-1}.

4.4.3 Collision induced vibrational relaxation of the upper and lower laser levels.

The important transfer processes are shown in fig.(4.1) and their values were obtained by surveying the following literature: In determining the translational rate constants K_{320} and K_{132}, the relationships given by Smith et al [11] were adjusted to fit the experimental results of Taylor et al [10]. Due to lack of data, the dependence on temperature, of the constants K_{2131} and K_{2231} was neglected. Hence the values used by Chatwin [12] and Khahra [13] were adopted. Thus

$$K_{320} = (K_{C-C} + K_{C-N} + K_{C-H}) \times 9.657 \times 10^{18}/T \quad (4.20)$$

where

$$\left.\begin{aligned} K_{C-C} &= 6.0 \times 10^{-10} \exp(-77/T^{1/3}) P_{CO_2} \\ K_{C-N} &= 1.23 \times 10^{-10} \exp(-77/T^{1/3}) P_{N_2} \\ K_{C-H} &= 0.84 \times 10^{-10} \exp(-45/T^{1/3}) P_{He} \end{aligned}\right\} \quad (4.21)$$

were used.

An expression similar to equation (4.20) was also developed for K_{132} where

$$\left.\begin{aligned} K_{C-N} &= 6.38 \times 10^{-18} \exp(-83/T^{1/3}) P_{CO_2} \\ K_{C-N} &= 1.38 \times 10^{-11} \exp(-55.6/T^{1/3}) P_{N_2} \\ K_{C-H} &= 5.07 \times 10^{-10} \exp(-83/^{1/3}) P_{He} \end{aligned}\right\} \quad (4.22)$$

The values of K_{2131} and K_{2231} are given by

$$\left.\begin{aligned} K_{2131} &= 6 \times 10^5 P_{CO_2} \\ K_{2231} &= 5.15 \times 10^5 P_{CO_2} \end{aligned}\right\} \qquad (4.23)$$

4.4.4 Gain

The gain (g) was evaluated from the product of absorption coefficient (σ) and the population inversion,

$$g = \sigma(n_{00^0 1} - \frac{g_1}{g_2} n_{10^0 0}) \quad (cm^{-1}) \quad (4.24)$$

where g_1 and g_2 are the energy level degeneracies. Neglecting the unit change in rotational quantum number, these degeneracies may be dropped and equation (4.24) partitioned, such that [12]

$$n_{10^0 0} = 0.408 n_{21} \qquad (4.25):$$

the transition is on the P20 line.

The absorption coefficient is that due to high pressure collision-broadening (pressure> 5 torr) where the intensity distribution function describing the line shape is Lorentzian. Vlasses [13] gives an approximate value of $\sigma = 700/nT$ (cm^{-2}) and Hoffman [14] gives one of $\sigma = 718/nT$ (cm^{-2}). These expressions however do not take into account the substantial line broadening effects of helium. Therefore the following expression,

$$\sigma = 692.5/T\{n_{CO_2} + 1.063 n_{N_2} + 1.4846 n_{He}\} \quad (4.26)$$

was developed and is used herein.

This allows equation (4.24) to be written as

$$g = \sigma(n_1 - 0.408n_{21}) \ (cm^{-1}) \quad (4.27)$$

4.4.5 Gas flow rate

Applying the first law of thermodynamics for an open system, the following equation

$$Q_{c.v} + m_i(h_i + V_i^2/2 + g_i z_i) = E_{c.v} + m_e(h_e + V_e^2/2 + g_i z_e) + W_{c.v} \quad (4.28)$$

is obtained for a given control volume (c.v). At any instant of time, the control volume is uniform. Also, in the case of a laser cavity, there is no work done and kinetic and potential energy changes can be neglected. Equation (4.28) then becomes

$$Q_{c.v} = mC_p(T_e - T_i) + mC_v d\{T_e + T_i\}/2dt \quad (4.29)$$

where the internal energy is evaluated by using the average temperature. Assuming , a perfect gas, the equation

$$dT_e/dt = \{2/mC_v\}dQ/dt - 2\frac{\dot{m}c_p}{mc_v}(T_e - T_i) - dT_i/dt \quad (4.30)$$

is obtained.

Since the cavity dimensions are small, the flow velocity through the cavity is taken as constant.

4.5 Solution of the equations

A computer program has been developed to solve the set of equations (4.7) to (4.12) using Merson's version of the Runge-Kutta method [15].

4.5.1 Initial and boundary conditions for the rate equations

When in thermodynamic equilibrium, the relationship

$$n_i/n_j = (g_i/g_j)\exp(-(E_i-E_j)/kT) \qquad (4.31)$$

holds between the population densities n_i and n_j of any two vibrational energy levels E_i and E_j. At low pressures (p), when intermolecular forces and molecular volume can be neglected, the total population per unit volume (n_t) can be evaluated according to the equation of state for an ideal gas,

$$n_t = p/kT \quad (\text{molecules/cm}^{-3}) \qquad (4.32)$$

The sum of the populations in all the energy levels and ground levels is equal to 'n_t', hence, using equations (4.31) and (4.32) the initial populations of all the energy levels may be evaluated.

In considering the gas flow, the temperature at the entrance to the cavity must be constant since a continuous flow of gas is taking place. Hence the boundary condition at inlet is

$$dT_i/dt=0 \qquad (4.33)$$

The initial gas temperature is taken as ambient. The initial value of I_p is due to the spontaneous emission term and is given by

$$I_p = n_1 G \qquad (4.34)$$

These preceeding initial and boundary conditions are sufficient to solve the rate equations.

4.5.2 Input power

The rate equations were solved for two successive 10 microsecond electrical input pulses with an interpulse gap of 90

microseconds giving a p.r.f of 10kHz. The current and voltage profiles of these input pulses which are depicted in fig.(4.2), are based on Khahra's experimental measurements [9].

4.6 Pulse profile descriptors

In analysing the laser output power, the following parameters were used and have been detailed in fig.(4.3):

Delay time:

. Delay time is defined as the difference in time between the start of the current input pulse and the start of the laser output pulse. The laser output pulse is assumed to have started if the power output is 7.0 w/cc. This value was chosen because when transformed into a power intensity by multiplying by the cavity dimensions, it gives the minimum power necessary for material processing applications [9].

Pulse duration:

. This is the time taken, after the delay time, for the pulse power to fall to 7.0 w/cc.

Dimensionless spike power:

This is the maximum power of each pulse made dimensionless by dividing it by 230w/cc, the maximum input power.

Dimensionless flat pulse power:

This is devised to show the mean flat pulse power, made

dimensionless by referring it to the maximum input power.

Maximum gas temperature:

This is defined as the maximum temperature of the gas reached during each pulse.

Efficiency:

Two efficiencies are used: Firstly, the overall efficiency (η_{ov}) which is based on 120 microseconds and secondly the useful efficiency (η_{us}), for each pulse, which is taken over the period when the power output is high enough for material processing, that is over the pulse duration.

As shown by Bakewell [16], pulse length affects the temperature profile in the material thereby affecting the minimum required pulse repetition rate and efficiency of the machining processes.

It is known that thermal power intensities have an optimum maximum above which they result in the formation of a blanking plasma on the metal surface. Peak power and delay time are important for control of the plasma.

Efficiency is an important metric because of the need to reduce the thermal load on the system and for economic reasons. Even though the overall efficiency (η_{ov}) gives the percentage of energy obtainable from the laser, it does not show the fraction which is useful for material processing and which pulse

this comes from. Hence the useful efficiency term, η_{us}, is introduced.

The dimensionless flat pulse power gives the mean pulse power obtainable from the laser. This is a useful parameter in matching laser beam power output to workpiece processing requirements.

Theoretical investigation:

The peak input power was held constant at 230 w/cc as this value was experimentally achievable for all the different gas mixtures considered [9]. These are shown in Table (4.1). It was decided to do a detailed analysis using the 1:3:2 mixture as this gave greatly improved laser parameters for the second pulse.

4.7 Results

Some of the results produced by solving the rate equations are shown in graphs (4.1) to (4.10). These solutions are plotted as functions of time. Graphs (4.5) and (4.6) show the output power for two successive electrical pumping pulses. Because the time taken to establish a significant population inversion is shorter than the cavity-intensity build up time, the initial output occurs in the form of a narrow spike. The primary gain-switched spike depletes the gain, however population inversion is rapidly re-established by resonant energy transfer from vibrationally excited Nitrogen molecules, by direct electrical excitation and by the emptying of the lower laser levels. The magnitude and duration of the output pulse depends on the proportions of helium, nitrogen and carbon dioxide, mirror

reflectivity, cavity length and the mass flow rate, hence the need to examine these variables.

4.8 Discussion of the effects of helium

4.8.1 Stimulated emission cross-section

Because of collision line broadening, helium reduces the stimulated emission cross-section. This can be seen by reference to equation (4.26) where the helium term has the dominant coefficient.

4.8.2 Coupling efficiencies

Table (4.1) shows that helium enrichment up to a partial pressure of 120 torr of the mixture increases the CO_2 and N_2 coupling efficiencies, thus increasing the direct excitation and de-excitation rates.

4.8.3 Average electron energy

The addition of helium results in a decreased average electron energy.

4.8.4 Excitation of the upper laser level (n_1)

The improvement in coupling efficiency produced by helium addition considerably increases the direct excitation rate, resulting in an increased population inversion gradient. For reasons explained later, helium enrichment also increases delay time (see graphs (4.5),(4.6) and (4.12)), which when combined with the increased inversion gradient results in a very much larger upper laser level population, graphs (4.1) and (4.2).

During the initial stages of excitation the net rate of resonance energy transfer is insignificant, however, once the upper laser level collapses, the net rate becomes substantial, graphs (4.3) and (4.4), contributing greatly to the oscillatory nature of the output. The higher the helium content the greater this de-stablising force as shown by graphs (4.5) and (4.6).

After direct excitation cut off, the upper laser level population falls off steadily for mixtures with a high helium content. This is due to the depopulation of the laser level directly to the 01^10 level by helium, that is, helium addition increases the term K_{132} as illustrated in fig.(4.1). This explains why upper laser level fall off rate increases with helium enrichment. These effects are shown by graphs (4.1) and (4.3). At the start of the second pulse, the population levels have almost reached a constant value.

4.8.5 Excitation of the upper nitrogen level (n_5)

The dominant effect of helium enrichment is an increased coupling efficiency which gives a greater direct excitation rate. When this is combined with an increased delay time it results in a very much increased upper nitrogen population.

After direct excitation cut off, the upper nitrogen level decays exponentially via its resonant interaction with carbon dioxide as depicted by graphs (4.3) and (4.4).

4.8.5 Growth of Stimulated Emission and its effects on Delay Time and Spike Height.

For this discussion the cavity dimensions and optics are taken as constant. Stimulated emission is a function of population inversion and stimulated emission cross-section (σ). For increasing helium the increasing inversion gradient is dominated by the reduction in cross-section resulting in reduced gain, see graphs (4.7) and (4.8).

Reduced stimulated emission combined with an increased direct excitation rate greatly increases the time required for stimulated emission to overcome direct excitation, this results in a greater delay time. Graph (4.12) shows this clearly. The second pulse delay time is smaller because of residual gain and power left by the previous excitation pulse. A high value of interpulse gain is of interest because of the useful effects it has on the second and subsequent pulses. Graphs (4.7) and (4.8) show that helium reduces the gain after direct excitation and hence minimizes the effect of residual gain on subsequent pulses.

An increased delay time means that when the stimulated emission magnitude is great enough to cause the upper laser level to collapse, the population inversion magnitude is so great that very large spikes develop. Hence as seen in graph (4.13), the dimensionless maximum power (spike height) variation follows a similar pattern to that of the delay time. The initial parabolic nature of the second pulse is due to the combined effects of helium and nitrogen which will be discussed later.

4.8.6 Mixture temperature

Helium affects the gas mixture temperature in two ways:

(i) Helium has a high thermal conductivity which leads to thermalization of the vibrational energy levels especially the lower laser levels and therefore increases the amount of energy dumped in the mixture.

(ii) Helium has a high heat capacity which leads to an increase in the gas mixture's capacity to store energy thereby decreasing the mixture temperature for a given input energy and in situations where its partial pressure is very large, the cooling of the mixture is very marked.

These two effects act against each other with the second effect being dominant. Thus increasing amounts of helium lead to a decreasing maximum mixture temperature but the rate of this reduction becomes smaller as the helium content is increased as shown by by graph (4.11) for different nitrogen - carbon dioxide ratios (NC). This decrease can be explained in terms of the energy deposition term dQ/dt in equation (4.12). Increased helium leads to a higher thermal conductivity and an increase in the rate constants due to both an increase in total pressure and the partial pressure of helium. Therefore more carbon dioxide molecules fall off to lower laser levels releasing energy. However, it also means an increase in heat capacity (mC_p). But as the helium content is increased further, the term dQ/dt rises faster than the increase in the heat capacity. Thus increased helium leads to a decreasing rate of temperature fall off. This

phenomenon is shown by both the first and second pulses, see graphs (4.9), (4.10) and (4.11).

After the first pulse cut off, the gas mixture temperature falls exponentially due to the first order differential equation relationship between time and temperature. (see graphs (4.9) and (4.10)). This makes it very difficult to reduce the temperature of the second pulse to that of the first one.

The maximum temperature obtained is well below 600K, which is the value obtained by Wassertrom et al [17] as the maximum allowed in the laser cavity.

4.8.8 Pulse duration and dimensionless flat pulse.

The pulse duration is determined to a large extent by the relaxation times of the excited molecules. Since these times become shorter at high pressures and increased helium contents, i.e the rate constants become larger, the pulse length, after an initial increase, decreases with increasing helium. This is depicted in graph (4.14). The above hypothesis does not however explain the initial rise in the curves when the helium content is still small. This behaviour can be explained by noting that the higher nitrogen mixtures or lower helium mixtures have a long power pulse tail so that when a small amount of helium is added, the wasted power in the tail is released sooner, within the main output pulse. This process of redistributing the energy into the main pulse is accomplished with small amounts of helium so that no more energy is left in the pulse tail for increasing helium to have a positive effect. The mean power increases as the percentage of helium is increased, as illustrated in graph

(4.15). However, for mixtures very rich in helium, this increase in mean power is accompanied by a highly oscillatory output that is not useful for machining applications, see graphs (4.5) and (4.6).

4.8.9 Efficiencies

Graphs (4.16) and (4.17) show the variation of efficiencies with helium content. They show a maximum at intermediate values of helium. These results give an efficiency in the range of 6 - 15 percent which is consistent with the experimental values of working carbon dioxide lasers [18].

The increase in efficiency is due to several factors:

(i) Up to a point, helium increases the coupling efficiency of the electrical energy into the upper Carbon dioxide and Nitrogen vibrational levels. This means more of the input energy is effectively absorbed and hence the output improved.

(ii) Helium causes the rapid depopulation of the 01^10 level. This can be seen from equation (4.10) and (4.21) where

$$K_{320} = \frac{9.657 \times 10^7}{T} \left\{ \begin{array}{l} 6.0\exp(-77/T^{1/3})P_{CO_2} \\ + 1.23\exp(-77/T^{1/3})P_{N_2} \\ + 0.84\exp(-45/T^{1/3})P_{He} \end{array} \right\} \quad (4.35)$$

The helium coefficient is far greater than those of nitrogen and carbon dioxide. Therefore helium has a greater effect on the depopulation of the lower laser levels. This is so because helium increases the

collisionally induced transfer of energy from one vibrational level to another with the excess energy being transferred to, or supplied by, the translational energy of helium atoms. These higher rates increase, or at least maintain the population inversion magnitude and hence increase the efficiency.

(iii) Helium, as already shown, reduces the gas temperature. This reduction helps to keep the lower laser level empty and hence maintain the population inversion. This too leads to an increased efficiency.

But as the same graphs show, the efficiency decreases after a certain level of helium is reached. This is partly due to a decrease in the coupling efficiencies (See Table (4.1)) and a rise in the relaxation rate K_{132}. From equation (4.8) and (4.22)

$$K_{132} = \frac{9.657 \times 10^7}{T} \left\{ \begin{array}{l} 0.064\exp(-27/T^{1/3})P_{CO_2} \\ + 1.38\exp(-55.6/T^{1/3})P_{N_2} \\ + 50.7\exp(-83/T^{1/3})P_{He} \end{array} \right\} \qquad (4.36)$$

the rate constant is small for low helium pressures but as the helium content becomes significant, the amount of excited molecules deactivated to the 32 level increases substantially leading to a decrease in efficiency.

Graph (4.17) shows that when efficiency is evaluated for the useful output (η_{us}), the efficiency for the second pulse is increased, especially for those mixtures containing a high amount of Nitrogen. As already explained, this is due to a finite positive gain and output power at the beginning of the second

pulse. Also the upper nitrogen level is left populated from the previous pulse.

4.9 Discussion of the effects of Nitrogen

The total pressure of CO_2 and N_2 was restricted to 40 torr, consequently as the partial pressure of N_2 was increased the partial pressure of CO_2 was correspondingly decreased. The Boltzmann equilibrium population of the lower laser level is much smaller for reduced CO_2 partial pressure, hence a far smaller laser upper laser population results in population inversion.

4.9.1 Stimulated emission cross-section (σ)

Since the N_2 coefficient is approximately unity and since the total pressure of Nitrogen and Carbon dioxide is fixed at 40 torr, the effect of Nitrogen on the stimulated cross-section by the collision broadening is very small.

4.9.2 Coupling efficiencies and average electron energy

The nitrogen molecule has an energy level close to that of the carbon dioxide laser level. Hence a resonant energy transfer process takes place between the $N_2(v=1)$ level and the $CO_2(00^01)$ level. The beneficial effects are due to the the fact that the N_2 electron excitation cross-sections are larger than those of the CO_2. This leads to an increased number of nitrogen molecules in the upper nitrogen level. The CO_2 vibrational populations are thus increased by interaction with excited nitrogen. Hence the coupling of electrical energy into the discharge is made more

efficient and an increased average electron energy decreases the rate of direct de-excitation.

4.9.3 Excitation of the Upper Laser level (n_1)

For increased nitrogen the rate at which the upper laser level is populated is diminished due to the two-fold effect of decreased ground level population and decreased rate constant.

Due to the reduced magnitude of upper laser level population collapse, the de-stablising effect of resonant energy transfer is decreased. This results in a reduction in output oscillation which is in full agreement with the experimental results of Vlases et al [13] and is shown in graphs (4.5) and (4.6).

After direct excitation cut off, the upper laser level tends exponentially to a value determined by the amount of nitrogen present, see graphs (4.3) and (4.4). Increasing nitrogen means that the upper laser level is replenished by a continuous supply of energy from the $N_2(v=1)$ level. This leads to a reasonably constant value of the upper laser level. These effects are further illustrated by comparing graphs (4.1) and (4.2).

4.9.4 The effect of Stimulated Emission on Delay Time and Spike Height

The dominant feature of increased nitrogen is the reduction of CO_2 partial pressure which reduces n_2 and allows very rapid population inversion. The resulting stimulated emission is very rapid to build up and quickly overturns direct excitation, giving a reduced delay time and spike height. Graph (4.12) shows this

reduction in delay time and graph (4.13) show the reduction in the spike height.

The main effect of nitrogen shows up on the second pulse. Increasing nitrogen produces a long output tail so that at the start of the second pulse, there is sufficient output power and gain to reduce the delay time and spike height. These effects disappear at high helium contents as helium acts to reduce the pulse tail, this explains the initial parabolic shape for the peak power and delay time, see graphs (4.12) and (4.13).

For high nitrogen content, the upper laser level is reasonably constant during the interpulse period. This leads to a constant interpulse gain being achieved; for lower nitrogen ratios and/or higher helium content, the upper laser level falls off due to insufficient numbers of excited molecules, the gain falls off accordingly. These results are shown in graphs (4.7) and (4.8).

4.9.5 Mixture temperature

For the same total pressures and a given input energy, an increase in the nitrogen content relative to the CO_2 hardly affects the maximum temperature because the thermal properties of N_2 are not very much different from those of CO_2 and since the total pressure of N_2 and CO_2 is held constant, no significant change in temperature is observed on increasing the nitrogen content. See graph (4.11).

4.9.6 Excitation of the upper nitrogen level (n_5)

The upper nitrogen level is populated very rapidly due to two effects. Firstly the increased ground level population and secondly the increased coupling efficiency, both factors reinforce one another to produce a large increase in the rate of direct excitation, as seen by comparing graphs (4.3) and (4.4).

The rate of upper nitrogen excitation dominates the effect of reduced delay time such that the final population at excitation cut off is always greater than that of mixtures with less nitrogen, compare graphs (4.3) and (4.4).

After direct excitation cut off, the population of the metastable nitrogen level $N_2(v=1)$ is determined by both the $CO_2(00^01)$ population and pressure ratio of CO_2 and N_2. This can be deduced from equation (4.10). After 10 micro seconds, α and β become zero so that

$$dn_5/dt = -K_{51}n_5 + K_{15}n_1 \qquad (4.37)$$

since the population of the upper nitrogen level (5) falls of immediately the incident pulse ceases,

$$dn_5/dt < 0 \qquad (4.38)$$

this implies that

$$-K_{51}n_5 + K_{15}n_1 < 0 \qquad (4.39)$$

so that

$$n_5 > K_{15}n_1/K_{51} \qquad (4.40)$$

Substituting for K_{15} and K_{51} ,

$$n_5 > P_{N_2}n_1/P_{CO_2} \qquad (4.41)$$

This means that increasing the nitrogen content relative to

carbon dioxide leaves more molecules trapped in the upper nitrogen level which are not used for exciting carbon dioxide molecules within the duration of the laser pulse. This is shown by graphs (4.3) and (4.4).

4.9.7 Pulse duration and dimensionless flat pulse power

Graph (4.14) shows the pulse duration variation with nitrogen. It can be seen that increased nitrogen leads to a higher pulse duration for both the first and second pulses. The difference between the pulse duration times of the first and second pulses increases, as expected, with increasing Nitrogen. This is due to the 'spreading effect' that nitrogen has on the output pulse profile, the energy is released over a longer time period. This means that at the beginning of the second pulse, there is sufficient residual pulse energy to increase the pulse duration. This 'spreading effect' and the increasing amounts of nitrogen left trapped in the upper nitrogen level result in a decreasing flat power pulse when the nitrogen goes up. This is depicted in graph (4.15).

4.9.8 Efficiencies

Due to the increased coupling efficiencies, nitrogen improves the laser efficiency. This increase can be seen both in the overall efficiency (graph (4.16)) and that of the effective efficiency (graph (4.17)). This means more energy is available for material processing with higher nitrogen mixtures. Also

because higher nitrogen mixtures leave a lot of energy in the pulse tail, the beneficial effect on the efficiency of the second pulse is marked.

4.10 Discussion of the effects of cavity length.

4.10.1 Pulse delay time and peak power

Increasing the cavity length increases the average distance a photon must travel before leaving the output window. Consequently, increased cavity length reduces photon loss resulting in a more rapid development of the photon flux. This leads to a decrease in the gain switched spike and therefore delay time, graph (4.18) and output peak power, graph (4.19). These same graphs also show that the pulse delay time and peak power of the second pulse are reduced by an increase of the cavity length. This is because, as the cavity length increases, the energy left in the tail increases leading to a decreased delay time and peak power for the second pulse. This effect is only observed up to a cavity length of 300cm whereafter the pulse delay time and peak power remain constant.

4.10.2 Pulse delay time and average pulse power

Graph (4.20) shows an increase in pulse length for both pulses which is consistent with a decrease in peak power. This decrease in peak power means that the pulse energy is spread out over a longer time period and hence the increase in pulse length. The effect of cavity length on the total energy output

per pulse is not as marked as the cavity length's effect on the pulse duration, this leads to a decreasing average flat pulse power as predicted by graph (4.21)

4.10.3 Efficiencies

As explained in the previous section, increasing the cavity length increases the energy output per pulse, hence both the overall and useful efficiencies are increased, especially up to 300cm, see graphs (4.22) and (4.23).

4.11 Discussion of the effects of front mirror reflectivity

The effects of increasing the front mirror reflectivity are similar to those of increasing the cavity length with a more marked variation after a reflectivity value of 0.7. That is, reduced spike height and delay time, increased pulse length and efficiency. These effects are shown in graphs (4.24) to (4.29). The higher the reflectivity, the better the performance of the laser, however, if the reflectivity is too high, physical problems of overheating and mirror damage occur. Hence a compromise is needed and a value of 0.9 is recommended.

4.12 Discussion of the effects of mass flow rate

Graphs (4.30) to (4.36) show the variation of the defined laser parameters with mass flow rate for the 1:3:2 mixture. Taking these parameters with respect to the first pulse, it can be seen that practically no change occurs. This is because the input energy is delivered in such a short period, 10

microseconds, that the effect of mass flow using the proposed flow rates is negligible.

Considering those of the second pulse, it can be seen that for mass flow rates of less than 0.2 kg/s, there is little change in the parameters. The mass flow rate has a marked effect once it is increased above 0.2 kg/s, after which it reduces the delay time (graph (4.31)), maximum spike power (graph (4.32)), and gas temperature (graph(4.30)) and increases the pulse duration (graph (4.33)) and efficiency (graphs (4.34) and (4.35)). So it can be said that above 0.2kg/s, convective cooling starts having a positive effect on the laser performance parameters. These improved parameters are obtained because of the reduction in the gas mixture temperature. A maximum value of the mass flow rate is determined by the capacity of the Root's blowers.

The above improvements are realised as the fresh gas is at a lower temperature and hence the lower laser level has a smaller population which enhances gain. If the gas flow rate was too fast, the loss of population inversion would result in a laser performance deterioration.

4.13 Conclusion

This work is aimed at identifying optimum parameters useful for tuning laser output characteristics for material processing applications. The calculations for the second pulse were carried out to see what effect the non-equilibrium initial conditions had on subsequent output pulses. The results show that the initial conditions have a substantial effect on the laser output, these

effects could be used to advantage for improving the laser output. The multipulse simulations are in close agreement with available experimental results [9,18].

It has been shown that the power outputs and profiles can be tuned by adjusting the mixture ratios, cavity dimensions, front mirror reflectivity and gas flow rates. It has been shown that increased helium reduces the gas temperature and leads to high pulse plateau powers, until the helium content is about six times that of CO_2. These increased powers are however compressed into a small time period so that maximum powers and delay times are quite high. These high peak powers are unsuitable for materials processing because of excessive plasma production. For helium rich mixtures, energy not released within the main output pulse is dissipated during the inter-pulse period, thus the second pulse does not benefit from the residual gain that is useful in suppressing the initial gain switched spike. The above problems limit full exploitation of the advantages furnished by helium enrichment. The use of high nitrogen content mixtures offers a solution to this problem since this leads to a long output tail which benefits subsequent pulses. Another approach is to switch the cavity to a low value of Q (Q-switching) during the interpulse period, thus preserving the interpulse gain and enhancing spike suppression. Preliminary results [19] are promising and are shown in graph (4.37). Time constants are sufficiently slow that mechanical Q switching is a feasible option. In the future, phase conjugate mirrors will allow switching of the mirror refectivity directly. This could also

improve laser efficiency.

It has been seen that for maximum efficiency, other parameters like temperature minimization have to be sacrificed.

The analysis has shown the importance of front mirror reflectivity and cavity length on the pulse profile. The mass flow rate does not seem to affect the first pulse characteristics but beyond a mass flow rate of 0.2 kg/s, its effect on the second pulse and therefore subsequent pulses is marked and beneficial. Hence the need for flow in gas lasers. The flow rate value of 1.0 kg/s (giving a flow velocity through the laser of 200 m/s) is chosen as reasonable taking into account the design limitations imposed by the blowers and heat exchangers. The mirror reflectivity value of 0.9 and cavity length of 300cm have been selected for a compact and practical design. The following mixture is recommended if all arguments of temperature and second pulse profiles are taken account of:

Gas pressure	P_{CO_2} :	P_{N_2} :	P_{He}	
	10	30	40	Torr

4.14 References

1 R.Spall Pulsed power supply for an unstable resonator and and mode simulation in unstable resonators. Ph.D Thesis, University of Birmingham, (1979)

3 A.Goldschmidt, A.Seginer and J.Stricker Effects of the excitation energy release on the quality of the lasing medium In Gas Flow and Chemical Lasrs,1984 Ed. A.S. Kaye and A.C.Walker Adam Higler Ltd, 1985

3 C.R.Chatwin and B.F.Scott High PRF Nitrogen-carbon dioxide laser for continuous manufacturing process in metals. 1st Int. Conf. on Lasers in Manufacturing Brighton, U.K 1983

4 P.V.Avionis Chapter 5, High Energy Lasers and their Applications. Edited by S.Jacobs et al, Addison-Wesley Publishing Company, 1974.

5 J.Gilbert, J.L.Lamchmbre, F.Rheault and R.Fortin Dynamics of the CO_2 atmospheric pressure laser with transverse pulse excitation. Can. J. Phys. vol.50 p.2523 (1972)

6 R.J.Andrews, P.E.Dyer and D.J.James

A rate equation model for the design of TEA CO_2 oscillators

J.Phys. E vol.8, p.493 (1975)

7 P.Tychinskii Powerful Gas Lasers

Sov.Phys.Uspekhi, Vol.10, No.2, p.131 (1967).

8 P.K.Cheo Lasers, Vol.3, Ed. by A.K.Levine and A.J.Demaria

Marcel Dekker N.Y (1971).

9 J.S.Khahra Optimisation of the output characteristics of a pulsed CO_2 laser for processing of materials

Ph.D Thesis, University of Birmingham, (1976)

10 R.L.Taylor and S.Bitterman

Experimental measurements of the resonant vibrational energy transfer between mode v_3 of CO_2 and N_2 J. Chem. Phys. vol.50 no.2 p.1720 (1969)

11 K.Smith and R.M.Thomson

Computer modeling of Gas Lasers.

Plenum Press. New York (1978)

12 C.R.Chatwin Thermodynamics of pulsed CO_2 laser for machining metals

Ph.D Thesis, University of Birmingham, (1980)

13 G.C.Vlases and W .M.Moeny

Numerical modelling of pulsed electric CO_2 lasers

J.Appl. Phys. Vol.43 NO.2 p.1840 (1972)

14 A.L.Hoffman and G.C.Vlases

A simplified model for predicting gain, saturation, and pulse length for Gas Dynamic Lasers.

I.E.E.E, J.of Q.Elec. Vol.8 No.2 p.46 (1972)

15 G.Hall and J.M.Watt (eds)

Modern Numerical methods for Ordinary Differential Equations Clarendon Press. Oxford, 1976

16 B.A.Bakewell

Perfomance of pulsed laser systems in relation to machining mechanisms

Ph.D Thesis, University of Birmingham, 1973

17 E.Wassertrom, Y. Crispin, J. Rom and J. Shwartz

The interaction between electrical discharges and gas flow, J. Appl. Phys. vol.49, p.81, 1978

18 A.L.Smith and J.Mellis

Operating efficiencies in pulsed carbon dioxide lasers

Appl. Phys. Lett. vo.41 no.11 p.1037, 1982

19 C.A.Byabagambi, C.R.Chatwin and B.F.Scott

Prediction of output power from high pulse repetition frequency CO_2 lasers for use in manufacturing processes.

3rd Int. Conf. On Optical and Optoelectronics, Applied Science and Engineering, Innsbruck, April 1986

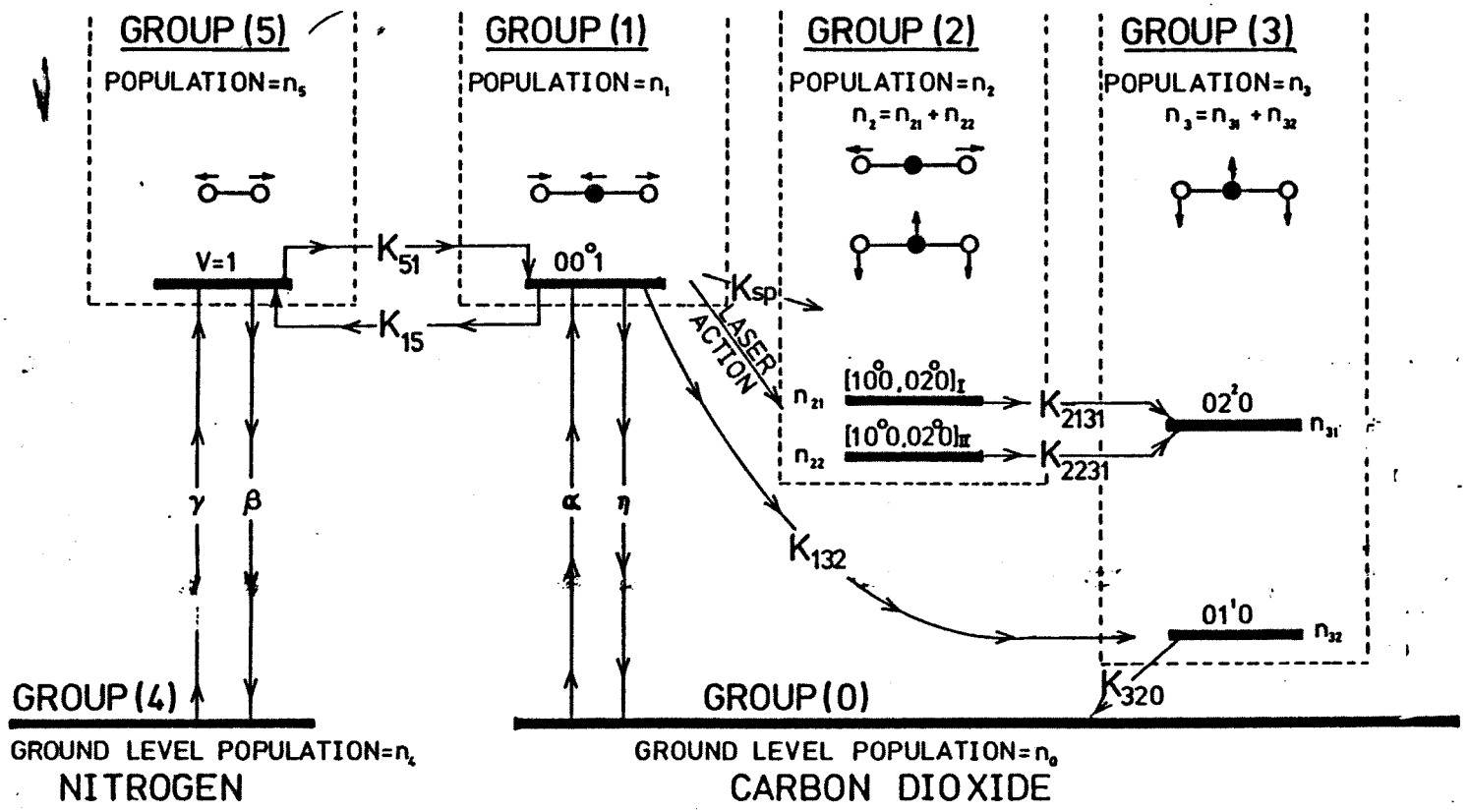

FIG. (4.1) SIX LEVEL ENERGY DIAGRAM FOR THE CARBON DIOXIDE LASER.

FIG(4·2) CURRENT AND VOLTAGE PULSE SHAPES

MAXIMUM INPUT POWER = $IP_{max} = I_{max} \times V_{max}$

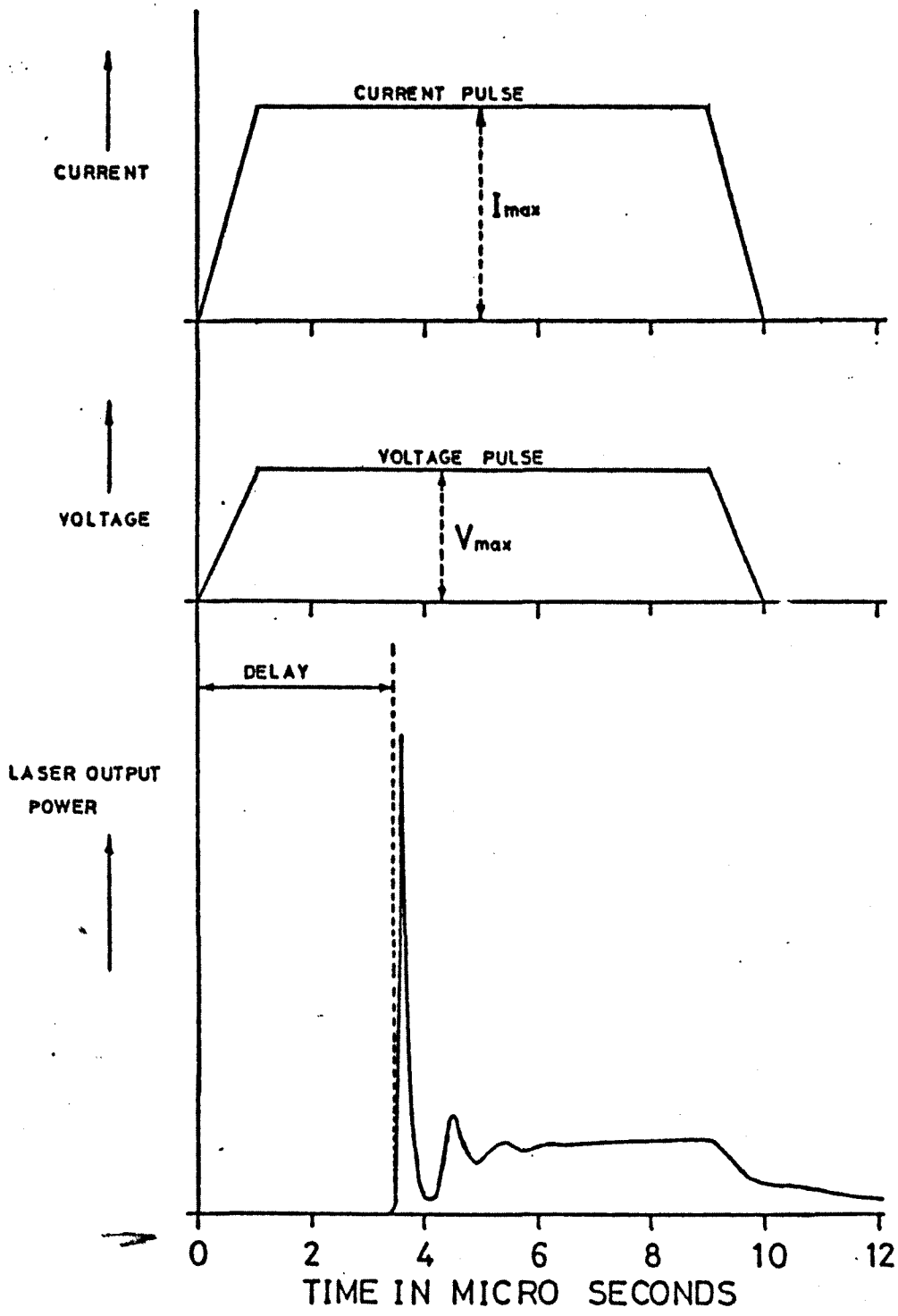

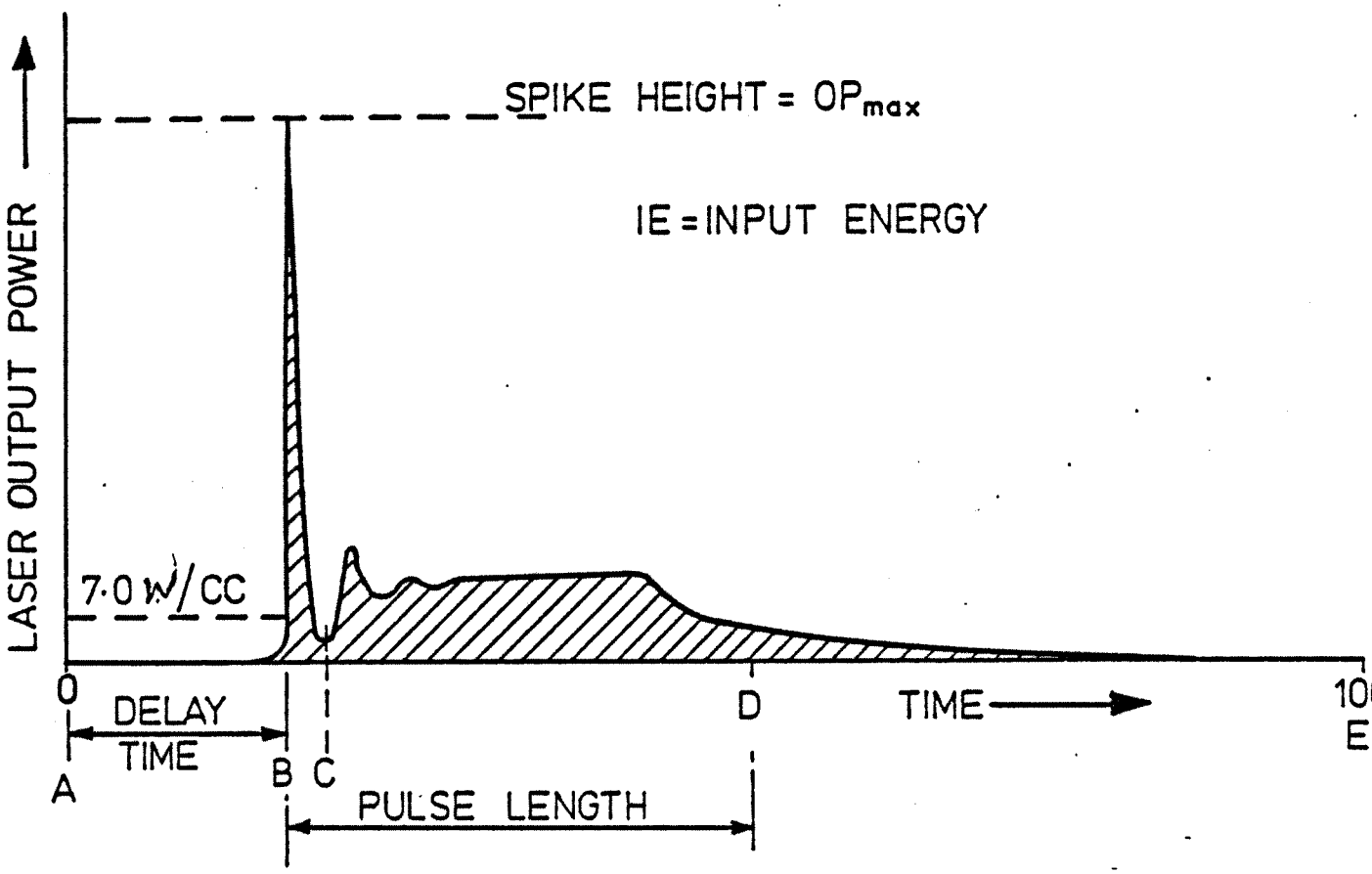

(i) PULSE ENERGY (PE) = INTEGRATE BETWEEN B AND D

(ii) TOTAL OUTPUT ENERGY (TOE) = INTEGRATE BETWEEN B AND E

(iii) FLAT PULSE POWER (FPP) = INTEGRATE BETWEEN C AND D AND DIVIDE BY TIME (C − D)

(iv) USEFUL EFFICIENCY, η_{us} = (PE / IE) × 100 %

(v) OVERALL EFFICIENCY, η_{ov} = (TOE / IE) × 100 %

Fig.(4·3) PULSE PARAMETER DEFINITIONS

TABLE (4.1) GAS DISCHARGE DATA EXTRACTED FROM KHAHRA[9] (CHAPTER 4 REFERENCE 9.)

Volume Ratio $CO_2:N_2:H_e$	Mixture Pressure = P (Torr) ($P_{CO_2} + P_{N_2} = 40$ Torr)	$\frac{V}{P}$ ($\frac{volt}{cm.Torr}$)	V ($\frac{volt}{cm}$)	Coupling Efficiency F_{CO_2}	Coupling Efficiency F_{N_2}	Average Electron Energy E_e (e.v.)	Current for 230 Watts/cm^3 input power (Amps)
1:1:0	40	29.35	1174	0.113	0.164	2.23	99.91
1:1:1	60	20.0	1200	0.132	0.184	2.0	97.75
1:1:2	80	15.5	1240	0.146	0.197	1.86	94.6
1:1:4	120	11.1	1332	0.170	0.216	1.63	88.06
1:1:6	160	8.8	1408	0.184	0.224	1.6	83.31
1:1:8	200	7.5	1500	0.184	0.223	1.48	78.2
1.2:0	40	25.75	1030	0.124	0.240	1.75	113.88
1:2:1	53.33	20.2	1077	0.130	0.255	1.65	108.94
1:2:2	66.67	16.6	1107	0.136	0.262	1.62	106.0
1:2:4	93.33	12.7	1185	0.146	0.274	1.50	98.96
1:2:6	119.98	10.5	1260	0.152	0.280	1.45	93.11
1:2:8	146.67	9.0	1320	0.155	0.283	1.42	88.86
1:3:0	40	24.5	980	0.124	0.283	1.54	119.69
1:3:1	50	20.2	1010	0.128	0.316	1.48	116.14
1:3:2	60	17.3	1038	0.132	0.324	1.47	113.01
1:3:4	80	13.65	1092	0.137	0.334	1.39	107.42
1:3:6	100	11.5	1150	0.142	0.342	1.36	102.0
1:3:8	120	10.1	1212	0.144	0.347	1.33	96.78

POPULATION OF UPPER LASER LEVEL VERSUS TIME

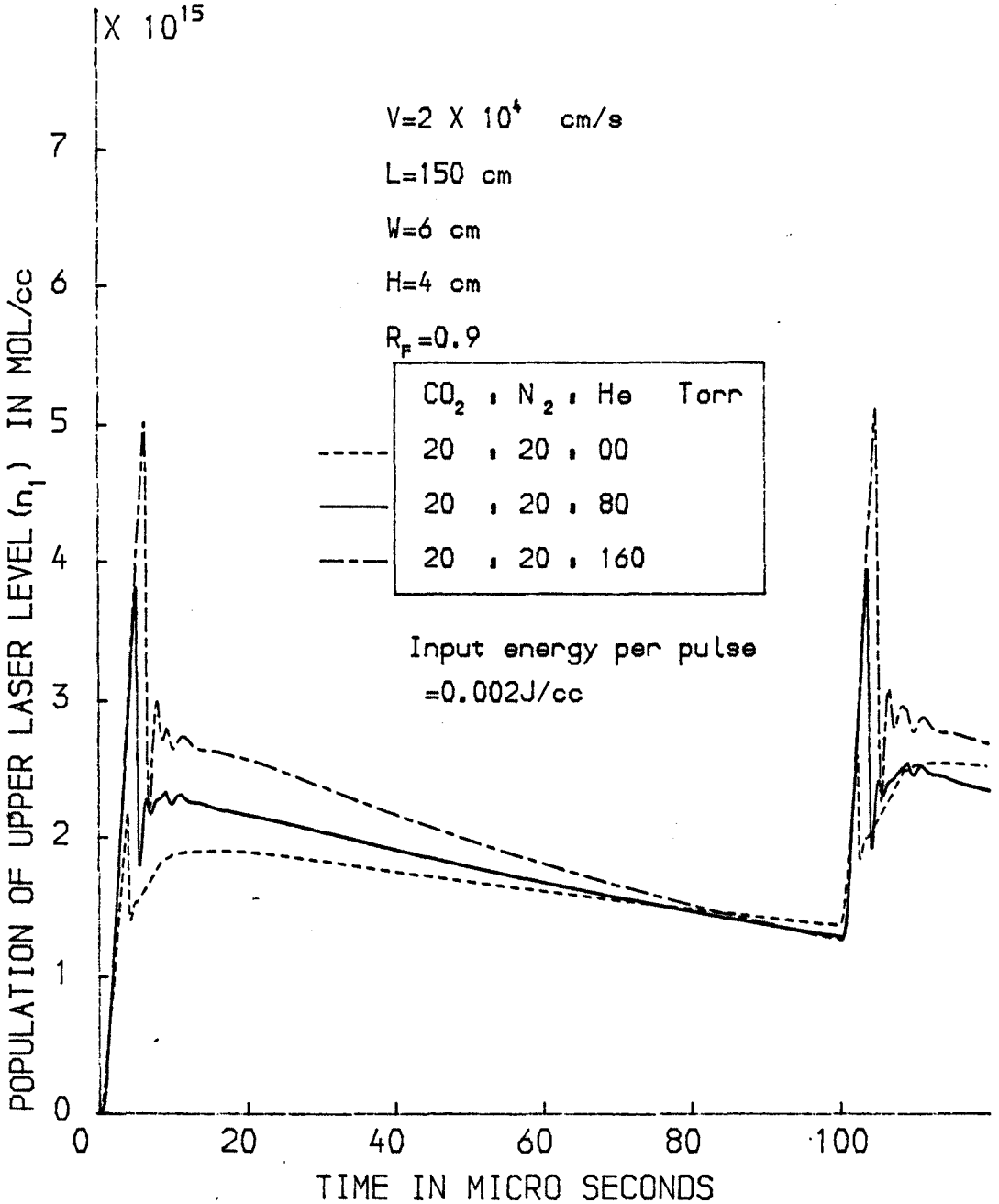

GRAPH (4.1)

POPULATION OF UPPER LASER LEVEL VERSUS TIME

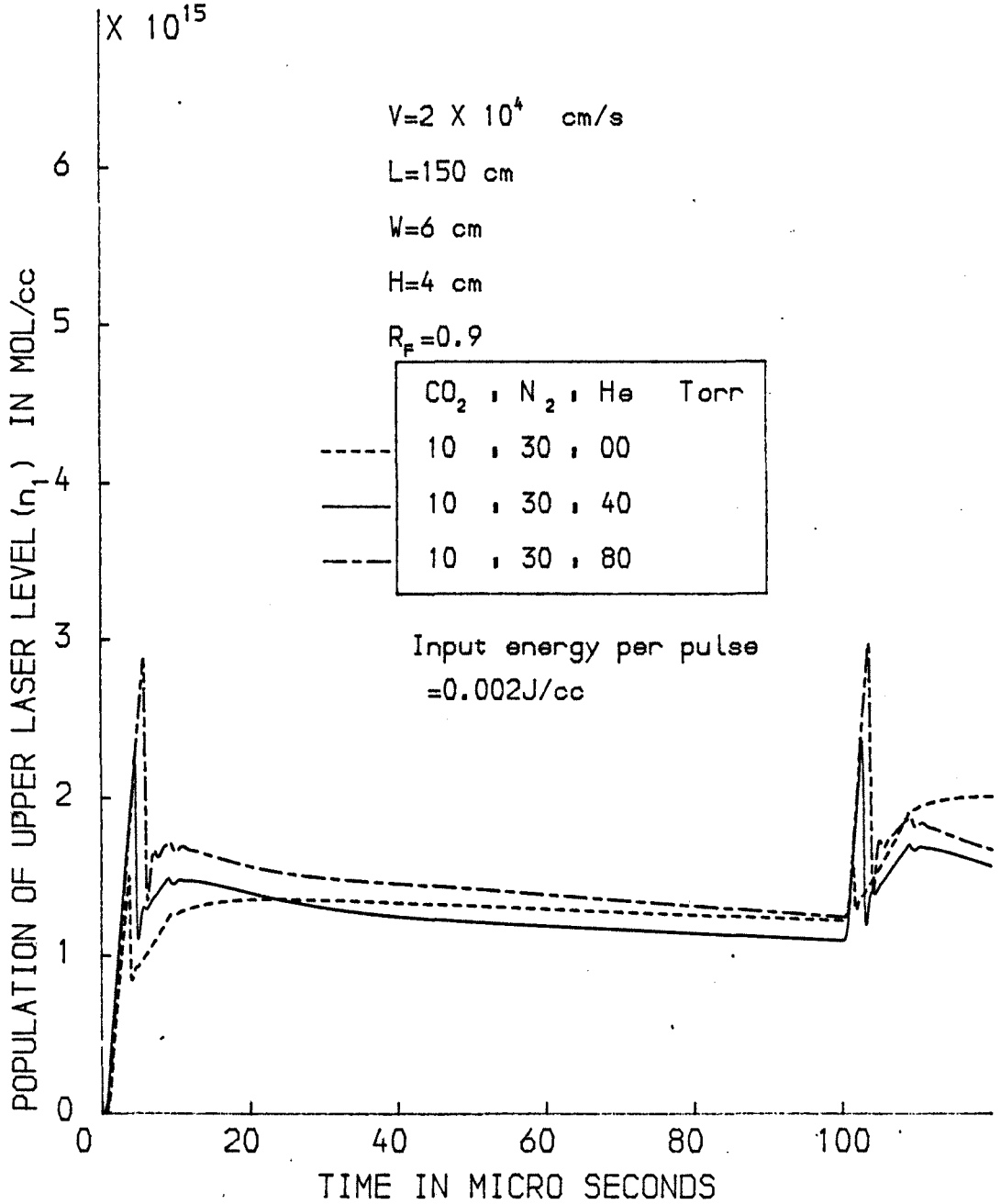

GRAPH (4.2)

POPULATION OF UPPER NITROGEN LEVEL VERSUS TIME

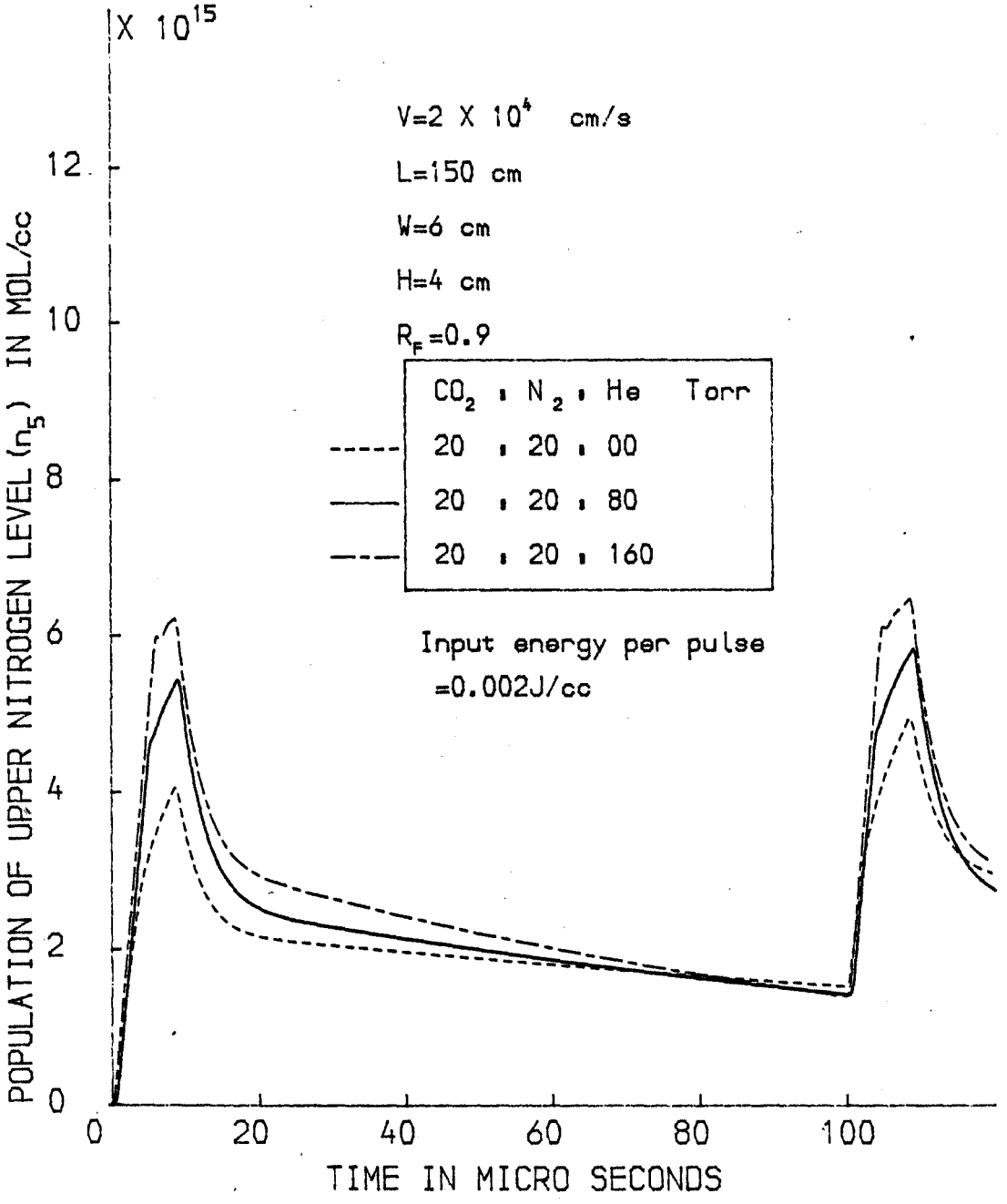

GRAPH (4.3)

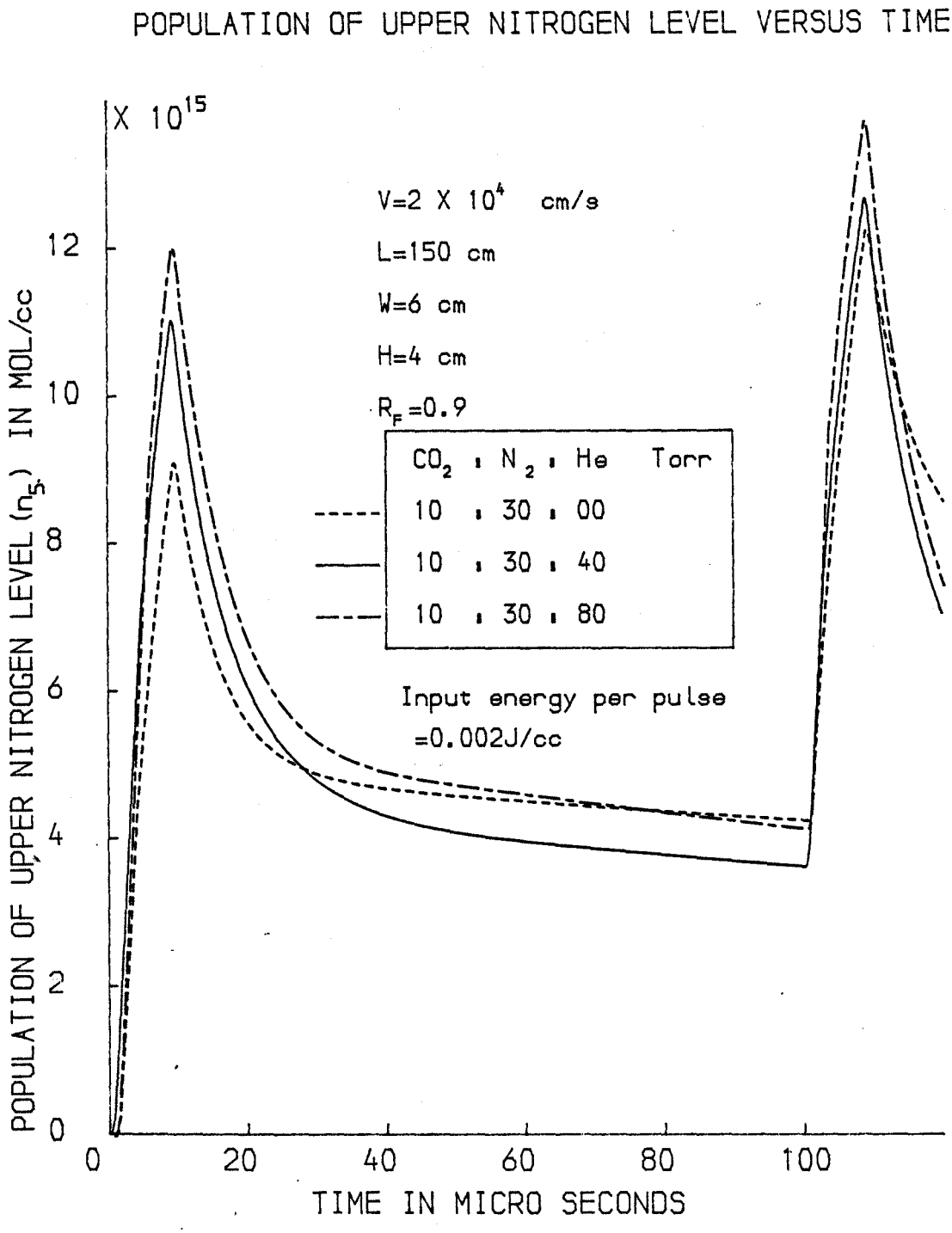
POPULATION OF UPPER NITROGEN LEVEL VERSUS TIME
X 10^15
V=2 X 10^4 cm/s
L=150 cm
W=6 cm
H=4 cm
R_F=0.9
CO2 : N2 : He Torr
10 : 30 : 00
10 : 30 : 40
10 : 30 : 80
Input energy per pulse
=0.002J/cc
POPULATION OF UPPER NITROGEN LEVEL (n5) IN MOL/cc
0
2
4
6
8
10
12
0
20
40
60
80
100
TIME IN MICRO SECONDS

GRAPH (4.4)

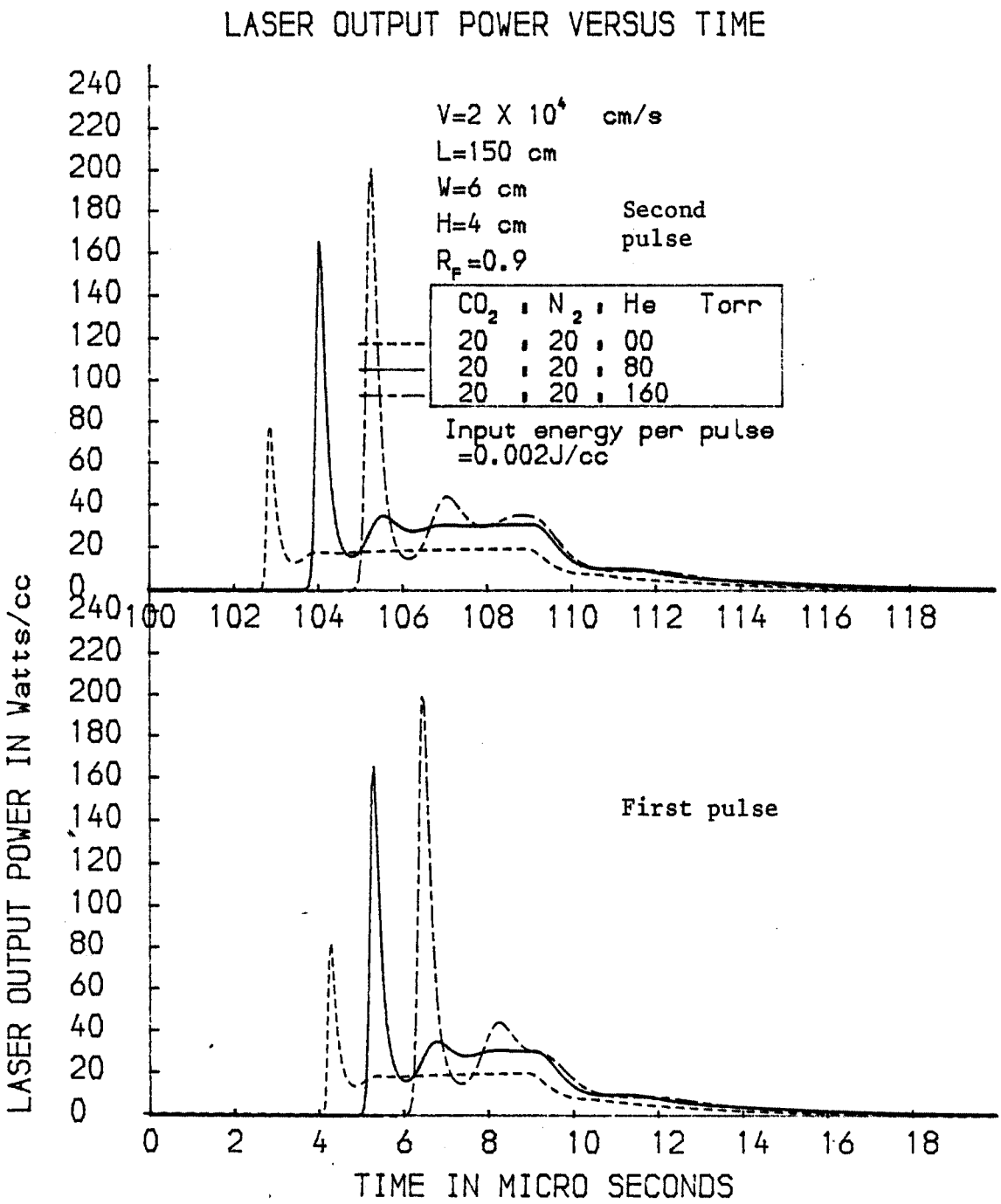
LASER OUTPUT POWER VERSUS TIME
V=2 X 10⁴ cm/s
L=150 cm
W=6 cm
H=4 cm
R_F=0.9
Second pulse
CO2 : N2 : He Torr
20 : 20 : 00
20 : 20 : 80
20 : 20 : 160
Input energy per pulse =0.002J/cc
First pulse
LASER OUTPUT POWER IN Watts/cc
TIME IN MICRO SECONDS

GRAPH (4.5)

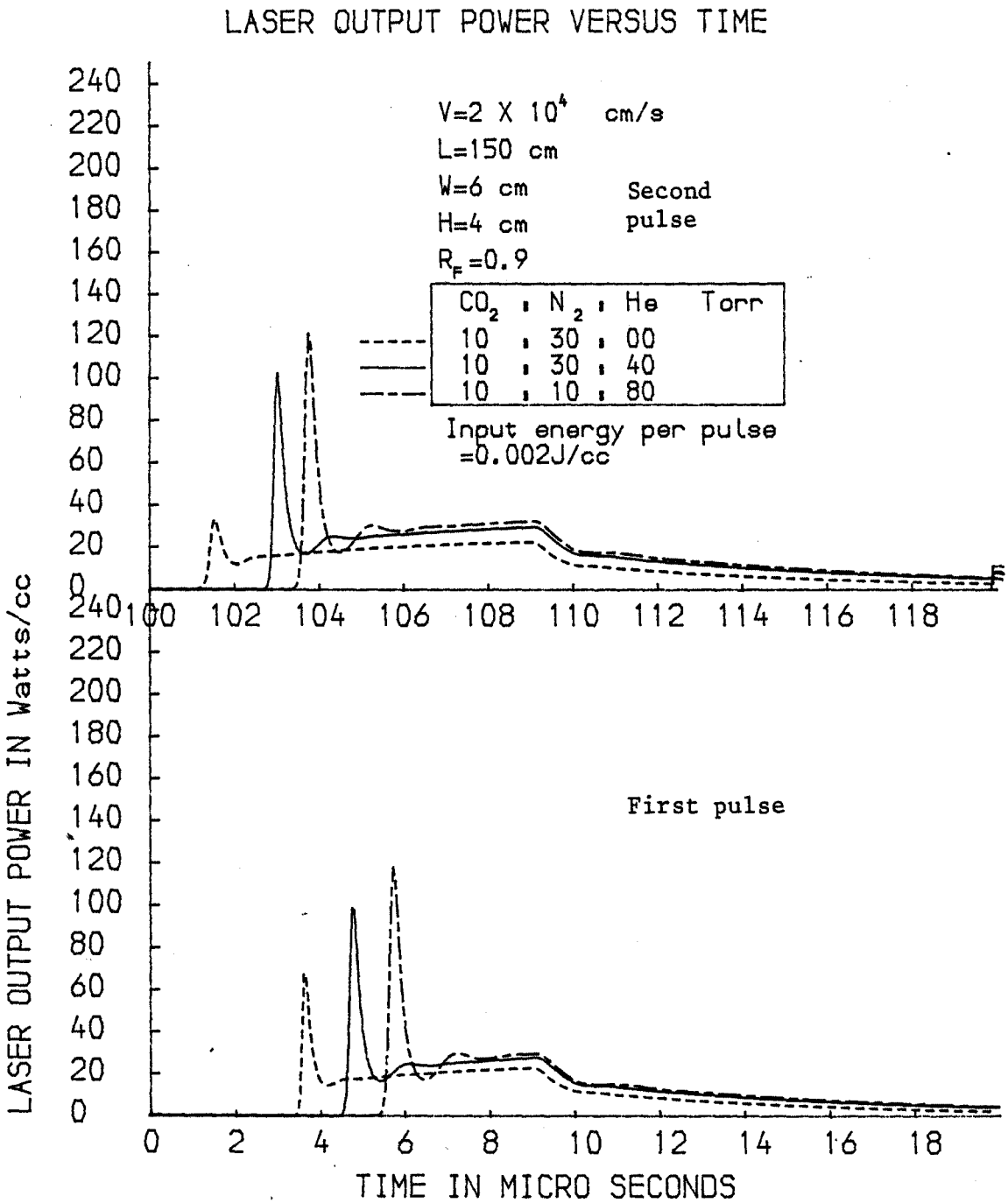
LASER OUTPUT POWER VERSUS TIME
V=2 X 10^4 cm/s
L=150 cm
W=6 cm
H=4 cm
R_F=0.9
Second pulse
CO2 : N2 : He Torr
10 : 30 : 00
10 : 30 : 40
10 : 10 : 80
Input energy per pulse =0.002J/cc
First pulse
LASER OUTPUT POWER IN Watts/cc
TIME IN MICRO SECONDS

GRAPH (4.6)

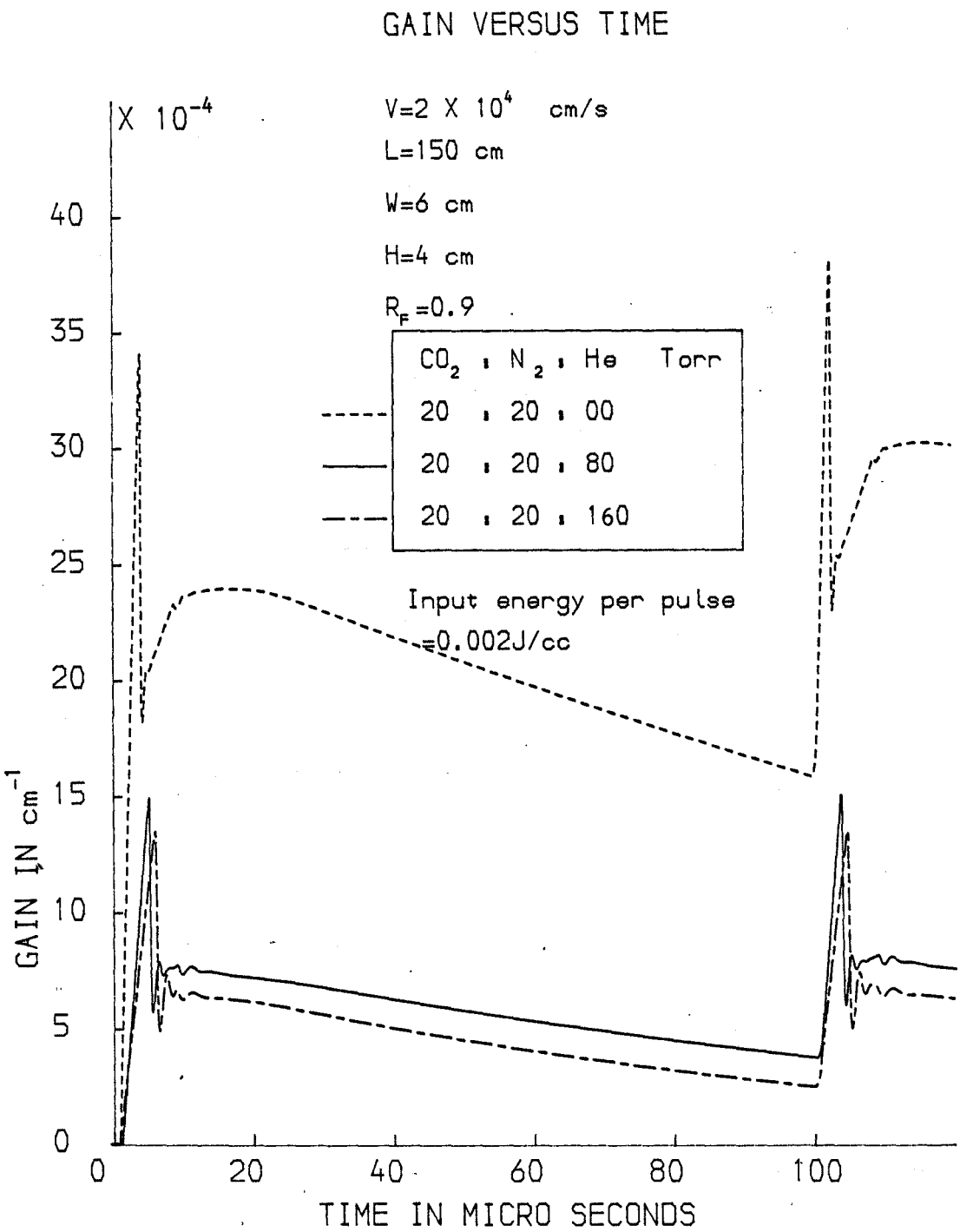
GAIN VERSUS TIME
X 10^-4
V=2 X 10^4 cm/s
L=150 cm
W=6 cm
H=4 cm
R_F=0.9
CO2 : N2 : He Torr
20 : 20 : 00
20 : 20 : 80
20 : 20 : 160
Input energy per pulse
=0.002J/cc
GAIN IN cm^-1
TIME IN MICRO SECONDS
0
5
10
15
20
25
30
35
40
0
20
40
60
80
100

GRAPH (4.7)

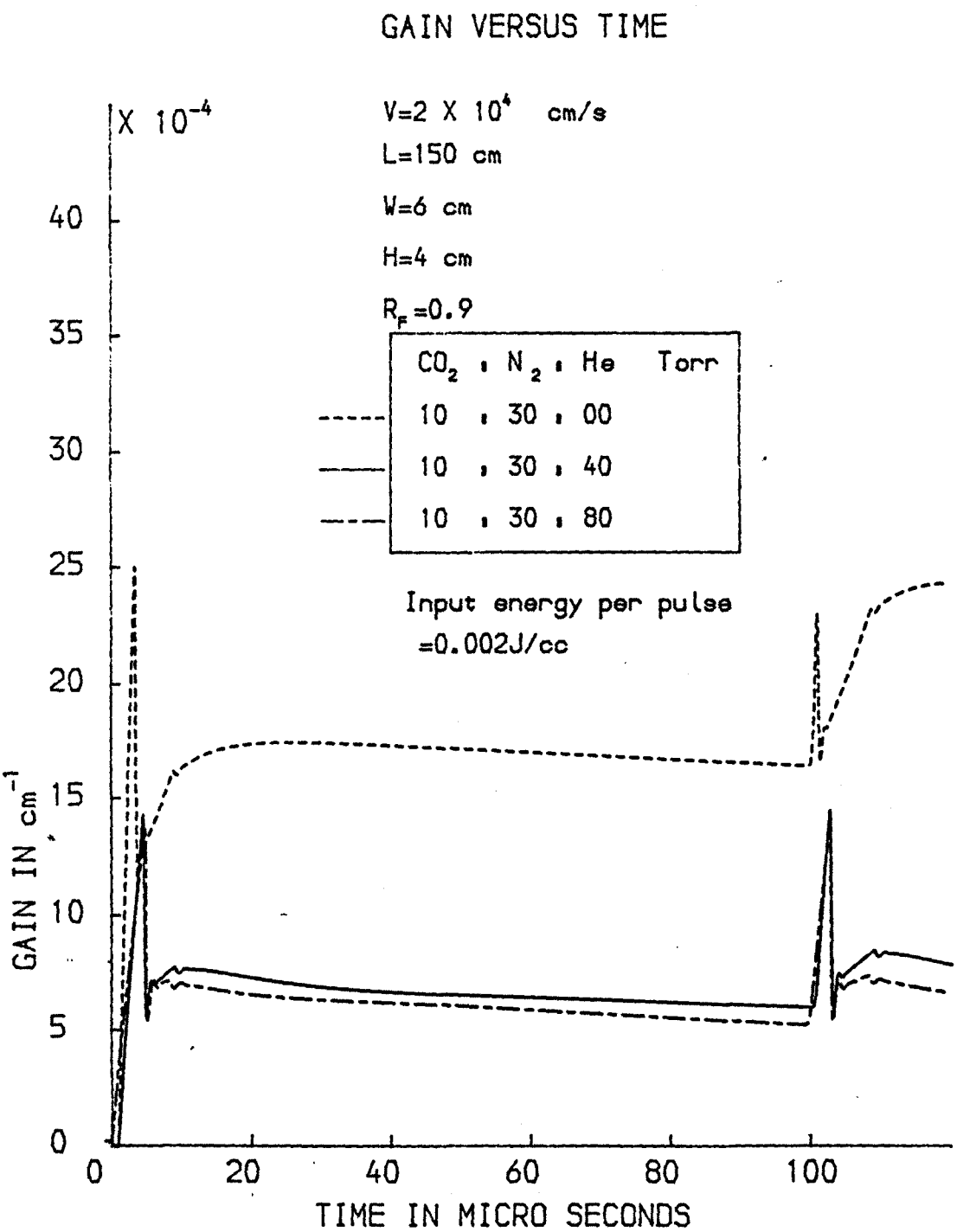
GAIN VERSUS TIME
X 10^-4
V=2 X 10^4 cm/s
L=150 cm
W=6 cm
H=4 cm
R_F=0.9
CO2 : N2 : He Torr
10 : 30 : 00
10 : 30 : 40
10 : 30 : 80
Input energy per pulse
=0.002J/cc
GAIN IN cm^-1
0
5
10
15
20
25
30
35
40
0
20
40
60
80
100
TIME IN MICRO SECONDS

GRAPH (4.8)

TEMPERATURE OF LASER GASES VERSUS TIME

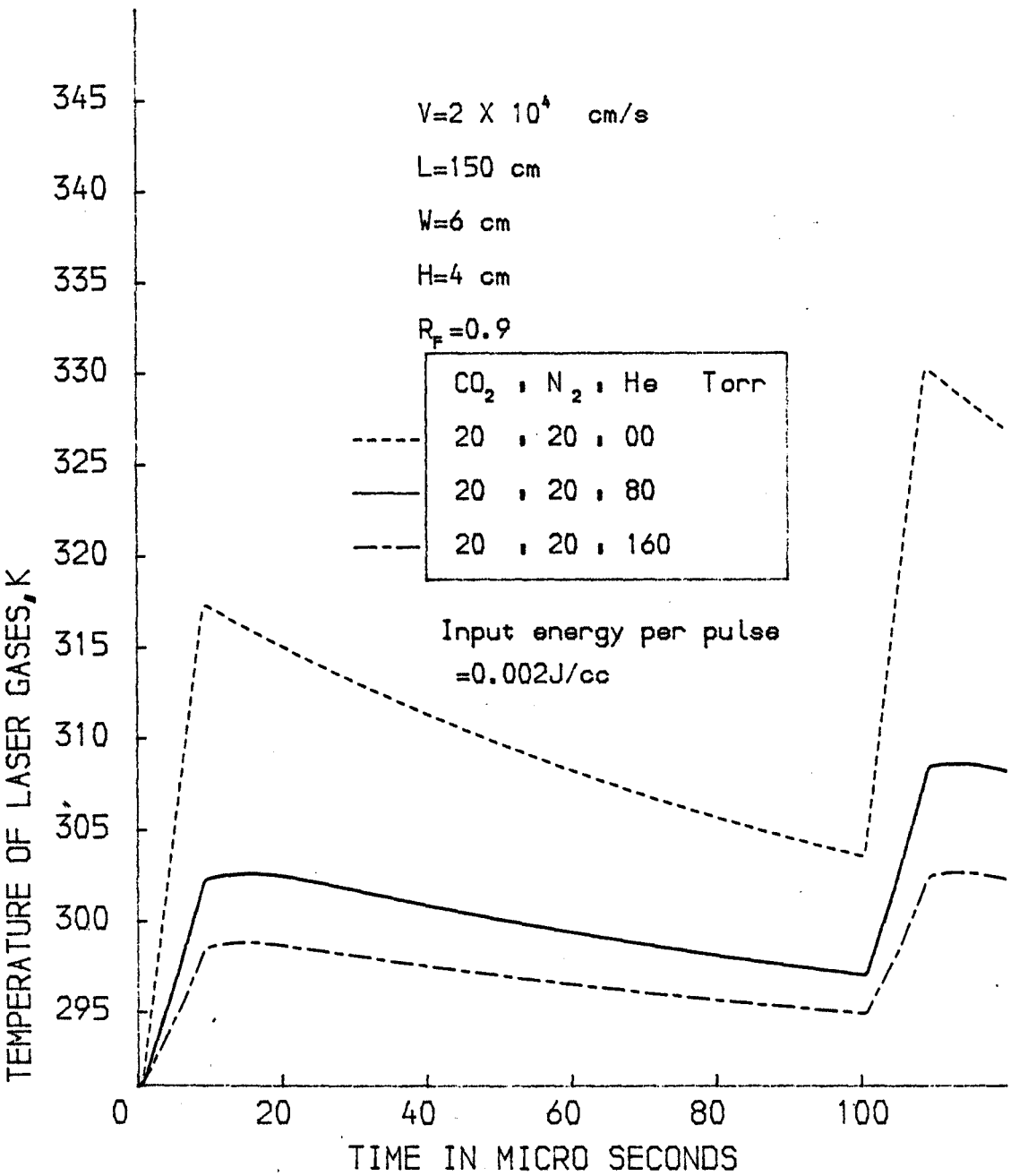

GRAPH (4.9)

TEMPERATURE OF LASER GASES VERSUS TIME

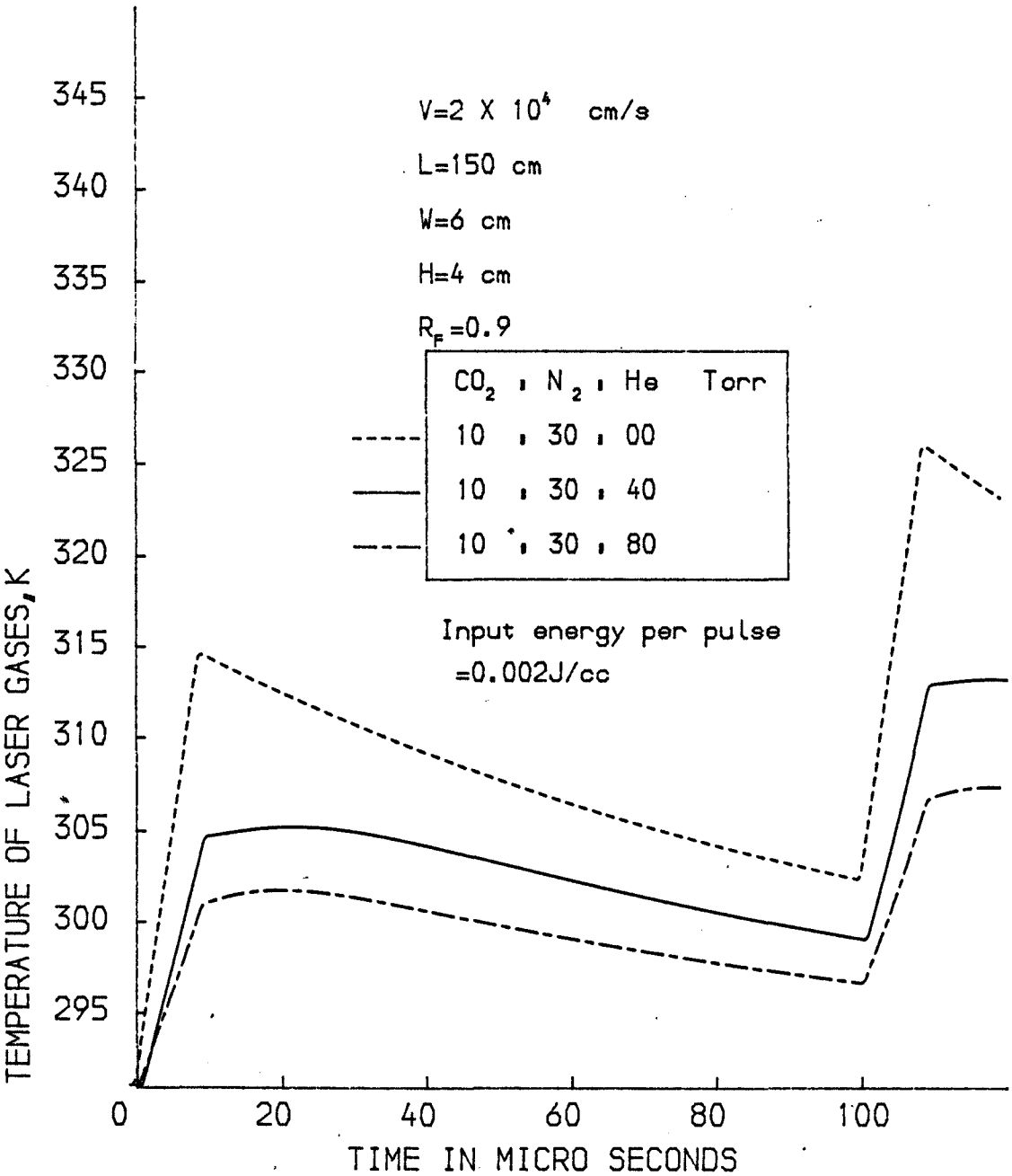

GRAPH (4.10)

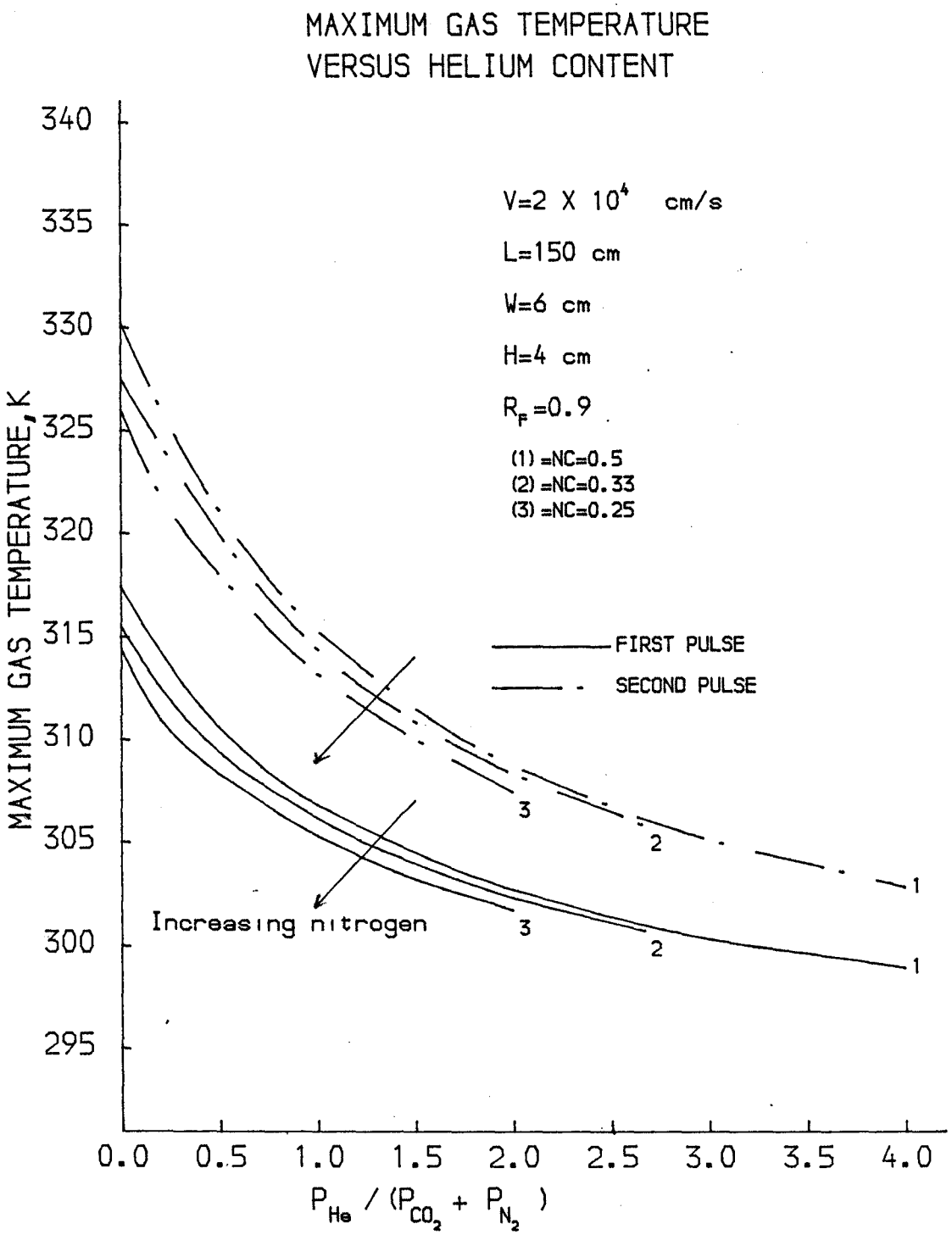
MAXIMUM GAS TEMPERATURE
VERSUS HELIUM CONTENT
MAXIMUM GAS TEMPERATURE, K
340
335
330
325
320
315
310
305
300
295
V=2 X 10^4 cm/s
L=150 cm
W=6 cm
H=4 cm
R_F=0.9
(1) =NC=0.5
(2) =NC=0.33
(3) =NC=0.25
FIRST PULSE
SECOND PULSE
Increasing nitrogen
1
2
3
0.0
0.5
1.0
1.5
2.0
2.5
3.0
3.5
4.0
P_He / (P_CO2 + P_N2)

GRAPH (4.11)

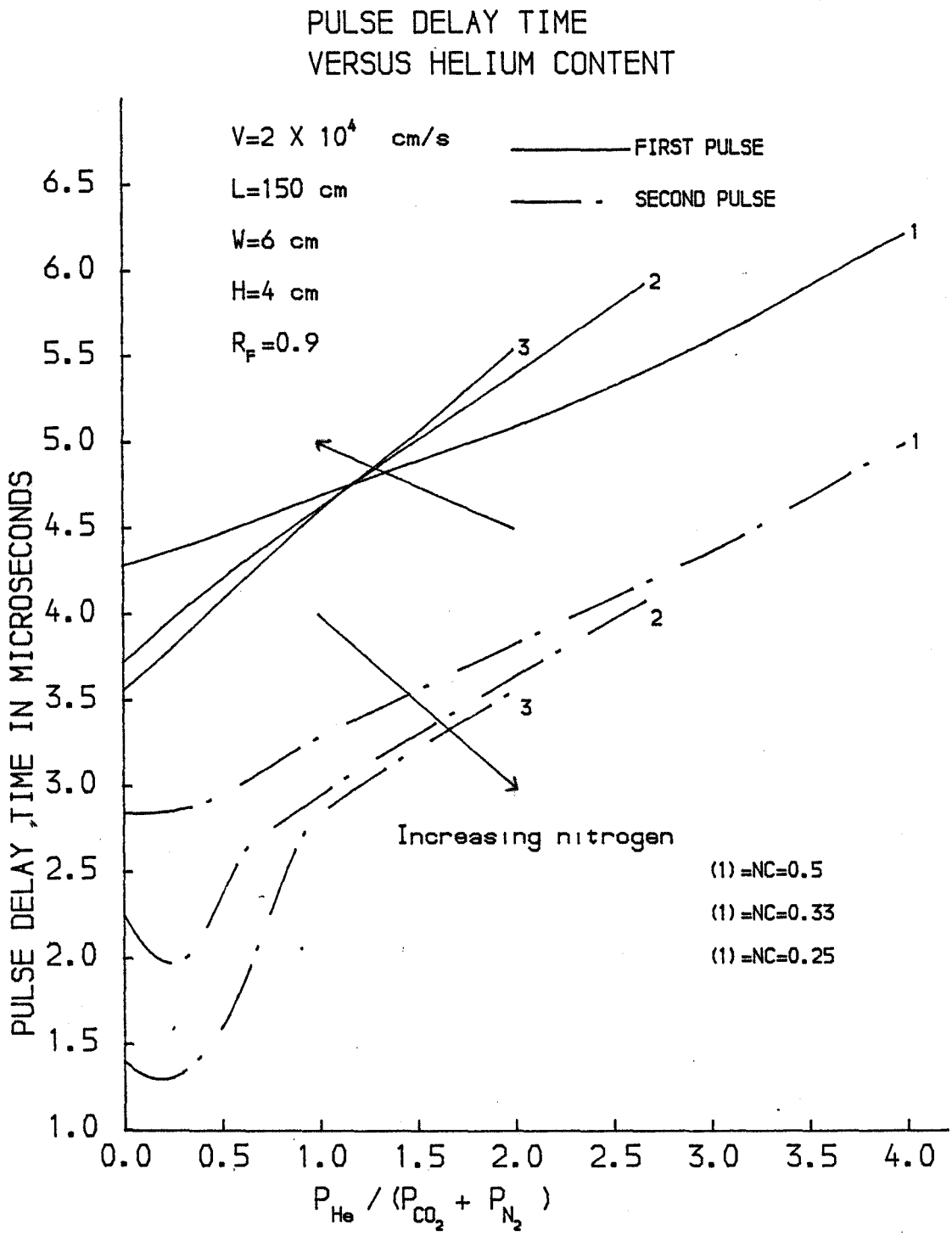
PULSE DELAY TIME
VERSUS HELIUM CONTENT
V=2 X 10^4 cm/s
L=150 cm
W=6 cm
H=4 cm
R_F=0.9
FIRST PULSE
SECOND PULSE
PULSE DELAY TIME IN MICROSECONDS
6.5
6.0
5.5
5.0
4.5
4.0
3.5
3.0
2.5
2.0
1.5
1.0
0.0
0.5
1.0
1.5
2.0
2.5
3.0
3.5
4.0
P_He / (P_CO2 + P_N2)
1
2
3
1
2
3
Increasing nitrogen
(1) =NC=0.5
(1) =NC=0.33
(1) =NC=0.25

GRAPH(4.12)

MAXIMUM POWER VERSUS HELIUM CONTENT

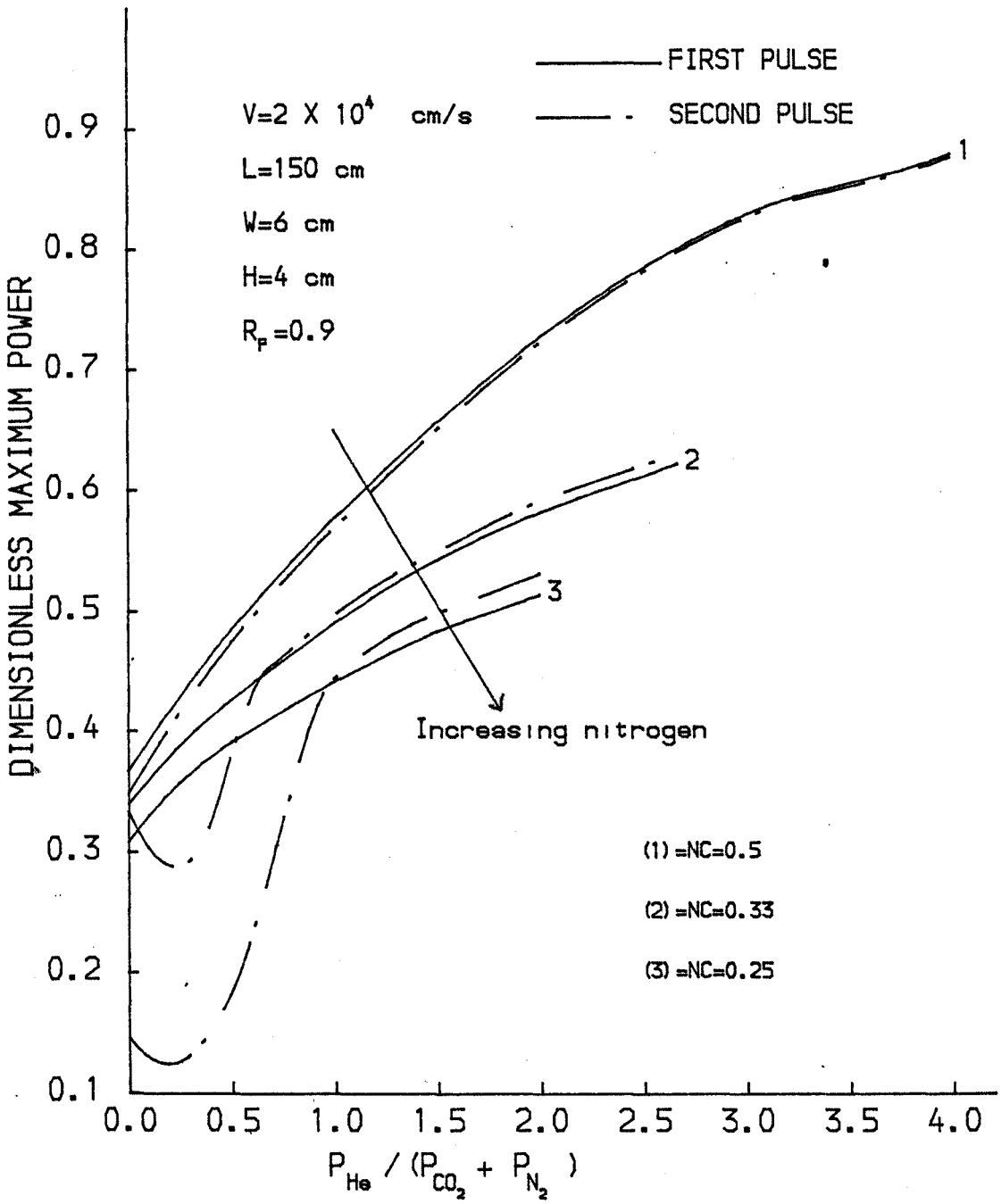

GRAPH (4.13)

PULSE DURATION VERSUS HELIUM CONTENT

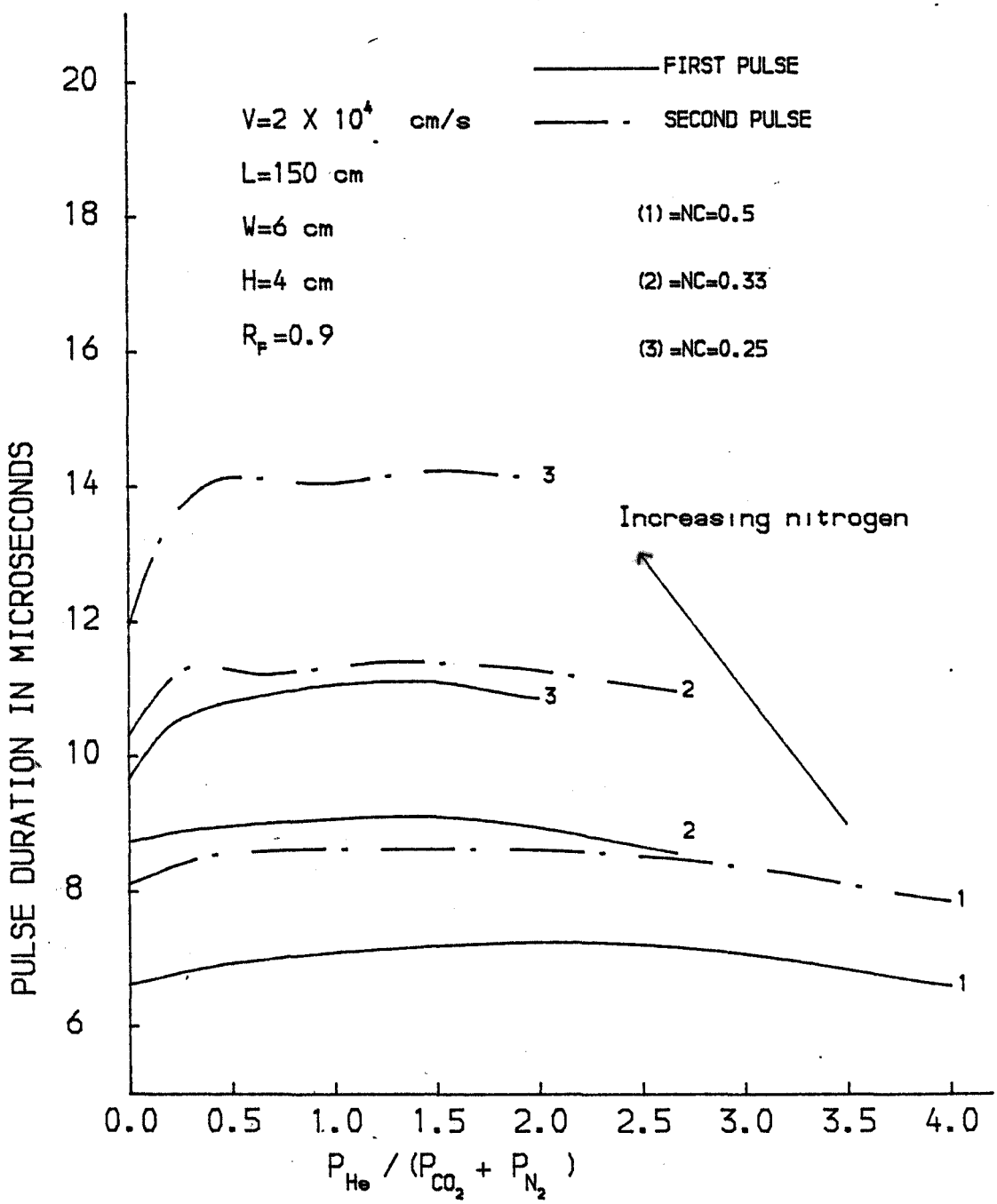

GRAPH (4.14)

AVERAGE POWER VERSUS HELIUM CONTENT

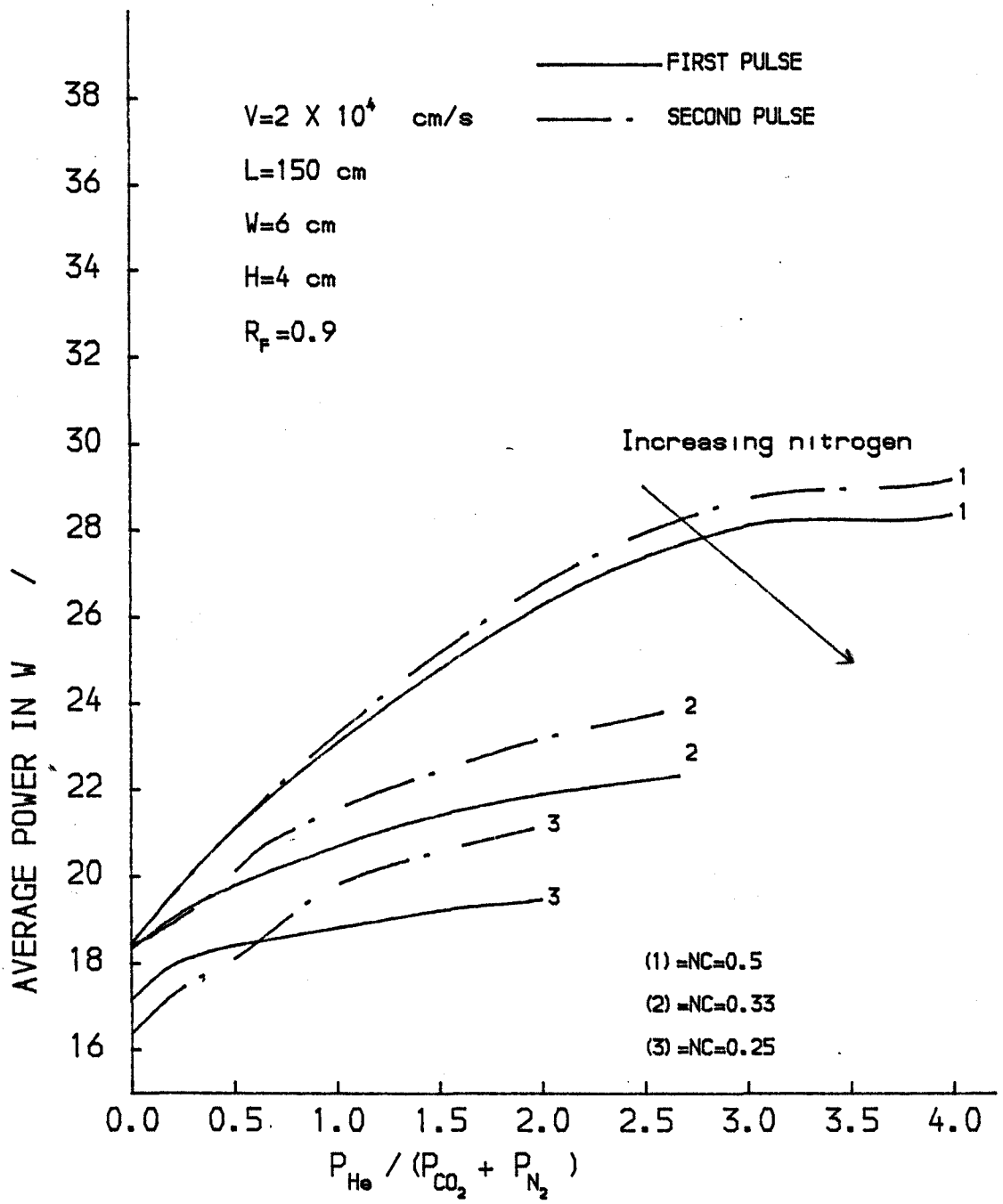

GRAPH (4.15)

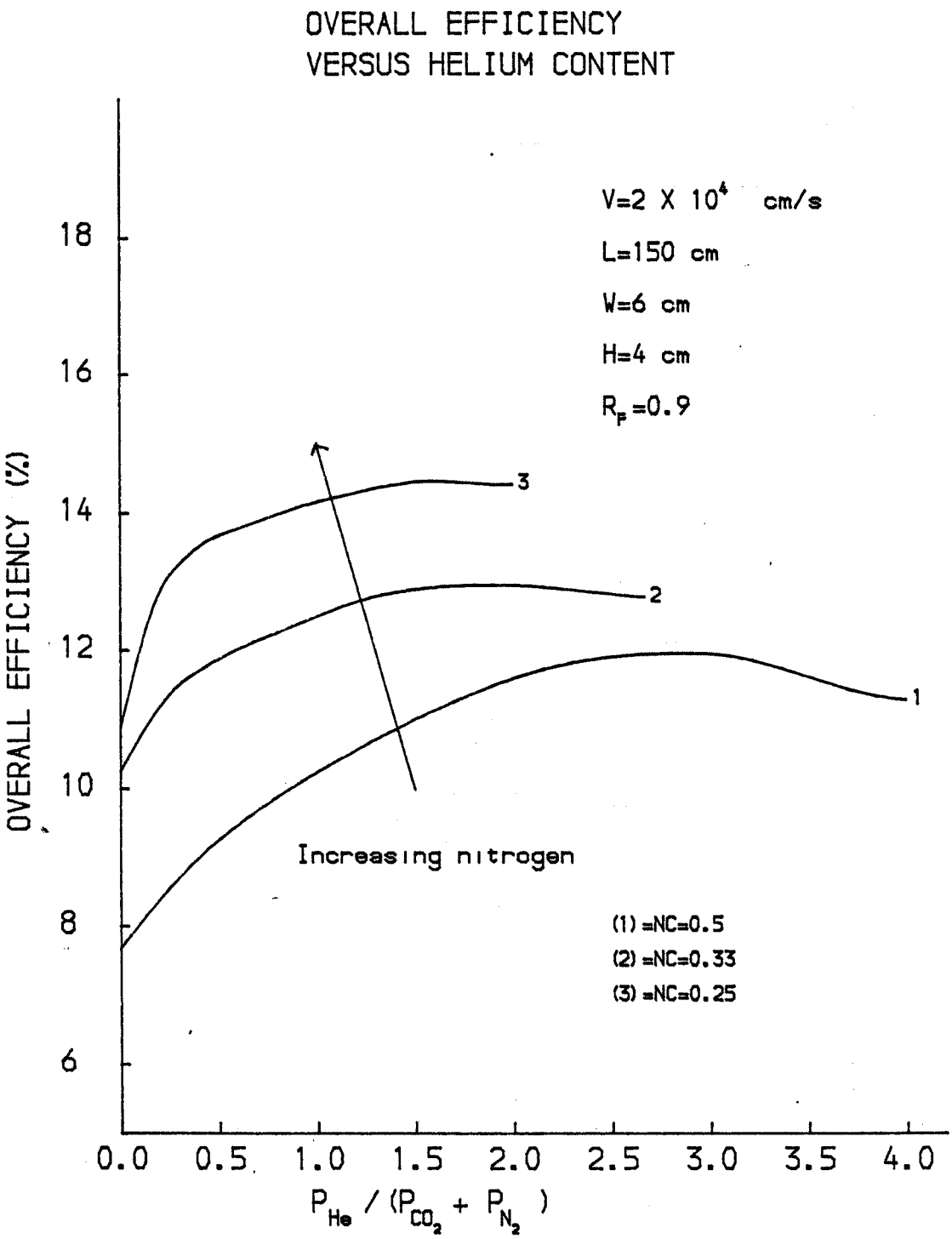
OVERALL EFFICIENCY
VERSUS HELIUM CONTENT
V=2 X 10^4 cm/s
L=150 cm
W=6 cm
H=4 cm
R_F=0.9
OVERALL EFFICIENCY (%)
18
16
14
12
10
8
6
3
2
1
Increasing nitrogen
(1) =NC=0.5
(2) =NC=0.33
(3) =NC=0.25
0.0 0.5 1.0 1.5 2.0 2.5 3.0 3.5 4.0
P_He / (P_CO2 + P_N2)

GRAPH (4.16)

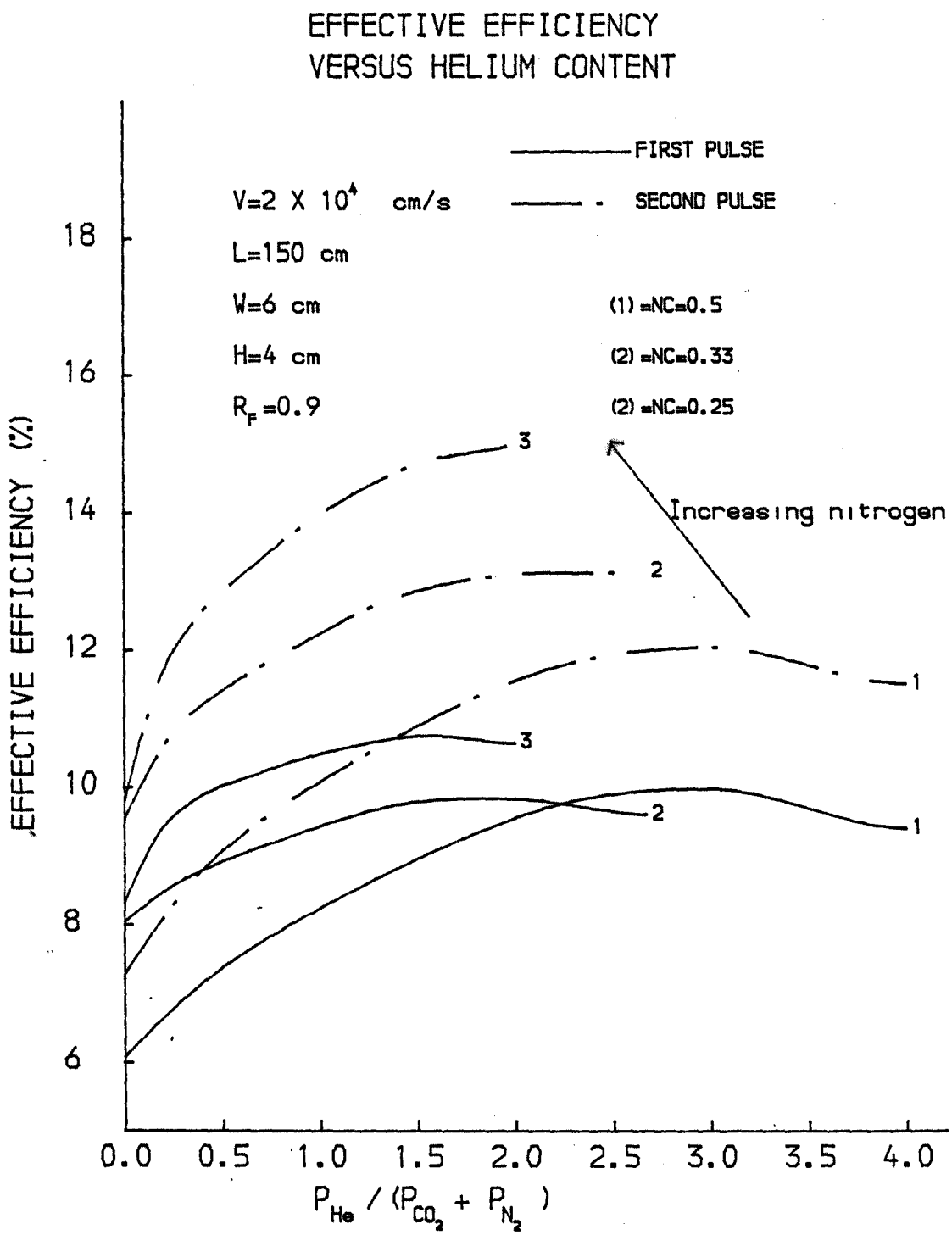
EFFECTIVE EFFICIENCY
VERSUS HELIUM CONTENT
FIRST PULSE
SECOND PULSE
V=2 X 10⁴ cm/s
L=150 cm
W=6 cm
H=4 cm
R_F=0.9
(1) =NC=0.5
(2) =NC=0.33
(2) =NC=0.25
Increasing nitrogen
EFFECTIVE EFFICIENCY (%)
18
16
14
12
10
8
6
0.0
0.5
1.0
1.5
2.0
2.5
3.0
3.5
4.0
P_He / (P_CO2 + P_N2)
1
2
3

GRAPH (4.17)

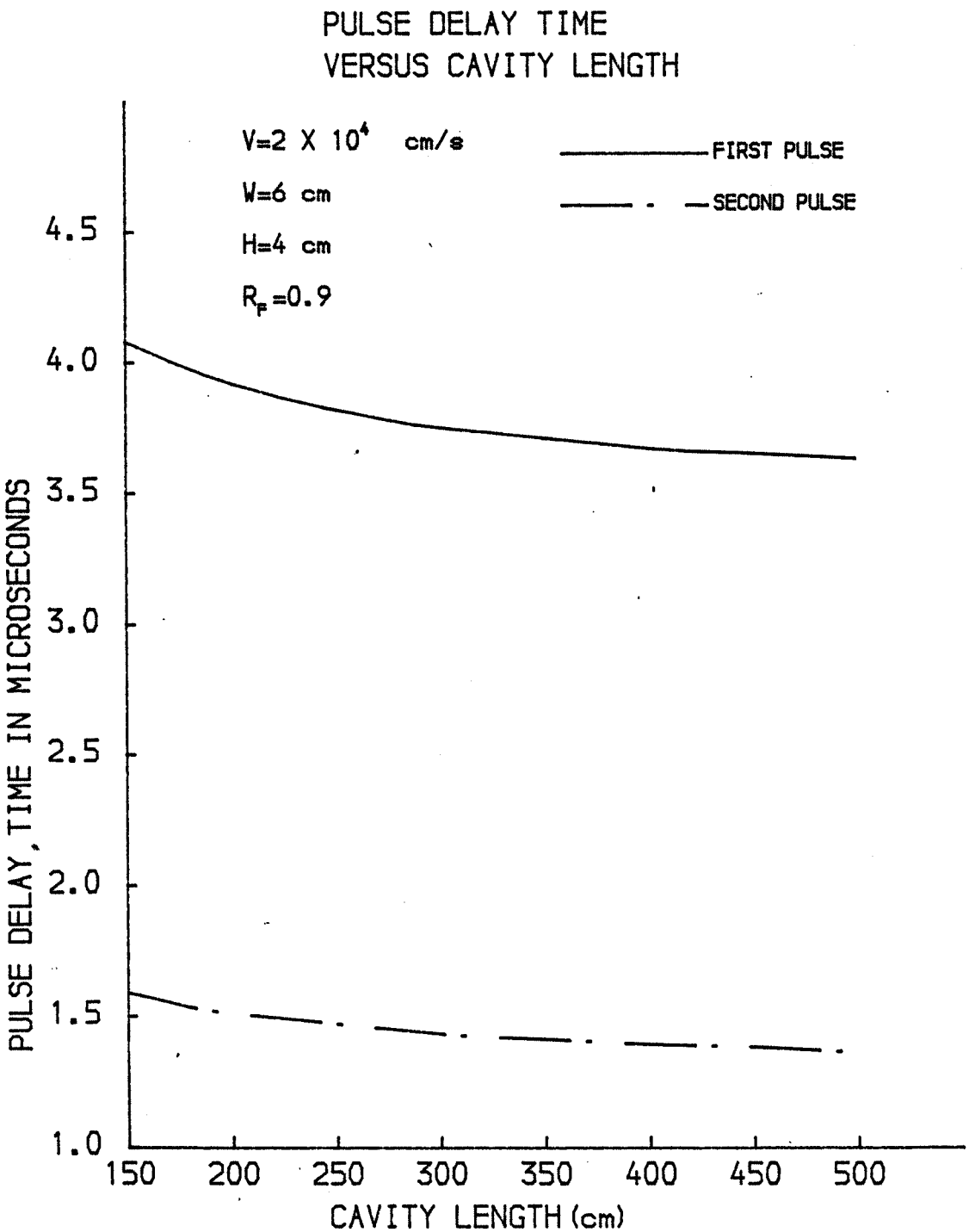
PULSE DELAY TIME
VERSUS CAVITY LENGTH
V=2 X 10⁴ cm/s
W=6 cm
H=4 cm
R_F=0.9
FIRST PULSE
SECOND PULSE
PULSE DELAY, TIME IN MICROSECONDS
4.5
4.0
3.5
3.0
2.5
2.0
1.5
1.0
150
200
250
300
350
400
450
500
CAVITY LENGTH (cm)

GRAPH (4.18)

MAXIMUM POWER VERSUS CAVITY LENGTH

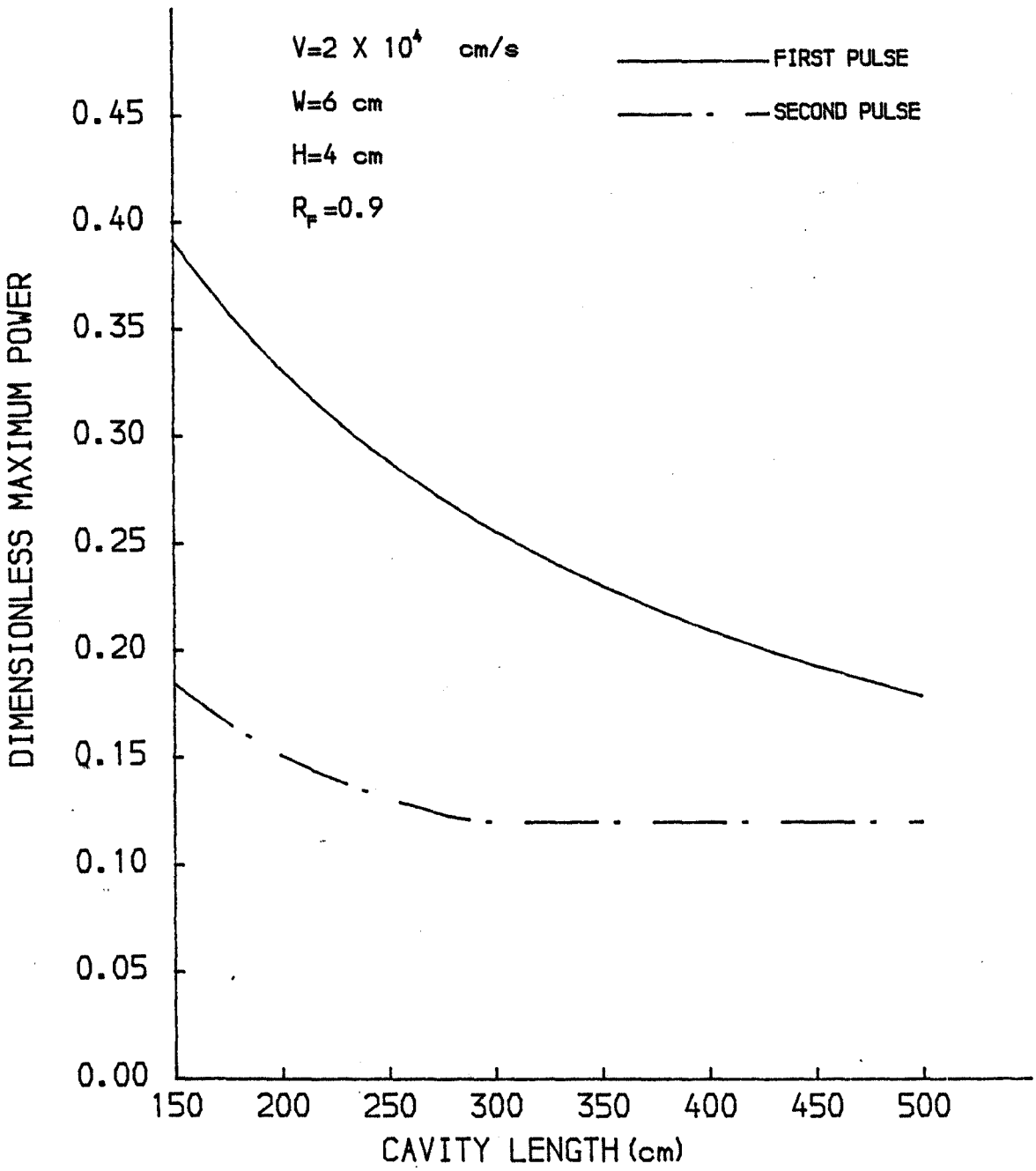

GRAPH (4.19)

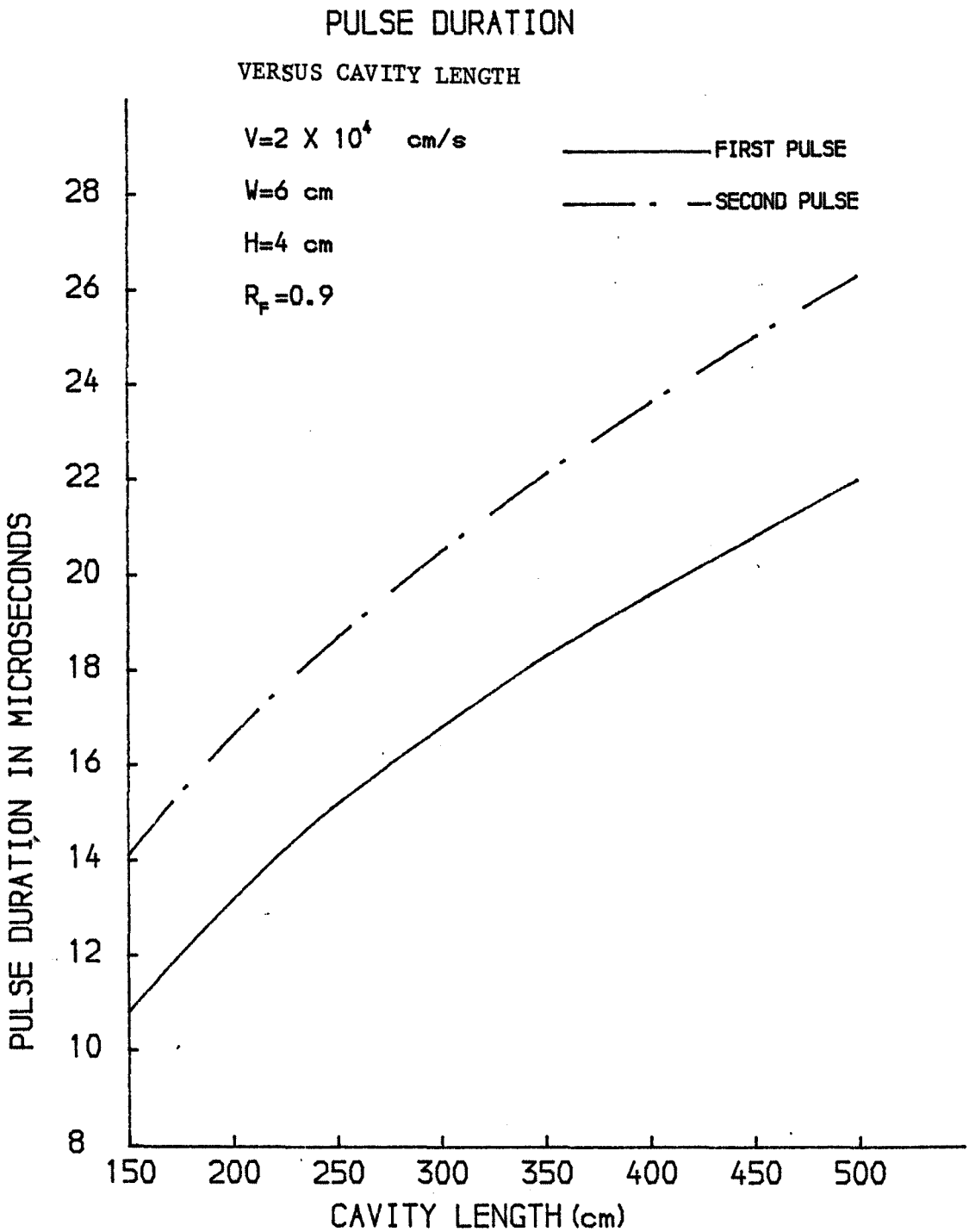
PULSE DURATION
VERSUS CAVITY LENGTH
V=2 X 10⁴ cm/s
W=6 cm
H=4 cm
R_F=0.9
FIRST PULSE
SECOND PULSE
PULSE DURATION IN MICROSECONDS
28
26
24
22
20
18
16
14
12
10
8
150
200
250
300
350
400
450
500
CAVITY LENGTH (cm)

GRAPH (4.20)

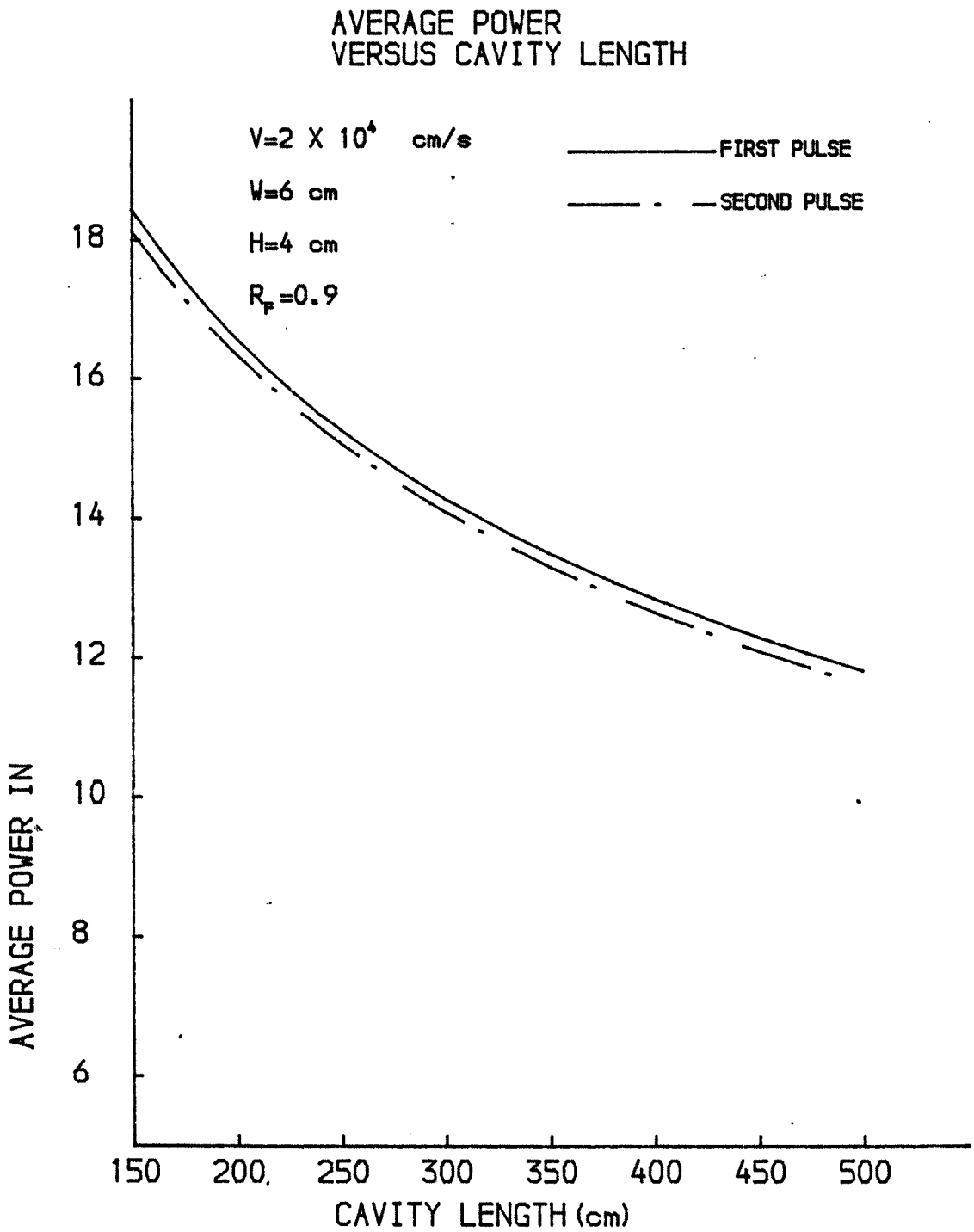
AVERAGE POWER
VERSUS CAVITY LENGTH
V=2 X 10⁴ cm/s
W=6 cm
H=4 cm
R_p=0.9
FIRST PULSE
SECOND PULSE
AVERAGE POWER IN
18
16
14
12
10
8
6
150
200
250
300
350
400
450
500
CAVITY LENGTH (cm)

GRAPH (4.21)

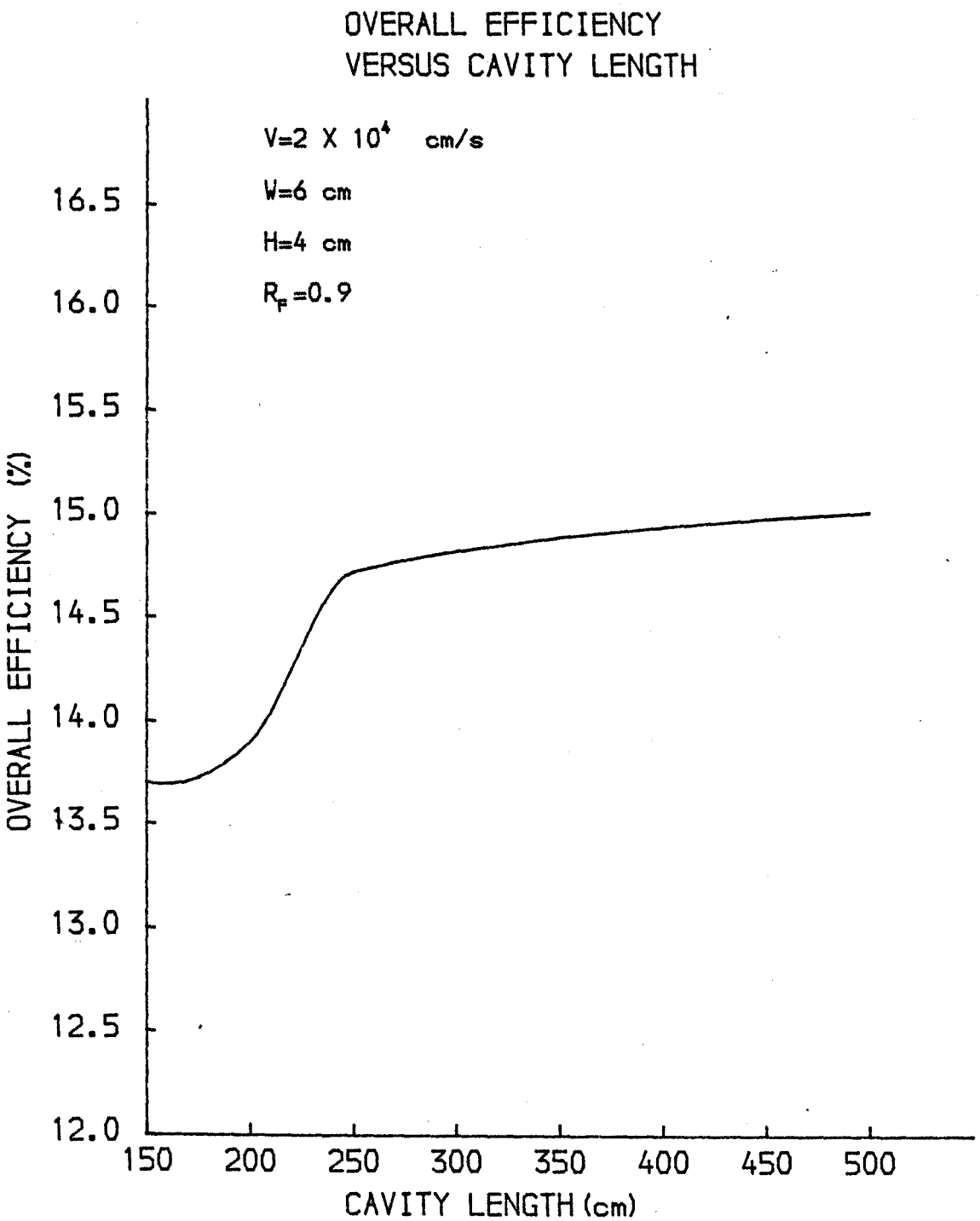
OVERALL EFFICIENCY
VERSUS CAVITY LENGTH
V=2 X 10⁴ cm/s
W=6 cm
H=4 cm
R_F=0.9
OVERALL EFFICIENCY (%)
16.5
16.0
15.5
15.0
14.5
14.0
13.5
13.0
12.5
12.0
150
200
250
300
350
400
450
500
CAVITY LENGTH (cm)

GRAPH (4.22)

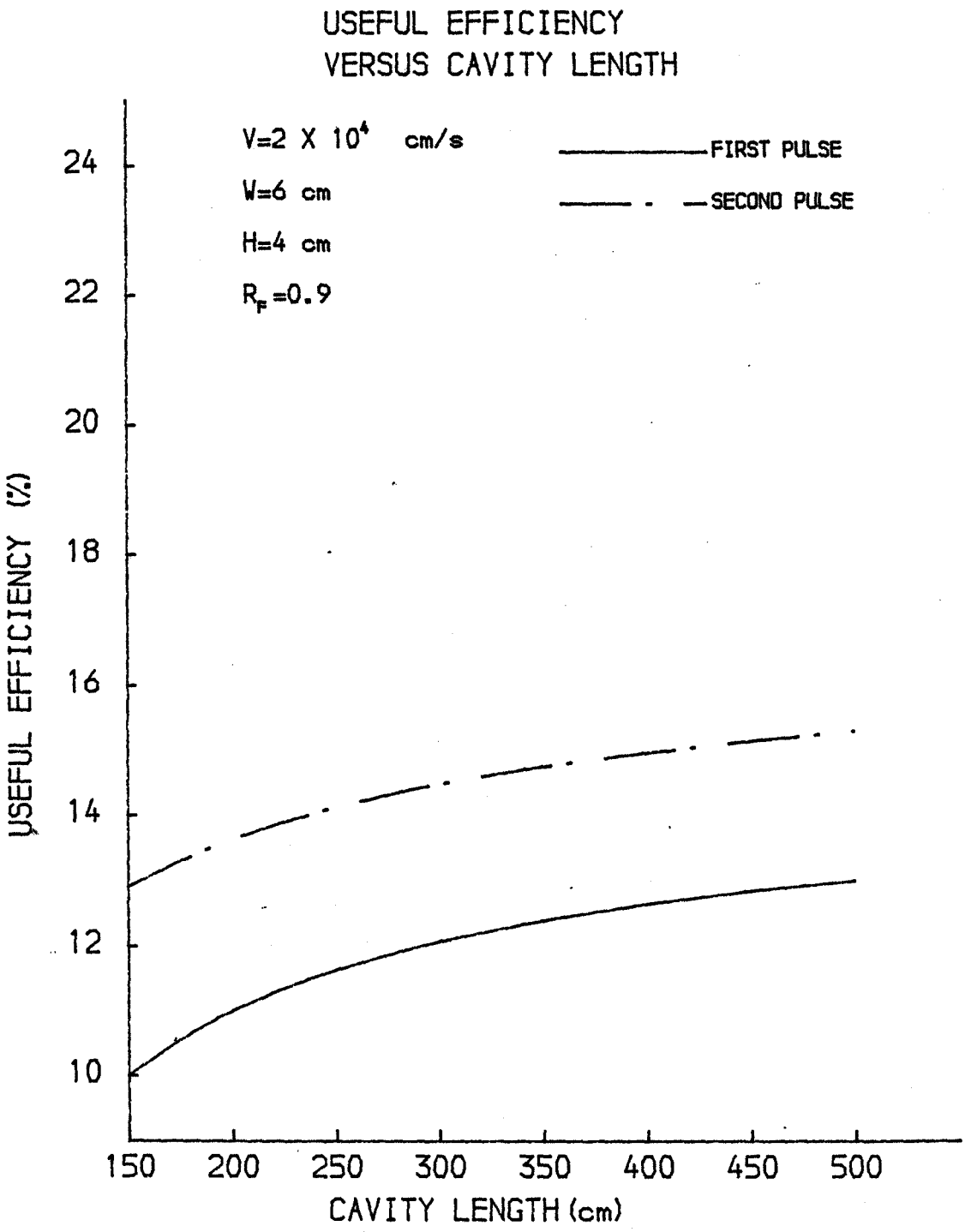
USEFUL EFFICIENCY
VERSUS CAVITY LENGTH
V=2 X 10⁴ cm/s
W=6 cm
H=4 cm
R_F=0.9
FIRST PULSE
SECOND PULSE
USEFUL EFFICIENCY (%)
24
22
20
18
16
14
12
10
150
200
250
300
350
400
450
500
CAVITY LENGTH (cm)

GRAPH (4.23)

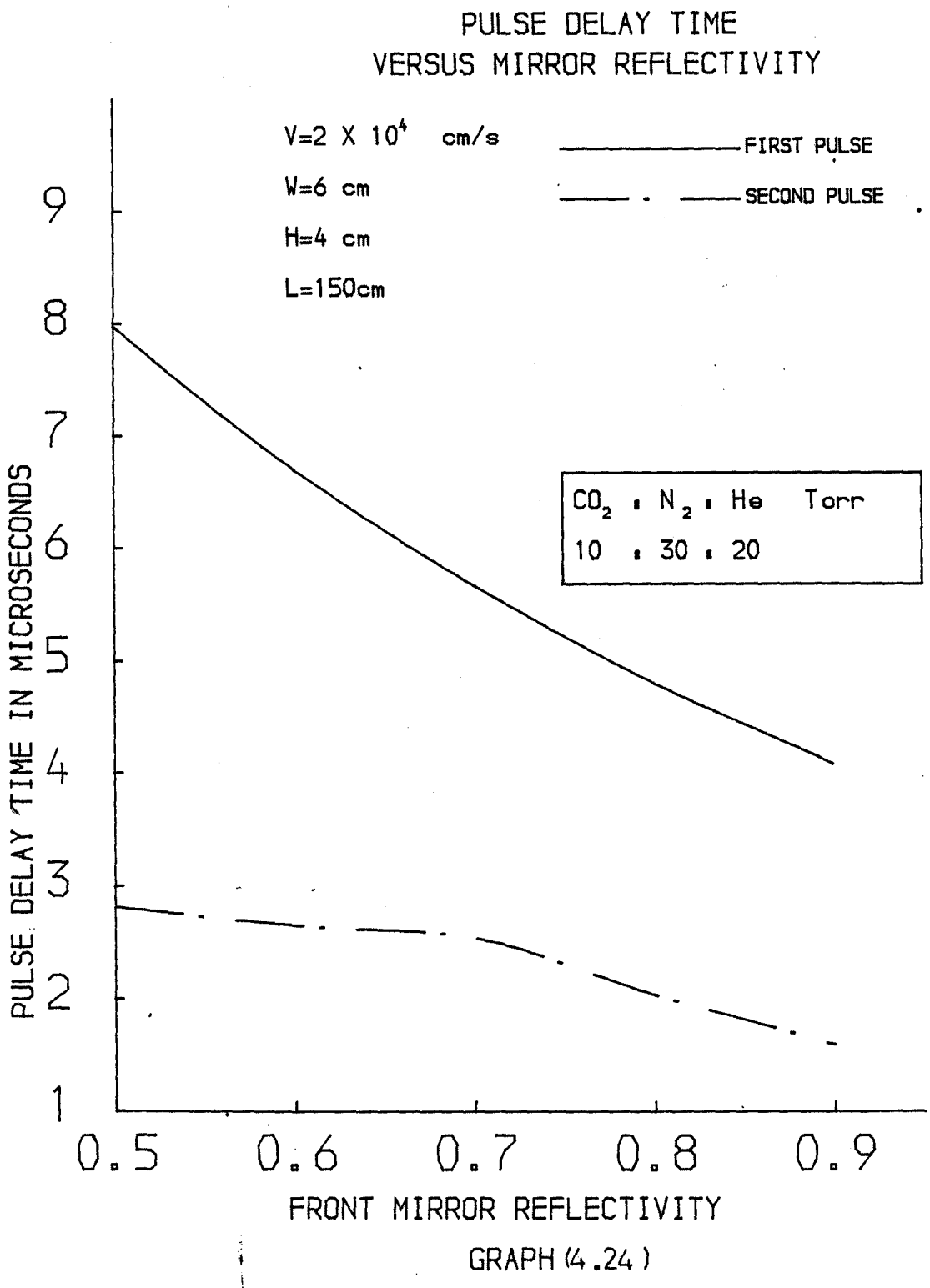
PULSE DELAY TIME
VERSUS MIRROR REFLECTIVITY
V=2 X 10^4 cm/s
W=6 cm
H=4 cm
L=150cm
FIRST PULSE
SECOND PULSE
CO2 : N2 : He Torr
10 : 30 : 20
PULSE DELAY TIME IN MICROSECONDS
1
2
3
4
5
6
7
8
9
0.5
0.6
0.7
0.8
0.9
FRONT MIRROR REFLECTIVITY

GRAPH (4.24)

MAXIMUM POWER
VERSUS MIRROR REFLECTIVITY

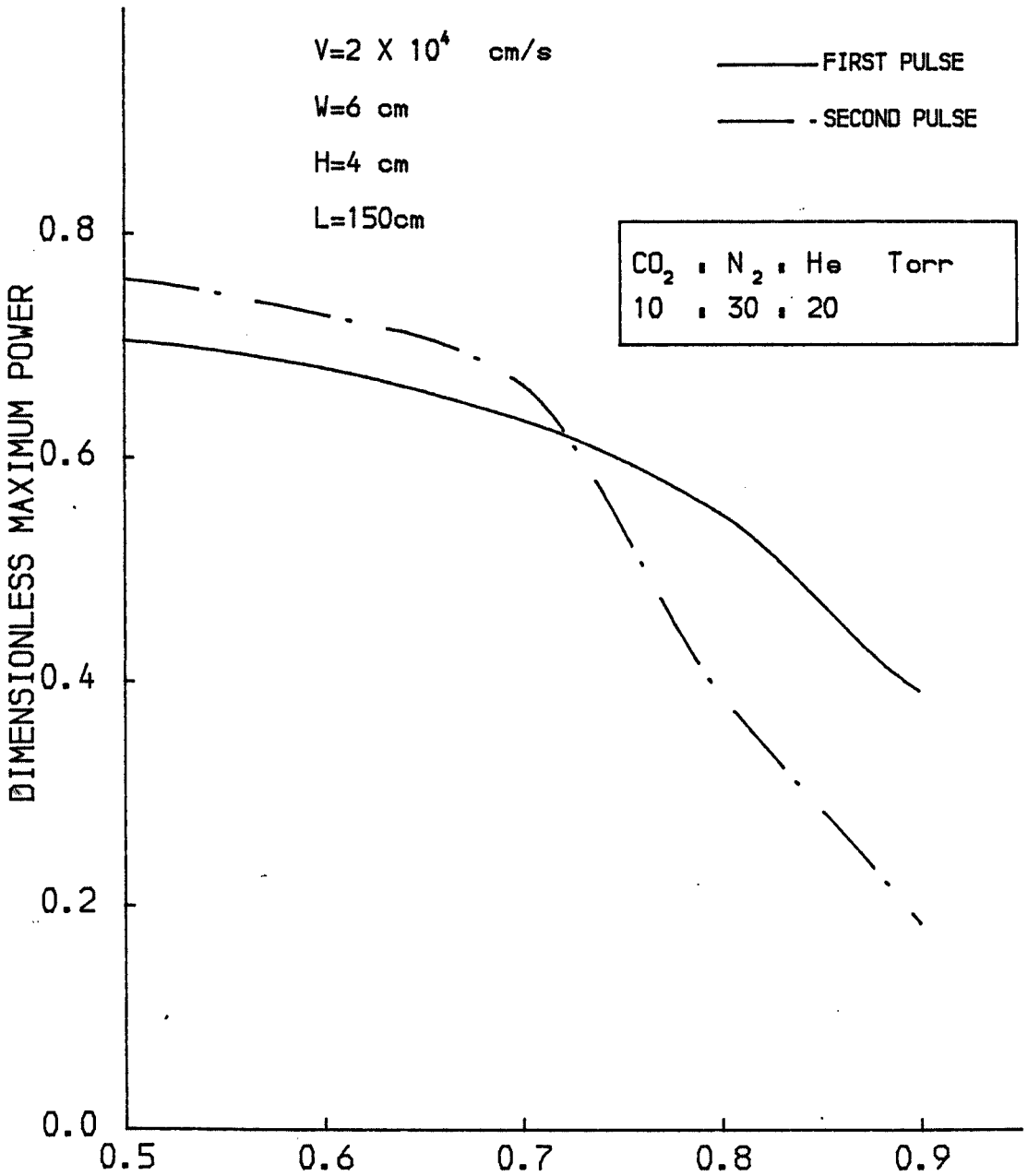

GRAPH (4.25)

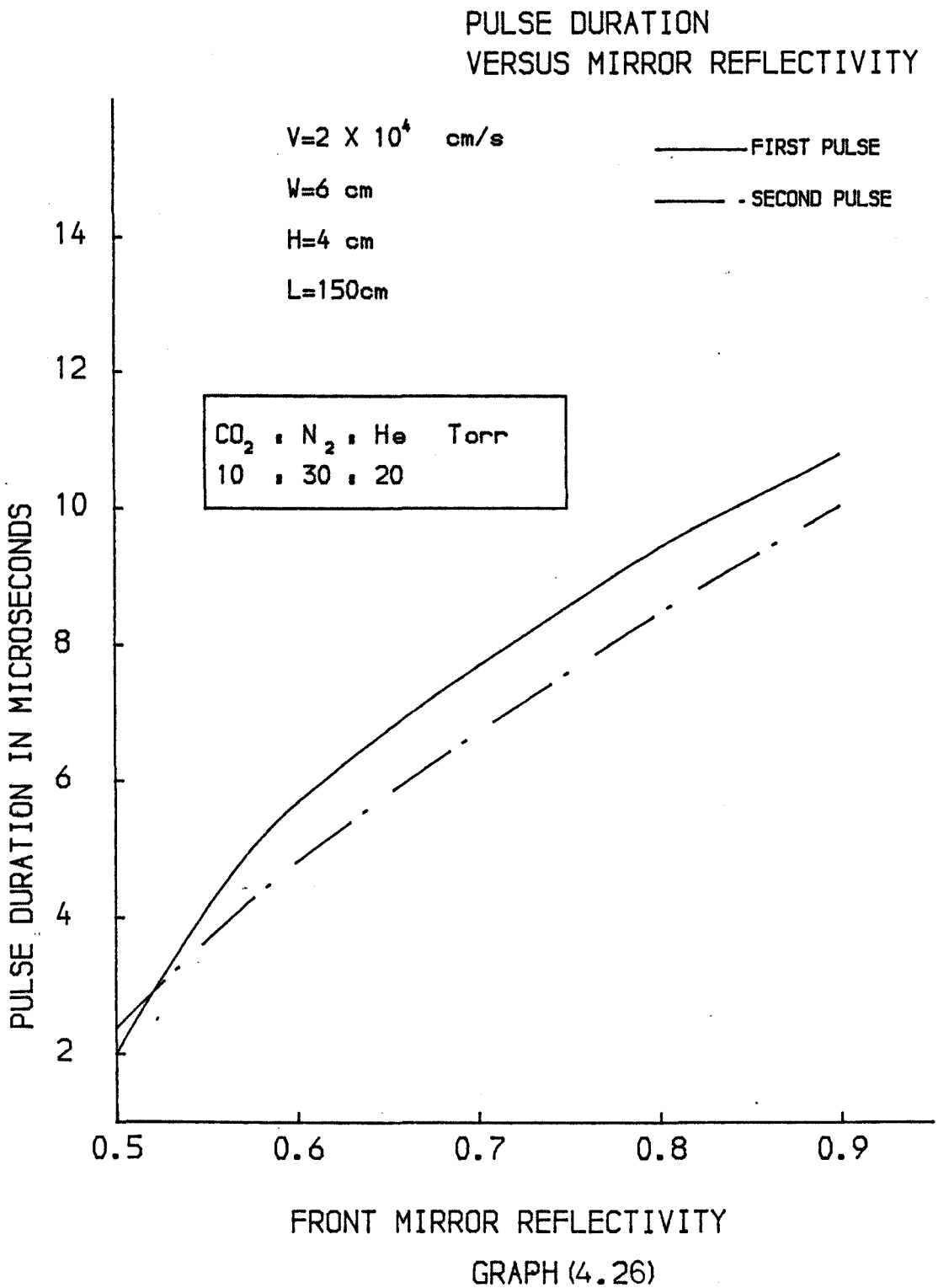
PULSE DURATION
VERSUS MIRROR REFLECTIVITY
V=2 X 10^4 cm/s
W=6 cm
H=4 cm
L=150cm
FIRST PULSE
SECOND PULSE
CO2 : N2 : He Torr
10 : 30 : 20
PULSE DURATION IN MICROSECONDS
14
12
10
8
6
4
2
0.5
0.6
0.7
0.8
0.9
FRONT MIRROR REFLECTIVITY

GRAPH (4.26)

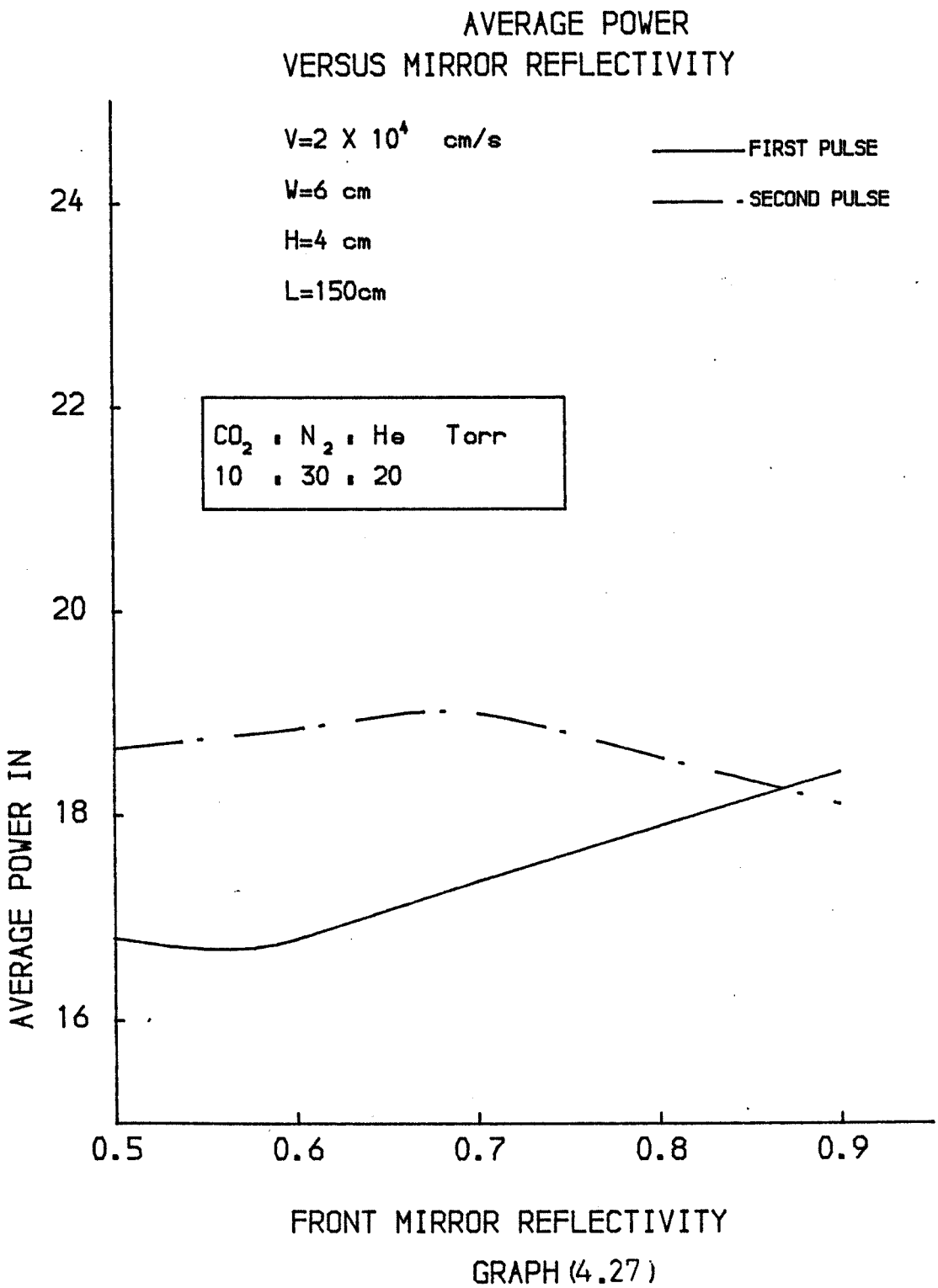
AVERAGE POWER
VERSUS MIRROR REFLECTIVITY
V=2 X 10^4 cm/s
W=6 cm
H=4 cm
L=150cm
FIRST PULSE
SECOND PULSE
CO2 : N2 : He Torr
10 : 30 : 20
AVERAGE POWER IN
24
22
20
18
16
0.5
0.6
0.7
0.8
0.9
FRONT MIRROR REFLECTIVITY

GRAPH (4.27)

OVERALL EFFICIENCY (%)
VERSUS MIRROR REFLECTIVITY

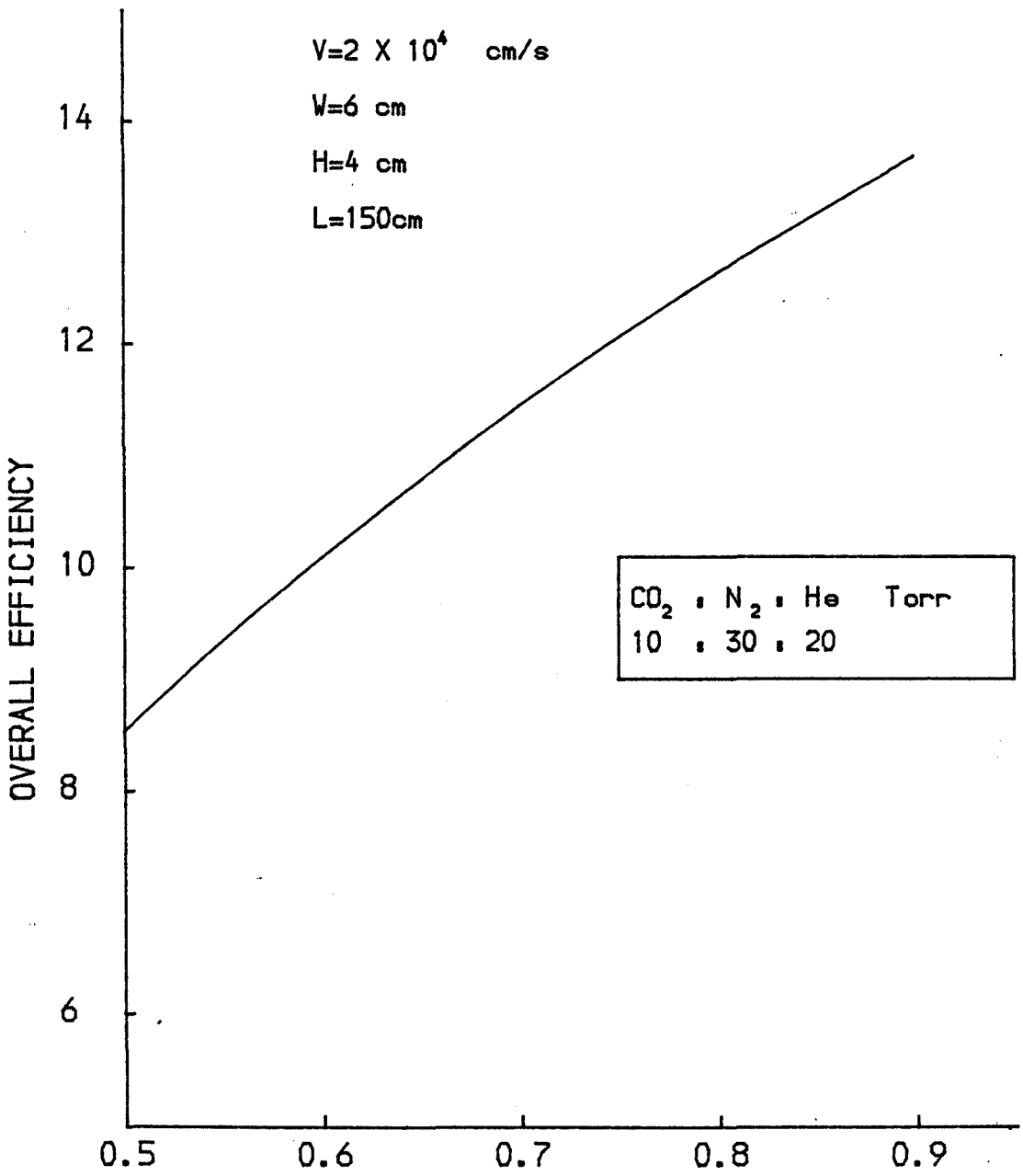

GRAPH (4.28)

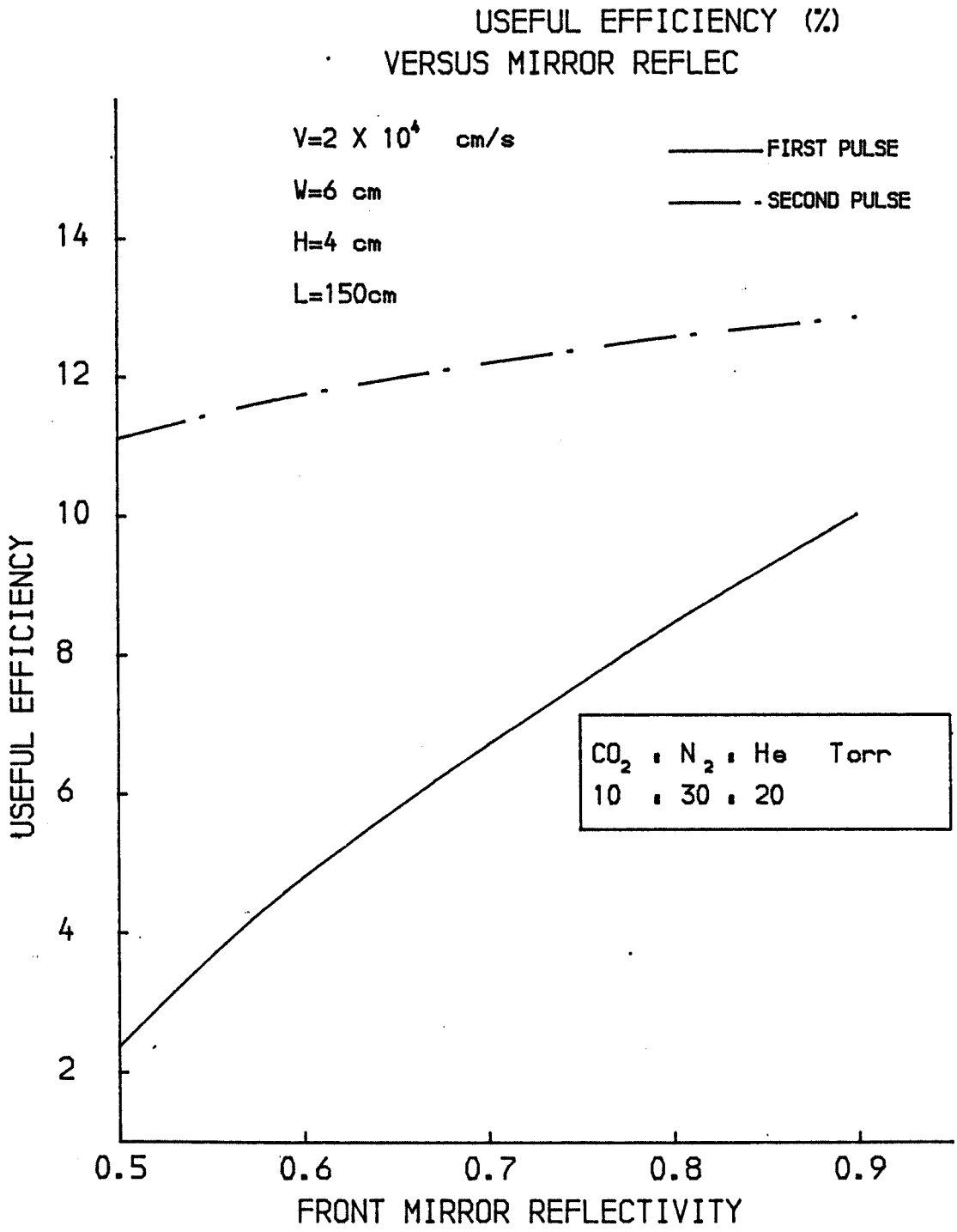
USEFUL EFFICIENCY (%)
VERSUS MIRROR REFLEC
V=2 X 10⁴ cm/s
W=6 cm
H=4 cm
L=150cm
FIRST PULSE
SECOND PULSE
14
12
10
8
6
4
2
USEFUL EFFICIENCY
CO₂ : N₂ : He Torr
10 : 30 : 20
0.5
0.6
0.7
0.8
0.9
FRONT MIRROR REFLECTIVITY

GRAPH (4.29)

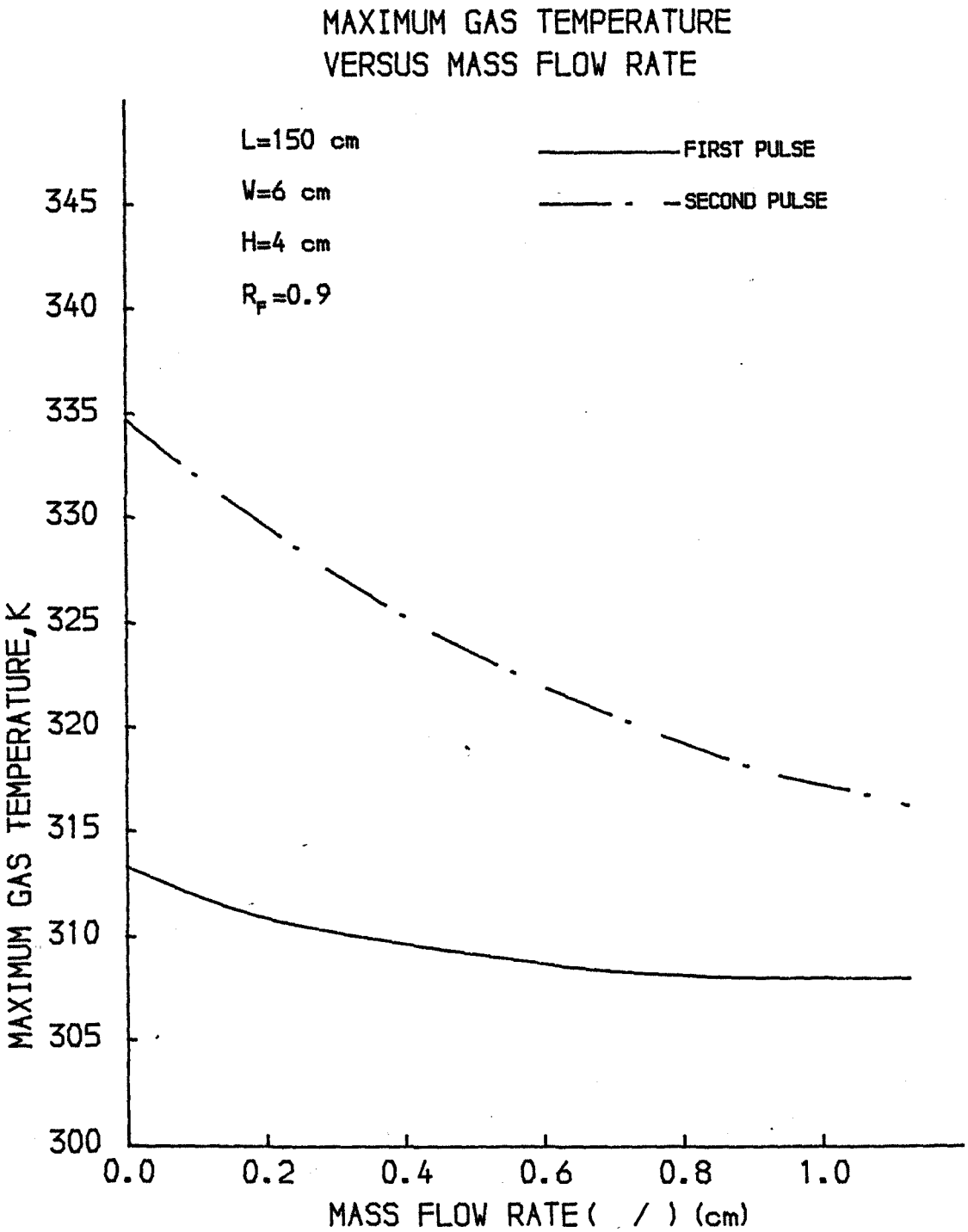
MAXIMUM GAS TEMPERATURE
VERSUS MASS FLOW RATE
L=150 cm
W=6 cm
H=4 cm
R_F=0.9
FIRST PULSE
SECOND PULSE
MAXIMUM GAS TEMPERATURE, K
345
340
335
330
325
320
315
310
305
300
0.0
0.2
0.4
0.6
0.8
1.0
MASS FLOW RATE(/) (cm)

GRAPH (4.30)

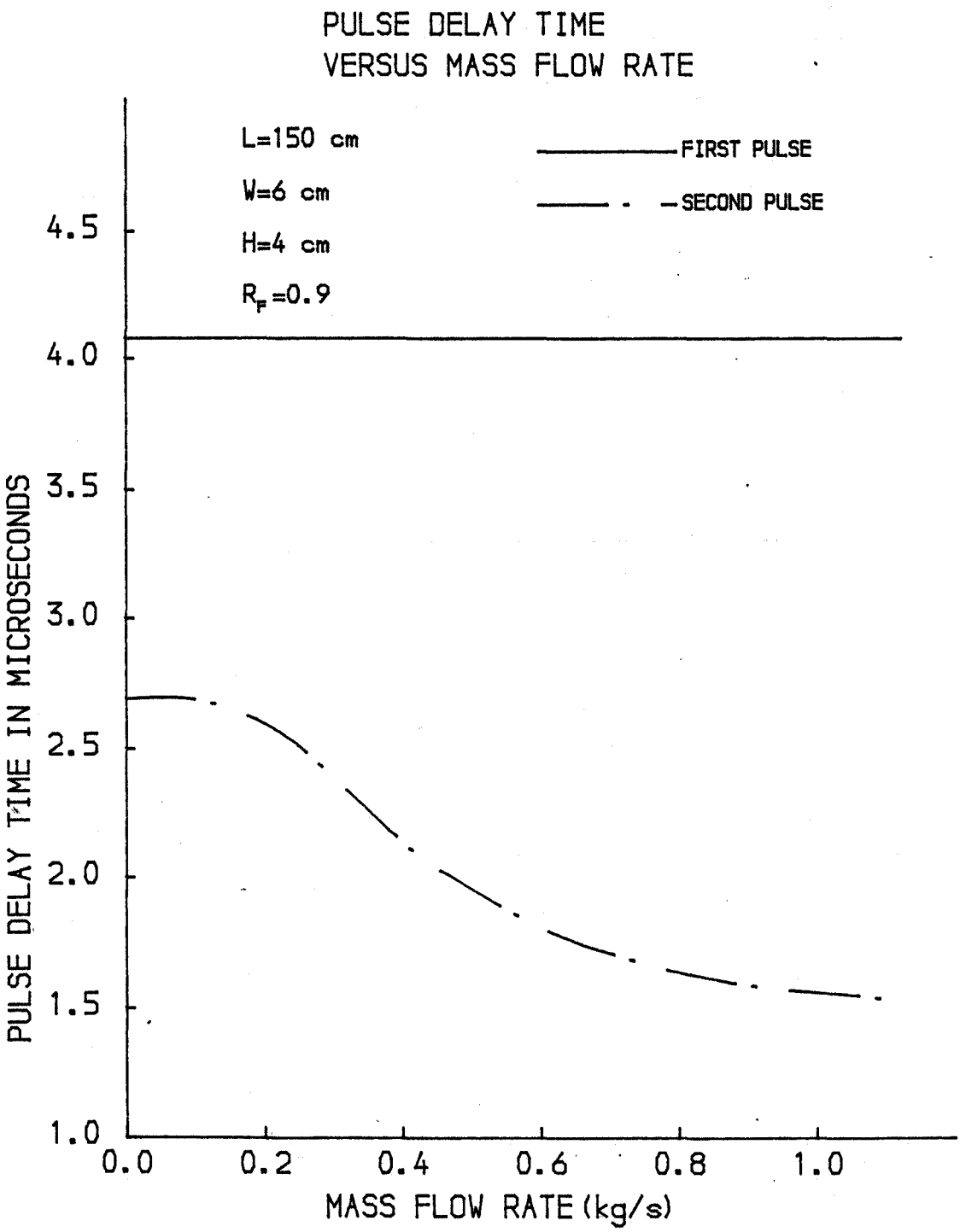
PULSE DELAY TIME
VERSUS MASS FLOW RATE
L=150 cm
W=6 cm
H=4 cm
R_F=0.9
FIRST PULSE
SECOND PULSE
PULSE DELAY TIME IN MICROSECONDS
4.5
4.0
3.5
3.0
2.5
2.0
1.5
1.0
0.0
0.2
0.4
0.6
0.8
1.0
MASS FLOW RATE (kg/s)

GRAPH (4.31)

MAXIMUM POWER VERSUS MASS FLOW RATE

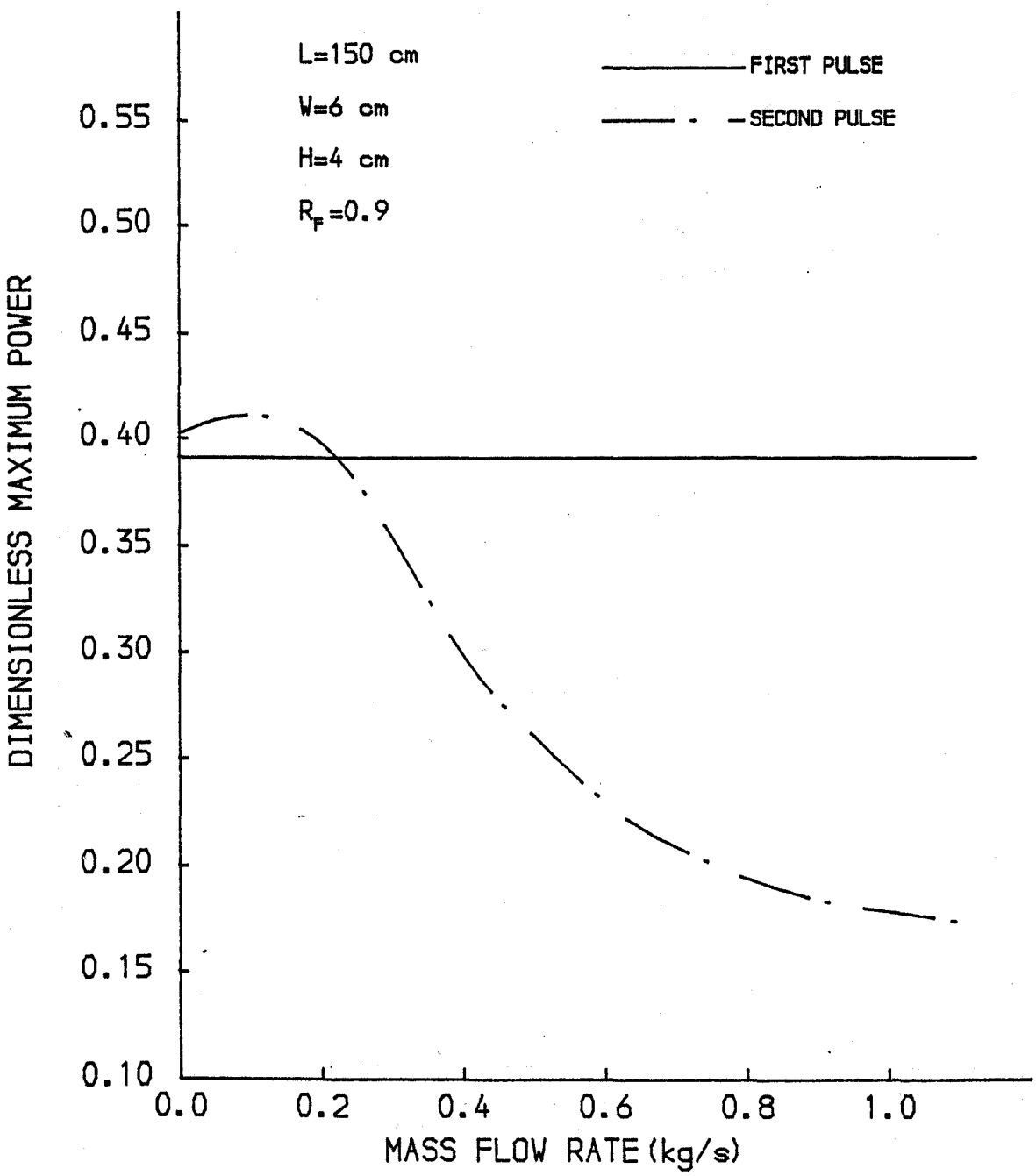

GRAPH (4.32)

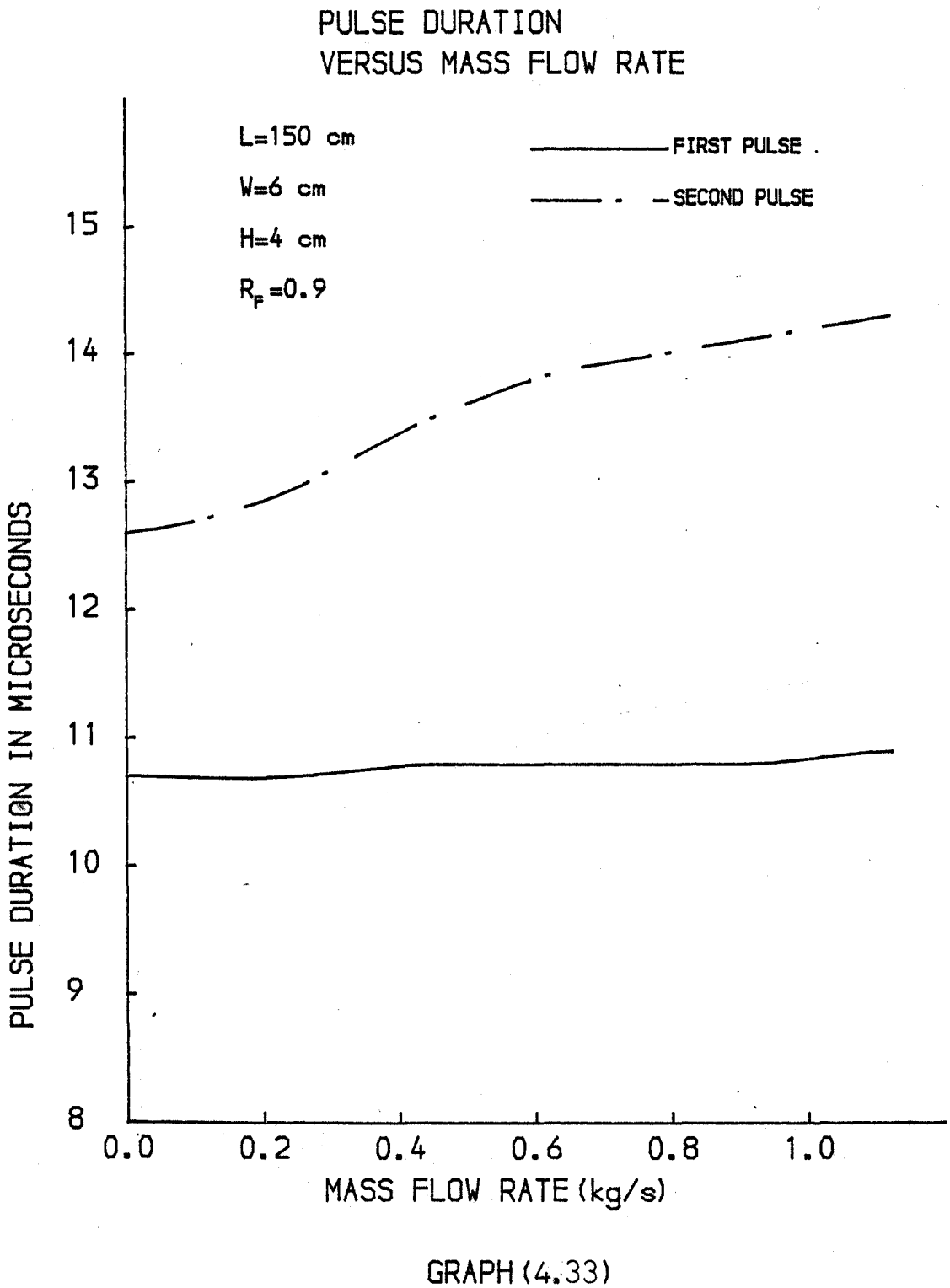
PULSE DURATION
VERSUS MASS FLOW RATE
L=150 cm
W=6 cm
H=4 cm
R_F=0.9
FIRST PULSE
SECOND PULSE
PULSE DURATION IN MICROSECONDS
15
14
13
12
11
10
9
8
0.0
0.2
0.4
0.6
0.8
1.0
MASS FLOW RATE (kg/s)

GRAPH (4.33)

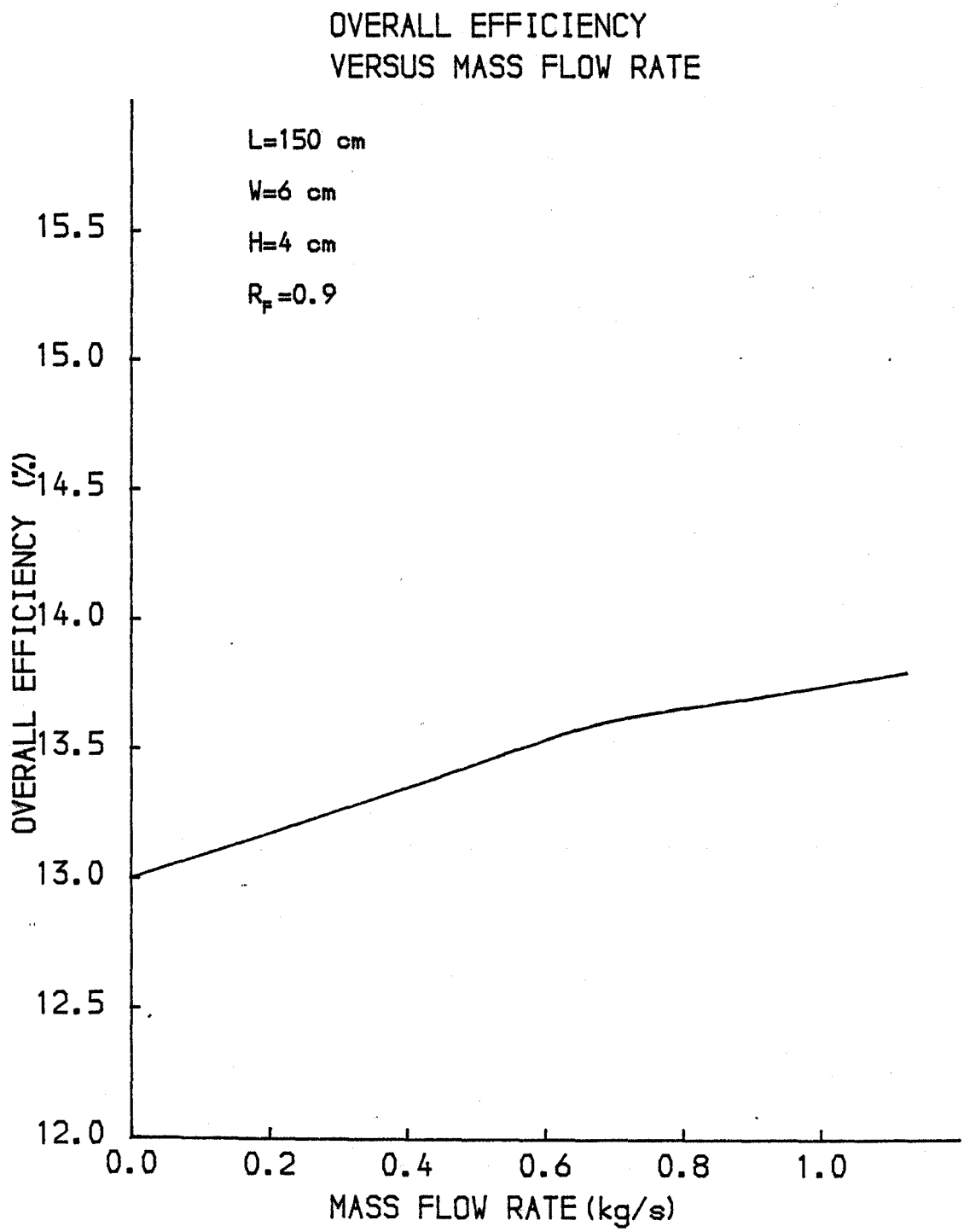
OVERALL EFFICIENCY
VERSUS MASS FLOW RATE
L=150 cm
W=6 cm
H=4 cm
R_F=0.9
OVERALL EFFICIENCY (%)
15.5
15.0
14.5
14.0
13.5
13.0
12.5
12.0
0.0
0.2
0.4
0.6
0.8
1.0
MASS FLOW RATE (kg/s)

GRAPH (4.34)

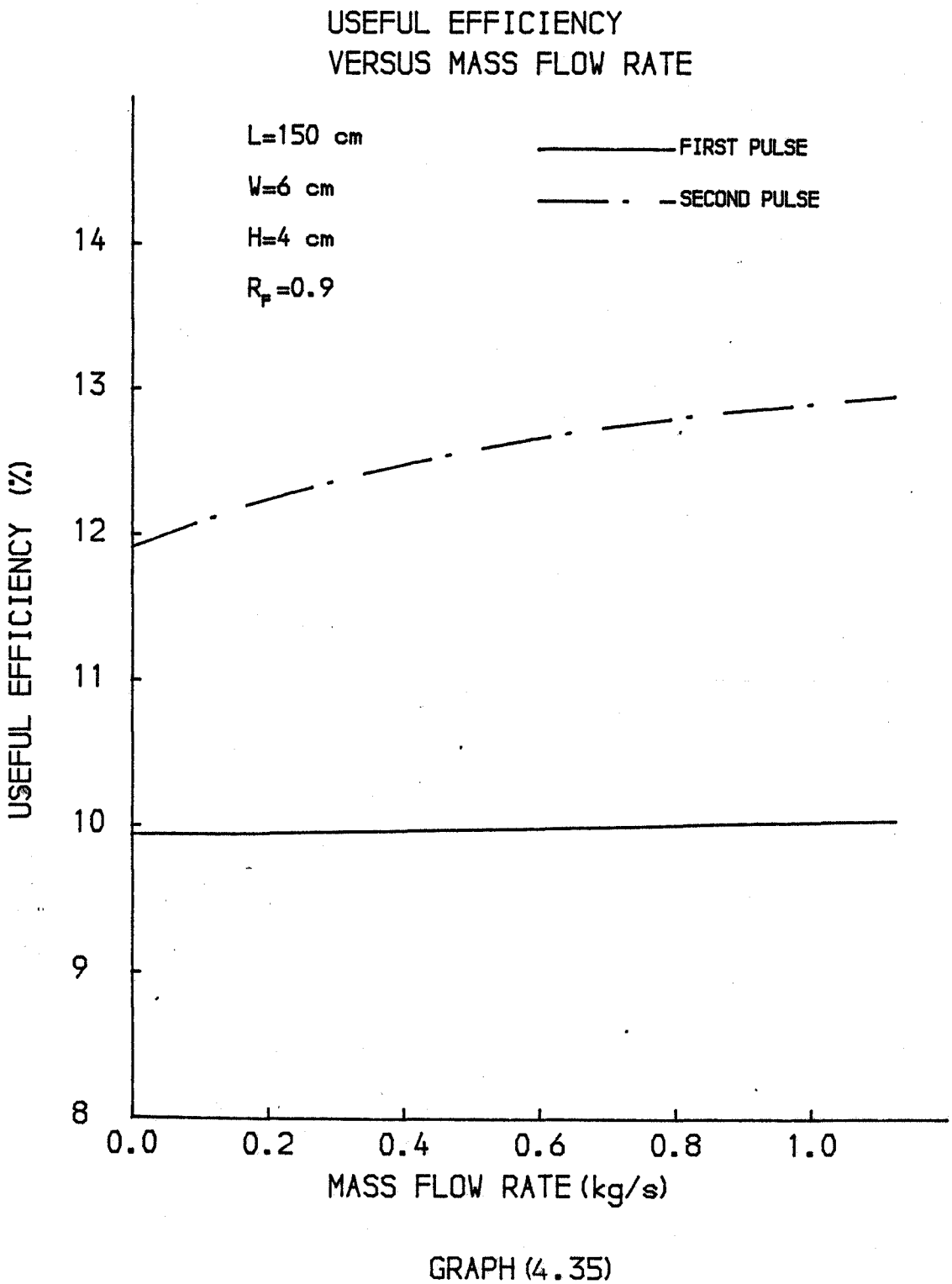
USEFUL EFFICIENCY
VERSUS MASS FLOW RATE
L=150 cm
W=6 cm
H=4 cm
R_p=0.9
FIRST PULSE
SECOND PULSE
USEFUL EFFICIENCY (%)
14
13
12
11
10
9
8
0.0
0.2
0.4
0.6
0.8
1.0
MASS FLOW RATE (kg/s)

GRAPH (4.35)

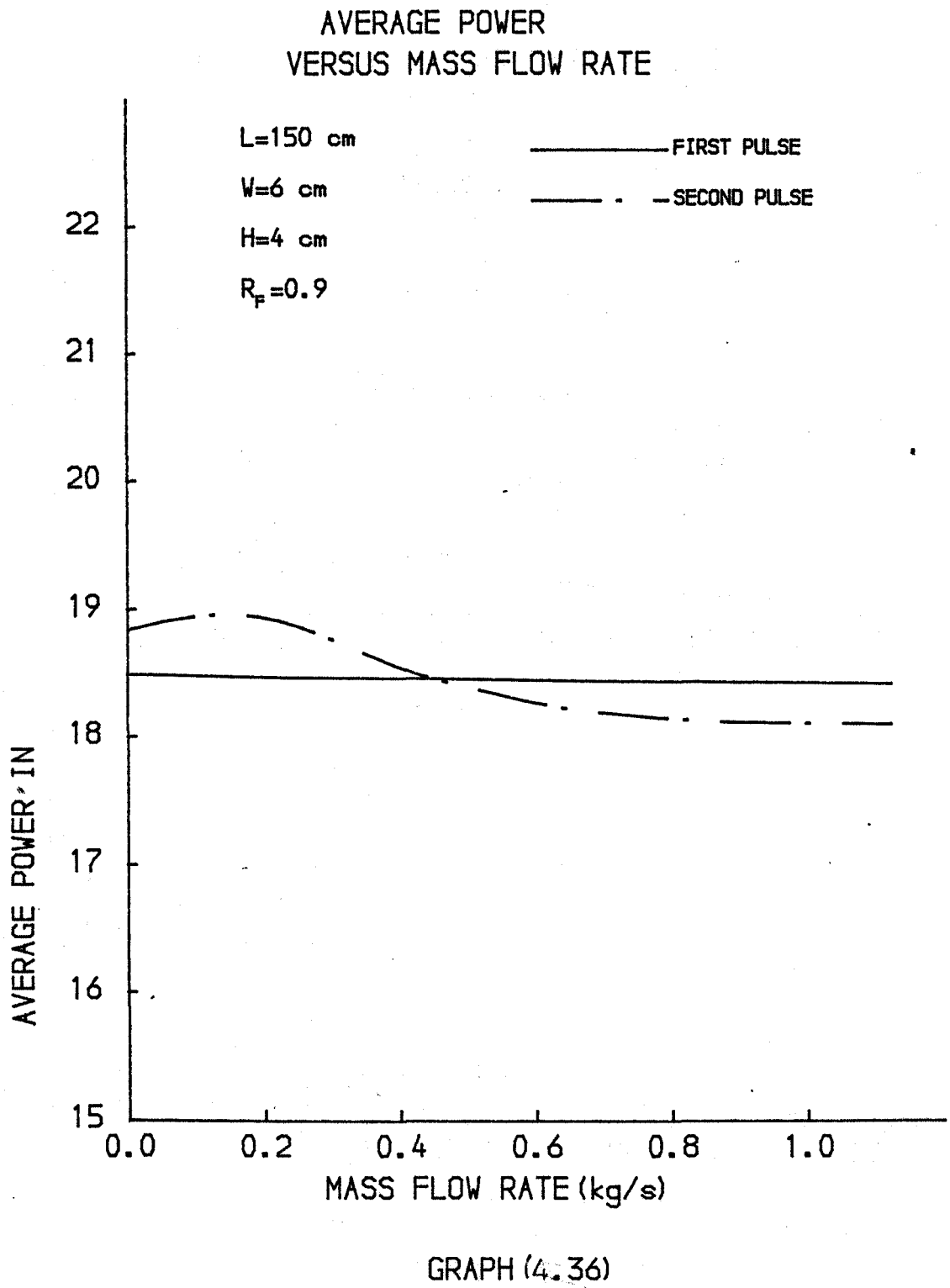
AVERAGE POWER
VERSUS MASS FLOW RATE
L=150 cm
W=6 cm
H=4 cm
R_F=0.9
FIRST PULSE
SECOND PULSE
AVERAGE POWER, IN
22
21
20
19
18
17
16
15
0.0
0.2
0.4
0.6
0.8
1.0
MASS FLOW RATE (kg/s)

GRAPH (4.36)

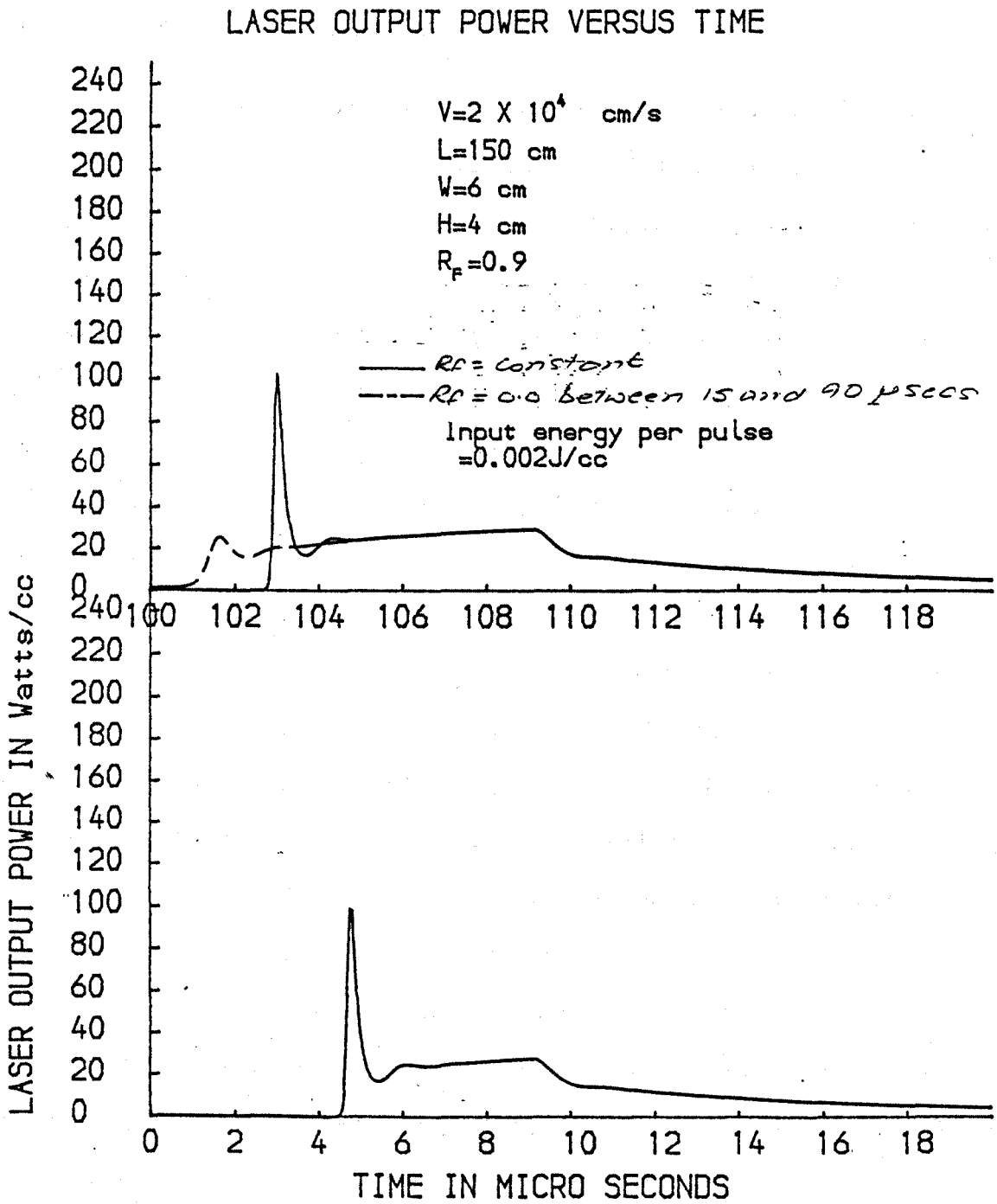
LASER OUTPUT POWER VERSUS TIME
V=2 X 10⁴ cm/s
L=150 cm
W=6 cm
H=4 cm
R_F=0.9
Rf = constant
Rf = 0.0 between 15 and 90 μsecs
Input energy per pulse
=0.002J/cc
LASER OUTPUT POWER IN Watts/cc
TIME IN MICRO SECONDS

GRAPH .(4.37)

CHAPTER FIVE

General conclusions and suggestions for future work

5.1 General Conclusion

5.1.1 Laser-metal interaction

If the laser output is to be matched to workpiece requirements, then the requirements of the workpiece must be known with reasonable accuracy. The Fourier conduction theory has previously been used to determine these requirements. Several workers have however shown that the Fourier theory underestimates the surface temperature. Since matching the laser output to the workpiece requirement is vital for the efficient machining of metals, new models have been developed herein, to rectify the situation.

The transient energy transport in metals caused by absorption of high power laser radiation has been examined, employing a one-dimensional Electron Kinetic theory and the Fourier theory has been used for comparison. Results for Aluminium, Copper, Iron, Nickel and Tantalum demonstrate that the Electron Kinetic theory predicts higher surface temperature and temperature gradients which are in closer agreement with experimental results than the Fourier theory. The graphs highlight the inadequacies of the Fourier theory as a simulation tool for the conditions created by high energy, fast rise time electromagnetic radiation.

The analysis is continued to include vaporisation where it is found that the subsurface energy transport is still a necessary model requirement even after evaporation has started contrary to some published results that assume conduction is neglible once vaporization becomes important. The maximum velocity obtained, of the vaporising front, which is of the order of 1m/s, is in very good agreement with experimental results.

5.1.2 Theoretical CO_2 Laser model

A model has been developed to optimize the laser output to the workpiece needs. The following conclusions summarise the most important points.

The low laser efficiency results in about 90% of the electrical input energy being dumped into the gas mixture thereby increasing the gas temperature. Equations have been developed to model this temperature rise and to simulate the effect of transverse gas flow in reducing the temperature and therefore increasing the laser output power. The results for the first and second pulses show that a significant temperature rise takes place if there is no flow and that a flow rate greater than 0.2 kg/s has a beneficial effect, giving improved laser performance.

In the literature, the solution of the molecular rate equations is normally started by giving the initial intensity an arbitrary value. A method of calculating the spontaneous emmision based on the the solid angle subtended by the mirrors has been

developed.

Computations were also performed for the second pulse since the first pulse is not representative of subsquent pulses due to the equilibrium initial conditions. The results obtained show that the pulse characteristics and power output of the second pulse are very much improved compared to those of the first pulse (i.e from the materials processing standpoint) and that the interaction between successive pulses can be exploited for output tuning.

The theoretical predictions have shown that the pulse profile, intensity and spike height can be controlled using gas mixtures, cavity length, mirror reflectivity and gas flow. These predictions give good qualitative agreement with the available experimental results. Once the laser has been constructed, the cavity length is fixed and the front mirror reflectivity is not readily adjustable. This leaves the gas mixture (total and partial pressures), the pumping pulse, and the gas flow as the parameters that can be used to match the pulse intensity to that required for the generation of non-conduction limited processes within the workpiece.

It has also been shown that changing the reflectivity to zero during the interpulse period and then switching it back just before the second pulse greatly reduces the spike height and delay time and increases the output energy of the second pulse.

Considering the above arguments, it can be concluded from the theoretical analysis that a good compromise would be :

Length between mirrors = 300 cms.

Output mirror reflectivity = 0.9

Mass flow rate = 1.0kg/s corresponding to gas velocity of 200m/s.

The probable range of values for the partial pressures of carbon dioxide, nitrogen and helium are 10, 30, 40 torr to 10, 30, 80 torr respectively.

5.2 Future work

5.2.1 Laser-material interaction

The Electron Kinetic theory can be extended to three dimensions and the effects of radial flow and pressure changes taken into account. This would allow the incorporation of variation of the power intensity distribution in the radial direction. Allowance would also have to be made for electron-phonon collision and phonon-phonon collision in the other directions.

The Electron Kinetic theory can be extended to non-metals such as semiconductors where, because of the small value of thermal conductivity, higher temperature gradients are generated than those obtainable in metals.

5.2.2 Laser modelling

Production of secondary species, especially oxides of nitrogen, carbon monoxide and oxygen, due to dissociation will be minimized due to the relatively high gas velocity through the laser cavity. It would however be worthwhile to determine the actual extent of dissociation especially since some gases like CO

have similar effects to that of nitrogen while free oxygen promotes arcing. Investigations into the effects of dissociation have just started.

Transverse as well as longitudinal variations in intensity result in three-dimensional variation in gain. These three-dimensional effects, the effects of gas transport and density variations with temperature can be dealt with by using a three-dimensional model. The major draw-back with this kind of model is the computing time required, however a model is under development.

APPENDICES

Appendix 2A

The f-parameter in relation to the rate at which the electrons loose energy in elastic collisions with phonons

In the Electron Kinetic theory presented in chapter 2, the parameter f is used to define the energy exchange in an electron-lattice collision process. Riley [1] discussed the problems involved in deriving an expression for the rate at which electrons loose energy in elastic collisions. His model failed to reconcile the idea of multiple collisions which take place in any given volume, with that of a single collision. Yilbas [2] faced similar problems and therefore used an arbitrary value of f (of the order of 10^{-4}) for all metals.

In this analysis, the expression derived by Cravath [3] is used. This expression takes into account the electrons striking the lattice from all angles. This therefore leads to an expression for the average excess energy loss in all collisions expressed as fraction, f, of the average energy difference between electrons and the lattice in any given volume. This expression is given as

$$f(x,t) = \frac{8mM}{3(m+M)} \left[1 - \frac{T_l(x,t)}{T_e(x,t)}\right] \qquad (1)$$

where m and M are the masses of the electron and lattice atoms

respectively, $T_e(x,t)$ and $T(x,t)$ are their temperatures at time t and distance x.

For electrons, $m/M \ll 1$, hence equation (1) becomes

$$f(x,t) = \frac{8m}{3M} \left[1 - \frac{T(x,t)}{T_e(x,t)}\right] \qquad (2)$$

References

1 K.Riley — The thermodynamics of laser induced intercation processes in metals
Ph.D Thesis, University of Birmingham, 1974

2 B.S.Yilbas — Heat Transfer mechanisms initiating the laser drilling in metals
Ph.D Thesis, University of Birmingham, 1982

3 A.M.Cravath — The rate at which ions lose energy in elastic collisions
Phy. Rev., vol.36 p.248 (1930)

Appendix 2B

Simplification of the laser energy term

The energy term is given by the integral

$$\int_{-\infty}^{\infty}\int_{0}^{\pi/2}\exp\left(-\frac{x-\varepsilon}{\lambda\cos\omega}\right)\frac{\sin\omega}{\cos\omega^{2}}\left|\int_{\varepsilon}^{x} I_{o}\,\delta\exp(-\delta p)dp\right|\,d\omega d\varepsilon \qquad (1)$$

The solution of the inner integral

$$\left|\int_{\varepsilon}^{x} I_{o}\,\delta\exp(-\delta p)dp\right| \qquad (2)$$

is obtained first.

This integral must be divided into three regions:

(i) $\varepsilon < 0$

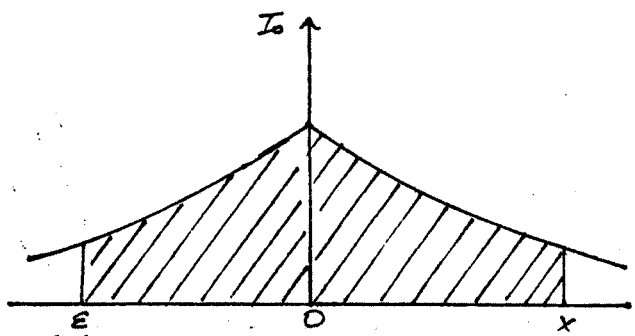

The integral becomes

$$I_0 - I_0\exp(\delta\varepsilon) + I_0 - I_0\exp(-\delta x) \qquad (3)$$

(ii) $0 < \varepsilon < x$

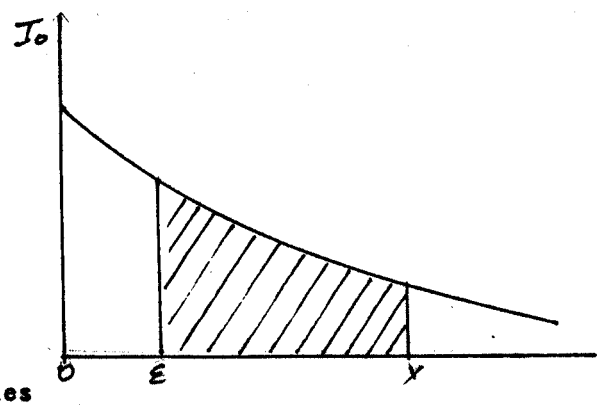

The integral becomes

$$I_0\exp(-\delta\varepsilon) - I_0\exp(-\delta x) \qquad (4)$$

(iii) $\varepsilon > x$

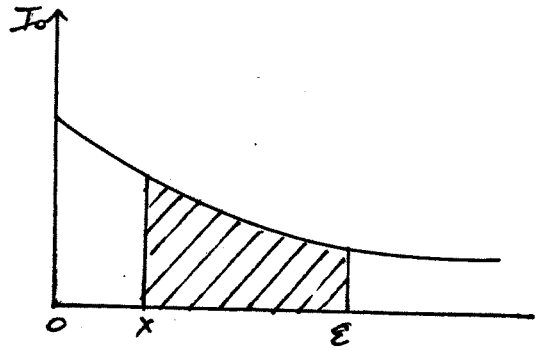

The integral becomes

$$I_0\exp(-\delta x) - I_0\exp(-\delta\varepsilon) \qquad (5)$$

Hence (1) becomes

$$\int_{\infty}^{0}\int_{0}^{\pi/2}\exp\left(-\frac{x-\varepsilon}{\lambda\cos\omega}\right)\frac{\sin\omega}{\cos\omega}\left[2I_0 - I_0\exp(\delta\varepsilon) - I_0\exp(-\delta x)\right]d\omega d\varepsilon$$

$$\int_{0}^{x}\int_{0}^{\pi/2}\exp\left(-\frac{x-\varepsilon}{\lambda\cos\omega}\right)\frac{\sin\omega}{\cos\omega}\left[I_0\exp(-\delta\varepsilon) - I_0\exp(-\delta x)\right]d\omega d\varepsilon$$

$$\int_{0}^{x}\int_{0}^{\pi/2}\exp\left(-\frac{x-\varepsilon}{\lambda\cos\omega}\right)\frac{\sin\omega}{\cos\omega}\left[I_0\exp(-\delta x) - I_0\exp(-\delta\varepsilon)\right]d\omega d\varepsilon \qquad (6)$$

Because of the tedious algebra involved in solving the above equations in the form given, the order of integration is reversed. Further simplification and substitution gives

$$I_0\lambda\left\{\exp(-\delta x)\cdot\ln\left|\frac{1+\lambda\delta}{1-\lambda\delta}\right| - 2\lambda^2\delta^2\int_{1}^{\infty}\frac{\exp(-xu/\lambda)\,du}{u(u^2-\lambda^2\delta^2)}\right\} \qquad (7)$$

As expected, integrating (7) all over x gives I_0, the power intensity getting in the material.

Appendix 2C

Existence of the singular integral

The existence of the integral

$$\int_b^\infty \frac{e^{-u}\,du}{u(u-a)(u+a)} \qquad \text{for } b<a \qquad (1).$$

This is shown graphically in fig. 1

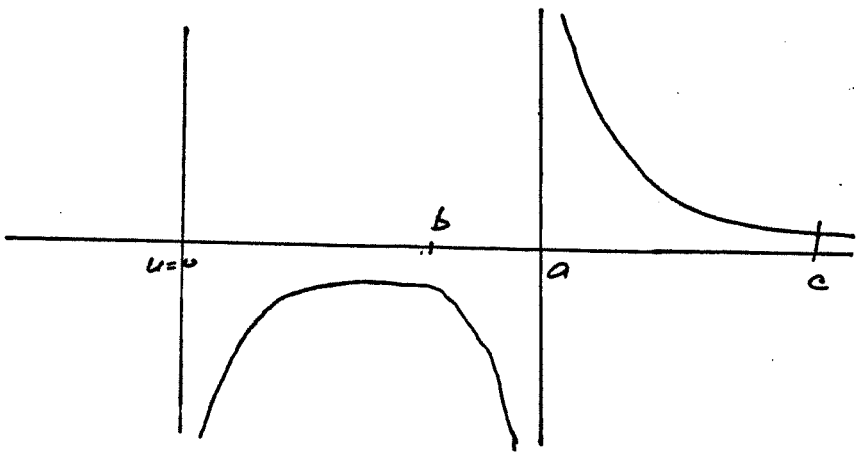

The principal value of the integral is given by

$$P\int_b^c \frac{e^{-u}\,du}{u(u-a)(u+a)}$$

$$= \lim_{\varepsilon\to 0}\left\{ \int_b^{a-\varepsilon} \frac{e^{-u}\,du}{u(u-a)(u+a)} + \int_{a+\varepsilon}^{c} \frac{e^{-u}\,du}{u(u-a)(u+a)} \right\} \qquad (2)$$

Letting u = a−v for the first integral and u = a+v for the second, equation (1) becomes

$$\lim_{\varepsilon\to 0}\left\{ \int_{a-b}^{\varepsilon} \frac{e^{-a}e^{v}(-dv)}{(a-v)(-v)(2a-v)} + \int_{\varepsilon}^{c-a} \frac{e^{-a}e^{-v}\,dv}{(a+v)(v)(2a+v)} \right\} \qquad (3)$$

$$= \lim_{\varepsilon \to 0} \left\{ -e^{-a} \int_{\varepsilon}^{a-b} \frac{e^{v}\,dv}{v(a-v)(2a-v)} + e^{-a} \int_{\varepsilon}^{c-a} \frac{e^{-v}\,dv}{(a+v)(v)(2a+v)} \right\} \quad (4)$$

Since the integral is well-behaved everywhere except at u=a, the proof can be simplified by the subtitution of

$$k = a-b = a-c \qquad (5)$$

without any loss of generality. Therefore equation (4) becomes

$$\lim_{\varepsilon \to 0} \left\{ -e^{-a} \int_{\varepsilon}^{k} \frac{e^{v}\,dv}{v(a-v)(2a-v)} + e^{-a} \int_{\varepsilon}^{k} \frac{e^{-v}\,dv}{v(a+v)(2a+v)} \right\} \quad (6)$$

$$= e^{-a} \lim_{\varepsilon \to 0} \left\{ \int_{\varepsilon}^{k} \frac{1}{v} \left[\frac{e^{-v}}{(a+v)(2a+v)} - \frac{e^{v}}{(a-v)(2a-v)} \right] dv \right\} \quad (7)$$

$$= e^{-a} \lim_{\varepsilon \to 0} \left\{ \int_{\varepsilon}^{k} \frac{1}{v} \left[f(v) - f(-v) \right] dv \right\} \quad (8)$$

where $f(v) = e^{-v}/(a+v)(2a+v)$ (9)

Using the Maclaurin's expansion for small v,

$$f(v) = a_0 + a_1 v + a_2 v^2 + a_3 v^3 + \ldots.$$
$$f(-v) = a_0 - a_1 v + a_2 v^2 - a_3 v^3 + \ldots. \qquad (10)$$

Therefore,

$$f(v) - f(-v) = 2a_1 v + 2\, a_3 v^3 + \ldots. \quad (11)$$

and $(f(v) - f(-v))/v = 2a + 2\, a_3 v^2 + \ldots. \quad (12)$

Hence the integral exists as $v \longrightarrow 0$.

Appendix 2D

Analysis of the Fourier heat conduction equation under lasing action

The form of the heat conduction equation appropraite to laser heating in a one-dimensional material can be described by:

$$\frac{\partial}{\partial t}\left[\rho C_p T\right] = \frac{\partial}{\partial x}\left[K\frac{\partial T}{\partial x}\right] + (1-R)\delta I_0 \exp(-\delta x) \qquad x > 0 \qquad (1)$$

where R = R(t) is the metal reflectivity at the surface. The assumptions made in the derivation of the above equation are well documented by Carslaw et al [1].

In equation (1), the first term is the energy change in the workpiece with respect to time, the second is the conduction term and the third is the energy term which is absorbed by the material. This equation, when stated in the form above makes allowance for the temperature dependence of the thermo-physical constants. Since a comparison is needed between the Kinetic theory and the Fourier conduction theory, the density and specific heat capacity are made independent of temperature. This gives

$$\rho C_p \frac{\partial T}{\partial t} = \frac{\partial}{\partial x}\left[K\frac{\partial T}{\partial x}\right] + (1-R)\delta I_0 \exp(-\delta x) \qquad x > 0 \qquad (2)$$

At the surface, the boundary conditions are

$$K\frac{\partial T}{\partial x}\Big|_{x=0} = 0 \qquad (3)$$

and

$$T(\infty, t) = T_0 \qquad (4)$$

with initial condition

$$T(x, 0) = T_0 \qquad (5)$$

The above equation, with its associated boundary and initial conditions is solved using the method of lines and Gear's method [2].

Variation of the thermal conductivity with temperature is taken account of by fitting second order polynomials to the available data [3,4].

References

1 H.S.Carslaw and J.C.Jaeger

Conduction of Heat In Solids

Clarendon Press, Oxford, 1959

2 I.Gladwell and R.Wait (editors)

A survey of Numerical methods for partial differential equations. Clarendon Press, Oxford 1979.

3 A.Goldsmith et al

Handbook of thermo-physical properties of solid materials. Vol. 1 - Elements (melting temperatures above 1000 F), Revised edition . Pergamon, N.Y 1961

4 C.J.Smithells

Metals reference book. 3vols. 4th edition

Butterworth 1967

APPENDIX 3A

Energy balance using the Fourier equation

Integrating the energy equation

$$\frac{\partial}{\partial t}\left[\rho C_p T\right] - V_s \frac{\partial}{\partial s}\left[\rho\, C_p T\right] = \frac{\partial}{\partial s}\left[K\frac{\partial T}{\partial s}\right] + \delta I_0 \exp(-\delta s) \qquad s > 0 \qquad (1)$$

with respect to the space-coordinate s,

$$\int_0^\infty \left[\frac{\partial}{\partial t}\left[\rho C_p T\right] - V_s \frac{\partial}{\partial s}\left[\rho C_p T\right] = \frac{\partial}{\partial s}\left[K\frac{\partial T}{\partial s}\right] + \delta I_0 \exp(-\delta s)\right] ds \qquad s > 0 \qquad (2)$$

is obtained.

Further simplification and the use of the initial and boundary conditions,

$$\left.\begin{aligned} \rho L(Ts)Vs &= K\frac{\partial T}{\partial s}\Big|_{s=0} \\ T(\infty, t) &= T_0 \\ T(0, s) &= T_0 \end{aligned}\right\} \qquad (3)$$

gives

$$I_o = \int_0^\infty \frac{\partial}{\partial t}(\rho C_p T)\, ds + \rho C_p V_s (T_s - T_o) + \rho L(T_s) V_s \qquad (4)$$

This equation is used to check the accuracy of the solution.